

UNIVERSITY OF
BIRMINGHAM

Novel Triggerable Phase Change Materials in Supercooled and Glassy State for Thermal Energy Storage：Synthesis, Characterization, and Performance Analysis

by

Xusheng Zhang

A thesis submitted to the University of Birmingham for the degree of

DOCTOR OF PHILOSOPHY

Birmingham Centre for Energy Storage

School of Chemical Engineering

University of Birmingham

February 2024

UNIVERSITY OF
BIRMINGHAM

University of Birmingham Research Archive

e-theses repository

This unpublished thesis/dissertation is copyright of the author and/or third parties. The intellectual property rights of the author or third parties in respect of this work are as defined by The Copyright Designs and Patents Act 1988 or as modified by any successor legislation.

Any use made of information contained in this thesis/dissertation must be in accordance with that legislation and must be properly acknowledged. Further distribution or reproduction in any format is prohibited without the permission of the copyright holder.

Abstract

This PhD research focuses on thermal energy storage (TES) technology, utilizing triggerable phase change materials (PCMs) for controllable energy release. Conventional PCMs typically release heat through spontaneous crystallization once the temperature falls below their freezing point, rendering them less effective for long-term storage applications. This research addresses these limitations by creating an energy barrier between liquids and crystals, forming supercooled liquids and glassy materials for long-term energy storage. Additionally, both stability and trigger sensitivity are enhanced through specific molecular design. This strategy facilitates simpler and more cost-effective methods for material design and preparation, enhancing the practicality and efficiency of PCMs for long duration storage use. The thesis comprises three distinct yet interconnected parts, and the key findings are summarized as follows:

- The first part is concerned with the development of a long-term mechanically triggerable metal-organic supercooled liquid named MME, using manganese (II) chloride, methylurea, and erythritol. MME features a core-shell molecular structure, where the metal-organic octahedral coordination core from 1 Mn2+ and 4 methylurea molecules and 2 erythritol molecules enhances stability, and the hydrogen bond shell formed by residual erythritol molecules offers triggerability. Characterization techniques such as XRD, EXAFS, XANES, UV-Vis, FTIR, NMR, TEM, and DSC assessed core-shell interactions and the reversible supercooled liquid-to-crystalline transformation, reliant on ligand exchange between erythritol and Cl- ions. By altering the content of erythritol, the storage stability and trigger

sensitivity can be controllably adjusted. For the MME series samples, they can release a maximum heat of approximately 215 kJ/kg and can be stably stored at room temperature for up to three months. The nucleation energy barrier for these samples is around 10-19 J, and the required triggering stress is less than 10 Pa. Thermal cycling showed less than 15% enthalpy loss after 1000 cycles.

- The second part of this work is on the development of a new glassy PCMs, named G-DMI, made from d-mannitol and myo-inositol. G-DMI is cost-effective, scalable, eco-friendly, and non-flammable, featuring a significant cold-crystallization enthalpy. Its crystalline form, DMI, has a charging temperature of 160 °C, a high latent heat of 280 kJ/kg, and a glass transition temperature of 22 °C. DMI can retain its glassy state for over a year at room temperature and rapidly releases nearly 180 kJ/kg of heat at about 60 °C upon thermal triggering. Characterization techniques such as FTIR, NMR, XRD, TEM, and DSC analysed its hydrogen bonding and crystallization. Additionally, iron oxide nanoparticles were integrated into DMI to create Solar DMI, a volumetric solar absorber that absorbs over 95% of solar radiation and efficiently releases stored heat, showcasing its utility in solar-thermal applications.
- The third part introduces a dual-layer thermosensitive energy storage smart window, combining transparent, triggerable PCMs with thermochromic technology to dynamically adjust light transmittance based on temperature. It also improves thermal comfort by heating indoor spaces during cold nights through triggered crystallization with light shielding. The

window consists of two layers: an outer light-regulating layer made of poly (N-isopropylacrylamide) (PNIPAM) modified with tartaric acid (TA) and dimethylacrylamide (DMA), which can tune its lower critical solution temperature (LCST) from 10-70 °C for precise light control. The inner layer, made of calcium chloride hexahydrate (CCH) modified with ethanol and urea, serves as the thermal energy storage layer with a melting point adjustable between 10 and 30 °C and maintains stability in a supercooled state.

Acknowledge

As I complete my dissertation, I am filled with immense gratitude and would like to express my deepest thanks to those who have supported, helped and encouraged me throughout my doctoral journey. This journey, full of challenges and growth, has been a pivotal time in which I have experienced fear and pride, avoidance and complacency, anxiety and strength. Every step, every achievement would not have been possible without your support and guidance.

Firstly, I would like to express my gratitude to Professor Yulong Ding for his invaluable guidance and advice on this research work. His rigorous academic attitude and relentless pursuit have set a benchmark for scholarly research. Throughout my PhD study, Professor Ding's supervision and motivation have been the greatest driving force for me.

I am also deeply grateful to Professor Zhubing He of Southern University of Science and Technology. He provided me with a precious experimental platform and academic guidance, along with tremendous help in both my research and personal life. His trust and recognition over these years have been crucial to me; his support has been an indispensable part of my research journey.

I would like to thank Dr. Zheng Du for introducing me to the world of scientific research and for his support both in research and in life. The many days and nights we spent together, solving problems and sharing successes, were incredibly important for my personal and professional development.

I would also like to thank Xuefeng Lin, Siyuan Dai and Zeyu Niu for their support and care in research and in life. Whether in moments of joy or sorrow, we could always talk and share the little things in life. These simple yet sincere moments have been a warm force that has pushed me forward.

I am grateful to my family, Yong Zhang, Youhua Xu and Xuhong Zhang, for their endless support and strength. Especially my mother, Youhua Xu, whose years of quiet devotion are beyond words. Every bit of progress and success is partly yours.

A special thank you to my girlfriend, Jia Xu, for your selfless support and love. When I felt discouraged and anxious, your encouragement and belief motivated me to carry on. Your understanding and patience gave me the space to focus on my research, even at the cost of our time together. Your company and support are my inexhaustible strength.

Finally, I would like to thank this period of my PhD study and myself during this time. These years of scientific life have not only deepened my understanding of life and the universe but have also become the most valuable asset as I face future challenges.

Table of Contents

Abstract II

Acknowledge V

Table of Contents VII

List of Figures XI

List of Tables XVII

Abbreviations XVIII

Nomenclature XXI

Chapter 1 Introduction 1

1.1 Background 1

1.2 Aims and Objectives 6

1.3 Layout of the Thesis 7

Chapter 2 Literature Review 9

2.1 Thermal Energy Storage Technologies and Materials 9

2.1.1 Thermochemical Energy Storage (TCES) and Materials 9

2.1.2 Sensible Heat Storage (SHS) and Materials 12

2.1.3 Latent Heat Storage (LHS) and Materials 14

2.2 Characteristics of Supercooled Liquids and Glass Transition 22

2.2.1 Supercooled Liquids 22

2.2.2 Conditions for the Formation of Supercooled Liquids 23
2.2.3 Glass Transition Temperature 29
2.2.4 Viscosity and Fragility of Supercooled Liquids 30
2.2.5 Dynamics and Thermodynamic Characteristics of Supercooled Liquids 32
2.3 Glass and Cold Crystallization 37
2.3.1 Glass 37
2.3.2 Cold Crystallization 38
2.4 Long-Term TES Based on Supercooled or Glassy PCMs. 40
2.4.1 Supercooled Liquids as Long-Term TES Materials 41
2.4.2 Glass State Materials as Long-Term TES Materials 53
2.5 Summary 57
Chapter 3 Metal-Organic Supercooled Liquids for Long-Term TES 60
3.1 Introduction 60
3.2 Experimental 62
3.2.1 Materials and Methods 62
3.2.2 Materials Characterizations and Solar Charging/Discharging Experiment 65
3.3 Results and Discussion 73
3.3.1 Coordination Core of Mn-Methylurea Glass 73
3.3.2 Metal Organic Supercooled Liquid 79
3.3.3 Thermodynamics and Kinetics of Phase-Transitions 98

3.3.4 Low Grade Heat from Solar for Charging and Discharging Demonstration ... 116

3.4 Conclusions ... 123

Chapter 4 Organic Glassy Materials for Long-Term TES ... 125

4.1 Introduction ... 125

4.2 Experimental ... 126

4.2.1 Materials and Methods ... 126

4.2.1 Materials Characterizations and Solar Charging/Discharging Experiment ... 127

4.3 Results and Discussion ... 131

4.3.1 Properties and Structure Characterization of G-DMI and DMI ... 131

4.3.2 Micro Morphologies of G-DMI and DMI ... 138

4.3.3 Kinetic Performance of G-DMI ... 141

4.3.4 Solar Charging and Discharging Demonstration. ... 144

4.4 Conclusions ... 147

Chapter 5 Dual-Layer Thermos-Responsive Energy Storage Smart Window ... 149

5.1 Introduction ... 149

5.2 Experimental ... 153

5.2.1 Materials and Methods ... 153

5.2.2 Materials Characterizations and Experiment Setup. ... 155

5.3 Results and Discussion ... 158

5.3.1 The Structure of DLTRES Smart Window and Working Mechanisms ... 158

5.3.2 PNIPAM-DMA or PNIPAM-TA as TRMs 161

5.3.3 CCH-EtOH and CCH-UR as Energy-Storage Layer Materials 166

5.3.4 Thermal and Mechanical Responsive Properties of DLTRES Device 171

5.3.5 Energy-Saving Demonstration 177

5.4 Conclusions 183

Chapter 6 Conclusions 186

6.1 Summary of the Main Conclusions 186

6.2 Recommendations for Future Work 189

Appendix Publications and Presentations 191

Bibliography 192

List of Figures

Figure 1-1 Energy-Related CO2 emissions (2010-2050). 9 2

Figure 1-2 Operating Temperatures and Time Ranges of TES Technologies Studied. 30 3

Figure 2-1 Schematic diagram of the charging and discharging mechanism in TCES. 49 10

Figure 2-2 Long-term SHS technologies..... 14

Figure 2-3 Schematic for Charging and Discharging Processes of Phase Change Material. 75 15

Figure 2-4 Classification of Phase Change Materials 88 17

Figure 2-5 Schematic of Principles for Supercooled and Glassy PCMs 21

Figure 2-6 The relationship of system volume or enthalpy changes with temperature during cooling. 107..... 23

Figure 2-7 Schematic of a Free Energy Barrier for Nucleation.110..... 24

Figure 2-8 Schematic Illustration of Free Energy Variation with Nucleus Size 25

Figure 2-9 Cooling Rate Manipulation for Avoiding Crystallization.112 27

Figure 2-10 The DSC Curve Near the Glass Transition Temperature. 118 30

Figure 2-11 The Variation Characteristics of Viscosity with Temperature in Different Supercooled Liquids. 121..... 31

Figure 2-12 The Dynamic Characteristics of Supercooled Liquids. 34

Figure 2-13 Map of Single Particle Displacements in a 2D Lennard-Jones Model of Supercooled Liquids. 135..... 36

Figure 2-14 Variation of Entropy Difference Between Supercooled Liquids and Crystals with Temperature in Different Systems. 37

Figure 2-15 High-Resolution TEM Images of Crystalline Metal (A) and Glassy Metal (B). 142 ... 38

Figure 2-16 Cold Crystallization in DSC Curve.145 39

Figure 2-17 Relationship between Cooling Rate and Number of Nuclei. 150 40

Figure 2-18 The Properties of Photo-Switchable PCMs. 180 46

Figure 2-19 Comparison of Different MOF Glasses.197 55

Figure 3-1 Preparation Methods and Processes for MM. 64

Figure 3-2 Experimental Setup for Solar Charging. 71

Figure 3-3 The Discharging System Device for Large-Scale Application. 72

Figure 3-4 The Properties of the MM. 74

Figure 3-5 Temperature-Dependent Viscosity of MM. 75

Figure 3-6 Local Geometric Environments around the Mn Atoms in the MM. 77

Figure 3-7 Schematic Illustration of the Elongated MM Octahedral. 78

Figure 3-8 Photographic Images and Optical Properties of the MM, MME1, and c-MME1. 82

Figure 3-9 X-ray Diffraction (XRD) Pattern and In-situ Test Results. 82

Figure 3-10 The thermal properties of MME1. 84

Figure 3-11 Comparison of Viscosity at Room Temperature between MME1and MM. 85

Figure 3-12 The Chemical Structure of MME1. 86

Figure 3-13 Experimental K-edge XANES Spectra of MME1 and c-MME1 and Reference Samples

(MnCl2, MM)..... 87

Figure 3-14 Local Chemical and Geometric Environments of Mn Atoms in MME1 and c-MME1.

..... 93

Figure 3-15 Schematic Illustration of Phase Transition between MME1 and c-MME1. 94

Figure 3-16 Cryogenic Transmission electron microscopy (cryo-TEM) images of MME1 and c-MME1. 97

Figure 3-17 Visual appearance of MME1 to MME4..... 98

Figure 3-18 Fourier-Transform Infrared (FTIR) Spectra of MME Series Samples 99

Figure 3-19 Scanning Electron Microscopy (SEM) Images MME Series Samples. 99

Figure 3-20 Thermal Properties of MME Series Samples. 101

Figure 3-21 Temperature-Dependent Viscosity Measurements of MME Series..... 102

Figure 3-22 Temperature-Dependent Viscosity Measurement and Curve Fitting Using the Vogel-Fulcher-Tammann (VFT) Model. 104

Figure 3-23 Measuring Crystallization Response Time to Shear Force at Rough Interfaces..... 106

Figure 3-24 Measurement of Temperature-Dependent Growth Rate in MME Series Materials.... 108

Figure 3-25 Supporting Figure II for Figure 3-24. 109

Figure 3-26 Supporting Figure III for Figure 3-24..... 110

Figure 3-27 Supporting Figure IV for Figure 3-24. 111

Figure 3-28 Supporting Figure V for Figure 3-24. 111

Figure 3-29 The Kinetic Properties of MME Series Samples. 115

Figure 3-30 Comparison of MME Series Materials, Xylitol, and Sorbitol for Nuclear Energy at Room Temperature. 116
Figure 3-31 Solar Thermal Storage Application. 118
Figure 3-32 The Solar Charging Temperature Traces. 119
Figure 3-33 World Map of Horizontal Solar Irradiation with the Intensity Criteria. 246 121
Figure 3-34 Characteristics for Large-Scale Demonstration. 122
Figure 4-1 The Solar Charging System. 131
Figure 4-2 Photographs of G-DMI and DMI. 132
Figure 4-3 XRD patterns for α-D-mannitol, β-D-mannitol, Myo-inositol, and DMI and G-DMI. 133
Figure 4-4 Chemical Interaction Analyses by FTIR and NMR. 135
Figure 4-5 Thermal Properties of DMI and G-DMI 136
Figure 4-6 XRD Analyses during Cold-Crystallization of G-DMI. 137
Figure 4-7 In Situ UV-Vis Transmittance Spectra of the G-DMI 138
Figure 4-8 Microstructure images of G-DMI and DMI. 140
Figure 4-9 Supporting Figure of Figure 4-3. 141
Figure 4-10 Kinetic Properties of G-DMI. 142
Figure 4-11 Temperature-Dependent Viscosity of G-DMI 143
Figure 4-12 Digital and IR Images of the Cold Crystallization Process of G-DMI. 143
Figure 4-13 Solar Charging and Discharging for Solar DMI. 145
Figure 4-14 Thermal Properties of Solar DMI. 146

Figure 4-15 The Solar Charging and the Thermal-Triggered Discharging Temperature Curve of Solar DMI. 147

Figure 5-1 Fabrication Process of DLTRES Demo Device 157

Figure 5-2 Experiments Setup 158

Figure 5-3 Schematic Diagram of the Structure and Principle of the DLTRES Smart Window. 160

Figure 5-4 LCST Tuning by Adding DMA and TA. 161

Figure 5-5 FTIR Spectra of PNIPAM, PNIPAM-DMA, and PNIPAM-TA. 162

Figure 5-6 Temperature-Dependent DLS of PNIPAM particles (white boxes), PNIPAM-TA particles (blue boxes) and PNIPAM-DMA particles (red boxes). 163

Figure 5-7 Contact Angles of PNIPAM, PNIPAM-TA, PNIPAM-DMA at Room Temperature 164

Figure 5-8 Specific Heat Capacity Curve for DI, PNIPAM-DMA, PNIPAM-TA with Respect to the Temperature. 165

Figure 5-9 Cycling Tests Curve of PNIPAM-DMA at the Wavelength of 532 nm. 166

Figure 5-10 Properties of Energy Storage Materials. 168

Figure 5-11 FTIR Spectra for CCH-EtOH. 169

Figure 5-12 Experimental 1H NMR Spectra of CCH, EtOH, and CCH-EtOH (d6-DMSO, 400 MHz). 170

Figure 5-13 DSC Trace of CCH-UR Recorded at a Heating/Cooling Rate of 5 K/min 171

Figure 5-14 FTIR for CCH-UR 171

Figure 5-15 Optical Properties of PNIPAM-DMA 172

Figure 5-16 In-Situ Optical Properties of CCH-EtOH. 174

Figure 5-17 Overall Optical Properties. 175

Figure 5-18 Digital and IR Camera Images of PNIPAM-DMA of Heating and Cooling Processes. 176

Figure 5-19 Digital and IR Camera Images of the CCH-EtOH Crystal Growth after Mechanical Stimulation. 177

Figure 5-20 Cyclic Diagram of the DLTRES Smart Window 178

Figure 5-21 Energy-Saving Demonstration of DLTRES Smart Window. 180

List of Tables

Table 2-1 Some Common Materials Used in TCES. 11

Table 2-2 Some Typical SHS Materials 13

Table 2-3 An Overview of Several Typical PCMs and Their Characteristics 18

Table 2-4 The Summary of SAT for Long-Term TES 43

Table 2-5 Some Single-Component Photo-Switchable PCMs and Their Properties. 49

Table 2-6 Some Composite Photo-Switchable PCMs and Their Properties 53

Table 2-7 The Summary of Organic Glass for Long-Term TES 57

Table 3-1 Curve Fit Parameters a for Mn K-edge EXAFS for MM. 78

Table 3-2 FTIR Peaks and Corresponding Vibrations for Erythritol 87

Table 3-3 FTIR Peaks and Corresponding Vibrations for Methylurea. 88

Table 3-4 Changes in FTIR Peaks and Vibrations for MME1 and c-MME1. 89

Table 3-5 Curve fit Parametersa of Mn K-edge EXAFS for MME1 94

Table 3-6 Curve fit Parameters a of Mn K-edge EXAFS for c-MME1. 95

Table 3-7 Comparative enthalpy of phase transition for c-MME materials. 101

Table 3-8 Comparison of the Viscosities of Different Supercooled Liquids 103

Abbreviations

Abbreviation	Description
TES	Thermal Energy Storage
TCES	Thermochemical Energy Storage
SHS	Sensible Heat Storage
LHS	Latent Heat Storage
PCM	Phase Change Material
PEG	Polyethylene Glycol
CNT	Classical Nucleation Theory
GFA	Glass-Forming Ability
MSD	Mean-Squared Displacement
SISF	Self-Intermediate Scattering Function
KWW	Kohlrausch-Williams-Watts
PLA	Polylactic Acid
SAT	Sodium Acetate Trihydrate
MOF	Metal-Organic Framework
XRD	X-Ray Diffraction
EXAFS	X-Ray Absorption Fine Structure
XANES	X-Ray Absorption Near Edge Structure
UV-Vis	Ultraviolet-Visible

FTIR	Fourier Transformed Infrared Absorption
MM	Mn-Methylurea (1:4) complex
MME	MM@Erythritols
c-MME	Crystalline MME
NMR	Nuclear Magnetic Resonance
SEM	Scanning Electron Microscopy
DSC	Differential Scanning Calorimetry
DLS	Dynamic Light Scattering
ATR	Attenuated Total Reflectance
TGA	Thermogravimetric Analysis
SAED	Selected Area Electron Diffraction
IEA	International Energy Agency
PNIPAM	Poly(N-isopropylacrylamide)
LCST	Low Lower Critical Solution Temperature
DLTRES	Dual-Layer Thermo-Responsive Energy-Storage
DMA	Dimethylacetamide
TA	Tartaric Acid
PNIPAM-DMA	DMA Modified PNIPAM
PNIPAM-TA	TA Modified PNIPAM
TRM	Thermo-Responsive Materials

EtOH	Ethanol

Nomenclature

Symbol	Description
Q	Energy
V	Volume
T	Temperature
C_p	Specific Heat
ρ	Density
M	Mass
H	Enthalpy
G	Free Energy
S	Entropy
ΔH	Enthalpy Difference
ΔG	Free Energy Difference
ΔS	Entropy Difference
g	Free Energy Density
Δg	Free Energy Density Difference
Δh	Molar Phase Change Enthalpy
R	Radius
σ	Surface Energy
Γ	Nucleation Time

k_B	Boltzmann Constant
j_N	Nucleation Rate
r	Cooling Rate
m	Fragility
η	Viscosity
E_a	The Activation Energy
T_k	Kauzmann Temperature
ΔT	Supercooling Degree
v	Growth Velocity of Crystal
k	Jump Frequency
f	Site Factor
D	Diffusion Coefficient
λ	Jump Distance
N_{Av}	Avogadro Constant
γ	Ledge Energy
W_s	Energy for Circular Layer Formation
$\Delta\mu$	Chemical Potential Difference
ΔG_N^*	The Minimum Nucleation Free Energy
φ	Solar-Thermal Conversion Efficiency
k	Heating Rate

T_{lum}	Luminous Transmittance
ΔT_{lum}	Luminous Transmittance Difference
T_{IR}	IR Transmittance
ΔT_{IR}	IR Transmittance Difference
ΔT_{sol}	Solar Modulating Ability
q	Heat Load Index
A	Area
t	Time

Subscripts

i	Initial
f	Final
m	Melting
s	Solid Phase
l	Liquid Phase
c	Critical Value
g	Glass Transition
min	Minimum
cc	Cold Crystallization
iso	Isomerization

p	Phase Change
tot	Total
v	Molar Volume
r	Responsive
sc	Surface Centre
bc	Body Centre
a	Ambient

Chapter 1 Introduction

1.1 Background

Climate change has been recognised to pose a significant challenge to humanity worldwide for several decades, and evidence of getting worse is ample. [1] It was after Paris Agreement that the world started seriously exploring ways to reduce greenhouse gas emissions and are committed to achieving long-term decarbonisation goals. [2–5] In the current energy landscape, with fossil fuels accounting for 82% of primary energy consumption. [6], the CO_2 emissions of the energy sector have soared to 36.8 Gt/year. [7] This underscores the role of coal, oil, and natural gas as the main drivers of global climate change, contributing to ~75% of worldwide greenhouse gas emissions and nearly 90% of all CO_2 emissions. [8] The urgency for decarbonizing the energy sector becomes apparent and paramount for mitigating the climate change impacts. As a result, an increasing number of countries, particularly the developed countries (e.g. EU & UK), and largest economies (e.g. US, China, India) have committed to achieve carbon neutrality around 2050-2070. **Figure 1-1** shows an example scenario for neat-zero 2050. One can see it is critical to cut global energy-related CO_2 emissions by 70%, with the majority of this reduction, more than 90%, needs to be accomplished through deep penetration of renewable generation as well as measures to improve energy efficiency. [9]

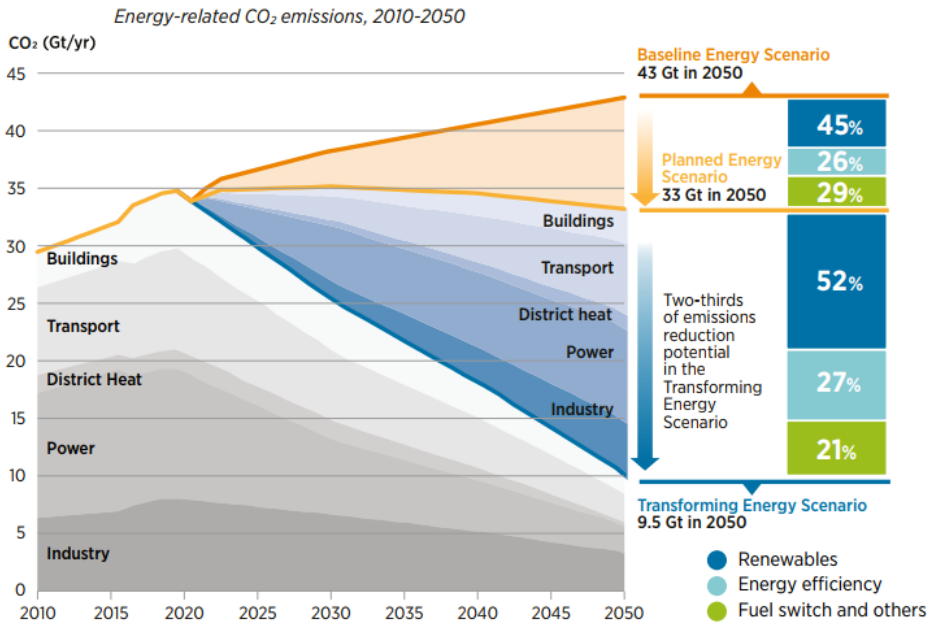


Figure 1-1 Energy-Related CO_2 emissions (2010-2050). [9]

The development of renewable energy technologies, despite being clean and low-carbon in nature, faces intermittency and unpredictability leading to huge challenges in supply-demand mismatches, energy network stability and energy security. [10] To address such challenges, energy storage technology has a key role to play. By storing excess energy and releasing it when needed, energy storage could effectively bridge the temporal and spatial mismatches between energy supply and demand. Energy can be stored in various forms, including mechanical [11–13], electrical [14,15], electrochemical [16–19], chemical [20–23], and thermal [24–27], and hence various storage technologies have been developed. Each of the technologies has merits, depending on the scenarios. One popular way of classifying energy storage technologies is using storage duration. Recent findings from the Royal Society highlight the UK's tiered energy storage needs for a renewables-driven system. Short-term storage requires approximately 100-120 GW/100-200 GWh for up to 6 hours. Medium-term needs,

extending up to a week, are estimated at 100-130 GW/2-6 TWh. For long-term storage, beyond a week, the system needs about 70-80 GW/35-40 TWh. [28] Thermal energy storage (TES) technology — the focus of this study — stands out for its capability to span medium to long storage durations (as shown in **Figure 1-2**). TES is highly scalable, independent of geographical or geological conditions, and has a low cost. [29,30] These position TES as a highly promising option with significant development potential among various storage technical solutions to net-zero 2050 goals.

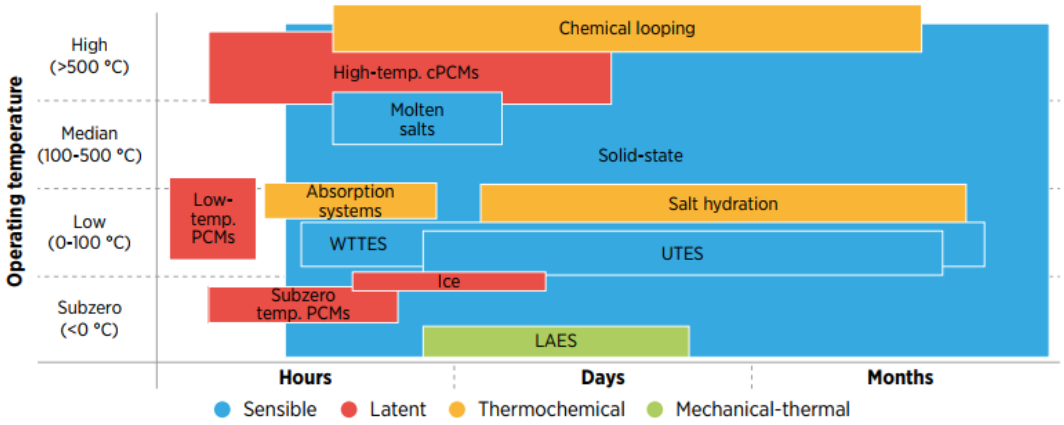


Figure 1-2 Operating Temperatures and Time Ranges of TES Technologies Studied. [30]

The rationale for the important role of TES also lies in the global final energy consumption: thermal energy accounts for more than 50%, while its related CO_2 emissions exceeds 40% of the total. [31] This unveils an undeniable truth for immediate actions: decarbonization of thermal energy should and must be at the heart of efforts towards energy sector decarbonization. Compared to other energy storage solutions, TES holds a unique position — it can harness energy directly from heat sources, e.g., solar, and waste heat from all sorts of sources, for use across industrial processes, building heating/cooling, and district heating. [31] This technology can bypass various intermediate stages of energy conversion, thus significantly enhances energy efficiency. The sources of thermal energy are

diverse, encompassing fossil fuels, solar, nuclear, geothermal, and industrial waste streams. Among these, solar energy, as the primary source of all energy on the earth, has an annual radiation totalling of approximately 1.73×10^5 TW, which is more than 10,000 times the world's total energy use. [32] Yet, a vast amount of solar energy remains unutilized, and wasted. Therefore, efficiently, and effectively harvesting and storing this abundant, clean thermal energy has become a key component in achieving thermal energy decarbonization. However, the utilization of solar energy also faces various challenges including seasonal demand imbalances and uneven geographical distribution, presenting new requirements for seasonal storage and regional transmission of thermal energy. Conventional technologies do not meet the needs due to a few factors, e.g. significant heat loss in seasonal storage, and short distance of thermal energy transport (< 100 km). Long-term TES technology offers a solution to these challenges, which can also be integrated with various energy technologies like solar thermal and heat pumps, enabling long-term, and effective energy storage to meet the clean heating needs. The development and application of such technologies are therefore crucial for optimizing the energy structure, enhancing energy efficiency, and advancing thermal energy decarbonization.

Current TES technologies can be categorized into three principal types based on their working principles: thermochemical storage (TCES), sensible heat storage (SHS), and latent heat storage (LHS). TCES is distinguished by its exceptionally high energy density and nearly zero thermal losses, showing an immense potential as a long-term TES material. However, due to the complexity of the

technology and the cycle stability issues of storage materials, it is currently confined mainly to laboratory research stages. [33,34] SHS, recognized for its low cost and high maturity, becomes a commercial choice for various energy storage applications, yet it faces challenges like low energy storage density, large footprint, and high insulation costs. [27] LHS, also known as a storage technology using phase change materials (PCMs), which absorbs and releases heat through the phase change transition of PCMs. Compared to TCES and SHS technologies, the LHS has a moderate energy storage density, an efficient energy conversion performance, and good reversibility and cycle stability, and therefore has become the focus of many research and industrial efforts. [35,36] However, LHS has been primarily applied to short and medium-term storage scenarios. For long-term storage, it is limited by the inherent properties of PCMs, especially under poor insulation conditions, where the heat contained in the liquid state of PCMs tends to dissipate quickly, reducing its potential for long-term TES applications. The development of PCMs that can achieve long-term TES and release heat on demand becomes a new frontier of TES research. A possible strategy is to establish an energy barrier between the liquid and solid states of the PCM to prevent uncontrolled release of heat when not required, while enabling heat release through a specific mechanism when needed. This requires the development of PCMs with stable, controllable metastable states, such as supercooled and glassy states. [37]

Work on the long-term PCM for TES has been ongoing for some time. However, current long-term TES technologies are based on supercooled liquids, including hydrated salts [38–41], photo-switchable

PCMs [42–44], and polyols [45,46], which face several significant challenges. In long-term thermal energy storage (TES) applications, the use of supercooled liquids faces major challenges, including insufficient storage stability and difficulties in triggering heat release. On the one hand, many supercooled liquids tend to crystallize spontaneously without triggering, leading to premature energy release. On the other hand, although some supercooled liquids are stable, they are difficult to trigger effectively for heat release. Thus, how to achieve a balance between the stability and triggerability of supercooled liquids for long-term TES applications has been thorny research question. Additionally, long-term TES materials in a glassy state, including metal-organic glasses [47] and organic glassy materials [48], also face numerous challenges, such as unsuitable glass transition temperatures, complex and time-consuming synthesis processes, and higher costs. In summary, despite the theoretical potential of PCMs based on supercooled and glassy states for long-term TES, their practical applications and widespread adoption require overcoming a series of technical difficulties and cost constraints. These motivated this PhD study.

1.2 Aims and Objectives

This Ph.D. work aims to develop a series of triggerable PCMs with different operating temperature ranges and triggering mechanisms. The goal is to establish energy barriers between amorphous and crystalline states through such as hydrogen bonding and coordination bonds, thus enabling long-term stable storage at room temperature and triggered by an appropriate method. This work focuses on the synthesis and characterization of these triggerable PCMs and the understanding of formation mechanisms of stable supercooled or glassy states, microscopic structure analysis, and

thermodynamic property evaluation. The work also explores the practical applications of these materials in energy storage demonstration devices and their potential applications in solar energy conversion, storage, and release. The specific research tasks include:

- The investigation of metal-organic supercooled liquids based on the synergistic effects of hydrogen bonds and coordination bonds as mechanically triggered long-term TES materials.
- The study on organic small molecule glass regulated by hydrogen bonding as thermally triggered long-term TES materials.
- The demonstration of application potential of room-temperature triggerable PCMs based on organic-inorganic hybrids in smart windows.

1.3 Layout of the Thesis

The thesis comprises the following six chapters:

- Chapter 1: Introduces the background of this work and thermal storage technologies.
- Chapter 2: Summarises relevant work in the literature.
- Chapter 3: Presents the preparation methods, the microscopic structures and morphologies, and thermodynamic and kinetic properties of the metal-organic supercooled liquids as well as solar-thermal conversion and storage performance of the material based on the synergistic effects of hydrogen bonds and coordination bonds.
- Chapter 4: Details the preparation methods, the microscopic structures and morphologies, and thermodynamic and kinetic properties of the organic small molecule glasses as well as studies on solar-thermal conversion and storage performance of the material regulated by hydrogen

bonding.

- Chapter 5: Demonstrates the application of room-temperature triggerable PCMs based on organic-inorganic hybrids in the field of smart windows.
- Chapter 6: Gives a summary of the main findings and contributions of the thesis, with suggestions for future work.

Chapter 2 Literature Review

This chapter is divided into four main sections. Section 2.1 summarises thermal energy storage (TES) technologies and related materials. Sections 2.2 and 2.3 provide the characteristics and properties of supercooled liquids and glassy materials, respectively. Section 2.4 reviews the current research status of using supercooled liquids and glassy materials as long-term TES materials, as well as discussing the challenges they currently face.

2.1 Thermal Energy Storage Technologies and Materials

TES technologies are classified into three main types based on their underlying working principles: thermochemical energy storage (TCES), sensible heat storage (SHS), and latent heat storage (LHS). The following sub-sections will explain the mechanisms, and materials associated with each type, providing a comprehensive understanding of their unique characteristics and uses.

2.1.1 Thermochemical Energy Storage (TCES) and Materials

TCES is a technology category that relies reversible chemical reactions leading to enthalpy changes; see **Figure 2-1**. [27,49] This technology can be classified into two main sub-categories based on the way chemical bonds are broken during the reaction process: reaction-based TCES and sorption-based TCES. The reaction-based TCES is mainly aimed at medium to high-temperature applications. Examples include methane reforming, ammonia synthesis and decomposition, metal hydrides, carbonates, metal oxides, and metal hydroxides. Thermal energy storage and release are achieved through the breaking and reformation of covalent bonds. Although reaction-based TCES possesses some advantages, such as notable enthalpy changes, high energy density, and a wide operating

temperature range, challenges persist in terms of cost, material corrosion resistance, cycle life span and gas storage. Further exploration of reaction mechanisms and optimization of reaction process control is required.

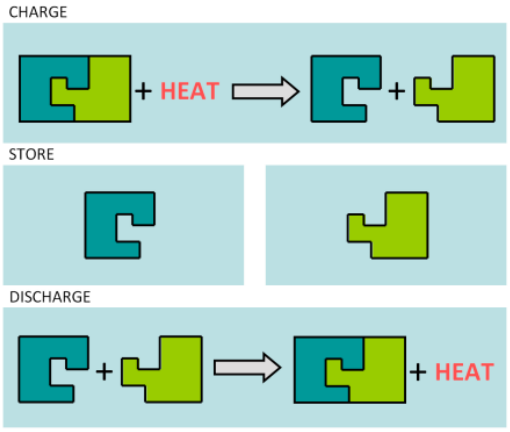


Figure 2-1 Schematic diagram of the charging and discharging mechanism in TCES. [49]

The sorption-based TCES can be further sub-divided into chemical adsorption and chemical absorption types. Chemical adsorption TECS rely on the adsorption and desorption between solid adsorbents and gaseous adsorbates, which depends on the breaking and reformation of intermolecular forces such as van der Waals forces, electrostatic forces, and hydrogen bonds. A typical example is silica gel widely used for moisture traps in analytical chemistry. Chemical absorption involves the formation and dissociation of coordination bonds and ionic bonds with common materials, including hydrate salts. 错误!未找到引用源。 lists some common materials used for TCES.

Currently, TCES technologies are mostly at a low technology readiness level (TRL), facing significant challenges due to system complexity, the requirement for extensive auxiliary equipment,

and initial high investment costs. Research efforts are urgently needed to address challenges in low cycle stability, costs, and the complex control processes of chemical reactions. [50,51]

Table 2-1 Some Common Materials Used in TCES.

Reaction Types	Materials	Charging Temperature (ºC)	Discharging Temperature (ºC)	Energy Density	Ref.
Reaction-base	MgH_2	380	230	75 kJ/mol	[52,53]
	$CaCO_3$	860	880	178 kJ/mol	[53–55]
	$PbCO_3$	450	300	88 kJ/mol	[56]
	$Mg(OH)_2$	150	100	81 kJ/mol	[57,58]
	$Ca(OH)_2$	450	25-400	104 kJ/mol	[58]
	BaO_2	690-780		77 kJ/mol	[59]
	NH_3	450 @9-150 bar	450 @ 10-300 bar	66.9 kJ/mol	[60,61]
	CH_4	950	530	250 kJ/mol	[62,63]
Chemical adsorption	Silica gel	100		1029 kJ/kg	[64]
	Zeolite	150		81-292 kJ/kg	[65]
Chemical absorption	$MgCl_2 \cdot 6H_2O$	200		252 kJ/mol	[66]
	$SrCl_2 \cdot 6H_2O$	62		59 kJ/mol	[67]
	$CaCl_2 \cdot 6H_2O$	130			[68]
	$MgSO_4 \cdot 7H_2O$	122		275 kJ/mol	[69]
	$SrBr \cdot 6H_2O$	71		300.6 kJ/mol	[70]

2.1.2 Sensible Heat Storage (SHS) and Materials

SHS technologies store and release energy through temperature changes in the material with no phase transition nor chemical reactions. [71] The amount of heat stored (Q) in a SHS material can be calculated by:

$$\mathrm{Q} = V \int_{T_i}^{T_f} \rho C_{\mathrm{p}} \mathrm{d}T \qquad (2-1)$$

where V is the volume of the material (m³); T_i and T_f are initial and final temperature of the material, respectively; ρ is the density of the material (kg/m³); and C_{p} is the average specific heat of the material (kJ/(kg·K)).

Materials with a high specific heat, density, and thermal conductivity are preferred for SHS, while gaseous materials are less suitable due to their lower density and thermal conductivities. Therefore, solid, and liquid media are commonly used for SHS. Examples of solid SHS materials include concrete, rocks, refractory bricks, metals, and inorganic salt composites, which are typically used for high-temperature applications. Examples of liquid SHS materials include water, thermal oil, molten salts, and liquid metals. **Table 2-2** lists some commonly used SHS materials. Water is the most commonly used SHS material due to its high specific heat capacity, abundance, low cost, safety, stability, and its dual role as both a storage medium and a heat transfer fluid. It is widely used for domestic hot water supply and space heating. Furthermore, SHS technology can also be used for long-term storage purposes, such as seasonal storage using hot water storage, gravel-water storage, borehole heat exchangers, and aquifer storage, as shown in **Figure 2-2**.

Table 2-2 Some Typical SHS Materials

Type	Materials	Working Temperature (°C))	Density (kg/m^3)	Specific capacity (kJ/(kg·K))	Ref.
Liquid	water	0-100	1000	4.19	[72]
	Thermal oil	0-400	850-900	1.6-2.1	[73]
	Nitrate salts	265-565	1870	1.6	[74]
	Liquid sodium	270-530	850	1.3	[74]
Solid	concrete	200-400	2200	0.85	[73]
	rock	200-300	1700	1.3	[73]
	fire bricks	200-1200	3000	1.2	[73]
	Cast steel	200-700	7850	0.56	[73]
	Sodium chloride	200-500	2150	0.85	[73]

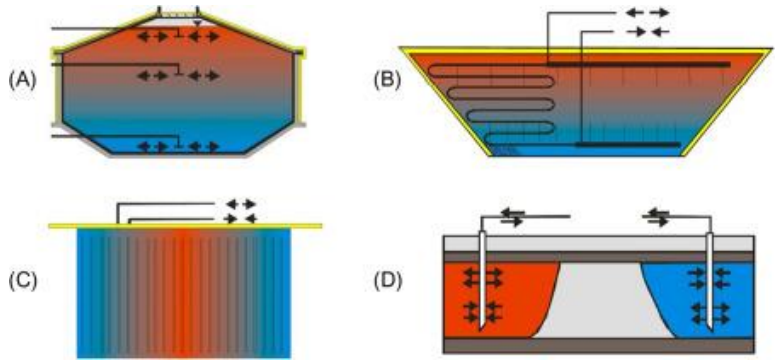


Figure 2-2 Long-term SHS technologies.

(A) hot-water store, (B) gravel-water store, (C) borehole-heat exchangers, (D) aquifer store. [75]

SHS has a high TRL and is widely used on a large scale. It has several drawbacks, including low energy storage density, significant temperature fluctuations, large system sizes, substantial long-term heat losses, and variable output temperatures. [71]

2.1.3 Latent Heat Storage (LHS) and Materials

LHS also termed as PCMs based storage technology, utilizes phase transition of a material to store and release thermal energy. This process of storing and releasing heat is accomplished by the reversible transformation between solid and liquid or liquid and gas. PCMs can be classified into three categories: solid-solid, solid-liquid, and liquid-gas, depending on the type of phase change involved. Among these, solid-liquid PCMs are the most commonly used in practical applications. This work focuses exclusively on solid-liquid PCMs, and all subsequent references to PCMs in this thesis refers only to this type.

PCMs absorb and release energy by breaking and reforming intermolecular forces, such as van der Waals forces, hydrogen bonds, and electrostatic forces. The energy involved in this process is known

as latent heat. The stored thermal energy in PCMs encompasses both sensible and latent heat parts. **Figure 2-3** illustrates the three stages of thermal energy storage and release: two sensible heat storage regions (the heating or cooling of the solid and the liquid) and one phase transition region between solid and liquid for latent heat storage or release. This latent heat storage process is nearly isothermal, which represents a significant advantage of using PCMs. The energy storage capacity, Q, of a PCM can be expressed as follows:

$$Q = \int_{T_i}^{T_m} mC_{p,s}dT + m\Delta H + \int_{T_m}^{T_f} mC_{p,l}dT \qquad (2-2)$$

where T_m is the melting point of the PCM; $C_{p,s}$ and $C_{p,l}$ are the specific heat of the solid and liquid phases, respectively; and ΔH represents the latent heat of phase change.

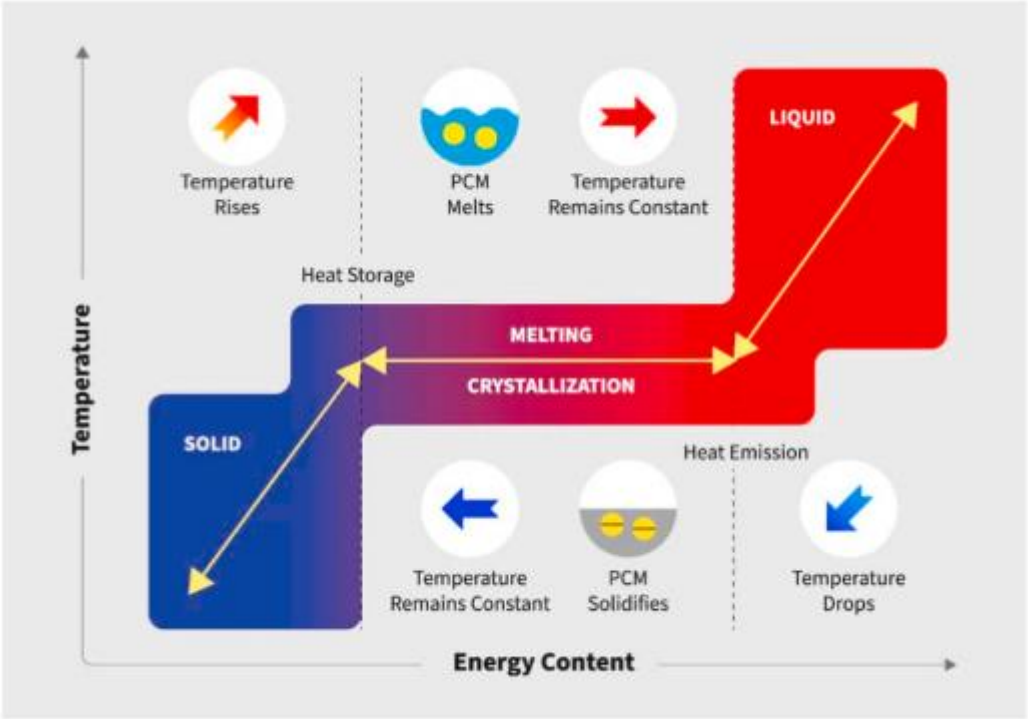


Figure 2-3 Schematic for Charging and Discharging Processes of Phase Change Material. [75]

Phase transition is a fundamental characteristic of materials, and many molecular crystals are capable

of undergoing such a transformation. However, not all molecular crystals are suitable for use as PCMs. As a result, it is crucial to consider a comprehensive set of criteria for screening PCMs for a specific application, which include thermal and physical properties, kinetics, chemical stability, and cost. [76] Based on the above criteria, PCMs can be classified into organic, inorganic, and eutectic sub-categories based on their composition (refer to **Figure 2-4**).

PCMs have a wide range of phase transition temperatures, from as low as <-200°C to as high as >1000°C, making them versatile for various applications including cryogenic storage, domestic heating, hot water supply, and solar thermal storage. Their energy storage density can be significantly higher than that of SHS, by 5 to 14 times for a given temperature range [77], which could significantly reduce equipment size and minimizes thermal losses during operation. Although PCMs offer numerous advantages, they also have specific limitations. For instance, paraffins and fatty acids are flammable, while polyols and hydrate salts are prone to supercooling. Additionally, hydrate salts also face challenges related to phase separation and corrosion. Moreover, except for metals and alloys, most PCMs have a low thermal conductivity, often below 1W/m·K. Fortunately, options for PCMs are ample for a specific operational temperature range, allowing for customization to counteract some of their inherent shortcomings. This facilitates more tailored and effective solutions for specific applications. Furthermore, the development of composite PCMs has also proven effective in addressing these challenges. To enhance thermal conductivity of materials, the addition of highly thermally conductive materials, such as metal nanoparticles [78], carbon materials [79], or internal

structures with high thermal conductivities [80–82] has been explored. Additionally, nucleating agents can be introduced to suppress supercooling [83–85]. For example for hydrate salts, thickeners can be added to reduce phase separation [86,87]. **Table 2-3** lists various PCMs with their characteristics.



Figure 2-4 Classification of Phase Change Materials [88]

Table 2-3 An Overview of Several Typical PCMs and Their Characteristics

Categories	Name	Materials	Melting point (°C)	Heat of fusion (kJ/kg)	Advantage & Disadvantage	Ref.
Organic	Paraffin	n-Dodecane	-10	216	● Thermal stability ● No corrosive ● No toxic ● No phase separation ● Little supercooling ● Low thermal conductivity	89
		n-Nonadecane	32	222		76
		n-Triacontane	65.4	252		76
	Ester	Isopropyl stearate	14	142	● Narrow operation temperature range	76
		Methyl palmitate	39	160.7	● Little or no supercooling	76
		Ethylene glycol stearate	63.2	251.8		76
	Fatty acid	Caprylic acid	16	148.5	● Low phase transition volume change ● High boil point	90,91
		Capric acid	32	152.7		90,91
		Palmitic acid	64	185.4		90,91

		(Carbon			● Very little or no supercooling ● Good cyclability ● Expensive ● Mildly corrosive	
	Alcohols	xylitol	93	280	● High enthalpy	[46,92,93]
		erythritol	117	344	● Huge supercooling	[94,95]
		Mannitol	165	341		[96,97]
	PEG	PEG 600	12.5	129.1	● Chemically and thermally stable ● Non-flammables ● Non-toxic ● Non-corrosive ● inexpensive	[98,99] [76] [76] [76]
		PEG 1000	40	168.6		
		PEG 20000	67.7	160.2		
		PEG 100000	70	174		
Inorganic	**Salt hydrates**	$MgCl_2·6H_2O$	117	168.6	● Inexpensive ● Relative high fusion heat ● Corrosive ● Huge supercooling ● Phase separation	[90] [90] [90] [90]
		$Mg(NO_3)_2·6H_2O$	89	162.8		
		$Na_2SO_4·10H_2O$	32	251		
		$CaCl_2·6H_2O$	29	190.8		

Molten salts	$Ca(NO_3)_2$	560	145	• Wide operation temperature range • High meting point • Relatively high thermal conductivity	[100,101]
	Na_2CO_3	854	276		[100,101]
	$CaCO_3$	1130	142		[100]
Meta and alloys	Zn/Mg (53.7/46.3)	340	185	• High thermal conductivity	[100]
	Mg/Cu/Zn (60/25/15)	452	254		[100]

PCMs have a lower energy density than TCES materials in general, but much higher than SHS materials. They provide a temperature range that can be more easily aligned with and controlled to suit practical application requirements. Coupled with their stability advantages, less equipment requirements, and much better cycling performance, PCMs offer a great potential for use in TES technologies. The major challenge for PCMs lies in the limited duration of storage.

To address the storage duration limitation challenges, a method has emerged through the creation of an energy barrier between the liquid and crystalline states, by e.g. strengthening intermolecular forces such as hydrogen bonding, to form a more stable supercooled liquid or glassy state. This approach has been found to achieve an inhibition of crystallization. **Figure 2-5** illustrates the

mechanism by which amorphous materials, such as supercooled liquids or glassy materials, store thermal energy for long-term. The key to their ability to store energy over extended periods is a specifically designed barrier that impedes crystallization. This barrier prevents the rapid release of thermal energy, enabling stable, long-term storage, in contrast to traditional PCMs that crystallize spontaneously when cooled. Additionally, this barrier can be overcome through specific triggers such as mechanical stirring or the addition of seed crystals, which promote nucleation and initiate the crystallization process in amorphous materials. Therefore, supercooled liquids or glassy materials can release stored thermal energy on demand. In the following sub-sections, some distinctive characteristics of supercooled liquids and glassy materials are examined to understand how they can be utilised to enhance the long-duration storage performance of PCMs.

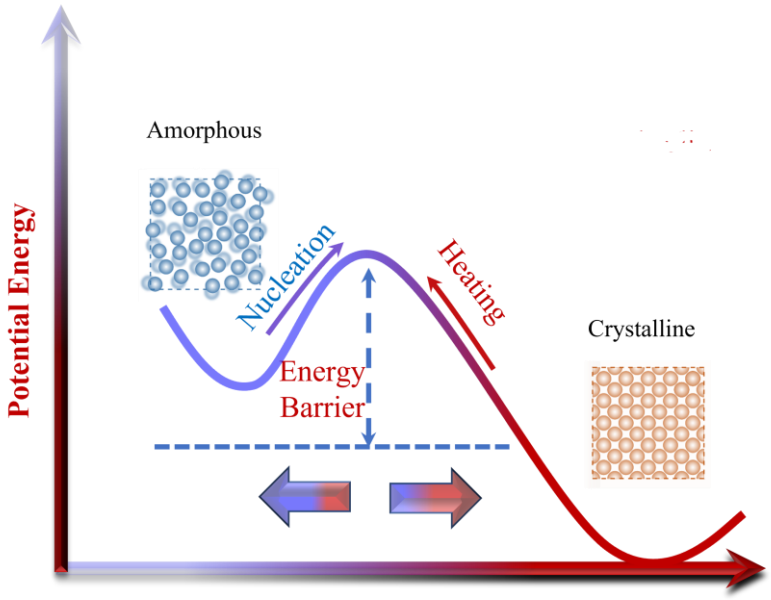


Figure 2-5 Schematic of Principles for Supercooled and Glassy PCMs

2.2 Characteristics of Supercooled Liquids and Glass Transition

2.2.1 Supercooled Liquids

The process of liquid cooling can follow two distinct paths, as shown in **Figure 2-6**. [102] Typically, when a liquid approaches its freezing point, its molecules/atoms tend to rearrange to form a long-range ordered crystalline structure, releasing heat. This is known as a conventional first-order phase transition, depicted by the blue line in **Figure 2-6**. However, under certain conditions, the liquid may avoid the crystallization below its freezing point, keeping in the liquid state – a phenomenon called supercooling, depicted by the grey line in **Figure 2-6**. Almost all liquids can be supercooled if the cooling rate is sufficiently high. [103,104] It is important to note that, with the exception of some materials with a strong ability to form amorphous structures, such as SiO_2 supercooled liquids [105], most supercooled liquids are not very stable. They may rapidly crystallize and release heat upon slight agitation, shaking, or the introduction of impurities or nucleation seeds. [106] To maintain the stability of a supercooled liquid, a sufficiently high nucleation barrier between the liquid and crystal is required. However, this barrier should not be excessively high, as it must be breakable when needed. For instance, if a supercooled liquid is used as a long-term TES material, it needs to remain stable during storage but should also be easily triggerable for crystallization. Therefore, an optimal nucleation barrier is essential.

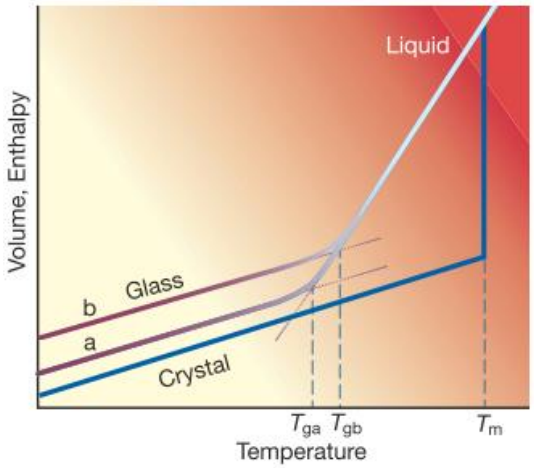


Figure 2-6 The relationship of system volume or enthalpy changes with temperature during cooling. [107]

Note, the above terms 'sufficiently high' cooling rate, 'excessively high' nucleation barrier, and 'optimal' nucleation barrier are subjective and qualitative descriptions. A more quantitative evaluation is needed, which requires further investigation of nucleation process of supercooled liquids. This includes the examination of key factors including the nucleation barrier, nucleation time, and nucleation rate on the performance.

2.2.2 Conditions for the Formation of Supercooled Liquids

To create a stable supercooled liquid, it is crucial to control the nucleation and crystallization processes well. The Classical Nucleation Theory (CNT) [104,108,109] proposes two mechanisms: homogeneous and heterogeneous nucleation, as shown in **Figure 2-7**. Homogeneous nucleation, which occurs less frequently, is driven solely by internal thermal fluctuations. In contrast, heterogeneous nucleation utilises surface impurities and the effects at material interfaces to initiate

crystallisation. For the sake of simplicity, the following discussion will only focus on the mechanism of homogeneous nucleation.

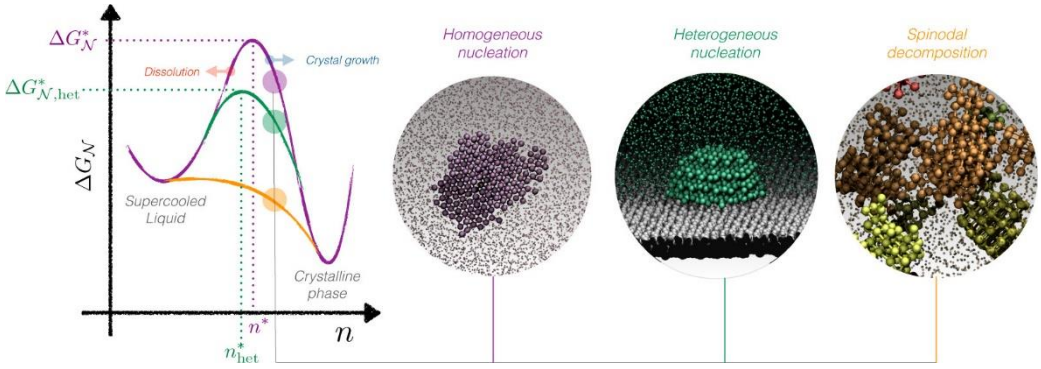


Figure 2-7 Schematic of a Free Energy Barrier for Nucleation.[110]

During homogeneous nucleation, crystal nuclei form from atoms or molecules aggregates within a supercooled liquid due to internal thermal fluctuations. The likelihood of these nuclei evolving into stable crystals is significantly influenced by the prevalent temperature. Above the melting point (T_m), the higher entropy of the liquid results in a lower Gibbs free energy (G = H - TS) compared to the crystal, hindering the formation of stable nuclei. Conversely, below T_m, the crystal has a lower free energy than the liquid, creating favourable conditions for nucleus generation.

The change in free energy (ΔG) associated with nucleus formation is dual-faceted: volumetric changes contribute to a decrease in free energy, facilitating nucleation, while surface creation, which demands energy, increases the system's free energy. This interplay is captured by the equation:

$$\Delta \mathrm{G} = 4\pi \mathrm{R}^2\sigma - \frac{4}{3}\pi \mathrm{R}^3 \Delta g \qquad (2-3)$$

Where, σ denotes the surface energy, and Δg represents the free energy density difference between liquid and solid phases, defined by:

$$\Delta g = g_{\mathrm{l}} - g_{\mathrm{s}} = \frac{\Delta h}{v}\left(1 - \frac{T}{T_m}\right) \qquad (2-4)$$

where Δh is the molar enthalpy of phase transition, and v is the molar volume of the crystal, the subscripts *l*, *s* stand for liquid and solid, respectively.

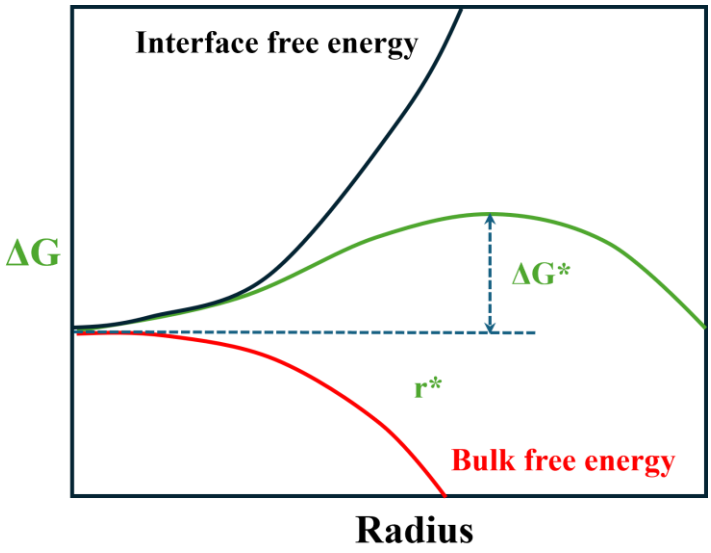


Figure 2-8 Schematic Illustration of Free Energy Variation with Nucleus Size

The interplay between these energy components dictates the growth dynamics of the nucleus, as shown in **Figure 2-8**. A critical nucleus radius (R_c), at which ΔG is maximized, delineates the threshold for stable nucleus growth. The critical radius is determined by setting the first derivative of ΔG to zero, yielding [111]:

$$R_c = \frac{2\sigma}{\Delta g} \qquad (2-5)$$

The maximum nucleation energy barrier is given by:

$$\Delta G(R = R_c) = \frac{16\pi\sigma^3}{3\Delta g^2} \qquad (2-6)$$

Hence, the steady-state homogeneous volume-based nucleation rate (j_N) and nucleation time (Γ_N) from the supercooled liquid can be written as:

$$j_N = j_0 \exp\left(-\frac{\Delta G + \Delta G_\eta}{k_B T}\right) = j_0 \exp\left(-\frac{16\sigma^3}{3k_B T \Delta g^2} + \frac{\Delta G_\eta}{k_B T}\right) \qquad (2-7)$$

$$\Gamma_N = \tau_0 \exp\left(-\frac{\Delta G + \Delta G_\eta}{k_B T}\right) = \tau_0 \exp\left(-\frac{16\sigma^3}{3k_B T \Delta g^2} + \frac{\Delta G_\eta}{k_B T}\right) \qquad (2-8)$$

where j_0 and τ_0 are the pre-exponential factor and k_B is Boltzmann constant. ΔG_η is the activation free energy for viscous flow, or the kinetic barrier for nucleation. ΔG is as mentioned above thermodynamic barrier for nucleation.

Figure 2-9 shows that the nucleation time, represented by the solid line, approaches infinity at both absolute zero temperature (T=0) and at the melting temperature ($T=T_m$), with a minimum nucleation time occurring at T_{min}. The dashed line represents the relaxation time, which increases significantly as the temperature decreases and becomes very small near T_m. The straight lines with different slopes represent different cooling rates, r ($r = \frac{dT}{dt}$), where the cooling rates are inversely proportional to their slopes. To prevent crystallization of the liquid (LQ), it is crucial to avoid cooling too slowly, as this may exceed the nucleation time and result in crystal (CR) formation. The tangent line to the nucleation time indicates the critical linear cooling rate r_c ($\sim \frac{1}{\Gamma_{min}}$), which is the slowest rate at which cooling can occur while still avoiding crystallisation. However, it is also important to avoid cooling too rapidly, as this may exceed the relaxation time and cause the system to fall out of equilibrium, resulting in the formation of a glass (GL). The dotted red line represents non-linear cooling, which is faster near the minimum nucleation time and slower at lower temperatures.

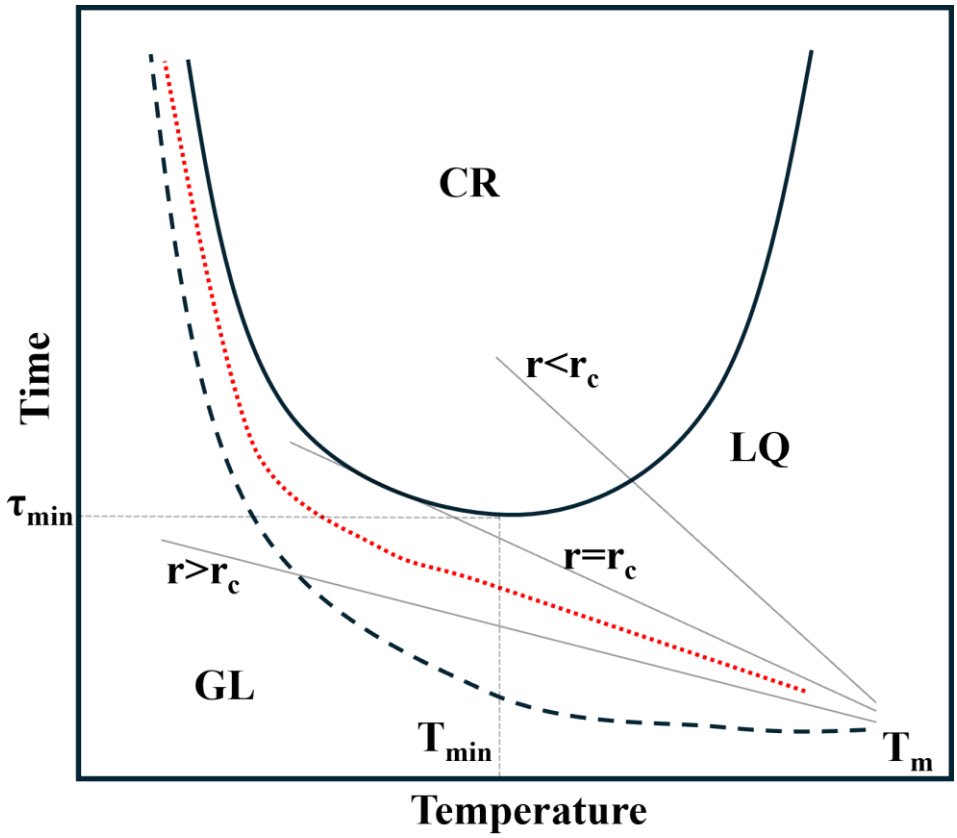


Figure 2-9 Cooling Rate Manipulation for Avoiding Crystallization.[112]

Given the difficulties in controlling the cooling rate, the preparation of supercooled liquids presents significant challenges. Furthermore, the cost of fabrication process must be considered, especially when evaluating their potential as long-term TES materials. The complexities and high costs of fabrication can render a TES material impractical for large-scale deployment. Consequently, research into thermal storage solutions suitable for large-scale applications necessitates the investigation of supercooled materials that can be prepared by natural cooling processes, with an emphasis on efficiency and economic viability.

Crystal growth initiates once a nucleus has formed. This process typically involves the attachment

of molecules or clusters to the most favourable sites on the crystal layer. Crystal growth is a complex phenomenon influenced by multiple factors, including the degree of supercooling, imperfections on the crystal surface; impurities; and the mobility of molecules at the surface. To describe this intricate process, particularly in the context of glass-forming liquids, three primary growth modes are recognized: normal growth, two-dimensional surface-nucleated growth, and screw dislocation growth. Each mode is suited to different physical conditions and material systems. Normal growth is a basic model typically applied in idealized environments, but it is less common in practical applications due to ubiquitous structural defects. Two-dimensional surface-nucleated growth is important in situations where crystal surfaces are smooth and defect-free, often seen in thin film deposition. Screw dislocation growth, however, is the most prevalent in industrial applications, particularly for the production of large-scale, high-quality crystals.

Using screw dislocation crystalline growth as an example, the general growth rate (v) from supercooled liquid can be described as follows:

$$v = kf\lambda\left(1 - \exp\left(-\frac{\Delta G}{k_{\mathrm{B}}T}\right)\right) \qquad (2-9)$$

where *k* is the jump frequency of molecules transitioning from the liquid to the crystal; *f* is the site factor representing the probability of incorporating impinging molecules into the crystal surface.

In accordance with the Stokes-Einstein equation, the jump frequency (*k*) can be further defined as:

$$k = \frac{6D}{\lambda^2} = \frac{2k_{\mathrm{B}}T}{\pi\eta\lambda^3} \qquad (2-10)$$

where *D* is the diffusion coefficient, η denotes the viscosity, and λ represents the jump distance, which is considered as the longest dimension of a supercooled liquid molecule.

2.2.3 Glass Transition Temperature

Supercooled liquids cannot be indefinitely supercooled due to the 'entropy crisis', which will be discussed in a later sub-section 2.2.5. **Figure 2-6** illustrates that during rapid cooling, supercooled liquids will deviate from the equilibrium upon reaching a specific temperature range (as indicated by T_{ga} or T_{gb}). Within this range, the system still maintains its liquid structure, but its relaxation time and viscosity increase significantly increase over a narrow temperature span of tens of Kelvin. [113,114] The process is characterized by a marked slowdown in dynamics, referred to as the glass transition, with the corresponding temperature is known as the glass transition temperature (T_g).

The relaxation time within the glass transition temperature range is approximately between 10^2 to 10^3 s. [115] This indicates extremely slow kinetics, effectively 'freezing' nucleation and crystallization within the timescale of experimental observation. T_g is generally about two-thirds of the corresponding T_m. [116] The commonly identified T_g is determined by the intersection of the liquid and glass tangents. However, T_g differs from T_m because it is not a precise temperature point but rather spans a narrow temperature range, influenced by the cooling rate of the supercooled liquid. Higher cooling rates result in higher glass transition temperatures, while lower rates yield lower transition temperatures, as shown by T_{ga} and T_{gb} in **Figure 2-6**. The influence of cooling rate is limited, with orders of magnitude differences in cooling rates corresponding to a T_g range of only 3-5 K. [102]

T_g is typically measured using two methods. The first method identifies T_g as the temperature at which the viscosity reaches 10^{12} Pa·s or the relaxation time spans between 10^2 and 10^3s. [112,117] The second method uses calorimetry to monitor changes in the material's specific heat or heat flow signal

as temperature varies, as illustration in **Figure 2-10** using calcium metaphosphate glass as example. [118] During the upscan, the glass-liquid transition is characterised by the C_p jump, ΔC_p (T_g), while the liquid-glass transition is indicated by the C_p drop. The standard glass transition temperature T_g is defined as the maximum value of the first order derivative of C_p or the intercept between the extrapolated glass C_p line and the line with the maximum tangent of the C_p rising curve.

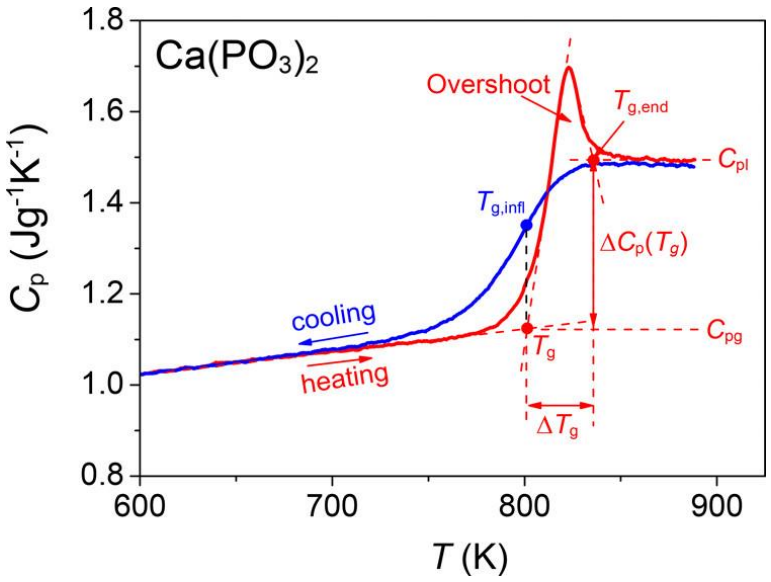


Figure 2-10 The DSC Curve Near the Glass Transition Temperature. [118]

2.2.4 Viscosity and Fragility of Supercooled Liquids

Supercooled liquids can be classified into covalent, ionic, metallic, and molecular types based on different bonding methods. [119] These types share a common dynamic behaviour: as the temperature approaches T_g, their dynamic properties (e.g. viscosity, relaxation time) dramatically decrease. [120] However, comparing their viscosity at different temperatures is challenging, as shown in **Figure 2-11 A**. To address this issue, T_g is used as a normalizing parameter to scale the viscosity of all systems.

This approach allows the kinetic properties of these supercooled liquids to be represented on the same graph with temperature variations, known as the 'Angell Plot'. [115,121] In this plot, the y-axis represents the logarithm of viscosity, and the x-axis signifies T_g/T, as shown in **Figure 2-11B**.

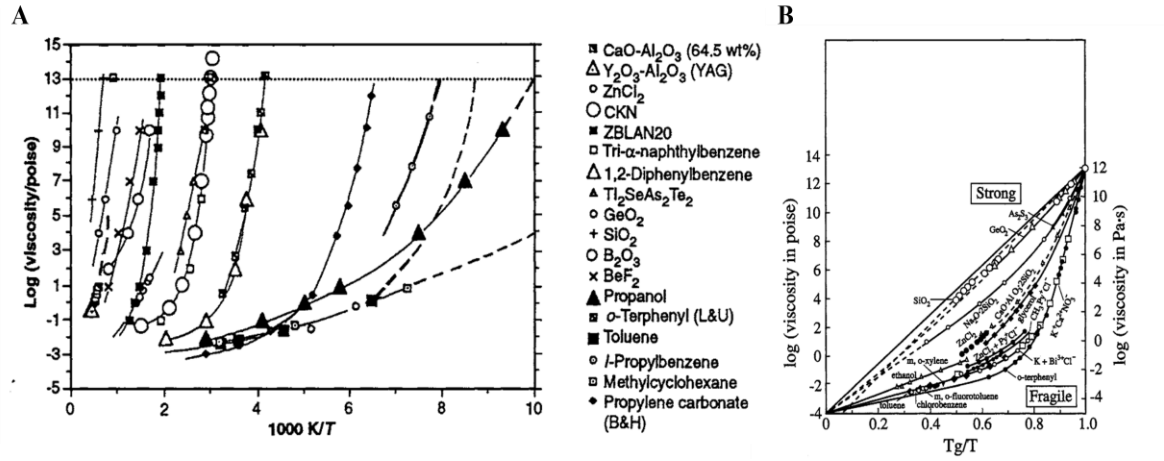


Figure 2-11 The Variation Characteristics of Viscosity with Temperature in Different Supercooled Liquids. [121]

(A) Arrhenius plot of the viscosity of several supercooled liquids. (B) T_g-scaled Arrhenius plot showing Angell's strong–fragile pattern.

The viscosity of different supercooled liquids clearly varies with temperature in distinct ways. Angell introduced the concept of 'fragility' to represent the apparent activation energy for structural relaxation at the glass transition. [31] This is defined as the slope of *X,* where *X* can be viscosity (η), structural relaxation time, or diffusion coefficient, versus temperature at T_g , as shown in the following equation [122]:

$$m = \left.\frac{\mathrm{dlog}(X)}{d\left(\frac{T_\mathrm{g}}{T}\right)}\right|_{T=T_\mathrm{g}} \qquad (2-10)$$

A small m value indicates a 'strong' liquid, where the relaxation time and viscosity exhibit a good Arrhenius relationship with the reduced temperature (as shown in the following equation) [122]:

$$\eta = A \exp\left(\frac{E_{\mathrm{a}}}{k_{\mathrm{B}}T}\right) \qquad (2-11)$$

where A is the pre-exponential factor; E_{a} is the activation energy; k_{B} is Boltzmann's constant. Conversely, a large m value indicates a 'fragile' liquid, for which the viscosity or relaxation time cannot be described by the Arrhenius relationship. Instead, the following Vogel-Fulcher-Tammann (VFT) empirical formula is often used [123–127]:

$$\eta = A \exp\left[\frac{B}{(T-T_0)}\right] \qquad (2-12)$$

where A is a pre-exponential factor; B is a constant; T_0 is a reference temperature.

The concept of fragility is useful for comparing the glass transition kinetics of different systems, which is strongly related to the system's thermodynamic characteristics by [128]:

$$\Delta C_P(T_{\mathrm{g}}) = \frac{m \cdot H_{\mathrm{m}}}{56T_{\mathrm{g}}} \qquad (2-13)$$

where $\Delta C_P(T_{\mathrm{g}})$ is the jump of the isobaric heat capacity; H_{m} is the heat fusion.

Furthermore, fragility is strongly linked to the stability of supercooled liquids, also known as glass-forming ability (GFA). A higher fragility results in a lower glass-forming ability and vice versa. [129,130] The so-called Kauzmann 'two-thirds rule', which determines GFA by checking whether Tg/Tm is greater than 2/3, supports this relationship; a higher Tg/Tm indicates greater GFA. [128,131,132] However, in practical applications, a lower fragility, which results in extremely high viscosity, is not always beneficial as it makes initiating crystallization challenging.

2.2.5 Dynamics and Thermodynamic Characteristics of Supercooled Liquids

This sub-section looks at the reasons for the slowing down or freezing of dynamics during the supercooled liquid and glass transition processes, although these are not the main focus of the PhD work. Supercooled liquids are notably characterized by their dynamic heterogeneity. [121,133–135] Due to the experimental challenges of measuring supercooled liquids, studies on their dynamic behaviour predominantly rely on computer simulations.

The dynamics of supercooled liquids are commonly characterized by the mean-squared displacement (MSD), defined as the square of the distance that atoms move over a period of time:

$$\langle \Delta r^2(t) \rangle = \frac{1}{N} \left\langle \sum_{j=1}^{N} \left[\vec{r}_j(t) - \vec{r}_j(0) \right]^2 \right\rangle \qquad (2-14)$$

where N is the number of atoms, and $\vec{r}_j(t)$ represents the position of atom j at time t. The MSD of supercooled liquids, as illustrated in **Figure 2-12A**, indicates that at short time intervals, atoms vibrate around their initial positions. As time progresses, the MSD will encounter a platform before continuing to increase, then ultimately displaying a diffusion motion pattern. The height of the platform decreases, while its duration extends as the temperature decreases. The platform of MSD can be explained by the fact that the movement of an atom is constrained by its neighbouring atoms, necessitating time to break free from these constraints. This phenomenon is commonly known as the 'cage effect'. As the temperature decreases, the density of atomic arrangements increases, thereby intensifying the cage effect. The duration of the platform in the MSD indicates the timescale during which the cage effect is in effect.

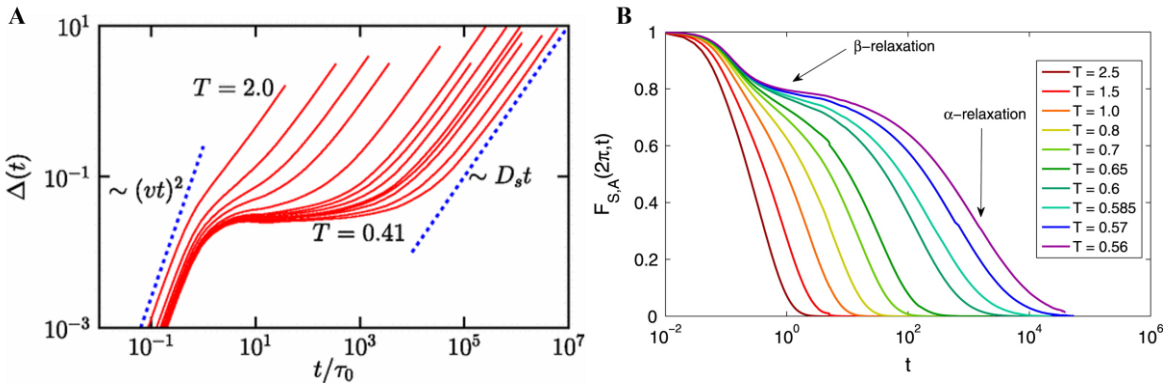


Figure 2-12 The Dynamic Characteristics of Supercooled Liquids.

*(**A**) The evolution of the mean square displacement of supercooled liquids as the temperature decreases.* [136] *(**B**) The evolution of the self-scattering function of supercooled liquids as the temperature decreases.*[137]

Another parameter for describing the dynamics characteristics is the self-intermediate scattering function (SISF), which reflects the degree to which atoms deviate from their initial positions, expressed as [113]:

$$F_s(q,t) = \frac{1}{N}\left\langle \sum_{j=1}^{N} \exp\left[i\vec{\mathrm{q}} \cdot \left(\vec{\mathrm{r}}_j(t) - \vec{\mathrm{r}}_j(0)\right)\right]\right\rangle \qquad (2-15)$$

where $\vec{q}$ is the wave vector, typically corresponding to the first main peak in the static structure factor. Supercooled liquids approaching T_g generally exhibit a two-step relaxation pattern in their SISF, as demonstrated in **Figure 2-12B**. The first step involves a rapid decay of $F_s(q,t)$ to a platform from 1 due to thermal vibrations within the cage, known as β-structural relaxation. The second step, α-structural relaxation, involves the central particle gradually escaping from its cage, its $F_s(q,t)$ eventually decaying to zero. In computer simulations, the structural relaxation time is usually defined according to $F_s(q,t)$, for example, when $F_s(q,t) = 1/e$.

Another important feature of $F_s(q,t)$ is the stretched-exponential α-structural relaxation, which can be fitted by the Kohlrausch-Williams-Watts (KWW) function:

$$F_s(q,t) = A\exp\left[-\left(\frac{t}{\tau_\alpha}\right)^{\beta}\right] \qquad (2-16)$$

where A is pre-exponential factor; t is the time; τ_α is the characteristic, temperature-dependent relaxation time; and β is the KWW stretch exponent. It has been found that the exponential β is always less than 1.0 in temperature ranges that exhibit a distinct plateau, indicating that the relaxation times of the different atoms in the system are varied. In other words, the system exhibits 'dynamic heterogeneity'. [113]

Dynamic heterogeneity has received extensive attention and research over the past two decades. [113] Its discovery was once considered a breakthrough in solving the problem of the glass transition. It is regarded as the most important characteristic of amorphous materials, especially supercooled liquids.[136] However, to date, dynamic heterogeneity is still difficult to confirm directly through experiments. Analyses and calculations of dynamic heterogeneity primarily come from computer simulations. The concept itself can be understood from the 'cage effect': in supercooled liquids, each atom is confined by its neighbouring atoms. Due to the disordered structure, different atoms experience varying degrees of confinement, necessitating coordinated movement among similarly confined atoms to achieve structural relaxation. This means that atoms in different regions have different mobility capabilities, as shown in **Figure 2-13**. It is observed that some regions exhibit a high degree of atomic mobility, while others exhibit a low degree of atomic mobility. These atoms

with differing mobility capabilities are not randomly distributed but tend to form clusters of varying sizes and shapes. Therefore, an important parameter characterizing dynamic heterogeneity is the 'dynamic correlation length', which is the average spatial size of the correlated motion regions. Additionally, the observation of dynamic heterogeneity is related to the selected time scale. It disappears at both very short and very long time intervals.

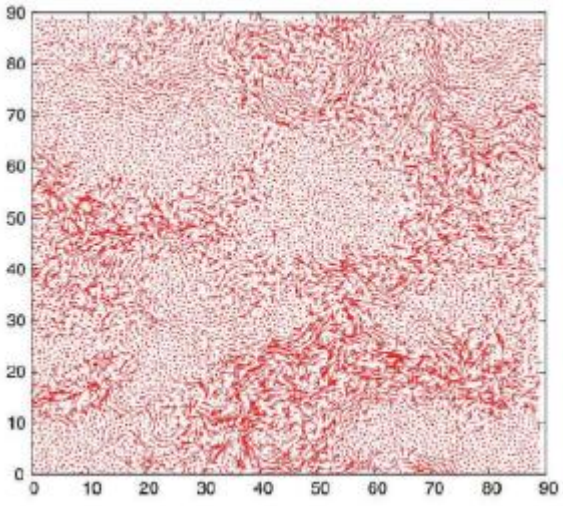


Figure 2-13 Map of Single Particle Displacements in a 2D Lennard-Jones Model of Supercooled Liquids. [135]

As previously mentioned, supercooled liquids cannot be indefinitely supercooled due to the 'entropy crisis', a concept first introduced by Kauzmann in 1948. [138,139] This concept suggests that the glass transition is an intrinsic characteristic of supercooled liquids. As the liquid is supercooled, its entropy decreases, reducing the entropy difference (ΔS) between the liquid and the crystal, as shown in **Figure 2-14**. [107] Extrapolation of the entropy change of supercooled liquids suggests that, without undergoing a glass transition, the entropy of the liquid would be equal to that of the crystal at a non-zero temperature T_k (known as the Kauzmann temperature). The entropy crisis occurs when the

entropy of a liquid becomes negative below T_k, which is impossible since the crystal's entropy approaches zero as temperature approaches 0K. To prevent this, supercooled liquids must undergo a glass transition above T_k. This highlights that the amorphous state and glass transition are inherent properties of matter.

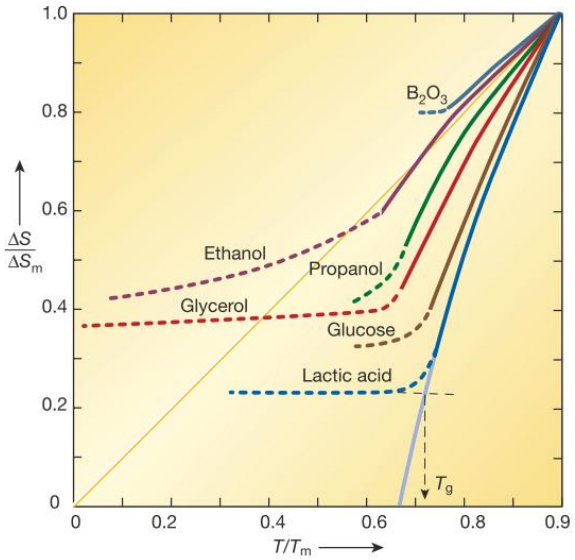


Figure 2-14 Variation of Entropy Difference Between Supercooled Liquids and Crystals with Temperature in Different Systems.

2.3 Glass and Cold Crystallization

2.3.1 Glass

Upon further cooling below T_g, the system's viscosity increases substantially to the point where flow becomes unobservable on a macroscopic time scale. At a microscopic level, particles form a 'cage', with central particles vibrating thermally within these 'cages', giving the system solid-like behaviours, known as glass. [140] Glass exhibits distinct structural features, including long-range disorder, short-range order, isotropy, macroscopic uniformity, and microscopic heterogeneity,

compared to their crystalline counterparts. [141] Studies using high-resolution electron microscopy have been conducted to investigate the microstructures of glassy metals and crystalline metals. [142] The results reveal that the atomic arrangements in glassy metals are disordered and chaotic, whereas in crystalline metals, atoms are arranged in a neat, crystalline structure, as illustrated in **Figure 2-15**.

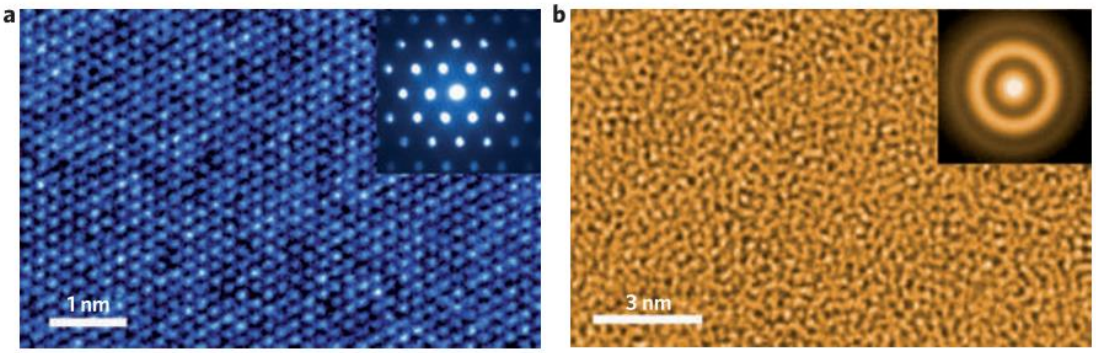


Figure 2-15 High-Resolution TEM Images of Crystalline Metal (A) and Glassy Metal (B). [142]

2.3.2 Cold Crystallization

Cold crystallization is a distinctive behaviour observed in many amorphous materials, particularly in polymers such as polylactic acid (PLA). [143,144] This phenomenon describes the crystallization process that occurs in glassy materials when they are heated to temperatures between the T_g and T_m. During cooling, the material does not crystallize but transitions from a liquid state to a supercooled or glassy state. During heating, as shown in **Figure 2-16**, the material undergoes a process of crystallization accompanied by heat release, known as cold crystallization. [145] This process reveals the internal energy transformation mechanisms within the material and highlights its potential in TES. Therefore, thermally-triggered exothermic glassy materials have become a focal point of research for long-term TES.

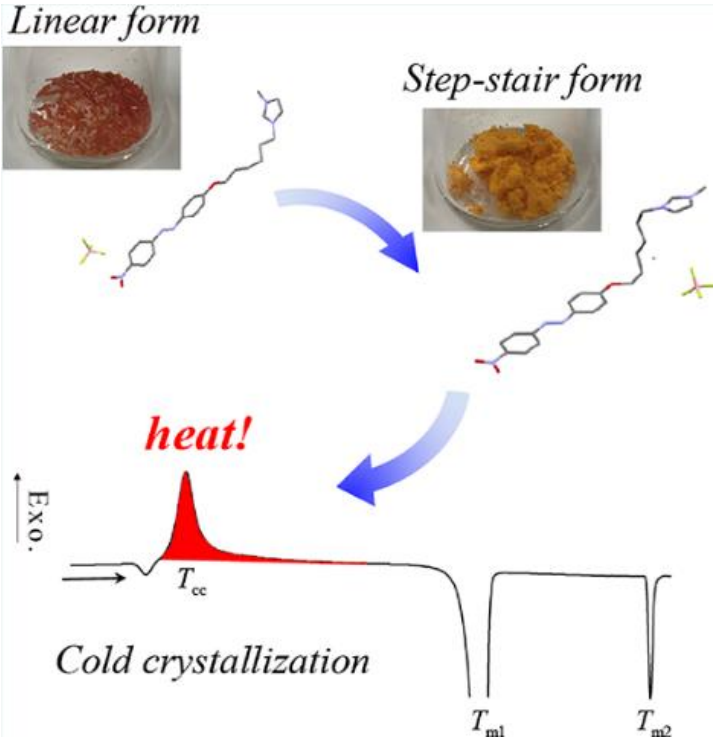


Figure 2-16 Cold Crystallization in DSC Curve.[145]

The phenomenon of cold crystallisation in the glassy state differs significantly from that of melt crystallisation. It is characterised by the formation of a greater number of smaller spherulites. This occurs because a greater number of nuclei are formed during the quenching of supercooled liquids or subsequent heating. [146,147] With regard to the kinetics of crystallisation, cold crystallisation typically occurs at a faster rate than melt crystallisation at the same temperature. The accelerated rate is attributed to the presence of nuclei or mesophase structures in the glass formed by quenching. Furthermore, the kinetics of cold crystallisation can be influenced by a number of factors, including the cooling rate and minimum cooling temperature. Sánchez et al. [148] observed that a lower cooling rate during sample preparation increases the number of nuclei in PLA glass, accelerating the cold crystallization process, as shown in **Figure 2-17**. Similarly, Santis et al. [149] found that the rate of cold crystallization in PLA increases as the minimum cooling temperature decreases, due to the formation

of more nuclei at lower temperatures.

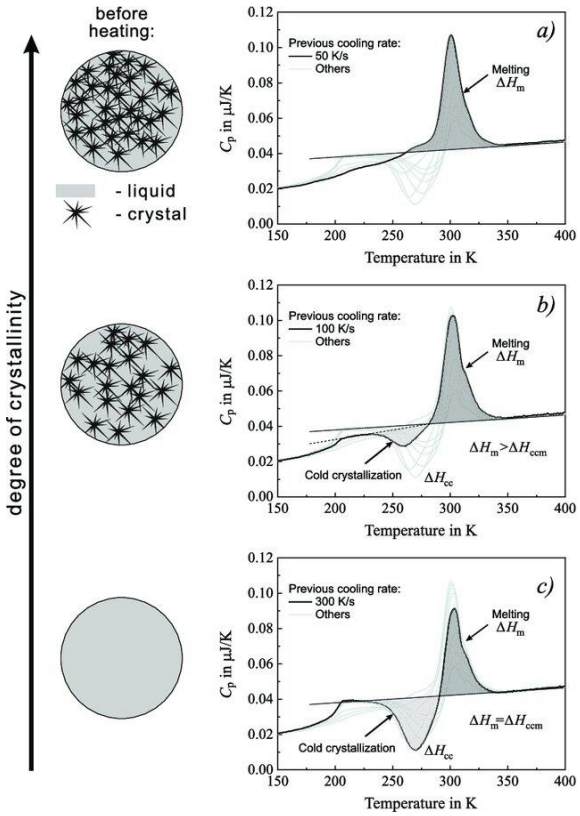


Figure 2-17 Relationship between Cooling Rate and Number of Nuclei. [150]

2.4 Long-Term TES Based on Supercooled and Glassy PCMs

Long-term TES is important for balancing seasonal fluctuations in energy supply and demand. This is particularly important for solar energy due to significant variations in solar irradiation between winter and summer, as well as the seasonal reversal in thermal energy demand. Storing solar energy from summer for winter heating or utilizing seasonal differences between hemispheres and year-round solar resources near the equator for cross-regional thermal energy transfer could significantly improve energy utilization and reduce costs. Long-term TES currently heavily relies on equipment and system design to minimize heat dissipation. [151,152] This method offers limited control and storage

duration, making it a less preferred choice. Supercooled liquids and glassy state TES materials offer a potential solution to this challenge. Subsequent sections will therefore focus on the research state-of-art research of supercooled liquids and glass state materials for long-term TES applications.

2.4.1 Supercooled Liquids as Long-Term TES Materials

Supercooling is a common phenomenon in the crystallization of PCMs, particularly in polyols and hydrate salts. This reduces their thermal storage capacity. The use of nucleating agents can mitigate this issue. Interestingly, achieving a stable supercooled state, offers significant benefits for long-term TES. Supercooling can be classified into controllable and uncontrollable types. It is rare but desirable to have heat release on demand in TES systems. The use of PCMs with controllable supercooling is a promising solution for long-term TES applications. This sub-section summarises recent research on this aspect.

2.4.1.1 Supercooled Hydrate Salts

Supercooled hydrate salts, such as sodium acetate trihydrate (SAT), are extensively studied as long-term TES materials due to their remarkable supercooling features. SAT can remain in a stable supercooled state at room temperature until it is triggered by external stimuli, such as seeding or an electric field, to initiate crystallization and release heat. [38,86,153–158] SAT has a great potential in building heating and solar water heating applications due to its favourable phase change temperature of 58°C and high latent heat of fusion (264 kJ/kg). Additionally, it is chemically stable, and non-toxic, and has a relatively low cost. However, its application is limited by various factors, such as unstable supercooling, spontaneous crystallization, phase separation, and corrosiveness. [159]

To tackle these issues, various methods have been explored, including the addition of water or additives to enhance supercooling stability, using thickeners to prevent phase separation and improve cyclic performance, and replacing copper or aluminium containers with non-corrosive ones made of stainless steel, polyethylene, or polypropylene. Although these efforts have improved the applicability of SAT to some extent, achieving supercooling stability still poses a significant challenge in large-scale preparation and application. Sample size, impurity levels, and surface roughness of containers are factors that can induce spontaneous heat release, leading to a small proportion of samples that can stably supercool and successfully release heat in large-scale experiments. The highest success rate is only 67%, and in some cases, it drops as low as 15%. These results highlight the challenges of supercooling stability that SAT faces in practical applications. Other supercooled hydrate salts, such as dodecahydrate disodium phosphate [160,161], calcium chloride hexahydrate [162], and sodium thiosulfate pentahydrate [163], are also being studied for their potential use in long-term thermal storage. These materials face similar application challenges to SAT. **Table 2-4** presents some recent examples of typical SAT materials.

Table 2-4 The Summary of SAT for Long-Term TES

Materials	Mass ratio	Mass Scale (kg)	Long –term Energy Density (kWh/m^3)	Supercooling Stability (%)	Ref.
SAT-H2O	60:40	5.5	-	33	
SAT- H2O -CMC	59.1:39.4:1.5	5.5	-	67	[41,157]
SAT- H2O -CMC	58.2:38.8:3	5.5	-	100	
SAT- H2O	91:9	199.5	57.2	35	[164]
SAT- CMC	99:1	220	72.8	67	
SAT- CMC - graphite	97:1:2	202	50.9	-	[40,86]
SAT- H2O -EDTA	98:1:1	202	54.3	-	
SAT- CMC	99:1	220	59.5	-	
SAT- H2O – Polymer	95:2:3	200	43.4	-	[165]
SAT- Xanthan rubber –graphite	95.1:0.5:4.4	116.3	67.0	15	[164]

SAT- H2O	94:6	116	43.4	41	
SAT- H2O	65:35	137.8	35.3	66	[153]

Remark:

1) Definition of stability (or term as success rates): Stability is defined as the ability of the storage system to maintain its supercooled state for 24 hours after being cooled down to 30°C. If the system manages to keep the supercooling for this duration, it is considered to have achieved stable supercooling.
2) Testing Method: To evaluate the stability, the supercooled PCM undergoes multiple thermal cyclic tests.
3) Calculation of Stability: The stability is calculated by dividing the number of successful cycles (where the PCM maintains the supercooling for 24 hours) by the total number of cycles conducted.

2.4.1.2 Supercooled Polyols

Polyols are compounds with multiple hydroxyl groups that can form strong intra- and intermolecular hydrogen bonds. This can lead to significant supercooling, which is particularly evident in substances such as xylitol [45,46,85,92,93,166–169] and sorbitol [170–173]. These compounds can remain stable as supercooled liquids at room temperature after melting and cooling, making them ideal materials for long-term TES. The suitability of these polyols is underscored by their non-toxic, non-flammable, and non-corrosive nature. Laboratory experiments have demonstrated that xylitol can be stably stored in its supercooled liquid form for up to many years. [174] However, the main challenge with xylitol as a long-term supercooling material lies in its slow crystallization rate and the difficulty of triggering crystallization due to the high viscosity of its supercooled liquid.

Erythritol, another polyol known for its substantial degree of supercooling, poses a challenge in forming a stable supercooled liquid on its own. [84,175] However, it can achieve a stable supercooled state when combined with other hydrogen bond donors. For instance, research by Deng et al. has

shown that adding sodium hydroxide to erythritol strengthens intermolecular hydrogen bonding, enabling the formation of a stable supercooled liquid that can be stored at room temperature for over 30 days, with crystallization induced by localized cooling or mechanical stirring. [176]

Although polyol-based supercooled liquids have potential for long-term thermal energy storage, their triggering performance and slow crystallization rate are significant challenges that need to be addressed.

2.4.1.3 Photo-Switchable PCMs

Photo-switchable PCMs operate based on the principle of undergoing molecular structural changes in polarity and conformation under light irradiation through isomerization reactions, facilitating supercooling and thermal energy storage. [42–44,177–183] This process is underpinned by molecular design, comprising two essential elements: a photochromic core that undergoes reversible isomeric transformations, and a phase-directing group (R) that, despite its structural constancy, significantly influences the intermolecular forces and materials phase state, as shown in **Figure 2-18a**. Energy storage in these PCMs results from the enthalpy associated with the transition from crystalline to liquid phase and the isomerization enthalpy between the E and Z states, as shown in **Figure 2-18b**. The energy charging can occur through a one-step light-induced liquefaction or a multiple-step process involving phase change and isomerization, depending on the material's characteristics.

Photo-switchable PCMs can convert from their Z-isomer to the E-isomer through thermal reversion

at high temperatures. This process reduces the efficiency of the E-Z conversion. To improve this conversion rate, solvent effects are used. Photo-switchable PCMs are categorized into single-component and composite materials, depending on whether a molten PCM is required as a solvent. The charging and discharging cycles of these PCMs are shown in **Figure 2-18 c** and **Figure 2-18 d**.

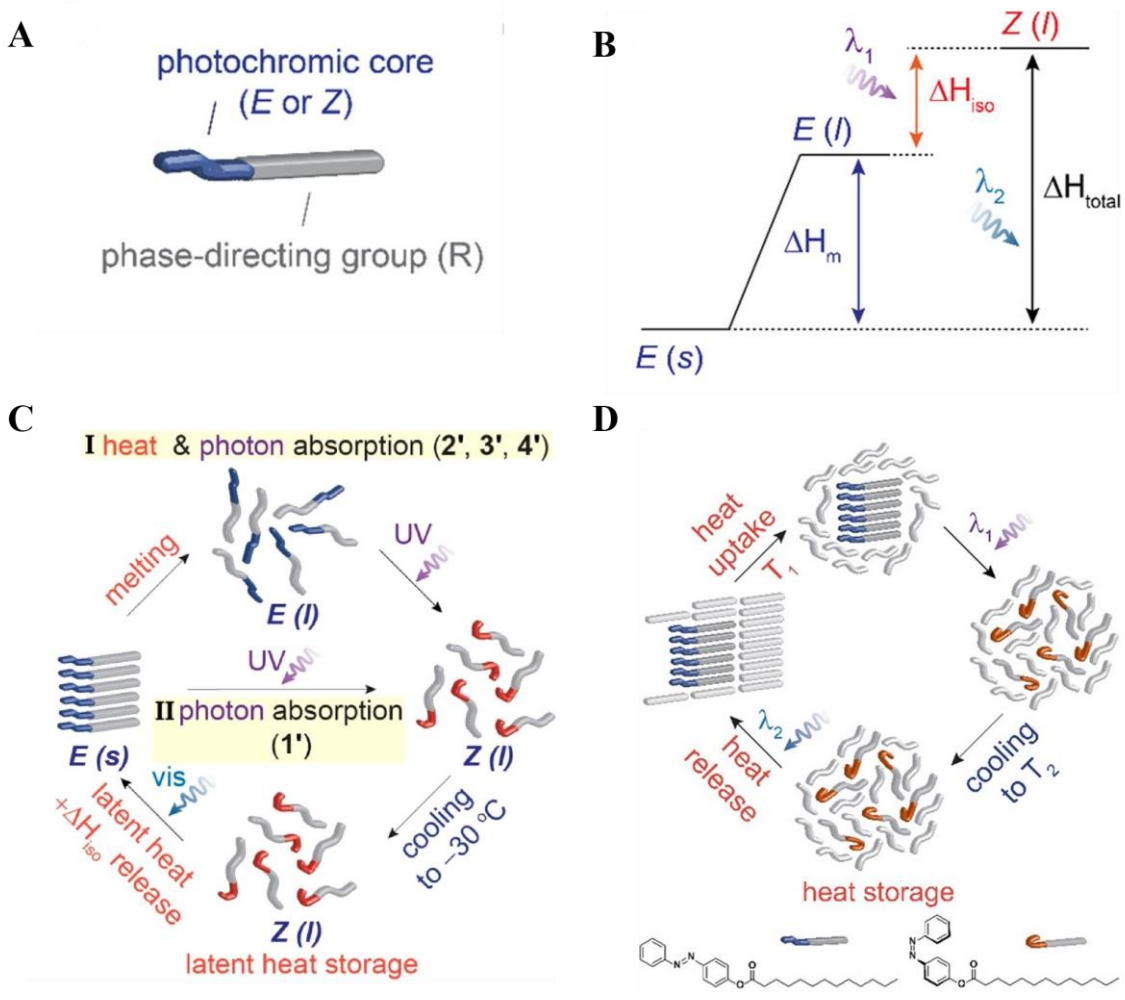


Figure 2-18 The Properties of Photo-Switchable PCMs. [180]

*(**A**) The structure of photo-switchable PCMs. (**B**) Total energy storage in photo-switchable PCMs. (**C**) The charging and discharging cycle of single-component photo-switchable PCMs. (**D**) The charging and discharging cycle of composite photo-switchable PCMs.*

To reduce the thermal reversion of Z-isomers at high temperatures in single-component photo-

switchable PCMs, chemical modifications are made to the core unit. These adjustments not only decrease thermal reversion but also extend the half-life and modify the triggering wavelength of the molecules. For instance, the addition of oxygen-containing functional groups can cause a redshift in the wavelength of n-π* transitions. Furthermore, the substitution of molecules with chlorine, fluorine, or heterocyclic groups can significantly extend their half-life. This effect can last for several decades in some cases. **Table 2-5** lists some single-component photo-switchable PCMs and their properties.

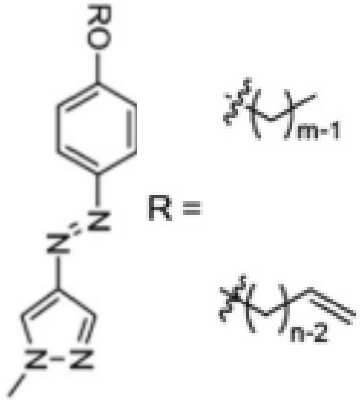
Composite photo-switchable PCMs are formed by blending a pure PCM with a specific ratio of photo-switchable PCM molecules that are soluble together. The objective is to dissolve the E-state photo-switchable PCM molecules in the molten PCMs. The preparation of composite photo-switchable PCMs involves a two-step process. Firstly, the pure PCM is melted using heat. Secondly, the photo-switchable PCM molecules are uniformly dispersed through solvent effects, followed by isomerization under UV light. The degree of supercooling in these materials is dependent on the concentration of photo-switchable PCM molecules and the type of base PCM. Materials with high polarity are more likely to interact with the Z-isomer dopants, resulting in increased supercooling. **Table 2-6** lists some composite photo-switchable PCMs and their properties.

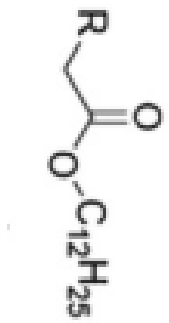
Photo-switchable PCMs have significant scientific potential, but they face numerous challenges towards practical application. Their synthesis involves long production cycles, complex procedures, and high costs, which limit their widespread adoption. The charging process depends on specific

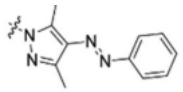
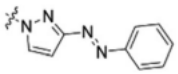
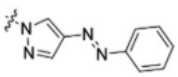
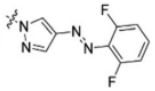
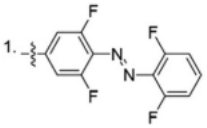
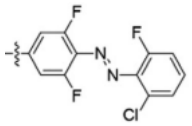
light wavelengths, which reduces efficiency and increases duration. Furthermore, the storage capabilities of these materials are limited due to their narrow supercooling range and susceptibility to photo-induced effects, which require storage in dark conditions. Additionally, the triggering process may be difficult by internal crystallization during the energy release phase, which can obstruct uniform light penetration. Although stirring or inducing flow can partially alleviate this issue, it also prolongs the energy release process. Therefore, these materials remain primarily in the experimental research stage, facing numerous technical and application challenges.

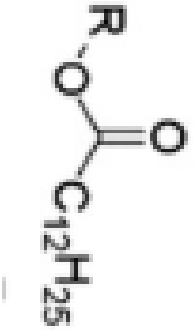
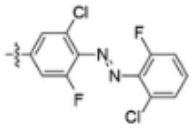
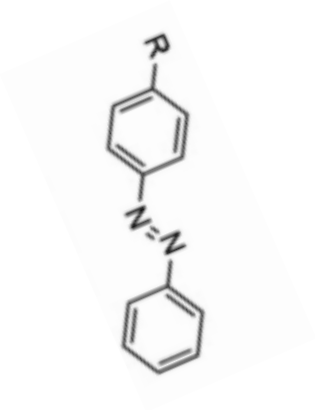
Table 2-5 Some Single-Component Photo-Switchable PCMs and Their Properties.

(ΔH_{iso} , ΔH_p , and ΔH_{tot} represent the energy of isomerization, phase transition, and the total energy, respectively; and $t_{1/2}$ denotes the half-life.)

Chemical Structure	R-Group	T_m (trans) (ºC)	T_m (cis) (ºC)	ΔH_{iso} (kJ/kg)	ΔH_p (kJ/kg)	ΔH_{tot} (kJ/kg)	$t_{1/2}$ 298K	Ref.
	m=1	93	27	180	150	330		
	n=6	82	25	190	140	330		
	n=7	83	35	180	160	340	~90d	[184]
	n=8	83	19	170	160	330		
	n=10	88	28	160	180	340		



n=11	92	37	160	200	360		
	67	Liq	110	80	190		
	91	53	110	120	230		
	71	Liq	100	120	220	-	185
	61	Liq	70	100	170		
1. 	45	-36	50	100	150	2.0 y	186
	56	-42	50	90	140	258d	

		78	Liq	50	70	120	322d	
	$-OC_{15}H_{31}$	81	31	130	40	170		- [187]
	$-OC_{13}H_{27}$	84	40	120	80	200		

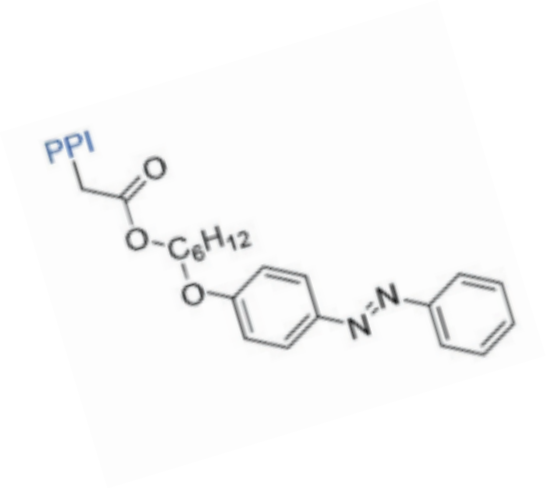
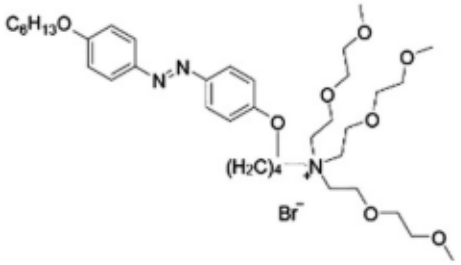
	65	-	180	30	210	32h	[188]
	87	Liq	79	70	149	-	[179]

Table 2-6 Some Composite Photo-Switchable PCMs and Their Properties.

Composite system	T_m (trans) (°C)	T_m (cis) (°C)	ΔT (°C)	ΔH_{iso} (kJ/kg)	ΔH_p (kJ/kg)	ΔH_{tot} (kJ/kg)	Ref.
C_nCOO-AZO + C_nCOOH	38	28	10	120	80	200	[189]
C_n-Azo + tetradecane	2.08 ~ 2.13	-6.71 ~ -1.96	4.04 ~ 8.80	20 ~ 70	80 ~ 190	150 ~ 210	[190]
C_n-Azo + C_nOH	35	29	6	60	180	240	[191]

2.4.2 Glassy State Materials as Long-Term TES Materials

Glassy state TES materials demonstrate significantly greater stability compared to supercooled one. This distinction is primarily attributed to the substantial reduction in their kinetic properties below T_g. The reduction leads to a dramatic increase in viscosity below T_g, giving the materials solid-like

properties. When T_g of a material is higher than room temperature, its storage stability under ambient conditions improves significantly. These materials exhibit solid-like behaviour and are less sensitive to triggering mechanisms used for supercooled materials, such as mechanical stirring, seeding, or localized cooling. However, it is still possible to trigger stored latent heat through a heating-induced cold crystallization process. Although this method may cause some loss of stored latent heat, the benefits in terms of enhanced material stability are substantial. Hence, metal-organic, and organic glass-state TES materials have become popular research topics due to their stability.

2.4.2.1 Metal-Organic Glass as TES Materials

Metal-organic glass state TES materials are created by forming coordination bonds between metal ions or clusters and organic ligands. Katsunori et al. first synthesized schiff-base nickel (II) complexes derived from three toluidine isomers, specifically bis[1-(3-methylphenyl) iminomethyl] naphthalen-2-olato] Nickel (II), for automotive exhaust heat management. [192] The material melts at ~290 °C with a melting enthalpy of 47.2 kJ/mol, transitions to glass at ~120 °C, cold-crystallizes at 167 °C with an exothermic enthalpy of 40.6 kJ/mol. However, the high cost of the ligands, higher charging temperatures, and lower mass energy storage density limit its widespread use in the recovery of low-grade thermal energy.

In recent years, there has been a growing research interest in glassy materials based on Metal-Organic Frameworks (MOFs). [193–197] They retain the structural diversity and design principles based on coordination chemistry of MOFs, while also exhibiting plasticity and the absence of grain boundaries. Although MOF glass find primary applications in areas such as gas separation [198,199], solid

electrolytes [200,201], and optical materials [202,203], their applications in thermal storage have not been extensively developed. This is mainly due to the high glass forming ability of most MOF glass, which hinders nucleation during cooling, leading to a limitation of cold crystallization ability upon secondary heating. Moreover, it is worth noting that the majority of MOF glasses have melting points that exceed 300°C, as shown in **Figure 2-19**, which renders them unsuitable for recovering low-grade thermal energy.

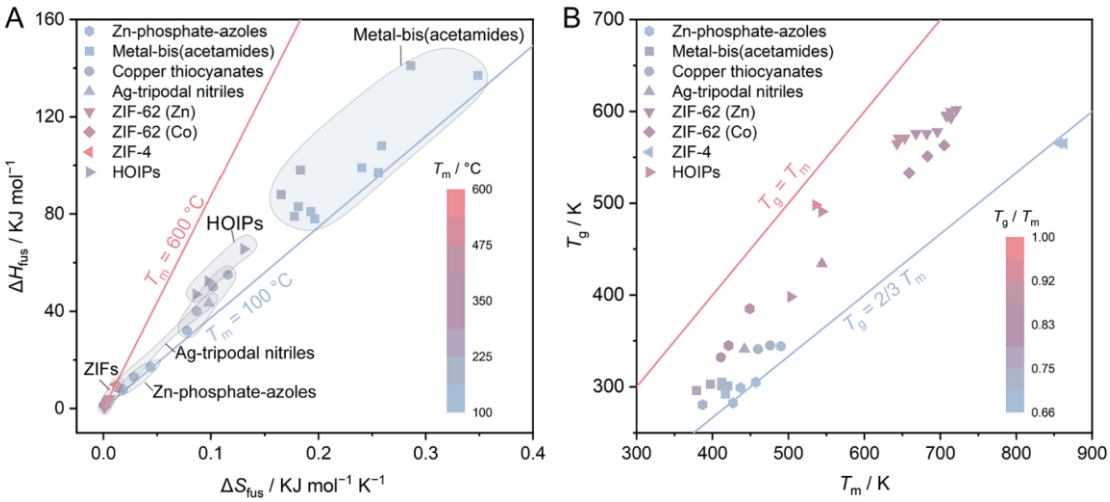


Figure 2-19 Comparison of Different MOF Glasses.[197]

(A) Comparison of difference in enthalpy fusion and entropy fusion. (B) Comparison of T_g and T_m.

Recent studies have revealed the potential of MOF glass in TES applications. However, exploration in this field is still in its early stages. For instance, Mason et al. synthesized Co(hmba)3[Co(NCS)4] MOF glass, which utilizes weak coordination bonds, flexible conformational bridging ligands, and weak electrostatic interactions between spatially separated cations and anions. These interactions between the components lead to a considerable decrease in fusion enthalpy and an increase in system

entropy, which significantly reduces the melting point to around 140 °C. [204] Although this material exhibits exceptional cold crystallization abilities, its potential for thermal energy recovery has not been thoroughly investigated. Overall, the development of glassy TES materials based on metal-organic glass faces multiple challenges. These include unsuitable operating temperatures, low cold crystallization enthalpy, and high ligand costs. Therefore, these materials are currently in the laboratory research stage.

2.4.2.2 Organic Glass as TES Materials

Glassy TES materials are formed by organic molecules through intermolecular force interactions. These materials are usually prepared by methods such as melting or solvent evaporation and are prepared through physical blending. Polyol-polymer-based glassy TES materials have recently gained significant research interest. This is largely due to the pioneering work of researchers such as Ari Seppala and their team. [48,166,169,205–208] They have successfully developed a series of glassy TES materials, including erythritol-sodium polyacrylate, mannitol-sodium polyacrylate, and erythritol-polyvinyl alcohol. Shi et al. also developed a glassy composite PCM consisting of erythritol, carboxymethyl cellulose, and tetrasodium ethylenediaminetetraacetate (ERY/CMC/EDTA-4Na). [209]

Table 2-7 lists the summary of organic glass for long-term TES materials which demonstrate favourable thermodynamic properties. The experimental data suggests that some of materials can store latent heat for up to 97 days in small samples (e.g. 160 g) and for a month in larger-scale device-level experiments (e.g. 6.5 kg). However, these materials still encounter challenges, such as complex preparation processes, lengthy synthesis cycles, and a relatively low glass transition temperature that

requires storage below room temperature to prevent spontaneous crystallization. Besides, the tetrafluoroborate salt of 1-{[4′-(4″-nitrophenylazo)phenoxy]}hexyl-3-methyl-1H-imidazol-3-ium ionic liquid also has potential in TES due to its cold crystallization capability. But its complex preparation and high costs limit its widespread application in large-scale thermal storage.

Table 2-7 The Summary of Organic Glass for Long-Term TES

Materials	T_g (ºC)	T_{cc} (ºC)	ΔH_{cc} (kJ/kg)	T_m (ºC)	ΔH_m (kJ/kg)	Storage Time (days)	Ref.
Eryhtritol-PAANa	-47~-25	10~70	150	95~110	150~260	30	[166]
Erythritol-PVA/SC	-39~28	-5~28	102~156	105~116	218~266	90	[206]
Eryhtritol-PAANa	-18~-6	48~59	109~128	106~108	138~173	97	[205]
Eryhtritol-PAANa	-33~-12	17~57	113~135	106~111	162~245	-	[207]
(ERY/CMC/EDTA-4Na	-	43~52	150~178	104~105	~182	>60	[209]

2.5 Summary

This literature review investigates recent research developments in TES technologies and related materials, with a particular focus on the study of supercooled liquids and glassy materials in terms of their kinetic and thermodynamic properties. By discussing the current research status and challenges faced by these materials for long-term TES, the review draws the following conclusions:

- Among the three TES technologies and related materials, LHS technology based on PCMs demonstrates developmental potential due to its moderate energy storage density, excellent stability, simplified equipment requirements, and good cycling performance. However, it is limited by the inherent properties of PCMs, especially under poor insulation conditions, where the heat contained in the liquid state of PCMs tends to dissipate quickly, reducing its potential for long-term TES applications. The development of supercooled and glass materials aims to address this challenge.

- A deep understanding of the physical properties of supercooled and glass materials is crucial for guiding experimental research. Recognizing their properties aids in the effective design and optimization of long-term TES materials.

- Supercooled long-term TES materials mainly consist of hydrate salts, photo-switchable phase change materials (PCMs), and polyols. However, most of these materials exhibit insufficient storage stability, while others face difficulties in triggering heat release. Therefore, the main challenge for supercooled liquids as long-term TES materials is to balance stability and triggerability.

- Glassy long-term TES materials are mainly divided into metal-organic glasses and organic glass materials. However, these materials face several challenges, such as unsuitable glass transition

temperatures, complex and time-consuming synthesis processes, and high costs.

Chapter 3 Metal-Organic Supercooled Liquids for Long-Term TES

3.1 Introduction

Low-grade thermal energy, with a room-temperature deviation of ca.100 ºC, dominates (63%) of the global energy consumption [210], such applications involve a wide range of scenarios such as thermal management of electronics and data centres, heating buildings and vehicles, and utilisation of industrial waste heats etc. [211] The low-grade heat has a clear and important role to play in the carbon-zero strategy worldwide. Due to temporal, spatial and grade mismatches, the effective use of the low grade heat is highly challenging. Long-term storage of the heat using PCMs provide an avenue to address this challenge, particularly to resolve the temporal and spatial mismatches. The main reason for this is that most conventional PCMs of van de Waals interaction and hydrogen bond can harvest low-grade heat but is easily dissipated the heat when the temperature declines below the crystallization points. [211] Furthermore, the transportation of heat across space over time would require ideally that the PCMs can store latent heat stably at not far from the room temperature without the use of much heat insulation. The long-term supercooled PCMs could fulfil such requirements. Supercooling is undesirable for short-term TES systems as it delays and lowers the temperature of heat release and hampers the system's ability to rapidly adjust to fluctuations in energy demand or supply. Conversely, stable supercooling proves beneficial in long-term TES applications. It enhances the management of storage duration and facilitates controlled heat release when needed. By sustaining supercooling, PCMs prevent premature crystallization, thereby preserving their stored energy until it is strategically necessary to release it.

The use of hydrogen bond networks to create an energy barrier providing a route to develop stable supercooled materials, such as metal-salt hydrate e.g. sodium acetate trihydrate (SAT) [212] and special sugar alcohols e.g. xylitol [213]. However, the supercooled metal-salt materials suffer from poor

cyclability due to loss of hydro-molecules and phase segregation, as well as impurity induced fast crystallization. [106] On the other hand, supercooled xylitol is difficult to be triggered due to excessively dense hydrogen network. [167] Despite of numerous efforts of modulating the hydrogen bond network density with e.g. doping of azobenzene derivatives [189], alkali hydroxides [176], and polyelectrolytes [48], the controllability of phase transition has not been achieved. Mutual acquisition of both phase stability and trigger-ability of phase transition become the most important criterion of PCMs for the practical long-term storage applications. As a result, PCMs with hydrogen bonds only are insufficient.

With a higher strength than the hydrogen bonds, metal-organic coordination bonds may create a deeper supercooling or a more stable glass-state at the ambient [193197214215], which could address the above critical issues of phase stability and transition controllability issues. However, at the opposite side of the coin, there are difficulties for the metal-organic complex to release energy in a rapid crystallization process via a low-cost stimulus due to the stronger strength of coordination bonds. An intrinsic conflict therefore exists between phase stability and trigger-ability of the reversible phase-transition. Only resolving such a conflict can stable glass-state materials be turned into usable products.

In this PhD work, a new strategy is proposed that combines the coordination and hydrogen bonds to create a supercooled liquid in a core-shell coordination structure. This unique core-shell coordination structure as will be presented in this chapter is found by combining information gathered by using various tools such as X-ray diffraction (XRD), Extended X-ray absorption fine structure (EXAFS), X-ray absorption near edge structure (XANES), ultraviolet-visible (UV-Vis) and Fourier transformed infrared absorption (FTIR). It was found that an elongated octahedral Mn-methylurea (1:4) complex (MM) acted as the core, offering two active sites in longer bond to coordinate two other ligands like Cl^- ions. Once energy-harvesting units of high enthalpy are incorporated, such as erythritol, it would replace Cl^- ion already coordinated with MM core in the melting process due to the larger splitting energy, to form a supercooled liquid MM@erythritols (MME) with excess erythritols surrounding

the MM core via hydrogen bonds as the shell, after natural cooling from the melting temperature to room temperature. Glass-state MM was shown to exhibit a high glass-forming ability (GFA) of 0.75 and an impressive viscosity of 10^8 Pa·s at the room temperature, which dominates the thermal stability of supercooled liquid MME and hence the phase stability.

The thermodynamics and kinetics of the phase transition between the supercooled liquid and crystalline MME have also been explored. As will be detailed in this chapter, the reversible phase transition relies critically on the ingenious ligand exchange between erythritol and Cl^- ion coordinated with MM core, which can be driven by a local exotic shear stress smaller than 10 Pa. The heat release from a 425g-MME sample can be stimulated within tens of seconds in a demonstration experiment which could last for over 10 hours. Room-temperature energy barriers of MME series were measured at ~10^{-19} J, upon combining with their suitable diffusion rates (~10^{-10} cm^2/s), showed a great stability of MME. The enthalpy loss for the intrinsic MME materials was found to be lower than 15% after 1000 service cycles of thermal charging and discharging, demonstrating a great cyclability stability. As will be detailed in this chapter, this strategy successfully addressed the conflict of phase stability and triggerability challenge. Furthermore, it will be shown that, by tuning the erythritol load simply, the MME material system can meet different heat transmission needs across a day and even cross-season, making it possible for long-distance heat transportation applications, across cities.

3.2 Experimental

3.2.1 Materials and Methods

- **Materials**

Manganese (II) chloride anhydrous ($MnCl_2$, ≥99% trace metals basis), 1-Methylurea ($C_2H_6N_2O$, 98%), meso-Erythritol ($C_4H_{10}O_4$, 99%) were purchased from Shanghai Aladdin Biochemical Technology Co., Ltd (China), and were used at they were without any purification.

- **Preparation of MM Glass (Methylurea-$MnCl_2$ Complex)**

There are two methods for the preparation, melting method and solution method. Due to the precise composition of the prepared samples, the melting method is suitable for characterizing the structure of materials and testing their properties. However, the disadvantage of the melting method is that the preparation process is time-consuming and not suitable for large-scale production. The solution method is more appropriate for large-scale production, but its main drawback is that trace solvent molecules may remain in the prepared MM, thus the samples may not accurately reflect the material's structure. Therefore, in this work, samples for the characterization of structure and properties are prepared using the melting method, while samples over 50 grams for experiments are prepared through the solution method. **Figure 3-1** shows the details. This work used the melting method. 0.04 mol of methylurea was accurately weighed and heated to 105 °C, melting to give a clear liquid. Next, 0.01 mol of $MnCl_2$ was dried in an oven at 150 °C for 1 hour to remove any moisture. The dried $MnCl_2$ was then added to the molten methylurea while continuously stirring using a magnetic stirrer. The mixture was vigorously stirred until complete dissolution of $MnCl_2$ was achieved, resulting in the formation of a greenish-clear molten liquid. Finally, the molten liquid was cooled down to room temperature to obtain the MM glass.

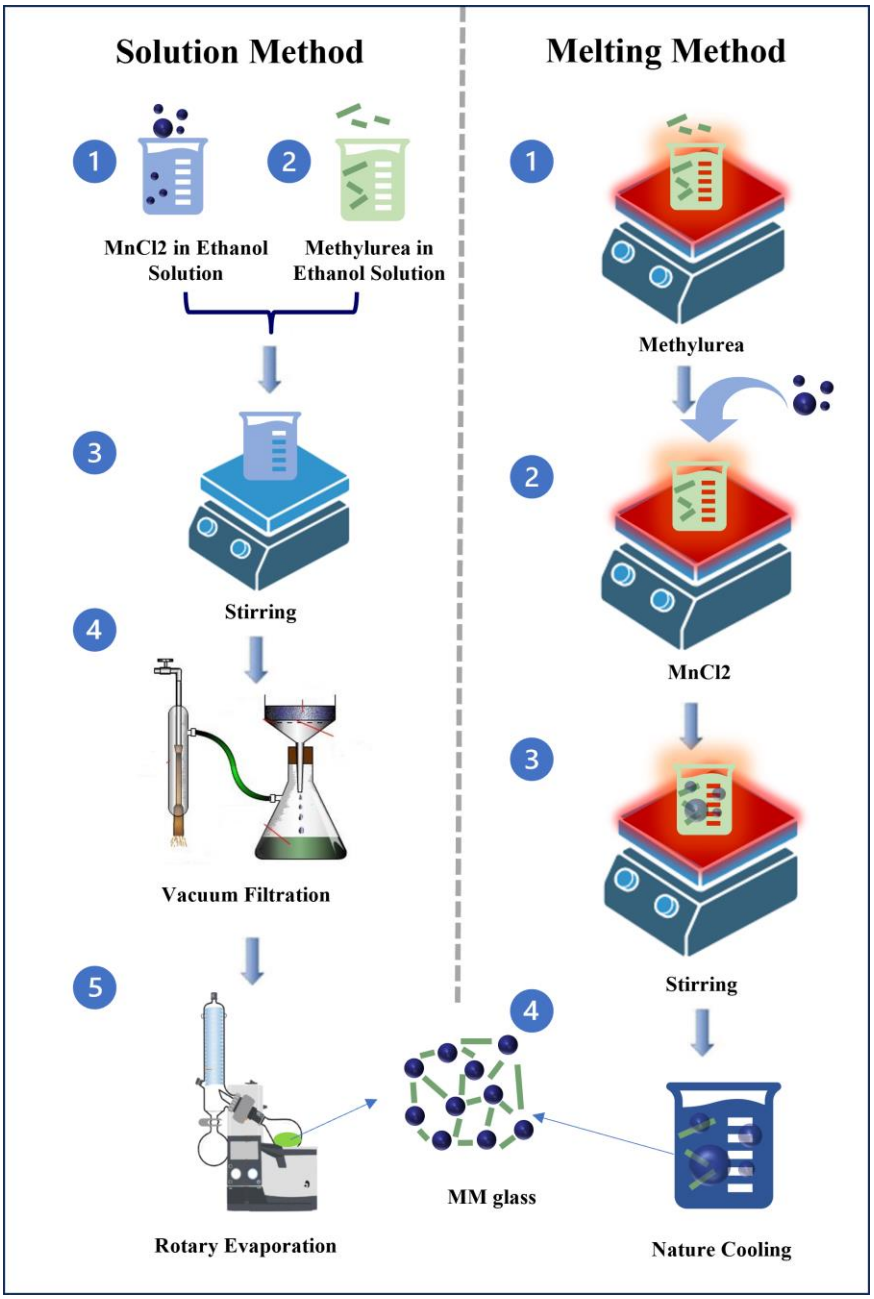


Figure 3-1 Preparation Methods and Processes for MM.

- **Preparation of Metal Organic Supercooled Liquids**

In a typical experiment, 0.01 mol of MM was weighed and heated at 105 °C in a vial. Erythritol of either 0.04, 0.08, 0.12, or 0.16 mol was added while continuously stirring. The four mixtures were heated to 125 °C until thoroughly mixed, resulting in a transparent wine-red liquid, which upon

cooling to room temperature gave viscous MME1, MME2, MME3, and MME4 were obtained, respectively.

3.2.2 Materials Characterizations and Solar Charging/Discharging Experiment

- **X-Ray Diffraction (XRD) and In-Situ XRD**

X-ray diffraction analysis on the samples were performed using a Bruker D8 Advance diffractometer with Cu Kα radiation (λ = 1.5406 Å) operated at 40 kV and 40 mA. For doing so, the samples were ground into a fine powder before placed in the sample holder, while the amorphous samples were melted and deposited onto a sample holder. These samples were flattened to make their surface flat. The diffraction angle (2θ) was from 10° to 80° at a step size of 0.02° and a scan speed of 1°/min. Temperature-controlled XRD was conducted in the 9kW Rigaku SmartLab with a temperature-controlled stage (Anton Paar DCS 500).

- **Ultraviolet-Visible (UV-vis) Transmittance Spectra**

The PerkinElmer Lambda 750s UV/VIS/NIR spectrometer was used to obtain UV-VIS spectra. For doing so, the sample was placed in a quartz cuvette with an optical path length of 1 cm. The spectrum was acquired over the range of 300-800 nm with a resolution of 1 nm.

- **Fourier Transform Infrared (FTIR) Spectra**

The FT-IR spectra were acquired using a Bruker Vertex 70v spectrometer equipped with a diamond attenuated total reflectance (ATR) accessory.

- **Nuclear Magnetic Resonance (NMR)**

The ^{1}H NMR spectra in liquid state were obtained using a Bruker Advanced III 500 MHz NMR

spectrometer. The deuterated solvent used was DMSO-d6. Chemical shifts were expressed in ppm and referred to as the residual peak of the solvent peak.

- **Scanning Electron Microscopy (SEM)**

SEM images were obtained using a TESCAM MIRA3 high-resolution field emission scanning electron microscope operated at an acceleration voltage of 3 kV. To improve the conductivity and reduce charging effects, the samples were sputter-coated with a thin layer of platinum. The images were captured using both the secondary electron detector and the backscattered electron detector.

- **Transmission Electron Microscopy (TEM)**

High-resolution scanning transmission electron microscopy-high-angle annular dark-field (STEM-HAADF) images were obtained using a Talos F200X G2 (Thermo Fisher) transmission electron microscope. The TEM specimens were prepared using the melt-dragging method. For doing so, the copper grid was heated to 100 °C on a heat stage, and then the molten samples were dropped onto the stage using a capillary tube. The grid was then dragged at high temperature to achieve a suitable thickness of the sample layer. Finally, the specimen was dried and cooled to the room temperature. The STEM-EDX data was acquired using a FEI Talos transmission electron microscope (TEM) with Super-X energy dispersive X-ray EDX operate in the STEM-HAADF mode.

- **Cryogenic Transmission Electron Microscopy (cryo-TEM)**

Cryo-TEM images were acquired using a Titan Krios G3i (D3845) transmission electron microscope. The sample vitrification process was performed with an automated vitrification robot (FEI Vitrobot Mark III) equipped with a humidity and temperature-controlled glove box. The sample was observed

at ~-170 °C under low-dose conditions using a cryo-electron microscope equipped with a direct electron camera (Falcon IV, Thermo Fisher Scientific) to acquire high-resolution images.

- **Differential Scanning Calorimetry (DSC)**

DSC measurements were performed using a TGA/DSC1(Mettler Toledo) under a nitrogen atmosphere. Approximately 5 mg of the sample was placed in a standard aluminium pan and heated at a rate of 5 °C/min, 2.5 °C/min, 1 °C/min, and 0.2 °C /min from -65 °C to 130 °C, and then cooled to -65 °C, with a 50 mL/min N_2 flow into the sample cell. An empty aluminium pan was used as a reference.

- **Isothermal Calorimeter**

A Calvet-type heat-flux calorimeter (C-80, Setaram) was used to measure the heat generated during stirring-induced crystallization for microcalorimetry. The sample was weighed with an accuracy of 4-5 g, placed in a platinum crucible, sealed, and loaded into the sample holder. Shear forces were applied to the sample at room temperature using the stirring attachment under a nitrogen atmosphere.

- **Thermogravimetric Analysis (TGA)**

TGA was conducted using TGA/DSC 1 equipment manufactured by Mettler Toledo. The samples were heated from 30 to 500 °C at a heating rate of 5 °C/min in an N2 atmosphere (50 mL/min).

- **Rheological Analysis**

Rheological measurements were conducted using a HAAKE MARS III rheometer equipped with a Peltier temperature control system. In a typical experiment, a sample was placed onto the rheometer stage, incubated for 10 s, before the measurements was started. A 20mm titanium plate was used for

the analysis, and the gap height was set to 0.1mm. The temperature was strictly controlled between 30 and 100 °C using a Peltier system. Each was repeated multiple times with different batches to ensure data reliability and repeatability. The viscosity was monitored under an applied shear rate of 0.1 s^{-1}.

- **Extended X-ray Absorption Fine Structure Spectroscopy (EXAFS)**

The extended X-ray absorption fine structure (EXAFS) spectra at the Mn K-edge were collected at BL14W1 of the Shanghai Synchrotron Radiation Facility (SSRF) using the Si (311) double crystal monochromator (DCM) in transmission mode. The experimental X-ray absorption near edge structure (XANES) spectra at the Mn K-edge were normalized to +100 eV after the absorption edge and the atomic absorption background were subtracted using the Demeter package.

- **EXAFS Sample Preparation**

- **Preparation of Standard Powder Sample**

In a typical experiment, a powder sample were ground to a particle size that passing through approximately 400 mesh. To achieve the best signal-to-noise ratio, the absorption length per square centimetre of the sample was determined using Hephaestus software before conducting the transmission experiments. Additionally, the required sample amount should be calculated, which is used to weight sample for shaping into a circular disk with a diameter of 13mm, sealed with Kapton tape.

- **Preparation of MM Glass and Supercooled MME1**

In a typical experiment, a sufficient quantity of MM or c-MME1(~0.5 g) was placed in a sample cell

and heated to 100 °C until the sample completely melted. The cell was then cooled down to room temperature to obtain MM glass or MME1. The sample cell was made by drilling a circular through-hole with a diameter of 15 mm at the centre of a rectangular aluminium sheet measuring 15 cm by 10 cm with a thickness of 0.1 mm and sealing the bottom surface with Kapton tape. Once all bubbles from air have been removed by heating, seal the top surface with Kapton tape. Then, use a glass plate to press the area containing the sample to ensure a uniform sample thickness.

- **Preparation of Solid c-MME1 Sample**

The solid c-MME1 sample was made by triggering with a needle tip (from a 2 mL syringe) to induce complete crystallization inside the sample cell.

- **Extended X-ray Absorption Fine Structure (EXAFS) Spectra Data Analysis**

IFEFFIT-based Demeter software package was used to analyse the EXAFS data. The raw data were first deglitched and processed in Athena before further analysis. [216] The data at Mn K-edge can provide quantitative structural information about the local coordination around Mn atoms. The structural parameters were fitted using the following EXAFS equation [217]:

$$\chi(k) = \sum \frac{S_0^2 N_j F_j(k) \exp\left(-2k^2\sigma_j^2\right)}{kR_j^2} \sin\left(2kR_j + \delta_j(k)\right) \qquad (3-1)$$

where the j refers the coordination shells of atoms, k is the photoelectron wavenumber, S_0^2 is the passive electron reduction factor, N_j is the coordination number of atoms in each shell, the R is bond distance and the σ_j^2 is called the mean-square relative displacement of bond distance. The effective scattering amplitude $F_j(k)$ and total phase shift $\delta_j(k)$ are dependent upon the scattering atoms. The non-linear least square fitting of the spectra was performed using the above equation as implemented

in the Artemis in the Demeter 0.9.26 package. [216] The Mn foil could not be easily fit to Mn metal models, likely due to the presence of Mn oxides and due to the difficulty of collecting high quality reference data in tandem with sample data at the lower energy Mn K-edge. Therefore, MnO was used as a reference to determine S_0^2. The resulting S_0^2, which was 0.93, was then used as a fixed parameter for other samples.

- **Crystallization Growth**

To quantify the crystal growth velocity of MME samples, an experiment was performed using the RheoScope Module. In a typical such experiment, an MME sample were placed between a plate and a transparent glass substrate with a 0.1 mm gap. Crystallization in the supercooled liquid was triggered by introducing a seeding crystal. The growth velocity of the dendrite tips was determined by measuring the growth distance and time span under different temperatures using an inverted microscope.

- **Thermal Imaging Analysis**

Thermal imaging was conducted on the sample using a Fluke 480 Pro thermal camera equipped with a 17 μm detector over a temperature range of -40 °C to 550 °C. The camera was set to manual mode, and the emissivity was set to 0.95 for all samples. The samples to be analysed was placed on a black background and allowed it to reach room temperature before the measurement was taken. The camera was positioned approximately 40 cm away from the sample.

The characterised samples were subject to solar charging/discharging test.

- **Solar Charging Experiment**

Considering the best balance between triggering and stability of MME2 in the MME series samples, MME2 with an enthalpy of 163.1 kJ/kg was selected among them to demonstrate the application potential in long-term TES. To evaluate the feasibility of the use of solar energy to charge a unit with c-MME2, a solar charging experiment, as shown in **Figure 3-2,** was conducted. The Arc Lamp Solar Simulators (ABET) was used as the energy source. A double-layer beaker was used as both the container and thermal insulation. Solar energy was converted into thermal energy using a selective solar absorber film with a diameter of 100 mm (eta plus, ALANOD). The thermal energy was then conducted into c-MME2 through a round pin heatsink with dimensions of 70 mm (diameter) x 120 mm (length), as shown in the inset of **Figure 3-2 A**. Thermocouples were strategically positioned during the charging process, as depicted in **Figure 3-2 B**. The experiment used 70 g of c-MME2 for charging and the data were recorded using a Data Acquisition System (DAQ, Advantech USB-4718).

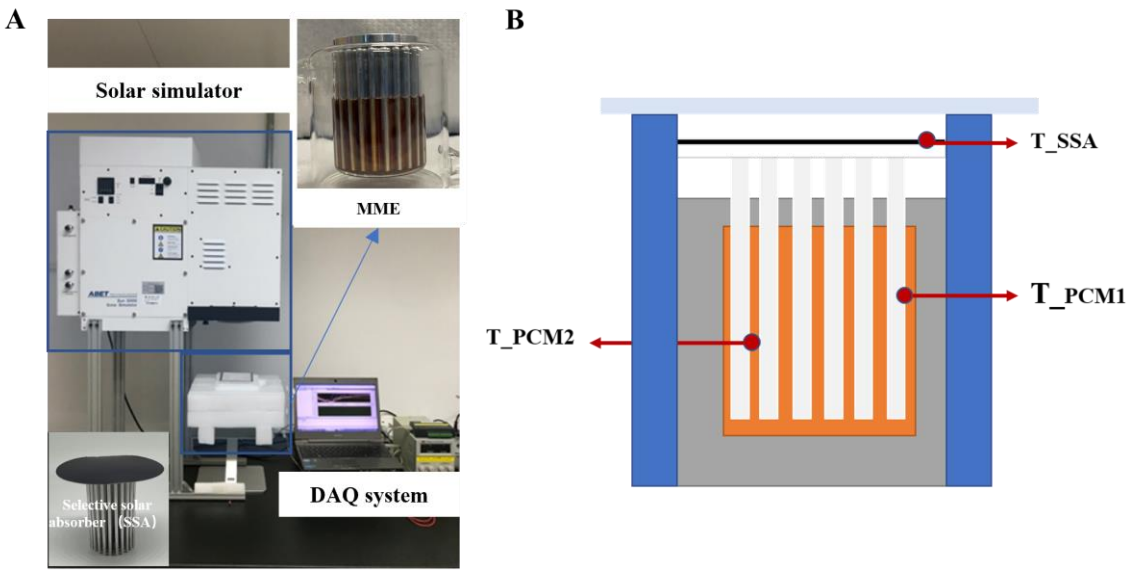


Figure 3-2 Experimental Setup for Solar Charging.

*(**A**) Solar charging system. (**B**) Temperature monitoring sites of thermocouples.*

- **Discharging Experiment**

An experiment was conducted to evaluate the discharging performance of MME2. 425g of MME2 were used to heat the airflow; see **Figure 3-3**. Compressed air from a compressor was used, and a pressure control valve was employed to regulate the gauge pressure. The air flow was dried using a pair of silica gel desiccators. To control the airflow, a flowmeter (FCM, max. 50L/min, CKD, Japan) was used. The airflow was then heated through a copper coil exchanger by the heat released during the stirring-induced crystallization of MME2. K-type thermocouples were placed at the inlet and outlet of the flow pipe, and two additional thermocouples were inserted into the MME2 to monitor the temperature increase. All experimental data were recorded using a Data Acquisition System (DAQ, Advantech USB-4718).

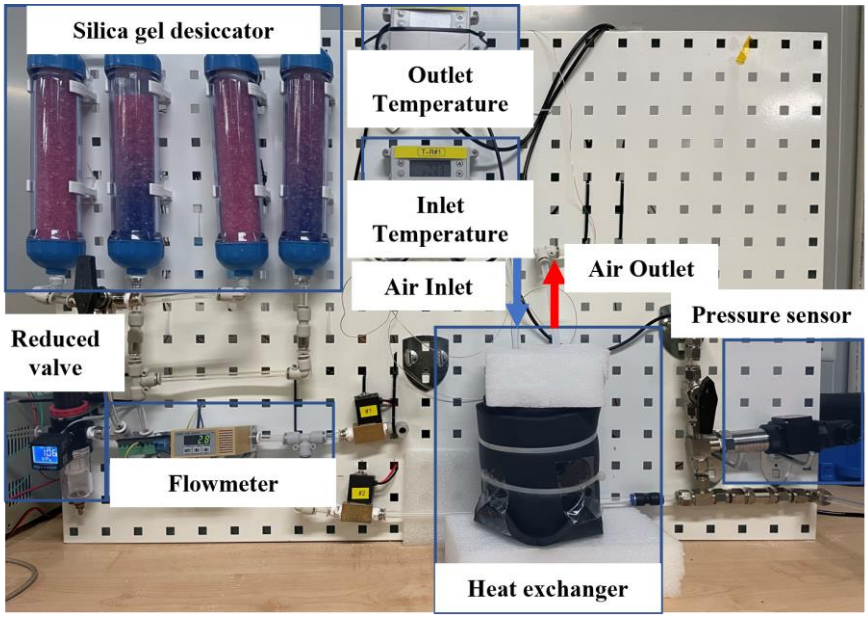


Figure 3-3 The Discharging System Device for Large-Scale Application.

3.3 Results and Discussion

3.3.1 Coordination Core of Mn-Methylurea Glass

A stable glass-state MM complex determines the stability of the core-shell coordination system. The glass-state MM was synthesized in a naturally cooling process after dissolving 1 mol $MnCl_2$ into 4 mol melted methylurea (105 °C). Its amorphous characteristic at the ambient environment is verified by the XRD pattern of MM compared with the crystalline structures of methylurea and $MnCl_2$ in **Figure 3-4 A**. The DSC analysis demonstrates a glass transition temperature (T_g) of 10 °C (**Figure 3-4 B**) whereas decomposition temperature can reach 160 °C as shown by the thermogravimetric analysis (TGA) in **Figure 3-4 C**. The cooling trace (the blue line) further confirms that it follows a non-crystallization process, which is also reflected by the data obtained under different cooling rates (**Figure 3-4 D**). Glass-forming ability (GFA) is often used to evaluate the crystallization resistance by the ratio of T_g/T_m [218]. Here, the melting temperature of MM, T_m, is determined as 102.8 °C with the sample crystallized after sufficiently grinding due to its high glass-state stability, shown by the grey DSC curve in **Figure 3-4 B**. One can find a T_g/T_m ratio of 0.75. This is significantly greater than 2/3 according to the Kauzmann law, [218,219] signifying a high GFA and herein high anti-crystallization ability of MM. The glass-state materials can be further classified by a fragility index (m). [220,221]

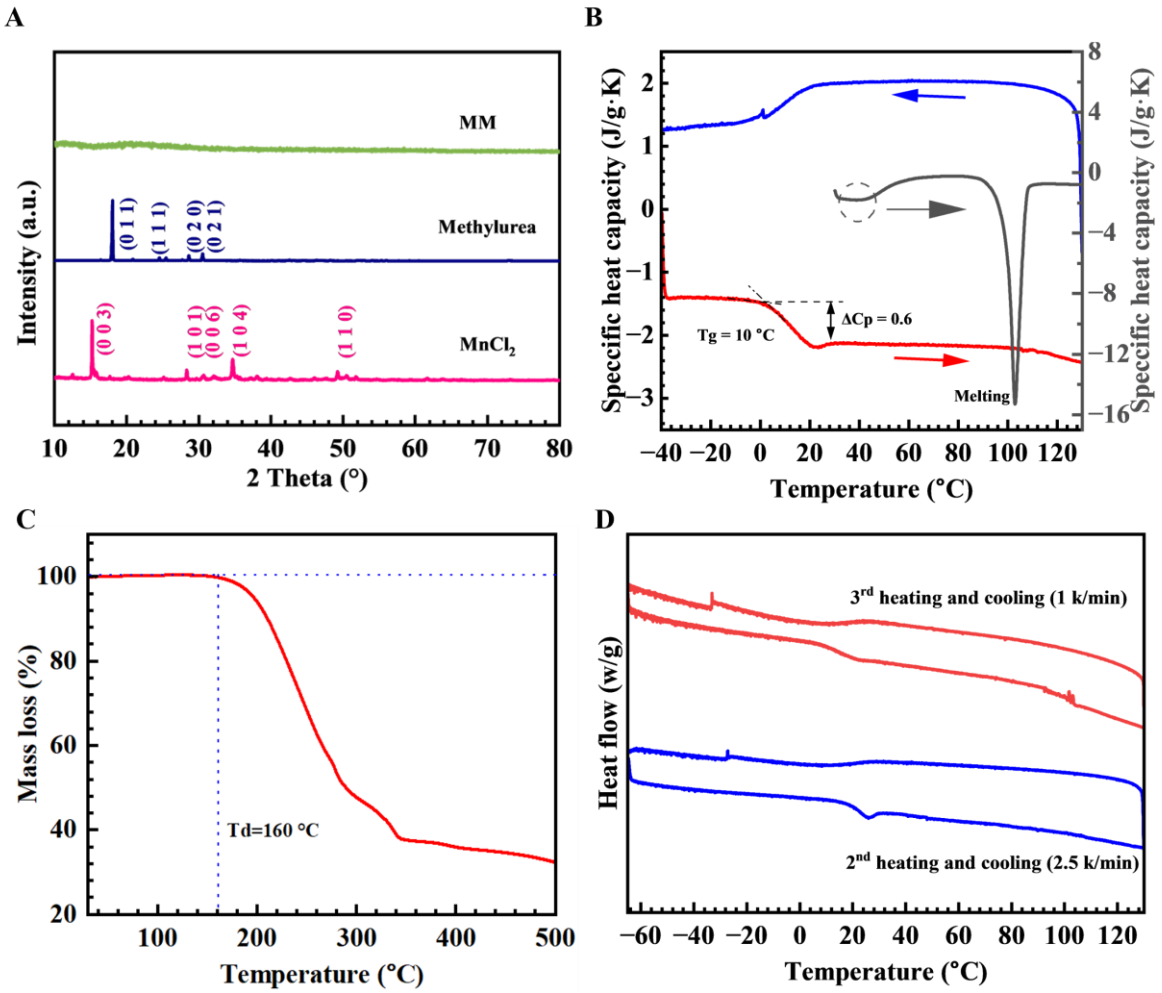


Figure 3-4 The Properties of the MM.

*(**A**) XRD patterns of $MnCl_2$, methylurea, and MM. (**B**) DSC traces for crystalline MM (grey line for heating, blue line for cooling) and glassy MM (red line for heating) with a heating/cooling rate of 5 K/min. (**C**) Thermogravimetric analysis (TGA) profile of MM. (**D**) DSC traces for MM in the second and third cycles, with a heating/cooling rate of 2.5 K/min and 1 K/min, respectively.*

Fitted by MYEGA equation [123], the fragility index of 64 for MM belongs to the intermediate zone with a considerable ability to control thermally induced collapse, but obviously deviates from such

Arrhenius behaviour as SiO_2 glass (m=20) [220] (**Figure 3-5**). That difference between MM glass-state material and typical covalent SiO_2 glass comes from the bond difference.

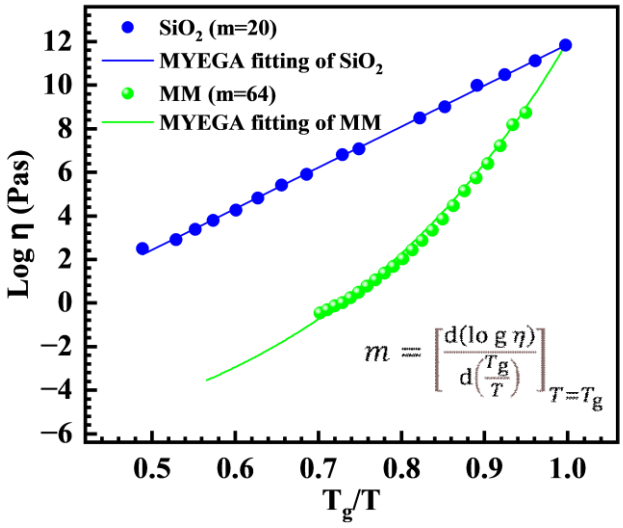


Figure 3-5 Temperature-Dependent Viscosity of MM.

Angell plot showing the fragility of MM alongside SiO2 [107]*. Solid lines are fits to the measured viscosity-temperature relation of the model derived in previous literature* [115,123].

The EXAFS was used to quantitatively determine the coordination number and distance of Mn referring to the first shell energy information of K-edge energy. **Figure 3-6 A-C** and **Table 3-1** show the measured real and imaginary parts of Mn-O coordination EXAFS spectra, with a theoretically fitted curve. These results confirm that the coordination number of Mn-O in MM is 4.0 with its coordination distance of 2.21(2) Å, and that the number of Mn-Cl is 1.4(9) with the coordination distance of 2.46(4) Å. To further understand that coordination configuration, the XANES was used to analyse its Mn K-edge, with a reference to such standard manganese compounds Mn foil, $MnCl_2$, MnO, MnO_2, and $KMnO_4$. **Figure 3-6 D** shows the results. One can see that MM coincides $MnCl_2$

and is closer to MnO in the absorption edge, located between Mn foil and MnO_2, indicating that the valence state of Mn ion in MM is +2 without any redox reaction [222]. Different from a strong pre-edge peak like tetrahedral $KMnO_4$ of low symmetry, the Mn-O coordination in MM has no pre-edge peak and is akin to high-symmetry octahedral MnO and MnO_2. This is because the electron transition from 1s to 3d orbital is dipole forbidden in high-symmetry octahedrons while it is dipole allowed in low-symmetry tetrahedrons like $KMnO_4$ due to d–p hybridized orbital [223,224]. To facilitate clarity, **Figure 3-7** displays the elongated octahedral configuration of MM, illustrating a distinct coordination structure where a Mn ion is coordinated with four methylurea in close distance and two Cl ions at a longer distance. The longer and weaker Mn-Cl dative bonds tend to be easily broken by other stronger field ligands. Such an asymmetrical interaction in MM also allows the larger moving degree of freedom [225], leading to increase structure disorder and eventually increased the GFA of MM.

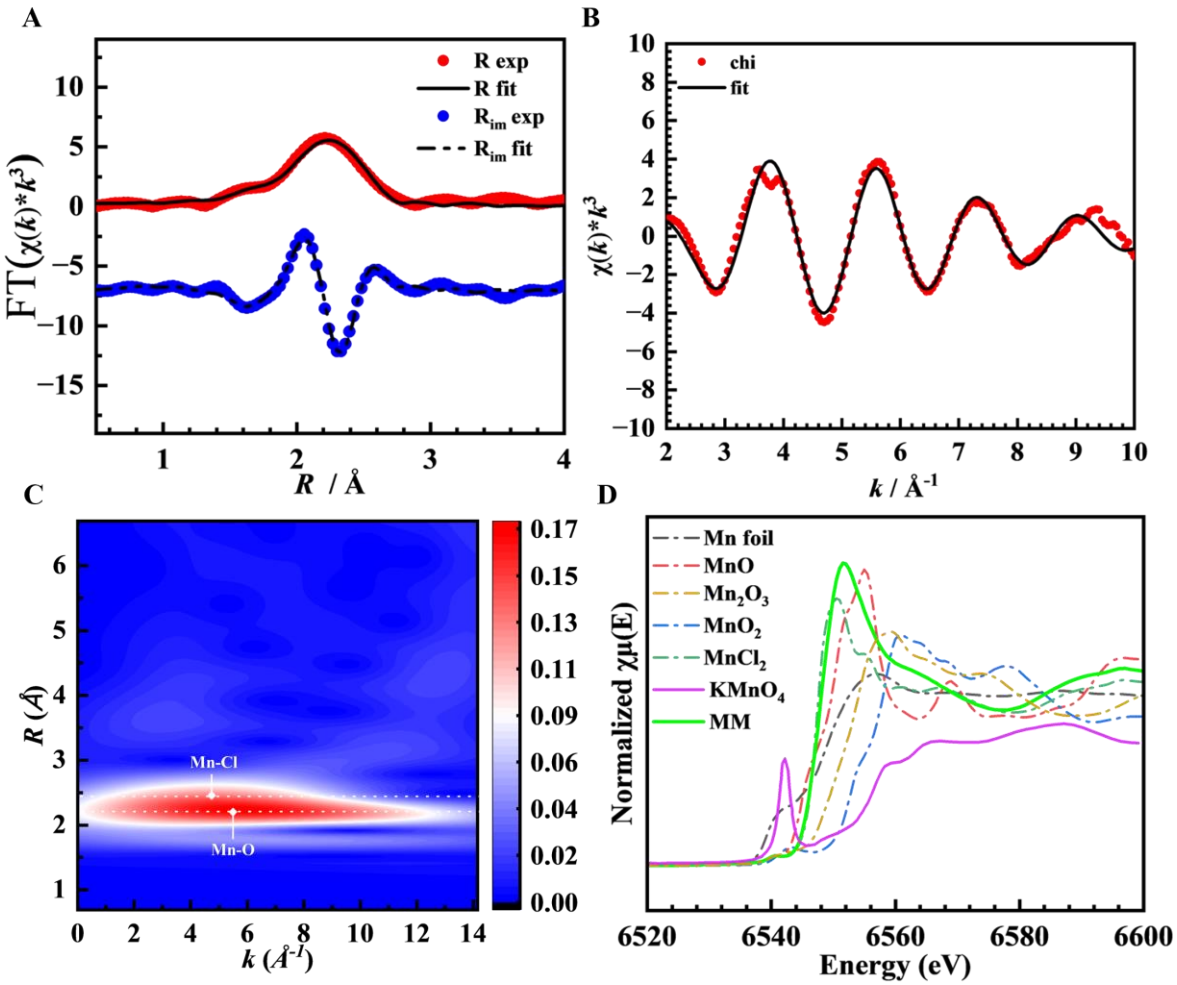


Figure 3-6 Local Geometric Environments around the Mn Atoms in the MM.

*(**A**) Fourier transforms of Mn K-edge EXAFS data (points) and model-based fits (line) of MM in R-space. The data are k^3-weighted and with phase correction. (**B**) Mn K-edge EXAFS (points) and the curve fit (line) for MM, shows in k3 weighted k-space. (**C**) Normalized WT-XAFS for the correlation between R-space and K-space data for MM. (**D**) Experimental K-edge XANES spectra of MM and reference samples (Mn foil, MnO, Mn_2O_3, MnO_2, $MnCl_2$, $KMnO_4$).*

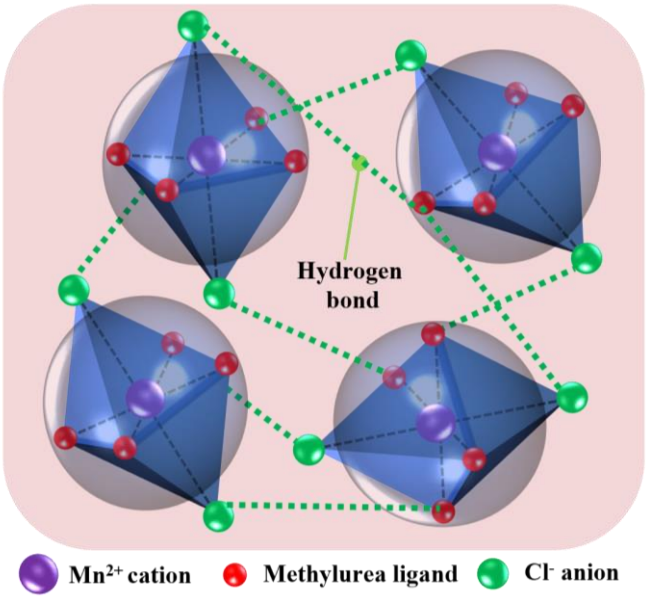


Figure 3-7 Schematic Illustration of the Elongated MM Octahedral.

Table 3-1 Curve Fit Parameters [a] for Mn K-edge EXAFS for MM.

Path	d [b]/Å	N	R/Å	σ^2/Å^2
Mn-O	2.247	4.0[c]	2.21(2)	0.009(2)
Mn-Cl	2.552	1.4(9)	2.46(4)	0.02[d]

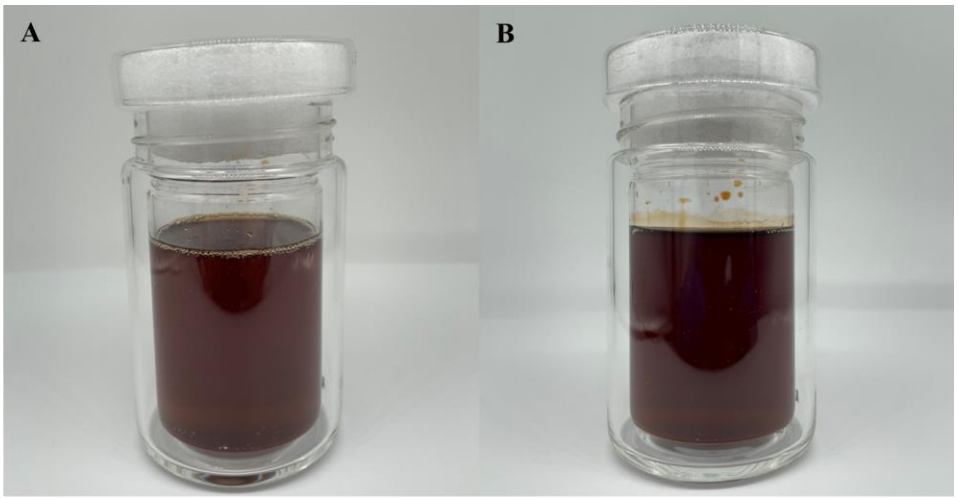
[a] S_0^2 was fixed as 0.93. ΔE_0 was refined as a global fit parameter, returning a value of (0.9±1.8) eV. Data range: $2.0 \leq k \leq 10$ Å^{-1}, $1.0 \leq R \leq 2.5$ Å. The number of variable parameters is 5, out of a total of 7.4 independent data points. R factor for this fit is 1.0 %. [b] The distance for Mn-O is from the crystal structure MnO. The distance for Mn-Cl is from the crystal structure $MnCl_2$. [c] The coordination number was constrained as N (Mn-O) = 4 based on the previous study. The Debye-Waller factors were constrained as 0.02 for decreasing the correlation.

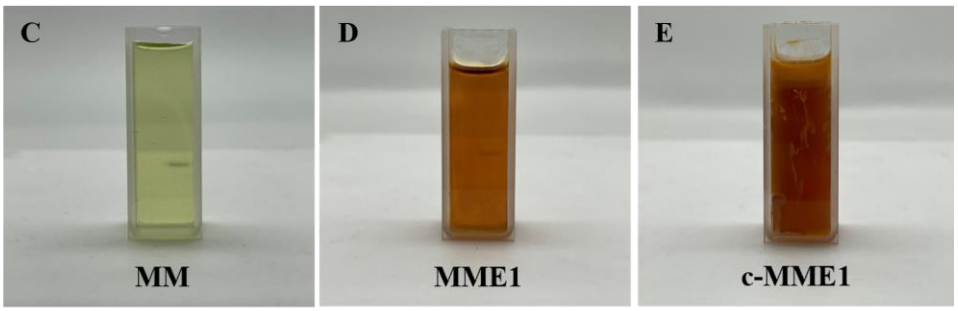
3.3.2 Metal Organic Supercooled Liquid

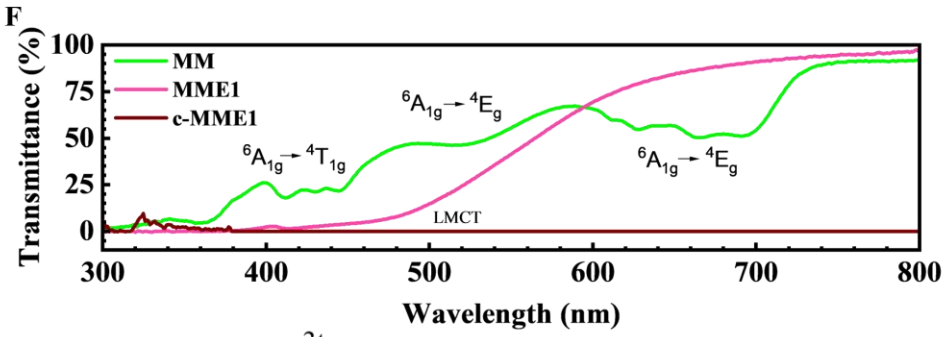
Because of a large supercooled degree between the crystallization point (20 °C) and the melting point T_m =120 °C [94], erythritol with a high enthalpy of 330 kJ/kg is selected as the energy storage materials in glass-forming liquids system for long-term heat storage and transmission. The hydrogen bonds in the pure erythritol supercooled liquids are too weak to be easily broken, and its crystallization is often out of control. [95,226,227] The unique elongated octahedral configuration of MM core offers two active coordinating sites for erythritol with dative bonds stronger than Mn-Cl, leading to a higher barrier for crystallization and herein a more stable supercooled liquids system. This also enlarges the trigger margin compared with systems with pure hydrogen bonds. In view of heat storage density, the amount of erythritol molecules should be as large as possible, limited by the stability of glass-forming liquids. Therefore, a series of composites with different MM:Erythritol ratios were synthesized, including 1:4 (MME1), 1:8 (MME2), 1:12 (MME3) and 1:16 (MME4). A higher ratio leads to a lower material stability. The composite above 1:16 turns easily crystallized and cannot meet required stability. Among these composites, MME1 was selected to analyse the composite structure, which showed a high stability with no apparent change after 180 days of storage (**Figure 3-8 A-B**), especially considering the stability under the irradiation of X-ray beams in XRD and EXAFS.

Although both MM and MME1 keep a transparent state, MM glass looks green while MME1 turns wine red after incorporating erythritol into the MM (**Figure 3-8 C-D**), along with their corresponding

transmittance spectra shown in **Figure 3-8 F**. Such colour transition is attributed mainly to the ligand exchange from Cl^- to C-OH of erythritol due to their splitting energy sequence with Mn^{2+} [227]. Regarding MM, the transitions of $^6A_{1g}(S) \rightarrow {}^4T_{1g}(^4G)$, $^6A_{1g}(S) \rightarrow {}^4E_g(^4G)$ and $^6A_{1g}(S) \rightarrow {}^4E_g(^4D)$ account for the absorption bands around 420 nm, 520 nm and 660 nm (**Figure 3-8 F-G**), respectively [228–231]. The absorption leads to the green but transparent colour shown in **Figure 3-8 C**. For MME1, the ligand to metal charge transfer (LCMT) from the hydroxyl ligand to manganese metal is responsible for the strong absorption band around 400 nm [232,233], which results in the wine red transparent appearance (**Figure 3-8 D**).


A
B
The first day
180 days later


C
D
E
MM
MME1
c-MME1


F
Transmittance (%)
100
75
50
25
0
MM
MME1
c-MME1
$^6A_{1g} \rightarrow {}^4T_{1g}$
$^6A_{1g} \rightarrow {}^4E_g$
$^6A_{1g} \rightarrow {}^4E_g$
LMCT
300
400
500
600
700
800
Wavelength (nm)

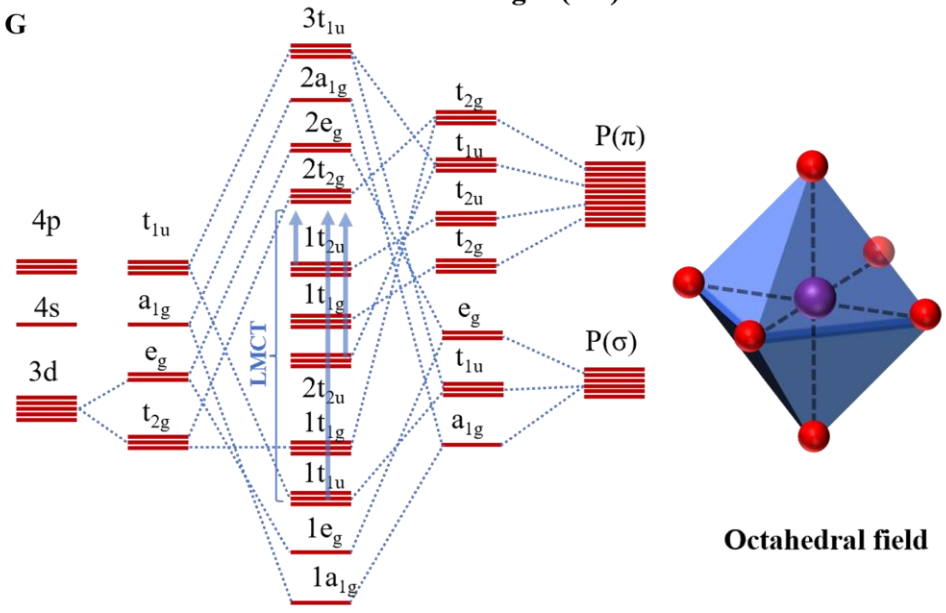

G
4p
4s
3d
t_{1u}
a_{1g}
e_g
t_{2g}
LMCT
$3t_{1u}$
$2a_{1g}$
$2e_g$
$2t_{2g}$
$1t_{2u}$
$1t_{1g}$
$2t_{2u}$
$1t_{1g}$
$1t_{1u}$
$1e_g$
$1a_{1g}$
t_{2g}
t_{1u}
t_{2u}
t_{2g}
e_g
t_{1u}
a_{1g}
P(π)
P(σ)
Octahedral field

Figure 3-8 Photographic Images and Optical Properties of the MM, MME1, and c-MME1.

*Comparative images of 140g MME1 before **(A)** and after (**B**) a 180-day period. Photographs of MM (**C**), MME1 (**D**), and c-MME1 (**E**) captured within a quartz cuvette (1 cm optical path length). (**F**) UV-vis transmittance spectra of the MM, MME1, and c-MME1. (**G**) Qualitative molecular orbital diagram for an octahedral complex.*

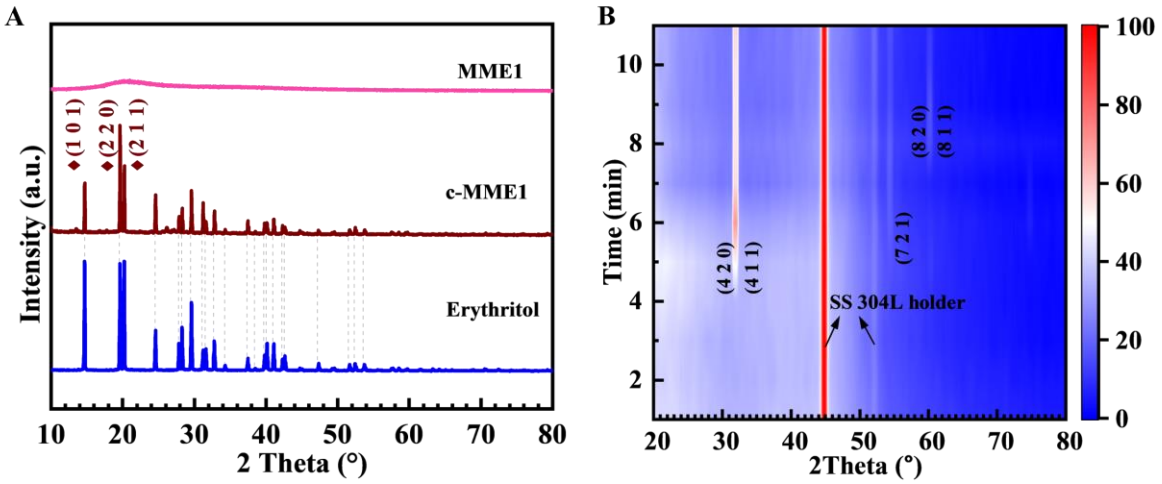


Figure 3-9 X-ray Diffraction (XRD) Pattern and In-situ Test Results.

*(**A**) XRD Patterns of MME1, c-MME1, and Erythritol. (**B**) In situ XRD patterns during crystallization for MME1 induced by seed crystal at 25 °C.*

Once triggered mechanically, MME1 transits from transparent to opaque as shown for 'c-MME1' in **Figure 3-8 E-F**, which is ascribed to the scattering effect of erythritol crystals in the system (**Figure 3-9 A**). Time- dependent in-situ XRD results (**Figure 3-9 B**) confirms only the crystallization of tetragonal-phase erythritol took place in the transition from amorphous to crystalline [234,235]. The reverse transition from crystalline to liquid recorded by DSC determines T_m= 83.2 °C and T_g= -36

°C for MME1 (**Figure 3-10 A-B**). Strikingly, no crystallization took place in its cooling although this should occur around 12.3 °C for pure erythritol (**Figure 3-10 C**). This demonstrates clearly MME1 belongs to the supercooled liquid at room temperature [112], by impressively shifting T_g from 10 °C for MM to -36 °C for MME1 due to the static molecule displacement or distortion in orientation [236]. The supercooled liquid phase of MME1 persists during the second DSC cycle without showing any crystallization peaks (**Figure 3-10 A**), even at a very slow scan rate of 0.5 $K \cdot min^{-1}$ (**Figure 3-10 D**). Simultaneously, the viscosity of MME1 supercooled liquid plunges to 10^2 Pa·s from 10^8 Pa·s of MM glass (**Figure 3-11**), which boosts the trigger ability of the MME materials. Upon mechanical triggering, MME1 exhibits an exothermic enthalpy of 83 kJ/kg shown as the red in **Figure 3-10 A**. Thus far, MME affords a stable supercooled liquid system simultaneously with a controllable trigger capability, which meets both stability and trigger-ability requirements for practical applications.

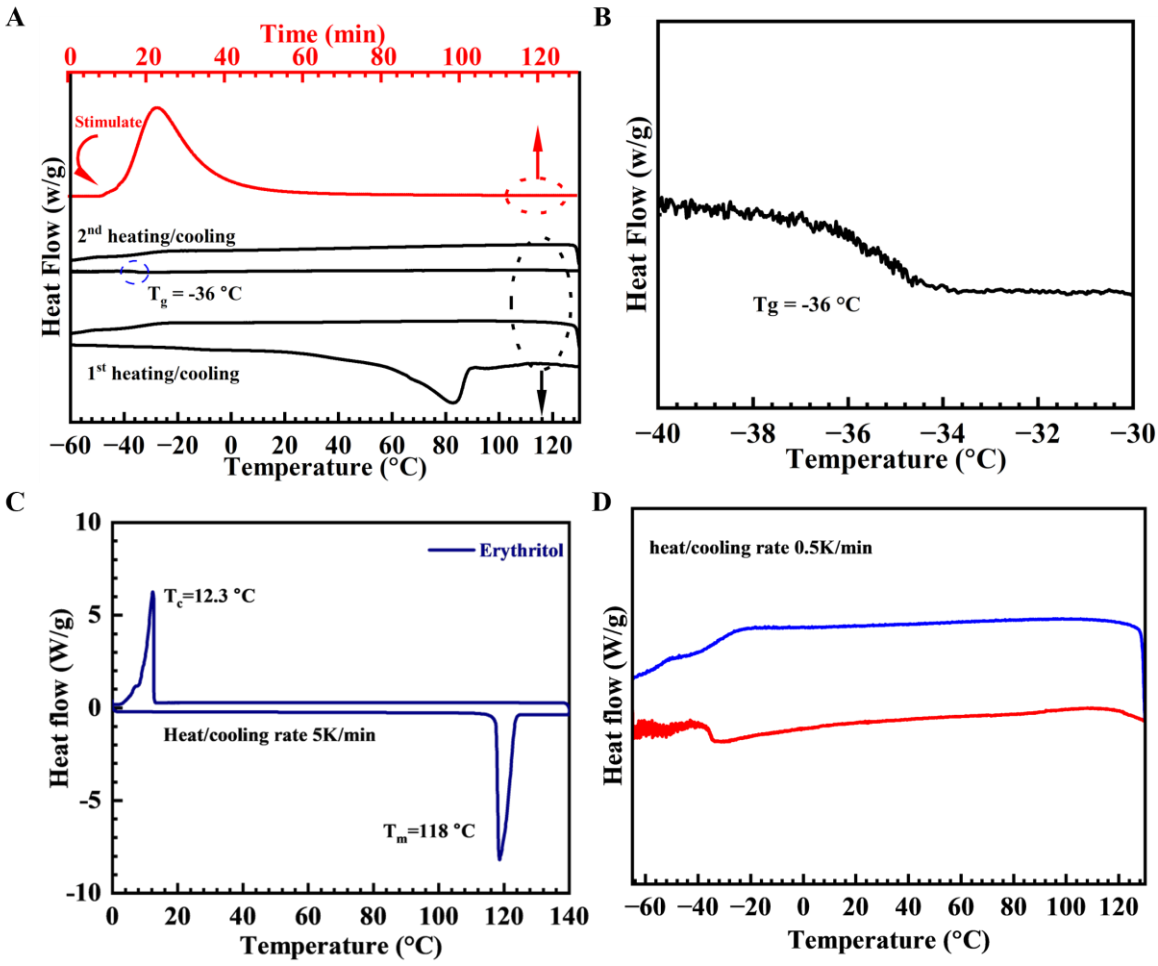


Figure 3-10 The thermal properties of MME1.

*(**A**) DSC traces for c-MME1 with a heating and cooling rate of 5 K/min in black line and stirring-induced crystallization curve at room temperature in red line. (**B**) DSC magnification plot of MME1 near the glass transition temperature. (**C**) DSC trace of erythritol recorded at a heating/cooling rate of 5 K/min. (**D**) DSC trace of MME1 recorded at a heating/cooling rate of 0.5 K/min.*

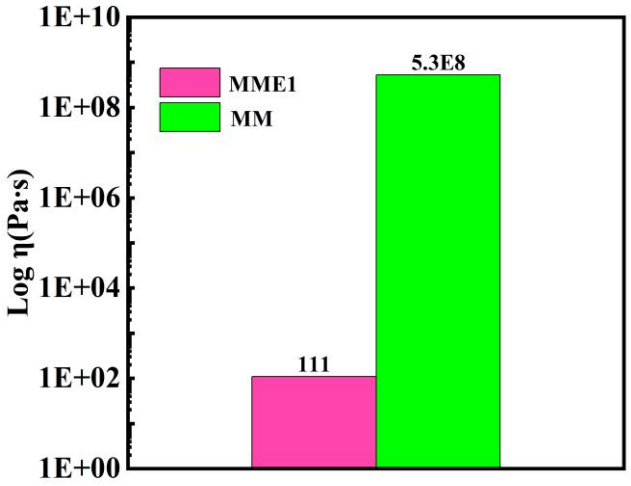


Figure 3-11 Comparison of Viscosity at Room Temperature between MME1and MM.

Furthermore, FTIR and NMR were utilized to probe the chemical interactions in MME1 and c-MME1 (**Figure 3-12 A-C, Table 3-2, Table 3-3, Table 3-4**). The O-H stretching signature (3230 cm^{-1}) of erythritol disappears and is replaced by N-H/N-$(H)_2$ stretches (3200 and 3400 cm^{-1}) of methylurea from crystalline c-MME1 to supercooled-liquid MME1. Simultaneously, the C-O vibration (1075 and 1038 cm^{-1}) of erythritol has a red shift in this transition. These shifts confirm that the close-packing erythritol molecules may be dissociated and then coordinated by Mn^{2+} ions of MM core, which also cause the C-H stretching band shift (around 2900 and 430 cm^{-1}) of erythritol. [237] On the other hand, compared with pure methylurea, the N-$(H)_2$ band of MME1 has a blue shift, indicating probable hydrogen-bond formation at the N-$(H)_2$ end with the O-H group of erythritol. The hydrogen bonding between methylurea of MM core, erythritol and Cl^- ion is further verified by the ^1H NMR peak shift and broadening of active hydrogen atoms from both methylurea and erythritol (**Figure 3-12 D**) [238,239]. Among them, that critical coordination structure evolution of MME1 from crystalline to supercooled liquid was further identified by XAFS. In the XANES spectra (**Figure**

3-13), the absorption edge of c-MME1 nearly overlaps that of $MnCl_2$, revealing that the oxidation state of Mn is approximately +2, consistent to that of MM core (**Figure 3-6 D**).

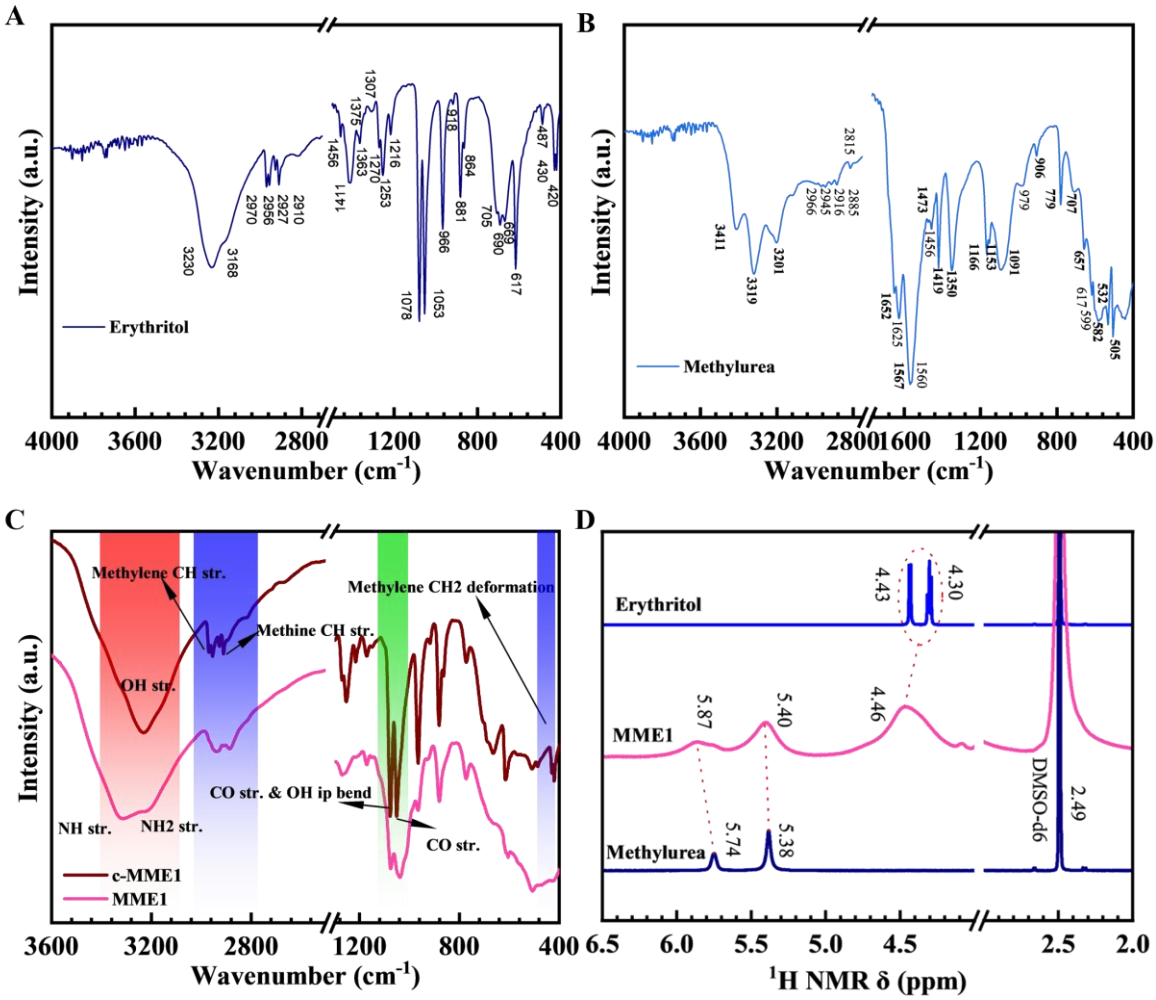


Figure 3-12 The Chemical Structure of MME1.

*FTIR spectra of (**A**) erythritol and (**B**) methylurea. (**C**) MME1 (pink line) and c-MME1(wine line) at the ambient temperature. (**D**) Experimental ^1H NMR spectra of erythritol, MME1, and methylurea (d6-DMSO, 500 MHz).*

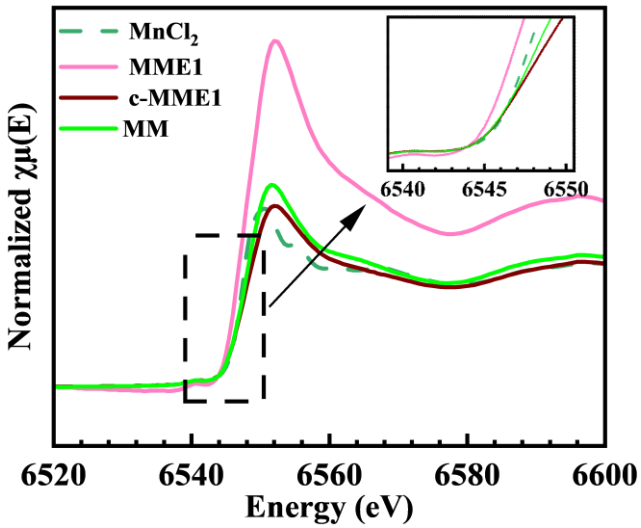


Figure 3-13 Experimental K-edge XANES Spectra of MME1 and c-MME1 and Reference Samples (MnCl2, MM).

Table 3-2 FTIR Peaks and Corresponding Vibrations for Erythritol

IR (cm^{-1})	Spectral Interpretation, approximate motion
3230 (b)	OH str.
3168(b)	OH str.
2970 (vs)	Asym. methylene CH str.
2956 (s)	Asym. methylene CH str.
2927 (s)	Methine CH str.
2910 (vs)	Methine CH str.
1456 (s)	Methylene CH2 deformation (scissor and wag)
1411 (vs)	Methine CH ip bend; CH op bend
1375 (w,sh)	Methine CH ip bend coupled with OH ip bend
1363 (m)	OH ip bend coupled with methylene CH2 wag

1307 (w)	Methylene CH2 wag and twist coupled with OH ip bend; CH op bend
1270 (s)	OH ip bend coupled with CH ip bend
1253 (s)	Methylene CH2 twist coupled with OH ip bend; methine CH op bend
1216 (m)	Methine CH ip and op bend; some CC str.
1078 (vs)	CO str., OH ip bend
1053 (vs)	CO str.
966 (vs)	CO str., OH ip bend, CC str.
918 (vw)	CC str., CO str. Coupled with some methylene CH2 rock
881 (vs)	CC str., CO str. Coupled with some methylene CH2 rock
705 (sh)	CC str. Coupled with CC skeletal bend
617 (vs)	CO op bend; some CC str. CO op bend
487 (m)	CO op bend, CC skeletal bend and some OH op bend
430 (m)	Methylene CH2 deformation (mainly op) coupled with OH op bend, CC skeletal

Table 3-3 FTIR Peaks and Corresponding Vibrations for Methylurea.

IR (cm^{-1})	**Spectral Interpretation, approximate motion**
3411 (s)	NH2 asym. Str.
3319 (s)	NH str.
3201 (s)	NH2 sym. Str.
1652 (vs)	C=O str.
1567 (vs)	Amide II and NH2 bending

1473 (vw)	CH2 asym. Def.
1419 (vs)	CH3 sym. Def.
1350 (vs)	Amide III
1166 (vs)	CH3 rock
1153 (sh)	NH2 rock
1091 vs)	CH3-N str. and CH3 rock
906 (s)	CN str.
779 (vs)	C=O def.
707 (s)	NH2 tor.
657 (s)	C=O def.
582 (s)	NH def.
532 (s)	NH2 wag
505 (s)	NCN def.

Table 3-4 Changes in FTIR Peaks and Vibrations for MME1 and c-MME1.

IR (cm^{-1})		**Types of changes**	**Spectral Interpretation, approximate motion**
c-MME1	MME1		
	3317	New peak	NH str.
3230		disappear	OH str.
	3209	New peak and blue shift	NH2 sym. Str.
2968			

2954	2935	bimodal becomes unimodal	Asym. Methylene CH str.
2927 2910	2885	bimodal becomes unimodal	Methine CH str.
1270	1270	Become weaker and broader	OH ip band coupled with CH ip bend
1253	1253	Become weaker and broader	Methylene CH2 wag and twist coupled with
1077	1075	Become weaker and broader	CO str., OH ip bend
1052	1038	Red shift	CO str.
965	965	Become weaker	CO str. OH ip bend, CC str.
917	928	Become broader	CC str. CO str. Coupled with some methylene
863	-	disappear	CC str. CO str. Coupled with some methylene
665		Almost disappear	CC str. Coupled with CC skeletal bend
614	604	Become weaker	CO op bend some CC str. CO op bend
485	-	disappear	CO op bend, CC skeletal bend and some OH
430	-	disappear	Methylene CH2 deformation (mainly op)
420	-	disappear	coupled with OH op bend, CC skeletal bend

EXAFS was employed to reveal that coordination structure of the MME1 and c-MME1 (**Figure 3-14**). **Figure 3-14 A-B** shows the Fourier-transformed spectra of MME1 with both real (red) and imaginary parts (blue) calibrated by the phase-shift treatment [240]. These data are used to determine the coordination number to be at 5.6(4) and the corresponding distance at 2.25(1) Å after data fitting (**Table 3-5**), which are larger than 2.21(2) Å of Mn-O distance but shorter than 2.46(4) Å of Mn-Cl

distance in MM (**Figure 3-6 A-B**). These indicate that 2 erythritol molecules substitute the bonded Cl^- ions to coordinate MM core, abiding by the splitting energy sequence [227]. In contrast, for c-MME1(**Figure 3-14 C-D**), its coordination number and the corresponding distance are determined at 3.8(7) and 2.18(2) Å for Mn-O along with 1.2(9) and 2.45(5) Å for Mn-Cl after fitting (**Table 3-6**), respectively, approaching the values of MM core. These suggests that the Mn-erythritol dative bonds are dissociated and hereafter replaced by Mn-Cl, returning to the glass-state MM core structure in the crystallization process from MME1 to c-MME1. To better visualize the atomic distribution of oxygen, wavelet transform XAFS (WT-XAFS) images of MM, MME1 and c-MME1 were utilized to analyse the correlation between the peak and k-space data (**Figure 3-14 E-F** and **Figure 3-6 C**). MM and c-MME1 have similar local environments with the peak-intensity lobes at around k = 5.6 $Å^{-1}$ and r = 2.21 Å for Mn-O dative bond, and with the peak-intensity lobes at around k = 4.7 $Å^{-1}$ and r = 2.45 Å for Mn-Cl dative bond. In contrast, the supercooled liquid MME1 clearly exhibits a narrower-distribution environment with the higher peak-intensity lobe at k = 7.4 $Å^{-1}$ and r = 2.25 Å. Combining the FTIR and NMR information with XAFS information, one can conclude that the supercooled liquid MME1 has a core-shell structure composed of an octahedral core with mixed ligands of 4 intrinsic methylurea and 2 extrinsic erythritol, as well as a shell of 2 coordination-free erythritol connected to the core through hydrogen bonding. The elongated Mn-erythritol dative bonds with a subtle strength can be broken by the crystallization driving force of erythritol, through breaking the peripheral intermolecular hydrogen bonds with an exotic trigger. During the breaking process, Cl^- ions refill the open sites of MM core while the 4 erythritol molecules assembly into

nanocrystals in the amorphous MM matrix in the crystallization process. A schematical illustration is shown in **Figure 3-15**. As a result, the stability of our supercooled liquid MME1 comes from the barrier mainly composed of the Mn-erythritol dative bonds. On the other hand, the trigger-ability is enabled by the energy release of erythritol crystallization after exotically breaking the weaker intermolecular hydrogen bonds in the supercooled liquid system.

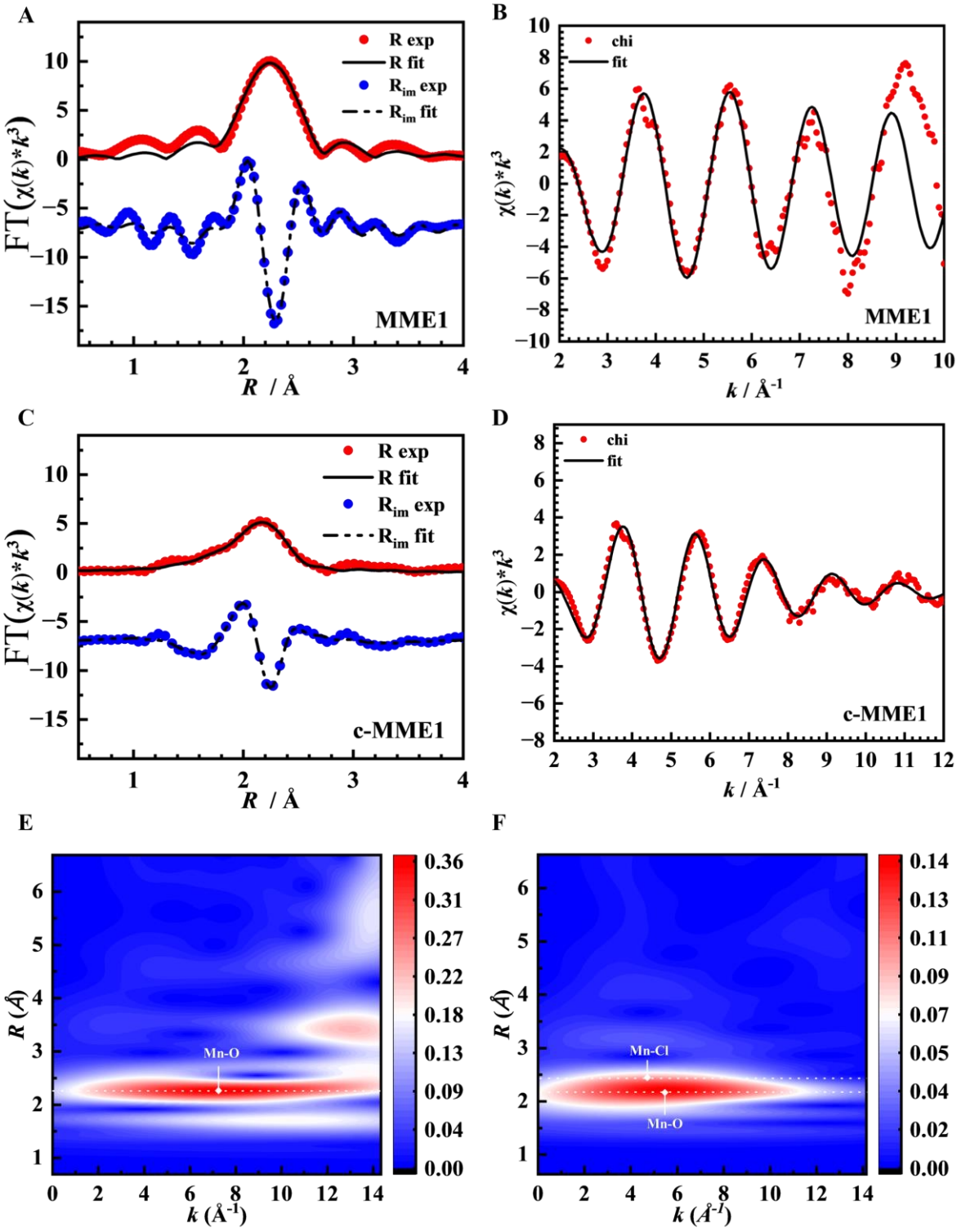


Figure 3-14 Local Chemical and Geometric Environments of Mn Atoms in MME1 and c-MME1.

*Fourier transforms of Mn K-edge EXAFS data (points) and model-based fits (line) for MME1 in (**A**) R-space and in (**B**) k^3 weighted k-space. Fourier transforms of Mn K-edge EXAFS data (points) and model-based fits (line) for c-MME1 in (**C**) R-space and in (**D**) k^3 weighted k-space. The data are with phase correction. Normalized WT-XAFS for the correlation between R-space and K-space data for MME1 (**E**), c-MME1 (**F**).*

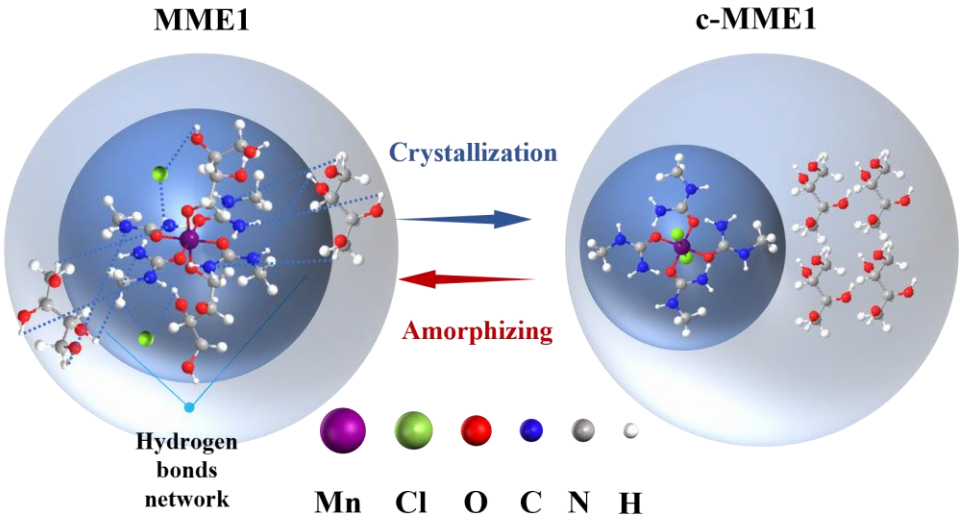


Figure 3-15 Schematic Illustration of Phase Transition between MME1 and c-MME1.

Table 3-5 Curve fit Parameters[a] of Mn K-edge EXAFS for MME1

Path	d [b]/Å	N	R/Å	σ^2/Å^2
Mn-O	2.247	5.6(4)	2.25(1)	0.002(2)

[a] S_0^2 was fixed as 0.93. ΔE_0 was refined as a global fit parameter, returning a value of (5.6±0.8) eV. Data range: $2.0 \leq k \leq 9$ Å^{-1}, $1.0 \leq R \leq 2.3$ Å. The number of variable parameters is 4, out of a total of 5.5 independent data points. R factor for this fit is 0.8 %. [b] The distance for Mn-O is from the crystal structure MnO.

Table 3-6 Curve fit Parameters [a] of Mn K-edge EXAFS for c-MME1.

Path	d [b]/Å	N	R/Å	σ^2/Å^2
Mn-O	2.247	3.8(7)	2.18(2)	0.007(2)
Mn-Cl	2.553	1.2(9)	2.45(5)	0.02 [c]

[a] S_0^2 was fixed as 0.93. ΔE_0 was refined as a global fit parameter, returning a value of (-0.6±1.9) eV. Data range: $2.4 \leq k \leq 12$ Å^{-1}, $1.0 \leq R \leq 2.5$ Å. The number of variable parameters is 5, out of a total of 7.4 independent data points. R factor for this fit is 0.5 %. [b] The distance for Mn-O is from the crystal structure MnO. The distance for Mn-Cl is from the crystal structure $MnCl_2$. [c] The Debye-Waller factors were constrained as 0.02 for decreasing the correlation.

The microstructures of the supercooled liquid, MME1, and its crystallized form, c-MME1, were studied by cryo-TEM and energy dispersive X-ray spectroscopy (EDX). Under the irradiation of an electron beam, the transmission electron microscopy image of the supercooled liquid, MME1, exhibits a bubble- or maze-like pattern without any discernible structure (**Figure 3-16 A-C**), consistent with the typical amorphous characteristics reported in the literature [142]. In contrast, c-MME1 is composed of erythritol nanocrystal clusters dotted in an amorphous layer (**Figure 3-16 D-E**). cryo-TEM study evidences the typical crystal planes of erythritol nanocrystals at different sites of the cluster (**Figure 3-16 E-I**), such as (501), (422), (600) and (402), in accordance with the XRD pattern of erythritol (**Figure 3-9**). According to the EDX images of c-MME1 (**Figure 3-16 J-M**), it is found that

Mn, N of methylurea, and Cl are dispersed across the whole layer covering both the clusters and residual regions, where the intensity contrast may be attributed to the height difference raised by erythritol nanocrystals. This indicates that a small portion of Mn-erythritol dative bonds in MM cores remains unchanged. But most Mn-erythritol dative bonds have been dissociated according to the EXAFS analyses (**Figure 3-6 A-C, Figure 3-14**). In comparison, all the three typical elements are dispersed uniformly in the supercooled liquid bubble of the MME1 (**Figure 3-16 N-Q**).

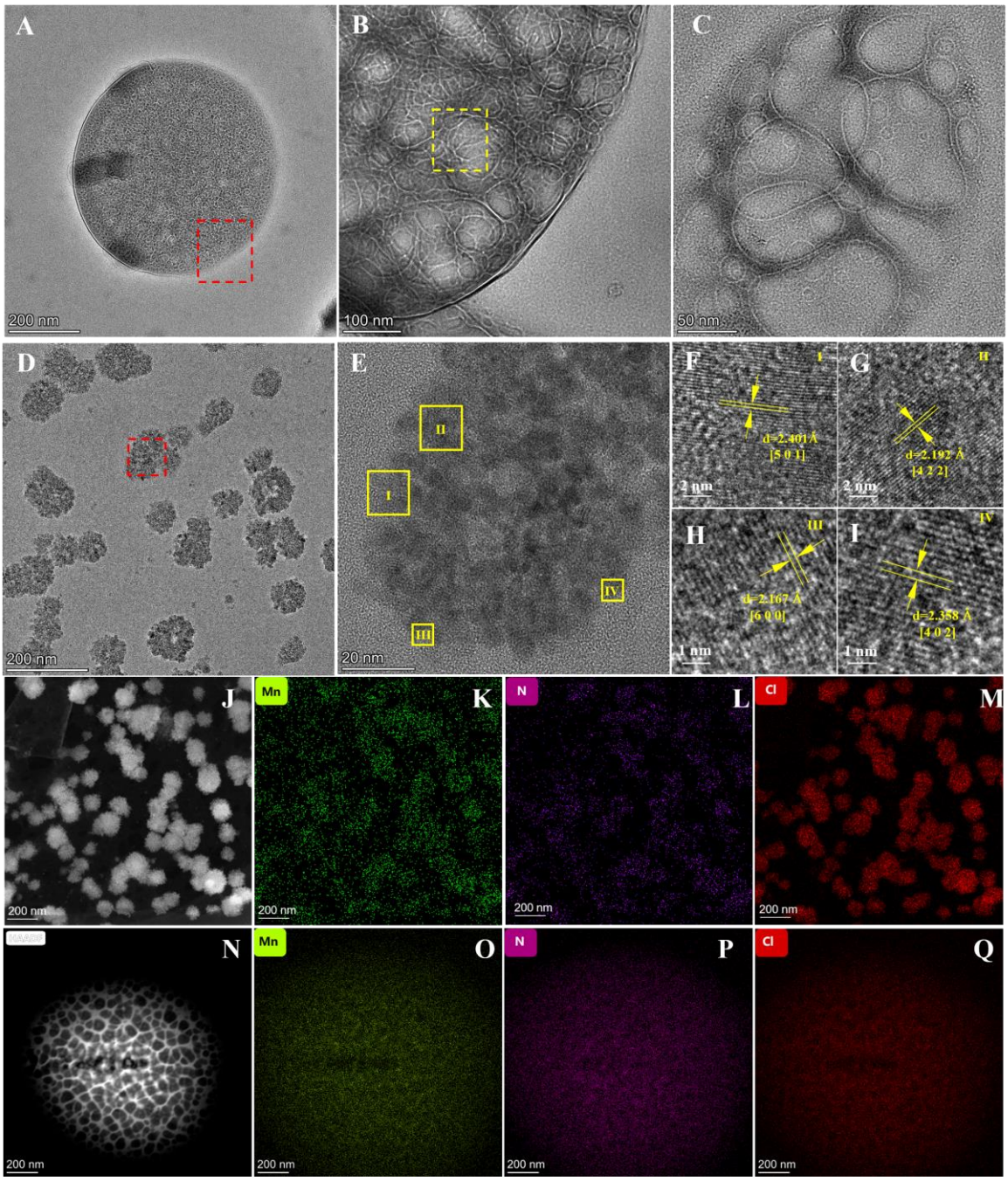


Figure 3-16 Cryogenic Transmission electron microscopy (cryo-TEM) images of MME1 and c-MME1.

*Cryo-TEM image of MME1, showing the overall structure (**A**) and a magnified view of the selected area marked in red (**B**). The highlighted yellow area corresponds to the region depicted in (**C**). TEM*

*image of c-MME1 (**D**), highlighting the selected area marked in red, which corresponds to the region depicted in (**E**). Selected-area electron diffraction (SAED) pattern for the I (**F**), II (**G**), III (**H**), and IV (**I**). (**J**) HAADF-STEM image and EDX maps of (**K**) Mn, (**L**) Cl, and (**M**) N for c-MME1. (**N**) HAADF-STEM image and EDX maps of (**O**) Mn, (**P**) Cl, and (**Q**) N for MME1.*

3.3.3 Thermodynamics and Kinetics of Phase-Transitions

With increasing load of erythritol as a heat storage element, samples MME1-MME4 show similar appearance (**Figure 3-17**) and chemical structures (**Figure 3-18**) as MME1. As shown in **Figure 3-19**, in the crystalline state, the occupancy rate of the crystals increases with the increment of erythritol loading from c-MME1 to c-MME4.



Figure 3-17 Visual appearance of MME1 to MME4.

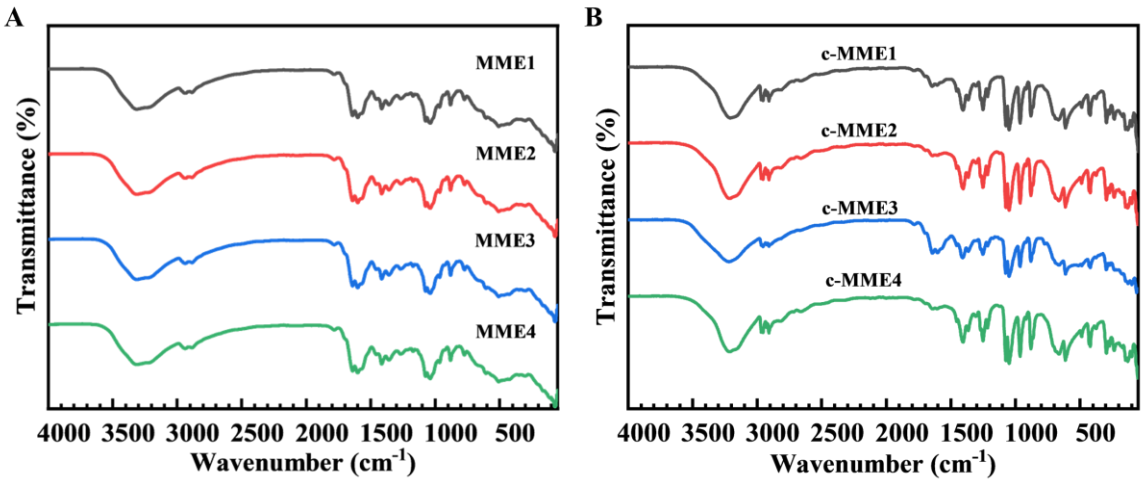


Figure 3-18 Fourier-Transform Infrared (FTIR) Spectra of MME Series Samples

*(**A**) FTIR spectra of MME1 to MME4 and (**B**) FTIR spectra of c-MME1 to c-MME4.*

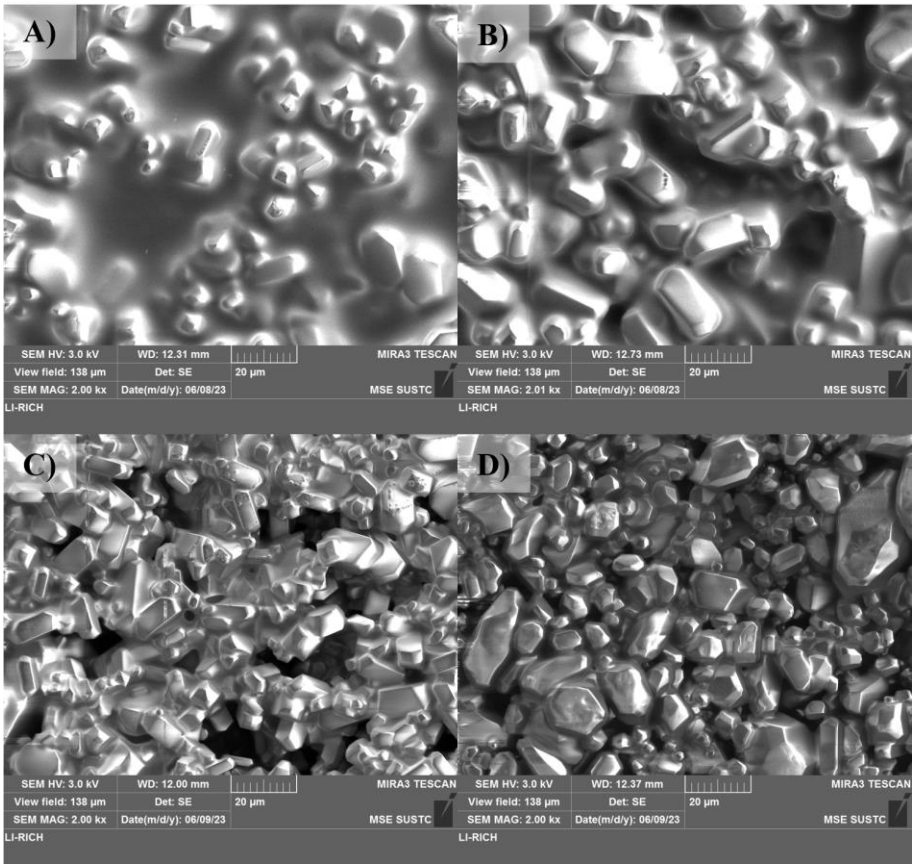


Figure 3-19 Scanning Electron Microscopy (SEM) Images MME Series Samples.

*SEM images of c-MME1 (**A**), c-MME2(**B**), c-MME3(**C**), and c-MME4(**D**).*

From the first DSC cycle, the enthalpies (ΔH) of MME1-MME4 are determined as 81.5, 163.1, 208.5 and 215.7 kJ/kg (**Figure 3-20 A**), which agree well with the value of subtracting the phase-change enthalpy of the erythritol load by the bond energy difference (E_{Mn-O} - E_{Mn-Cl}) for respective samples (**Table 3-7**). Correspondingly, the molar enthalpy increment is equal to the phase change enthalpy of 4 mol erythritol molecules. As expected, the absence of exothermic peaks during cooling confirms the retention of stored thermal energy inside the supercooled liquids. It is worthy to note here that the samples exhibit broadened endothermic peaks resemble the traits observed in semi-crystalline polymers, which can be attributed to a range of hydrogen bond environment formed, resulting in the varying thermal effect. In the second DSC cycle (**Figure 3-20 B**), MME1 and MME2 remain in a supercooled liquid state without crystallization peaks, even at a very slow cooling rate of 0.5 K/min. In comparison, with higher erythritol loads, MME3 and MME4 exhibit cold-crystallization peaks due to the erythritol clusters already formed in the previous cooling cycle, which promotes the cold-crystallization process. A higher cluster concentration would move the onset point of cold-crystallization forward to lower temperature. Furthermore, the glass transition points were found to decrease with an increasing erythritol load, resulting in successively degraded GFAs. This leads to a declined stability and a shorter heat storage duration. In contrast, the trigger ability is enhanced.

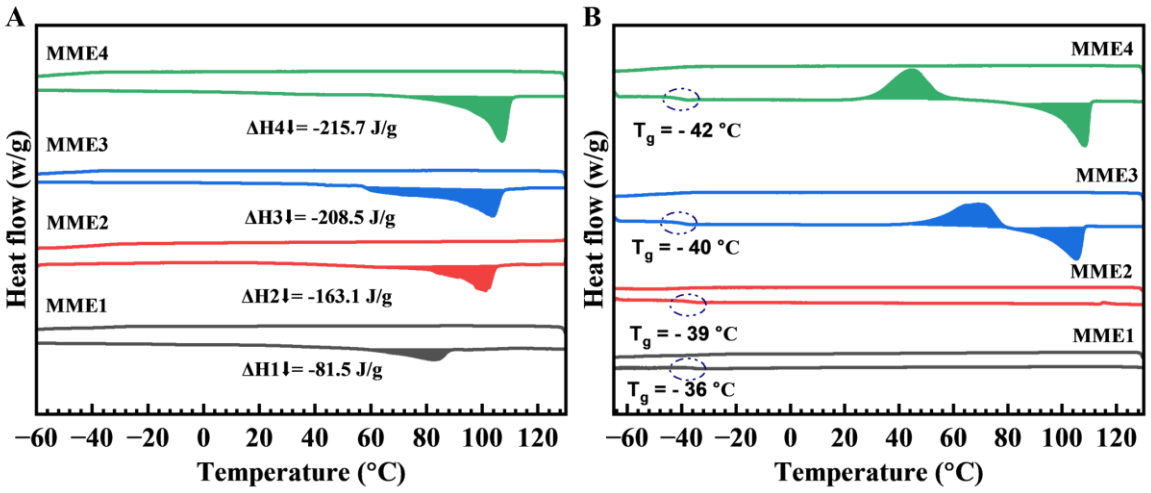


Figure 3-20 Thermal Properties of MME Series Samples.

(A) *The first DSC cycle for MME series materials with a heating and cooling rate of 5 K/min. (**B**) The second DSC cycle for MME series materials with a heating and cooling rate of 5 K/min.*

Table 3-7 Comparative enthalpy of phase transition for c-MME materials.

	c-MME1	**c-MME2**	**c-MME3**	**c-MME4**
Chemical formula	$C_{24}H_{64}N_8O_{20}MnCl_2$	$C_{40}H_{104}N_8O_{36}MnCl_2$	$C_{56}H_{144}N_8O_{52}MnCl_2$	$C_{72}H_{184}N_8O_{68}MnCl_2$
Molar mass	910.6 g/mol	1399.08 g/mol	1887.56 g/mol	2376.04 g/mol
$E_{Mn\text{-}O}$-$E_{Mn\text{-}Cl}$	40 KJ/mol [a]			
Theoretic molar enthalpy [b]	81.2 KJ/mol	242.4 KJ/mol	403.6 KJ/mol	564.8 KJ/mol
Theoretic mass enthalpy	89.1 KJ/kg	173.3 KJ/kg	213.8 KJ/kg	237.7 KJ/kg
Experimental mass enthalpy	81.5 KJ/kg	163.1 KJ/kg	208.5 KJ/kg	211.2 KJ/kg

[a] $E_{Mn\text{-}O}$-$E_{Mn\text{-}Cl}$ was obtained from the previous study [241], and we have selected an appropriate value, 40 KJ/mol. [b] Theoretical molar enthalpy of c-MME was calculated using the following equation:

$$\chi E_{M,erythritol} - 2(E_{Mn-O} - E_{Mn-Cl}) \qquad (3-2)$$

Here, χ represents the molar number of erythritol, which is 4,8,12, and 16 for c-MME1 to c-MME4, respectively. $E_{M,erythritol}$ represents the molar enthalpy of erytritol, which is 40.3KJ/mol.

The temperature dependent viscosity of the glass-forming liquids was characterized with a polished titanium rotor (**Figure 3-21 A**) and shown in **Figure 3-21 B**. Overall, the viscosities of MME series are comparable to or even higher than those of many network-forming liquids and glass-forming ionic liquids (**Table 3-8**). With an increased erythritol load, the viscosity decreases. Among them, MME1 owns the highest viscosity, reaching 111.8 Pa·s at room temperature. This determines the stability sequence of MME series because a higher viscosity gives to slower relaxation dynamics [242].

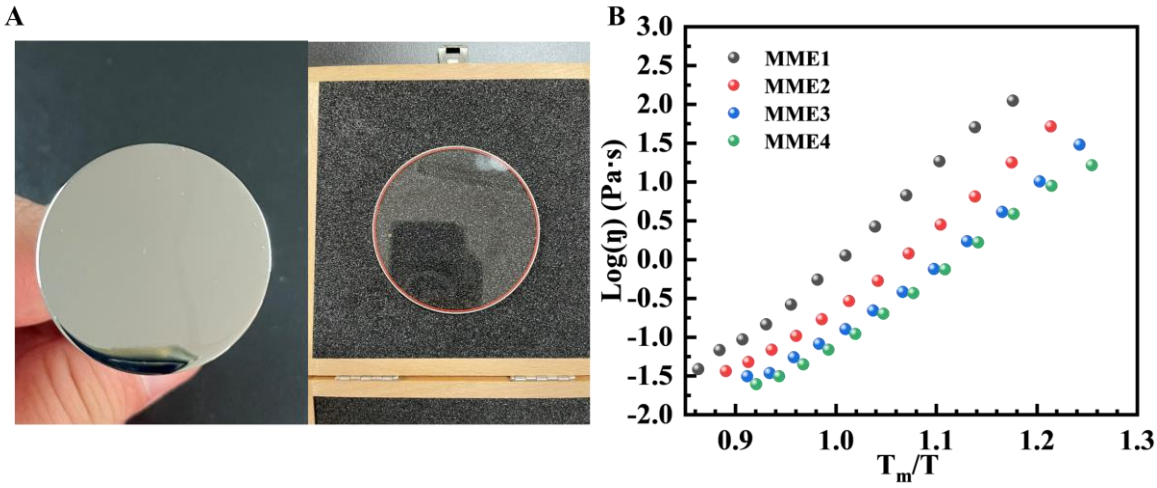


Figure 3-21 Temperature-Dependent Viscosity Measurements of MME Series

*(**A**) The polished titanium rotator (Φ20mm) and a glass substrate. (**B**) Temperature-dependent viscosity measurements of MME series materials. The measurement temperatures are normalized to each respective melting temperature.*

Table 3-8 Comparison of the Viscosities of Different Supercooled Liquids

Compound	Viscosity(mPa·S)	T (K)	T_m (K)	Ref
MME1	1122	353	356	this study
MME2	527	373	371	this study
MME3	381	373	376	this study
MME4	199	383	380	this study
Co(hmba)3[Co(NCS)4]	178	423	417	[204]
Co(hmba)3[CoBr4]	1313	393	379	[204]
Mn(bba)3[MnCl4]	214	453	445	[204]
[bmmim][BF4]	84	283	271	[174,243]
[bmim][PF6]	231	288	284	[174,243]
[bmim][BF4]	164	313	310	[174,243]

On the other hand, the temperature dependence of viscosity follows the Vogel−Fulcher−Tammann (VFT) equation (**Figure 3-22**) [123]. When extrapolated to a viscosity of 10^{12} Pa·s, the VFT model predicts T_g = -37, -41, -43, and -44 °C, respectively for MME1, MME2, MME3, and MME4, almost consisted with the above DSC results (**Figure 3-20 A**).

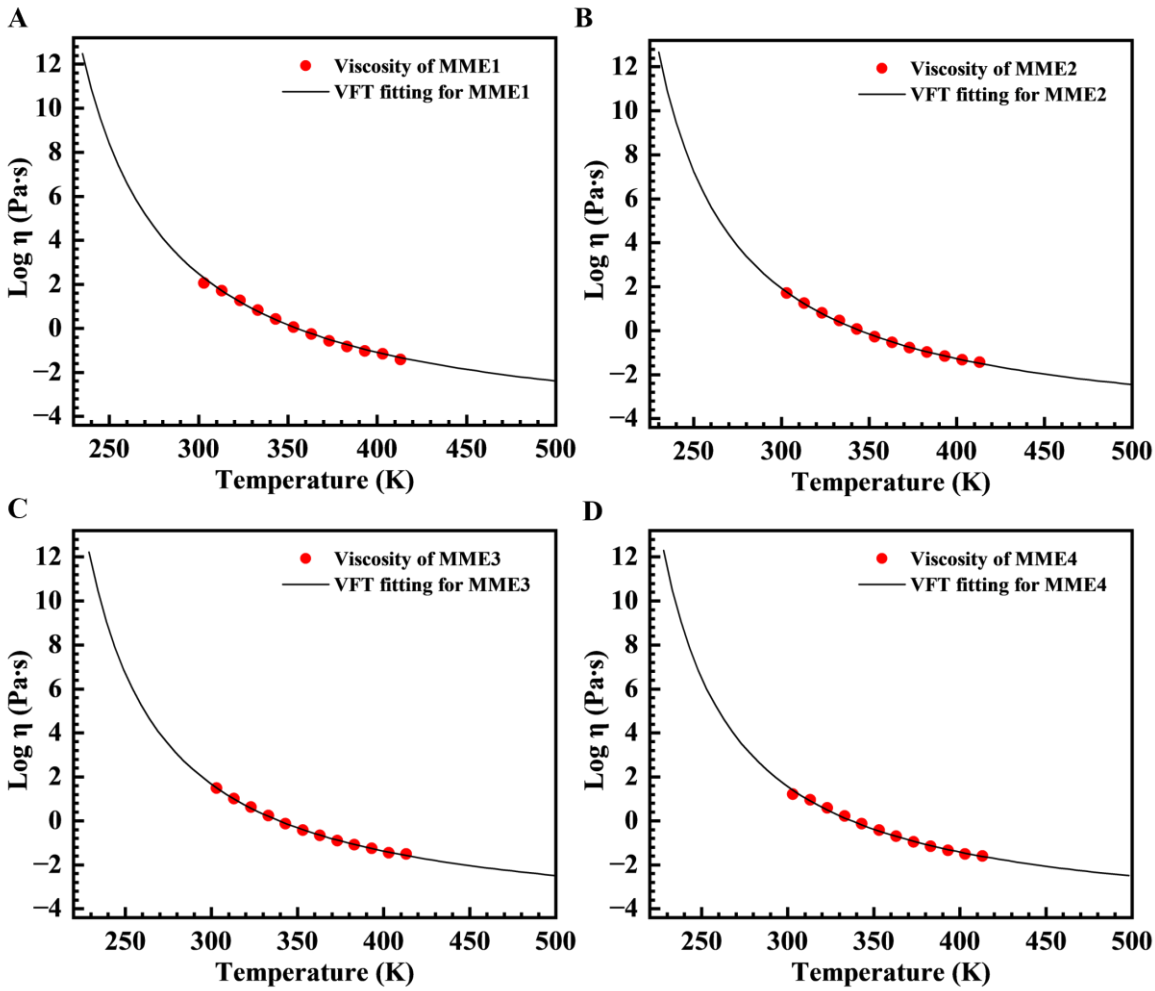


Figure 3-22 Temperature-Dependent Viscosity Measurement and Curve Fitting Using the Vogel-Fulcher-Tammann (VFT) Model.

*Temperature-dependent viscosity of MME1 (**A**), MME2 (**B**), MME3 (**C**), and MME4 (**D**) with Vogel-Fulcher-Tammann (VFT) fitting ($r^2 > 0.99$).*

To further evaluate their crystallization susceptibility quantitatively, all MME supercooled liquids were sandwiched between a titanium rotor and a base plate, both with a given surface roughness (**Figure 3-23 A**), and their viscosities were recorded. This allows the nucleation process to be

investigated under a fixed shear rate (0.1 s^{-1}) at 30 °C (**Figure 3-23 B-F**). In contrast to the trigger difficulty of the samples on polished plates, the rough surface provides abundant heterogeneous nucleation sites, leading to significantly lower energy barrier for nucleation [110]. Based on the rough surface results, the trigger time can be studied. The shear time thresholds were measured to be 425 s, 72 s, 41 s, and 37 s for MME1 to MME4 (**Figure 3-23 B**), respectively. All the samples exhibit a good controllability of phase transition at the ambient temperature with an enough margin in contrast to the prompt crystallization of conventional pure erythritol PCM. In comparison, that trigger time is 2481 s for sorbitol while that of xylitol cannot be even obtained due to long time needed. Although supercooled liquids such as sorbitol and xylitol are very stable, they are difficult to be triggered, which hinders their commercial applications. The efficient triggering of MME series can be ascribed to the ingenious ligand exchange occurred in the core-shell coordination complex and demonstrates their great potential in the practical utilization. Following, their kinetics is discussed.

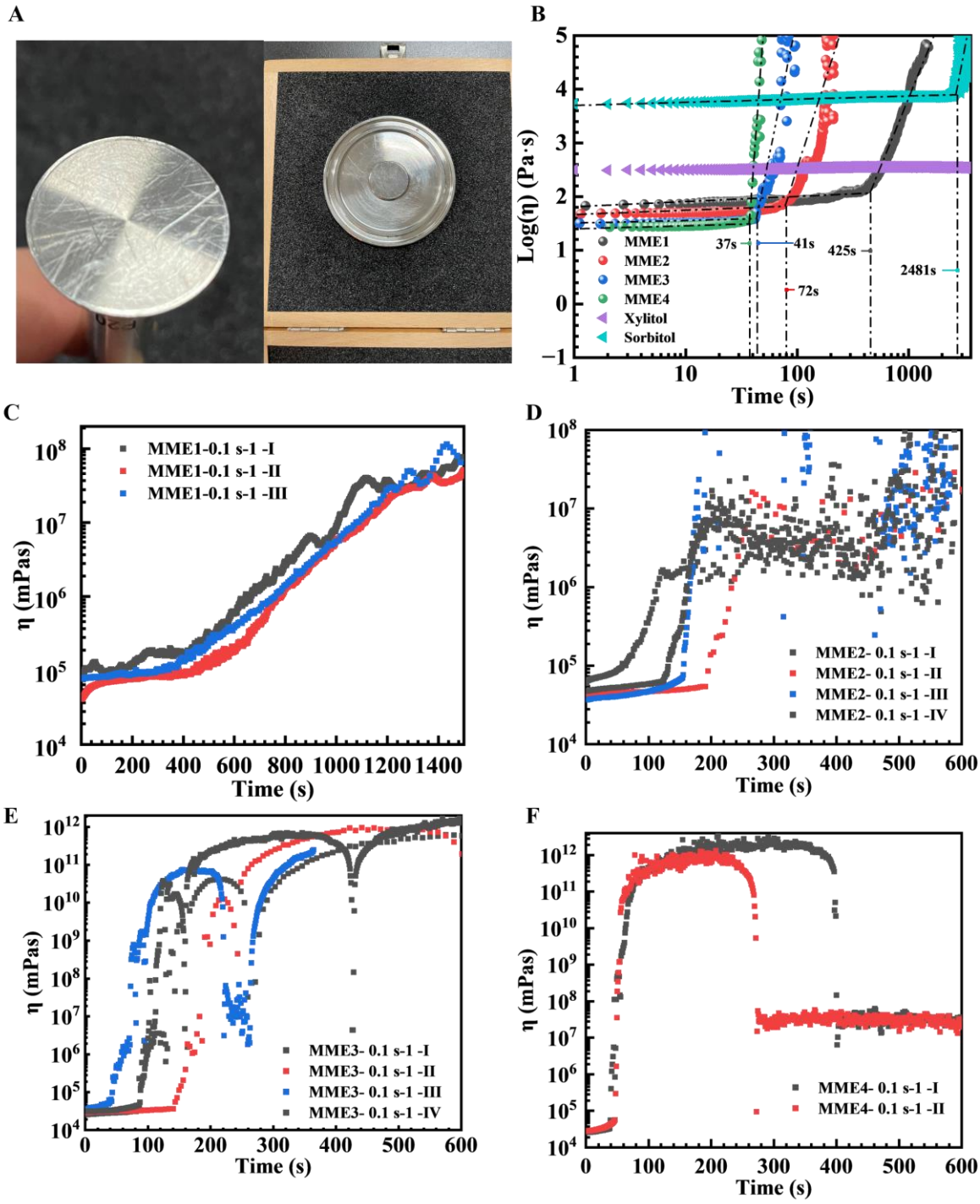


Figure 3-23 Measuring Crystallization Response Time to Shear Force at Rough Interfaces

Photographic images of (**A**) the titanium rotator (Φ20mm) with a rough surface and a titanium substrate. *(**B**) The threshold shear time for shear-induced crystallization in the MME series, xylitol,*

*and sorbitol samples under a fixed shear rate (0.1 s^{-1}) at 30 °C. Threshold shear time of (**C**) MME1, (**D**) MME2, (**E**) MME3, and (**F**) MME4 under a fixed shear rate (0.1 s-1) at 30 °C. The viscosity data presented in (**B**) were obtained by averaging multiple measurements for each sample.*

For crystallization, the quantitative investigation of crystal nuclei is rather difficult. However, nucleation involves the incorporation of solute molecules into a crystal surface; this identical process is also seen in crystal growth, which is more accessible to experimental study. Thus, the temperature-dependent growth rate at which molecules are incorporated into the crystal surface can be estimated by quantifying the growth kinetics of the dendrite tips. A rheometer with a transparent window for microscopic observation was therefore utilized to study the crystal growth (**Figure 3-24 A**). In the early and middle stages of crystal growth, the growth rate remains constant within the limits of experimental error. However, in the later stages of crystal growth there is a continuous decrease in the growth rate. Consequently, the quantification of the growth rate in the early and intermediate stages was carried out in this work. The results are shown in the extracted microscopic photos (**Figure 3-25 - Figure 3-28**), with the temperature dependent growth rates of each of the samples plotted in **Figure 3-24 B**, following a trace of rise and fall.

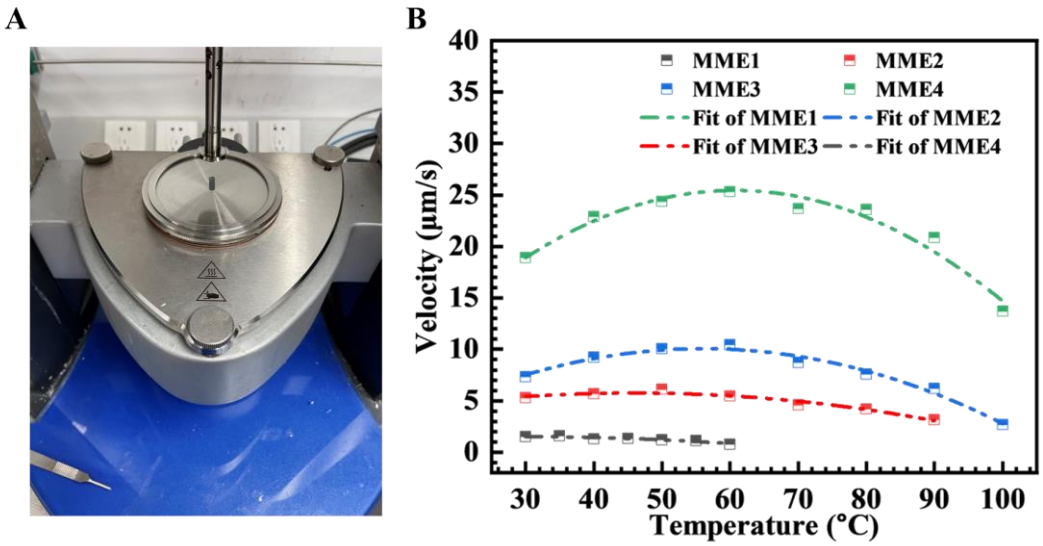


Figure 3-24 Measurement of Temperature-Dependent Growth Rate in MME Series Materials

*(**A**) Photograph of the device used for measuring the crystallization rate. (**B**) Temperature-dependent growth rate of the dendrite tip of MME series materials.*

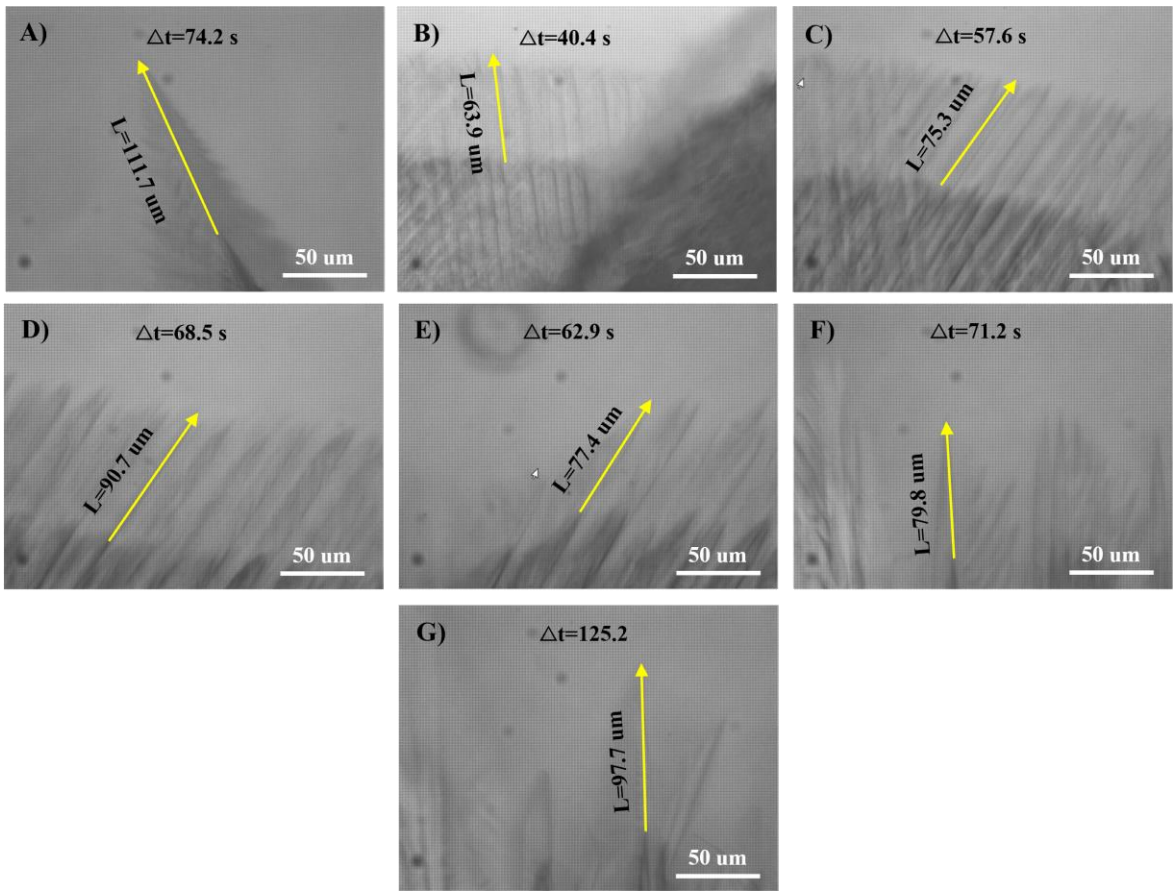


Figure 3-25 Supporting Figure II for Figure 3-24.

*Microscopy images depicting the crystallization process of MME1, initiated by seeding with an erythritol crystal, at different temperatures: (**A**) 30 °C, (**B**) 35 °C, (**C**) 40 °C, (**D**) 45 °C, (**E**) 50 °C, (**F**) 55 °C, and (**G**) 60 °C.*

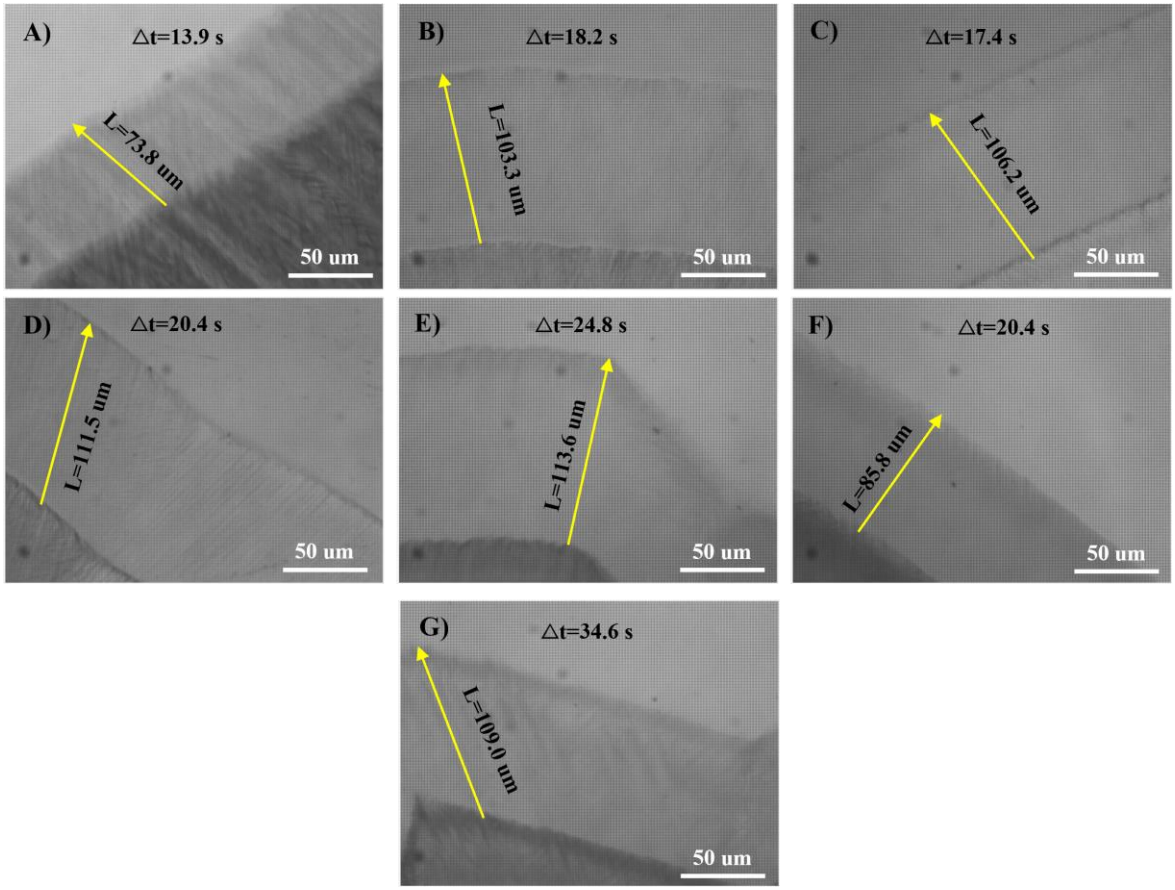


Figure 3-26 Supporting Figure III for Figure 3-24.

*Microscopy images depicting the crystallization process of MME2, initiated by seeding with an erythritol crystal, at different temperatures: (**A**) 30 °C, (**B**) 40 °C, (**C**) 50 °C, (**D**) 60 °C, (**E**) 70 °C, (**F**) 80 °C, and (**G**) 90 °C.*

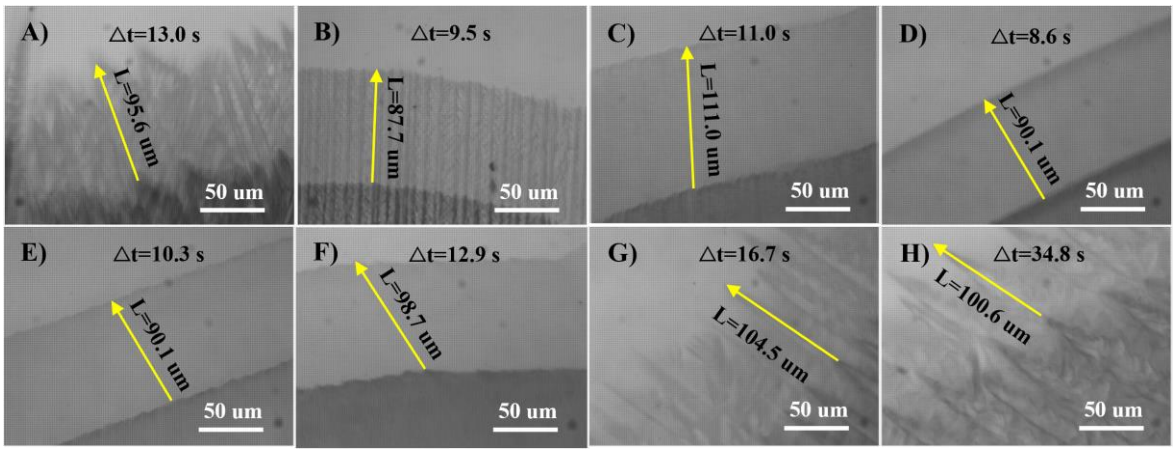


Figure 3-27 Supporting Figure IV for Figure 3-24.

*Microscopy images depicting the crystallization process of MME3, initiated by seeding with an erythritol crystal, at different temperatures: (**A**) 30, (**B**) 40, (**C**) 50, (**D**) 60, (**E**) 70, (**F**) 80, (**G**) 90, and (**H**) 100˚C.*

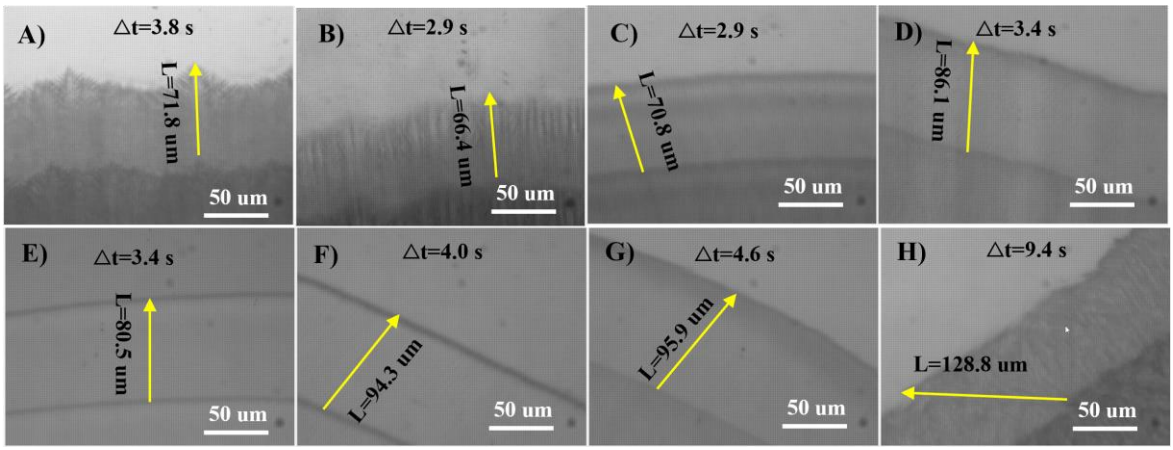


Figure 3-28 Supporting Figure V for Figure 3-24.

*Microscopy images depicting the crystallization process of MME4, initiated by seeding with an erythritol crystal, at different temperatures: (**A**) 30, (**B**) 40, (**C**) 50, (**D**) 60, (**E**) 70, (**F**) 80, (**G**) 90, and (**H**) 100˚C.*

The growth velocity (v) of crystals can be described by the following equation:

$$v = kf\lambda\left(1 - \exp\left(-\frac{\Delta\mu}{k_{\mathrm{B}}T}\right)\right) \quad (3-3)$$

where *k* is the jump frequency of molecules transitioning from the liquid to the crystal; *f* is the site factor representing the probability of incorporating impinging molecules into the crystal surface.

In accordance with the Stokes-Einstein equation, the jump frequency (*k*) can be further defined as:

$$k = \frac{6D}{\lambda^2} = \frac{2k_{\mathrm{B}}T}{\pi\eta\lambda^3} \quad (3-4)$$

where k_{B} represents the Boltzmann constant, *D* is the diffusion coefficient, *T* signifies the absolute temperature, η denotes the viscosity, and λ represents the jump distance, which is considered as the longest dimension of an erythritol molecule at 0.65 nm. For MME1 to MME4, the *D* values at the room temperature are deduced to be 3.6×10^{-10}, 7.9×10^{-10}, 14×10^{-10}, 25×10^{-10} cm^2/s, respectively.

Additionally, $\Delta\mu$ in **Equation (3-3)** refers to the difference in chemical potential of a molecule in the crystal and in the supercooled liquid, defined as:

$$\Delta\mu = \frac{\Delta h\Delta T}{T_{\mathrm{m}}N_{Av}} \quad (3-5)$$

where Δh corresponds to the molar latent heat, T_{m} signifies the melting temperature, ΔT represents the degree of supercooling, and N_{Av} is the Avogadro constant.

The ledge energy (γ) is a crucial parameter in crystal nucleation and is related to the side surface of the layer nucleus. To compute it, the site factor, *f*, in **Equation (3-3)** can be further expressed by as follows:

$$f = (\lambda^2 n_s^*)^{\frac{1}{3}} f_1^{\frac{2}{3}} i_s^{*\frac{1}{3}} \quad (3-6)$$

where f_1 represents the site factor for the ledge layer. It can typically be approximated as 1 according to previous study in literature [244], due to the generally higher site factor at ledges compared to surfaces, which is attributed to the rough nature of ledges. Additionally, i_s^* denotes the number of molecules in a critical layer nucleus. Since this number is usually small, it can also be reasonably approximated as 1. [244] n_s^* is the surface concentration of critical nuclei, defined as follows:

$$n_s^* = \frac{1}{\lambda^2} \exp\left(-\frac{W_s^*}{k_B T}\right) \quad (3-7)$$

where W_s^* is the maximum value of *W*, representing the work for critical nuclei to form, obtained from:

$$W = \pi r^2 \lambda \Delta\mu_v + 2\pi r \lambda \gamma \quad (3-8)$$

$$r_s^* = \frac{\gamma}{\Delta\mu_v} \quad (3-9)$$

$$W_s^* = \pi \frac{\gamma^2 \lambda}{\Delta\mu_v} \quad (3-10)$$

$$\Delta\mu_v = \frac{\Delta\mu}{\bar{V}} \quad (3-11)$$

where $\bar{V}$ is the molecular volume of erythritol, which is around 488.5Å^3.

Figure 3-29 A-B shows that the jump frequency (k) is found to increase monotonically, whereas the site factor (*f*) decreases monotonically, when temperature increases. During the initial stages of temperature rise, the jump frequency (k) predominates, restricting crystal growth primarily due to the diffusion rate of erythritol molecules. Consequently, the crystallization rate exhibits an upward trend. However, as the temperature increases, the site factor (*f*) becomes more influential, causing a

gradual hindrance for the crystal growth due to the equilibrium between erythritol molecules incorporated onto the crystal surface and dissolution from the crystal surface into the surrounding liquid. This leads to a decrease in the crystallization rate, eventually reaching zero near the melting point.

Figure 3-29 C shows the temperature-dependent behaviour of the ledge energy, following the same trace of rise and fall as the velocity (**Figure 3-24 B**). As the erythritol load increases, its ledge energy increases from MME1 to MME3 but halts at MME4. Drawing from a previous study [244], the ledge energy approximates the surface energy (σ) of spherical nuclei during supercooled nucleation. According to the classical nucleation theory, the minimum nucleation free energy (ΔG_N^*) can be expressed as:

$$\Delta G_N^* = \frac{16\pi}{3}\frac{\sigma^3}{{\Delta\mu_v}^2} \qquad (3-9)$$

Based on above results, **Figure 3-29 D** shows the energy barrier to form a nucleus for MME series materials, indicating that it increases with temperature. At the ambient temperature (30 °C), the energy barrier of MME1 is around 10^{-19} J but declines with the increase of erythritol load at a given temperature. This confirms quantitatively the stability sequence of the supercooled liquids in a view of kinetics. Considering the heat release occurs at the room temperature, **Figure 3-30** compares the room-temperature (30 °C) energy barriers of MME series with those of typical stable supercooled liquid polyols such as xylitol and sorbitol (Data for xylitol and sorbitol were obtained from the literature [171]). For MME series, the energy barrier declines with increasing erythritol load in the system, which accounts for the decrease of the trigger response time (**Figure 3-23 B**) and therefore

the trigger ability. However, the trigger-ability is a function of both the energy barrier and diffusion coefficient. Although both xylitol and sorbitol have a lower energy barrier than MME1, their much lower diffusion coefficients, due to their viscosities being one or two orders higher, limits the mass transfer during the crystallization within a local region after triggering, and hence affects the efficient crystallization avalanche needed for heat release.

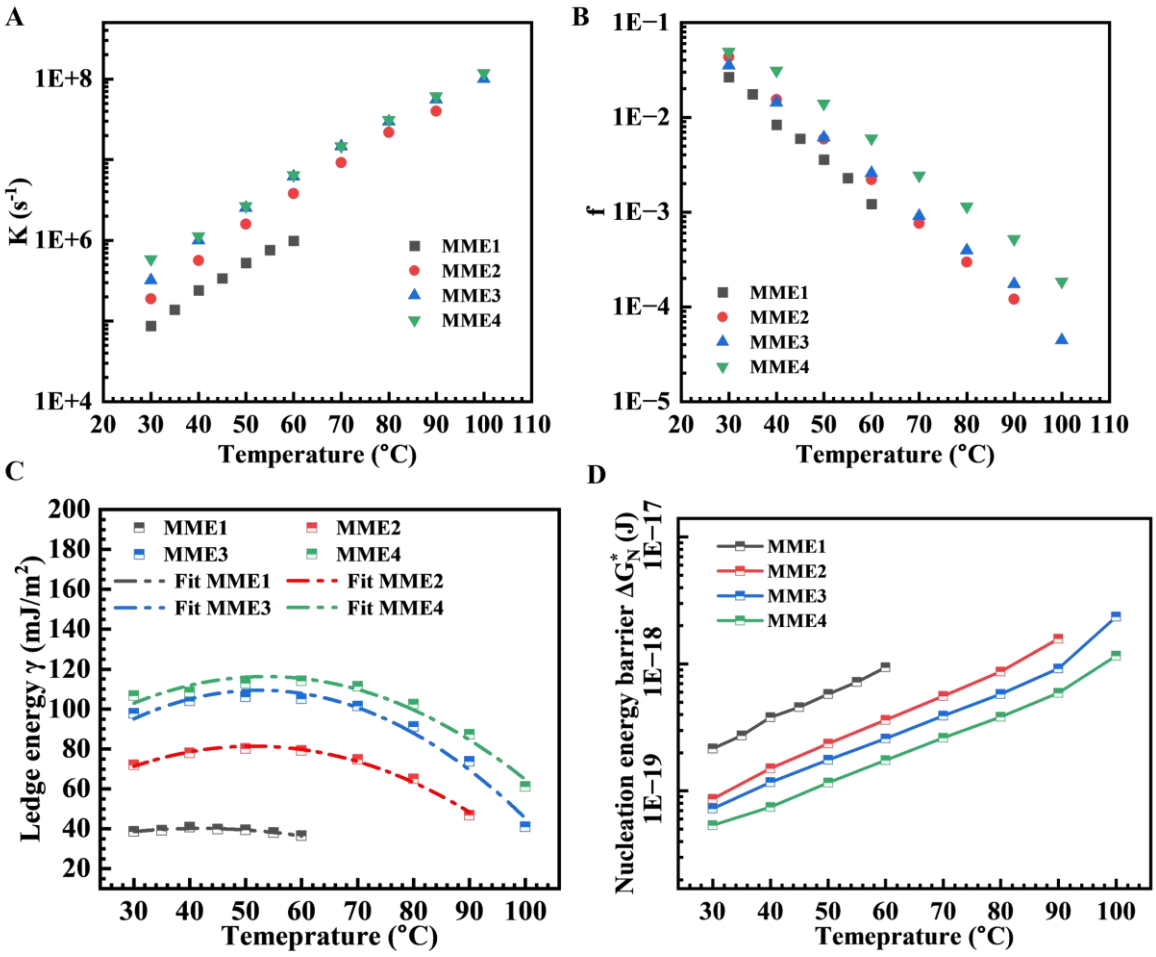


Figure 3-29 The Kinetic Properties of MME Series Samples.

*(**A**) The jump frequency, k; and (**B**) the site factor, f; and (**C**) the ledge energy, γ, of MME1 to MME4.*

*(**D**) The nucleation energy barrier for MME series samples.*

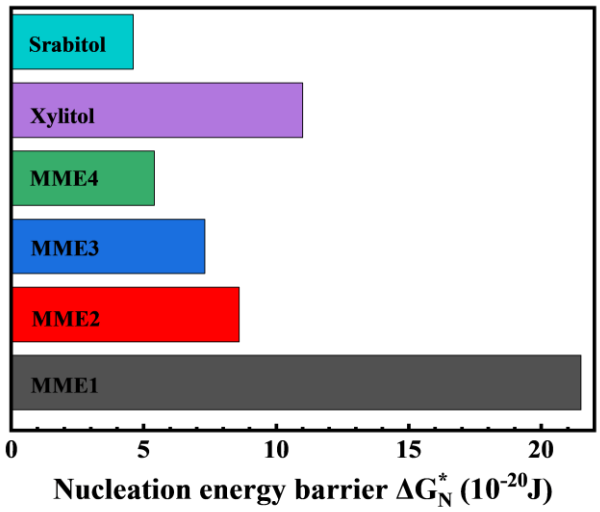


Figure 3-30 Comparison of MME Series Materials, Xylitol, and Sorbitol for Nuclear Energy at Room Temperature.

Thus far, MME series has been shown to an excellent material system that addresses the phase-stability and trigger-ability challenges, owing to the unique core-shell coordination structure and ligand-exchange mechanism as discussed above. Through changing the load of erythritol, one can modulate the phase stability and trigger-ability of the supercooled liquids of MME, on top of the ability to tune the energy storage density. These characteristics match well such different heat transmission needs, such as short- or long- storage time and short- or long-distance. In the following sub-section, an example material is used to demonstrate a practical application in solar harvests and storage.

3.3.4 Low Grade Heat from Solar for Charging and Discharging Demonstration

As presented above, the MME series shows a range of choices for applications in terms of heat storage density, trigger-ability, and stability. The MME2 with an enthalpy of 163.1 kJ/kg was

selected to demonstrate the potential for long-term heat storage applications, especially for charging with solar thermal energy. **Figure 3-31** shows the details. First, the ground-state crystalline composite (c-MME) absorbs solar energy and melts; see process ①. This is following by process ②, during which the molten liquid transforms into a stable supercooled liquid MME instead of the crystallized form by losing its sensible heat. This supercooled liquid still contains a large amount of captured energy owing to the unique energy barriers discussed in **Figure 3-30**, and such captured energy can be stored stably in long-term. When the stored energy is required, mechanical triggering is applied to release the latent heat, yielding the crystallized form of erythritols in the supercooled liquid MME. This trigger only requires a small shear stress to break a tiny part of hydrogen bonds between erythritol and MM core, leading to local crystallization of a small amount of erythritols. The yielded energy of such crystals can disrupt the neighbouring coordination bond between the two erythritols and Mn as discussed in sub-section 3.3.2, leading to local transition from the supercooled liquid to crystalline MME. Consequently, the yielded energy would enable an avalanche of the same crystallization process from MME to c-MME by a rapid release of the latent heat, as shown in process ④. The rapid latent heat release was recorded by an infrared camera (**Figure 3-31 B**), with 150 g MME2 as an example. Such energy release took place in around 61 s after the mechanical stirring, producing an avalanche from local to whole material and reached a temperature zenith of 58.5 °C in 388 s.

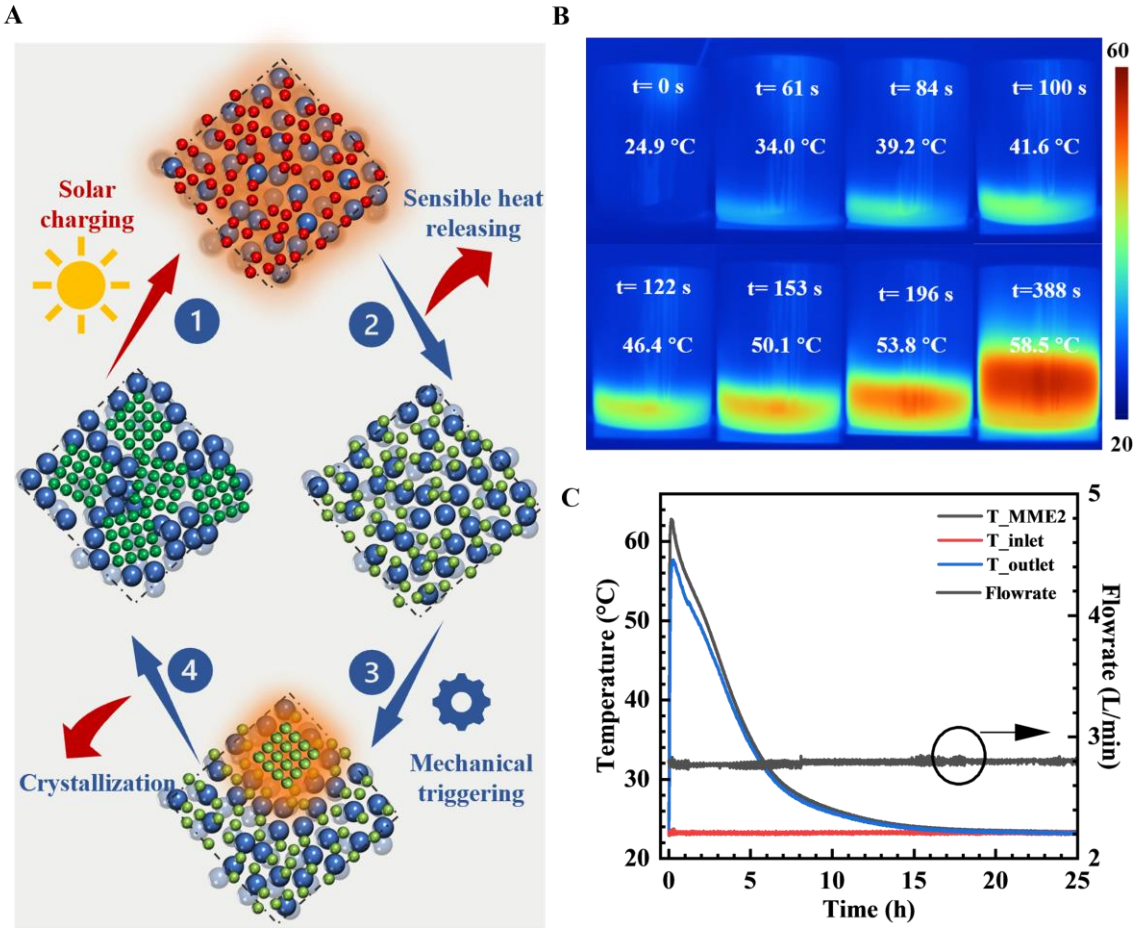


Figure 3-31 Solar Thermal Storage Application.

(A) Schematic illustration of a charging and discharging thermal cycle for MME. (B) Time-sequential infrared images of 150g MME2 in a discharging process triggered by mechanical stirring. (C) Temperature evolution curve for heat releasing process of 425g MME2.

To showcase furthers potential for applications at a large scale, 425 g of MME2 were used to heat an airflow within a copper coil as heat exchanger embedded in MME2 (**Figure 3-3**). As **Figure 3-31 C** shows, the temperature of MME2 surged from 23 °C to a peak of 63 °C within approximately 360 s by releasing the latent heat only, which can heat the airflow from ambient temperature of 23 °C to

58 °C, an impression increases of 35 °C. With simple routine insulation, the heat release can give the output airflow a temperature over 28 °C continuously at a flow rate of 2.79 L/min for over 10 hours. In terms of charging, any low-grade thermal energy can be used owing to the low melting point of 98 °C. Solar thermal provides a great source for this. The MME based demo-system was used capture solar energy; see **Figure 3-2 B**. With the same MME2, one can achieve the saturated temperature of 100 °C within 4600 s under the irradiation of a standard sun. Taking a 100 m² residential house as an example, with an 80% coverage of MME2 on the rooftop and a standard housing heat load of 60 W/m^2, the average solar energy requirement to provide 24-hour heat-supply in the house is ca. 3 kWh/m^2 per day (See the details in case study). This covers almost the whole global residents except those in Arctic, Alaska, Greenland, north of Canada, Russia, and north Europe at a latitude above around 58 ºN (**Figure 3-33**).

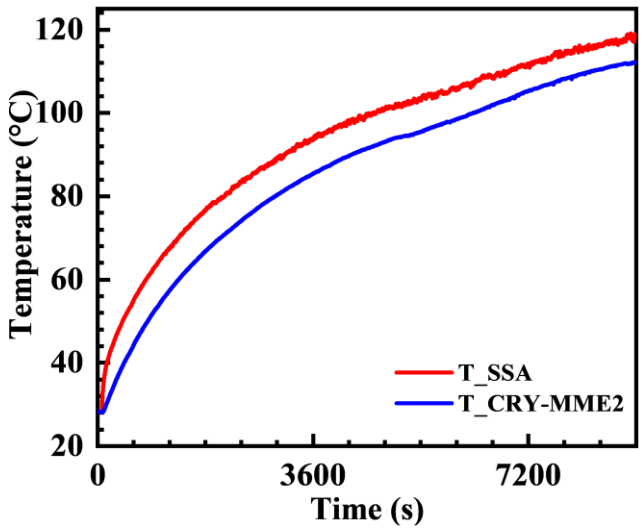


Figure 3-32 The Solar Charging Temperature Traces.

- **Case Study:** 100 m² house equipped with MME2 system.

Here solar energy is used as a heat source to provide heat to a 100 m² house. The heat load, Q_{load}, can be determined using the following formula:

$$Q_{\mathrm{load}} = q\mathrm{A} \cdot 10^{-3}$$

where q represents the heat load index (W/m^2), and A is the house floor area (m^2). The total required heat energy, Q, is determined by:

$$Q = Q_{\mathrm{h}} \cdot \mathrm{t}$$

where, t signifies the heating time in hours. For the 100 m^2 house, with $q = 60\ W/m^2$, a heating time of 24 hours, the required thermal energy is 144 kWh.

Based on the above calculation, the required volume of MME2 can be determined as follows:

$$V = \frac{Q_{sol}}{\Delta H \cdot \rho}$$

where ΔH represents the stored latent heat (kJ/kg), which is $163\ kJ/kg$, and ρ is the density of the MME2, at 1420 kg/m³. The calculations yield a required a volume of 2.24 m³.

If the entire energy supply comes from the solar, the required solar energy can be calculated as follows:

$$Q_{sol} = \frac{Q}{\varphi}$$

where, the φ is the solar-thermal conversion efficiency, which is approximately 0.85 (Alanod's commercial selective absorption coating absorbers, such as mirotherm® Control, mirotherm®, eta plus®, and mirosol® TS, boast an absorption rate of up to 95% and an emission rate of less than 5%. Considering losses during actual use, calculations are made using a reduced absorption rate of 85%.).

[245] Therefore, the required total solar energy is around 170 kWh per day.

By allocating MME2 to cover 80% of the roof area, with dimensions of 10m x 8m x 3cm to capture solar energy, the required average solar density is 2.1 kWh/m² per day. Considering that the solar irradiation in cold seasons is nearly half of that in hot seasons, the actually required average solar irradiation is approximately 3 kWh/m² per day.

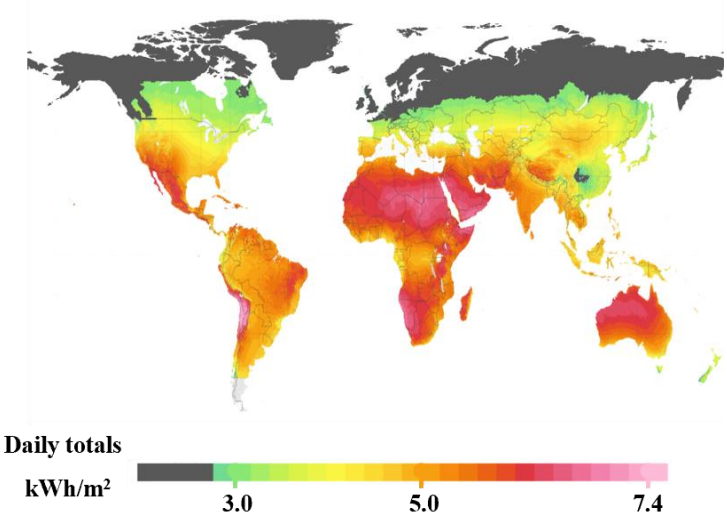


Figure 3-33 World Map of Horizontal Solar Irradiation with the Intensity Criteria. [246]

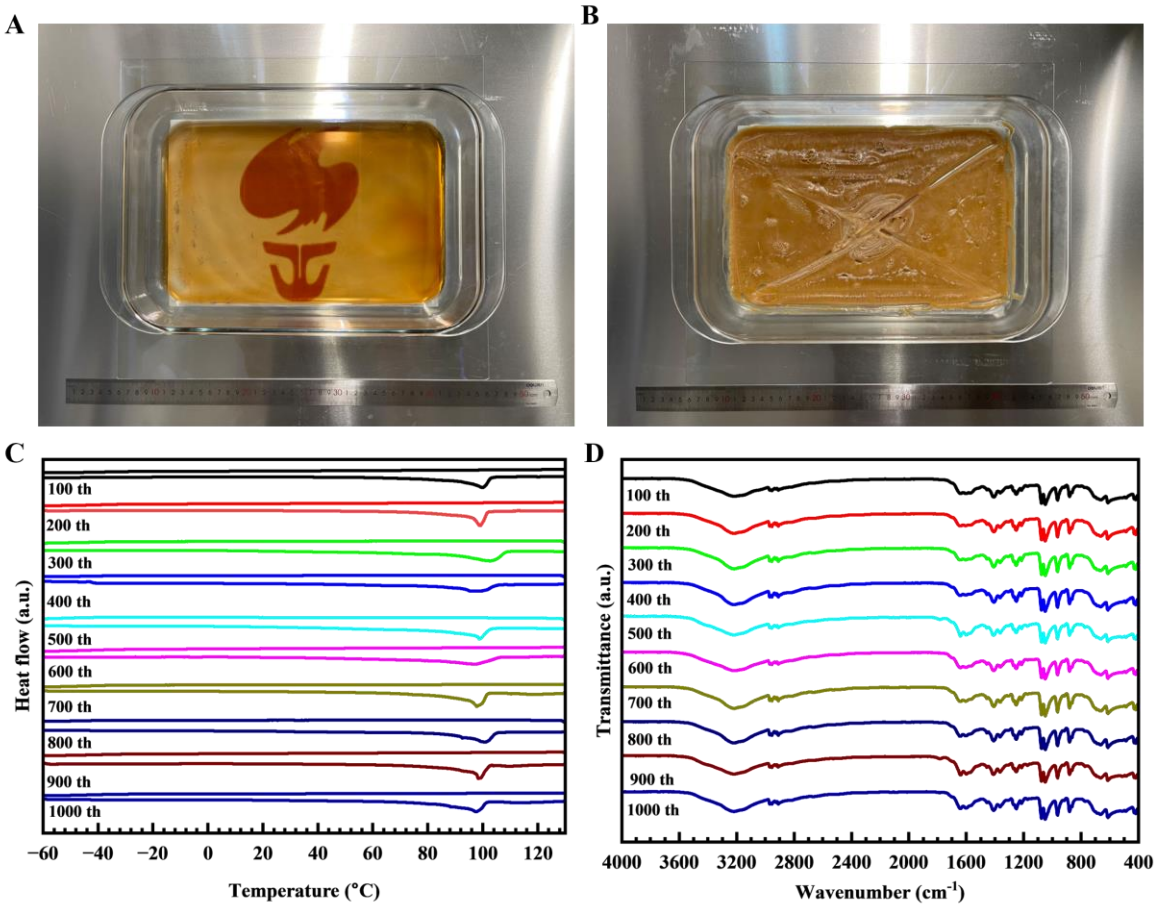


Figure 3-34 Characteristics for Large-Scale Demonstration.

*(**A**) Supercooled and crystallized states (**B**) of MME2 in a 38.5cm×24.5cm tank for an up-scaling demo. Another related video recorded the phase-transition course clearly, attached as a supplementary material. (**C**) Comparative DSC curves of MME2 after 1000 thermal cycles. (**D**) Comparative FTIR spectra of MME2 after 1000 thermal cycles.*

The above demonstrates the feasibility at least in terms of size and weight of the heat store. For the scale up system, one can also demonstrate a fast phase transition of MME2 by using a 38.5cm×24.5cm tank, from supercooled liquid to crystal, see photos in **Figure 3-34 A-B**, along with

its heat release process. These show unambiguously that the MME materials are extremely promising for the future mass production, considering that the material cost per Kg is 3 US dollars. Cyclability is another important criterion for practical material utilization. The results of the thermal cycling for MME2 are shown in **Figure 3-34 C**. One can see the stable supercooling performance with an enthalpy loss of 14% (from 163.1 kJ/kg to 140.4 kJ/kg) after 1000 thermal cycles of charging and discharging. Meanwhile, the FTIR results exhibit a negligible change of the chemical structure (**Figure 3-34 D**). The excellent cyclability further supports the potential for MME in practical application.

3.4 Conclusions

In this chapter, metal-organic supercooled liquids are studied for long-term storage. The main conclusions are summarized as follow:

- A new strategy of combining coordination and hydrogen bonds together to create a glass-forming liquid material in a core-shell coordination structure. The unique core-shell coordination structure was discovered clearly by combining such comprehensive protocols as XRD, EXAFS, XANES, UV-Vis and FTIR. In this new material, an elongated octahedral Mn-methylurea (1:4) complex (MM) acts as the core, offering two active sites in longer bond to coordinate two other ligands like Cl- ions. Once incorporating energy-harvesting units of high enthalpy like erythritol, it would replace Cl- ion already coordinated with MM core in the melting process due to the larger splitting energy, to form a glass-forming/supercooled liquid MM@erythritols (MME) with excess erythritols surrounding the MM core via hydrogen bonds as the shell, after natural cooling

from its melting temperature to room temperature. Glass-state MM has a high glass-forming ability (GFA) of 0.75 and impressive viscosity of 108 Pa·s, dominating the thermal stability of glass-forming liquid MME and herein guaranteeing their phase stability at room temperature.

- Thermodynamics and kinetics of phase transition between supercooled liquid and crystalline MME were also well explored. Strikingly, as revealed, this reversible phase transition relies critically on the ingenious ligand exchange between erythritol and Cl- ion coordinated with MM core, which can be driven by a local exotic shear stress smaller than 10 Pa. And the avalanche heat release can be stimulated within tens of seconds. Room-temperature energy barriers of MME series were measured at ~ 10^{-19} J, which combines with their suitable diffusion rates (~10-10 cm^2/s) to determine the wonderful controllability of MME phase transition. Moreover, the enthalpy loss for the intrinsic MME materials was lower than 15% after 1000 service cycles of thermal charging and discharging, which demonstrates its huge cyclability potential. By successful addressing the contradictory challenge of phase stability and trigger ability of phase transition, as well as cyclability, MME is confirmed to be an extremely promising material system for practical utilization of low-grade heat harvest and release. Moreover, by tuning the erythritol load simply, the MME material system can cover different heat transmission demands at ambient environments, trans-day or even trans-season and trans-city or even trans-continent. In addition, low cost of MME precursors foresees its huge market potential.

Chapter 4 Organic Glassy Materials for Long-Term TES

4.1 Introduction

This chapter reports the study on glassy materials as a long-term thermal energy storage material. In addition to crystallization and supercooled liquids as discussed before, the transition from a liquid to a solid state can also be achieved through vitreous. It is promising to use glassy materials for long-term TES applications. When a supercooled liquid is cooled below its glass transition temperature, a glassy material can be obtained. By adjusting the glass transition temperature above room temperature, the stability for long term energy storage can be significantly improved due to its high viscosity and low kinetic properties. As a result, latent heat can be stably stored for months or even years, even allowing for nucleation during the storage period, which is impossible for supercooled liquids. On the other hand, although methods such as mechanical stirring, which are effective for supercooled liquids, cannot trigger the transition due to the high viscosity. The triggerability of glassy materials can be easily achieved by applying a small amount of heat to induce cold crystallisation.

Although some works on glassy materials as long-term TES materials have been explored, as discussed in Chapter 2, there are limitations. For example, the use of polymer-based polyols by Ari Seppälä's group and a Schiff base Ni (II) complex glass by Kazuya Saito's group have faced challenges. These materials were limited by either the high cost of their ligands, complex preparation processes, lengthy synthesis cycles, or unsuitable glass transition temperatures.

In this PhD work, organic small molecules, d-mannitol and myo-inositol, were used to develop a novel long-term TES material, G-DMI. It is distinguished by its simple structure, which is not reliant on a polymer matrix but is instead stabilized by hydrogen bonding between mannitol and inositol molecules. G-DMI boasts cost-efficiency, straightforward preparation, eco-friendliness, non-flammability, and a high latent heat of cold crystallization, indicating its significant potential for

large scale applications. The melting temperature of DMI, the crystallisation form of G-DMI, is 160 °C with a fusion enthalpy of 280 kJ/kg. After natural cooling, it can transition to a glass state at 22 °C, endowing it with remarkable thermal stability at the room temperature and the ability to maintain this glassy state for over a year. It can be triggered by reheating to initiate a cold crystallization process at 60 °C and releasing heat of 180 kJ/kg. Information gathered by using various tools such as FTIR and NMR, have delved into the molecular-level interactions—specifically the hydrogen bonds between mannitol and inositol—that are crucial to the formation of G-DMI. Moreover, in situ XRD, TEM, DSC were used to analyse the kinetics and thermodynamics of DMI during the cold crystallization process. It was also found that the presence of residual nuclei in a glassy material by TEM. In order to realize both solar-thermal conversion and thermal energy storage, 0.1 wt.% Fe_3O_4 nanoparticles were evenly dispersed into G-DMI to obtain solar DMI, which can absorb over 95% of solar radiation. A solar-thermal charging and discharging experiment were conducted using solar DMI, which can rapidly charge under a double standard solar irradiance and efficiently release the stored latent heat through a heat-triggered mechanism.

4.2 Experimental

4.2.1 Materials and Methods

- **Materials**

D-Mannitol ($C_6H_{14}O_6$, 98%, CAS: 69-65-8), myo-Inositol ($C_6H_{12}O_6$, 99%, CAS: 87-89-8), Iron oxide (II, III) (Fe_3O_4, 99%, CAS:1317-61-9) were purchased from Shanghai Aladdin Biochemical Technology Co., Ltd (China), and were used at they were without purification.

- **Preparation of G-DMI glass**

In a typical experiment, 0.7 mol of D-mannitol was accurately weighed and heated to 220 °C, melting it into a clear liquid. Next, 0.3 mol of myo-Inositol was then added to the molten D-mannitol while

continuously stirring using a magnetic stirrer. The mixture was fully stirred until two materials were evenly melted, resulting in the formation of a transparent molten liquid. Finally, the molten liquid was naturally cooled down to room temperature to obtain the G-DMI glass.

- **Preparation of Solar G-DMI Glass**

In a typical experiment, 0.7 mol of D-mannitol was accurately weighed and heated to 220 °C, melting it into a clear liquid. Next, 0.3 mol of myo-Inositol was added to the molten D-mannitol while continuously stirring was applied with a magnetic stirrer. The mixture was vigorously stirred until two materials were evenly melted, resulting in the formation of a transparent molten liquid. Then 1.8 g Fe_3O_4 were added into the molten liquid and fully stirred until all the nano particles were dispersed evenly. Finally, the black molten liquid was naturally cooled down to the room temperature to obtain the solar G-DMI glass.

4.2.1 Materials Characterizations and Solar Charging/Discharging Experiment

Materials characteristics as done using a number of techniques, which are briefly summarised in the following.

- **XRD and In-situ XRD**

X-ray diffraction study of the samples was used performed using a Bruker D8 Advance diffractometer with Cu Kα radiation (λ = 1.5406 Å) operated at 40 kV and 40 mA. The preparation of the samples involved either grounding them into a fine powder crystal sample or melting them (amorphous samples) before depositing onto a sample holder, followed by flattening. The diffraction angle (2θ) was scanned from 10° to 80° at a step size of 0.02° and a scan speed of 1°/min.

Temperature-controlled XRD was conducted in the 9kW Rigaku SmartLab with a temperature-controlled stage (Anton Paar DCS 500).

- **UV-VIS-NIR transmittance spectra**

UV-VIS-NIR spectra were obtained using a PerkinElmer Lambda 750s UV/VIS/NIR spectrometer. In a typical experiment, the sample was placed in a quartz cuvette with an optical path length of 1 cm. The spectrum was acquired over the range of 250-2500 nm with a resolution of 5 nm.

- **FT-IR spectra**

FT-IR analyses were performed using a Bruker Vertex 70v spectrometer equipped with a diamond attenuated total reflectance (ATR) accessory.

- **NMR**

Liquid ^{1}H NMR spectra of the samples were obtained using a Bruker Advanced III 400 MHz NMR spectrometer. Deuterated solvent was DMSO-d6. Chemical shifts are expressed in ppm and are referred to the residual peak of the solvent peak.

- **SEM**

SEM images of the samples were acquired with a high-resolution field emission scanning electron microscope (SEM, TESCAM MIRA3) operated at an acceleration voltage of 3 kV. The images were acquired using a secondary electron detector and a backscattered electron detector.

- **TEM**

High-resolution scanning transmission electron microscopy with a high-angle annular dark-field (STEM–HAADF) was used to study the samples. The images were obtained using a Talos F200X

G2 (Thermo Fisher) transmission electron microscope. In a typical experiment, TEM specimens were prepared using the melt-dragging method. For doing so, the copper grid was heated to 160 °C on a heat stage, and then the molten samples were dropped onto it using a capillary tube. The grid was then dragged at high temperature to achieve a suitable thickness of the sample layer. Finally, the specimen was dried and cooled to room temperature before subject to TEM analyses.

- **DSC**

DSC measurements were performed using a TGA/DSC1(Mettler Toledo) under a nitrogen atmosphere. A typical measurement involved the use of approximate 5 mg of the sample was placed in a standard aluminium pan. The measurements were done at a heat rates of 5 °C/min, 10 °C/min, 15 °C/min 20 °C/min, 25 °C/min，30 °C/min and 35°C /min from 0 °C to 220 °C, before cooled to 0 °C, under a 50 mL/min N_2 flow into the sample cell. An empty aluminium pan was used as a reference.

- **TGA**

TGA was performed with a TGA/DSC 1 equipment (Mettler Toledo). In a typical experiment, the samples were heated from 30 to 500 °C at a heating rate of 10 °C/min in an N_2 atmosphere (50 mL/min).

- **Rheological analysis**

Rheological measurements were performed using a HAAKE MARS III rheometer with a Peltier temperature control system. In a typical experiment, a sample was placed onto the rheometer stage and hold for 10 s to allow for samples flowing evenly before the measurement was started. A 20 mm

titanium plate was used for the analyses, and the gap height before the places was set to the truncation height of 0.1mm. The temperature was controlled strictly from 160 to 135 °C using a Peltier system. The viscosity was obtained under an applied shear rate of 0.1 s^{-1}.

- **Thermal Imaging Analyses**

Thermal imaging measurements were performed on the samples using a Fluke 480 Pro thermal camera equipped with a 17 μm detector over a temperature range of -40 °C to 550 °C. The camera was set to manual mode and the emissivity was set to 0.95 for all the samples. The samples were placed on a heat stage and allowed to 60 °C before the measurements. The camera was positioned approximately 40 cm away from the samples.

- **Solar Charging and Discharging Experiment**

For doing so, an arc lamp solar simulator (ABET) was used as a simulated solar energy source. In a typical test, as shown in **Figure 4-1**, a 20 g solar DMI was placed in an uncovered evaporation dish with 15cm in diameter. No thermal insulation was used during the charging process. A Fresnel lens was used to concentrate the light, enabling the sample to be charged under conditions equivalent to twice of the intensity of standard solar illumination. Data were recorded throughout the experiment using a Data Acquisition System (DAQ, Advantech USB-4718).

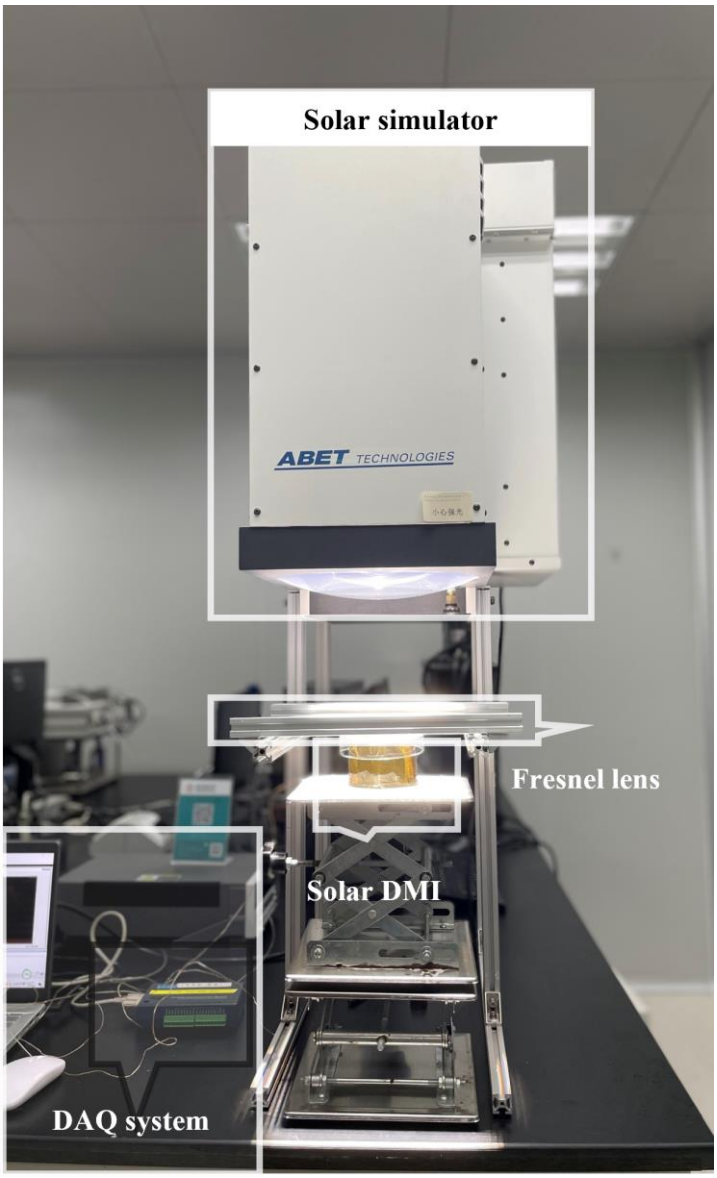


Figure 4-1 The Solar Charging System.

4.3 Results and Discussion

4.3.1 Properties and Structure Characterization of G-DMI and DMI

As discussed earlier, the G-DMI composed of pure organic small molecules, was synthesized by dissolving 3 mol of myo-inositol in 7 mol of molten d-mannitol (170 °C) before naturally cooled to the room temperature. The characteristics results show that, at ambient conditions, G-DMI presents

as a colourless and transparent glassy substance, as shown in **Figure 4-2 A**. Upon reheating, G-DMI undergoes a cold crystallization process, transitioning to a white and opaque crystalline state, named DMI, as illustrated in **Figure 4-2 B**. At the room temperature, G-DMI exhibits a significantly slow kinetic behaviour, resulting in exceptional thermodynamic stability. To demonstrate its stability, 150 g of G-DMI were prepared. The results show that it can be stored for over 360 days under ambient conditions without spontaneous crystallization, as evidenced in **Figure 4-2 C**-**D**. This characteristic makes it a suitable option for long-term thermal energy storage.



Figure 4-2 Photographs of G-DMI and DMI.

*Photographs of G-DMI (**A**), and DMI (**B**) captured within a quartz cuvette (1 cm optical path length).*

*Comparative photographs of 150g G-DMI (**C**) before and (**D**) after a 360-day period.*

XRD patterns of G-DMI and DMI obtained at the room temperature were compared with those of d-mannitol and myo-inositol crystalline structures, as shown in **Figure 4-3 A**, to understand their structures. One can see a prominent halo between 15-25°, a characteristic feature of amorphous materials. [247] This indicates that in this state, the molecules of d-mannitol and myo-inositol lack long-range ordered arrangement, aligning with the properties of an amorphous state. However, the XRD patterns of G-DMI also displayed some peaks of lower intensity. These may arise from crystalline films formed at interfaces in contact with air, or pre-nucleation clusters within the amorphous structure which will be discussed below. Further, when G-DMI undergoes a cold crystallization process to transform into DMI, its molecules realign to form an ordered crystalline structure,

manifested as sharp and distinct diffraction peaks in the XRD patterns. Comparing the diffraction peaks of DMI with those of pure d-mannitol and myo-inositol crystals, DMI is seen to retain some characteristic peaks of myo-inositol, such as those at 14.47° and 15.20°, corresponding to the (0 2 0) and (0 2 1) crystal planes [248,249], respectively. Due to the lower content of inositol in DMI, peaks from inositol are relatively weak and sometimes overshadowed by other peaks. Additionally, the high-intensity diffraction peaks in DMI, in comparison to pure d-mannitol, show significant changes. After comparison of the XRD pattern of the sample with the standard PDF card, it is found that the three strong peaks in DMI at 18.91°, 21.36°, and 23.57° correspond to the (0 1 3), (1 0 1), and (0 2 1) planes of the α-phase d-mannitol, respectively, while other diffraction peaks also exhibit corresponding shifts, as shown in **Figure 4-3 B**. [250–253] This indicates that during the formation of DMI, the more stable β-phase d-mannitol completely transformed into the α-phase. Such a transformation might be the result of changes in lattice stress, crystal structure adjustments, and thermodynamic factors. [247,254,255] This indicates further that although no chemical reactions occur between d-mannitol and myo-inositol during the formation of DMI, their intermolecular interactions and crystallographic compatibilities induce a change in the arrangement of d-mannitol molecules, significantly affecting the overall crystal structure of DMI.

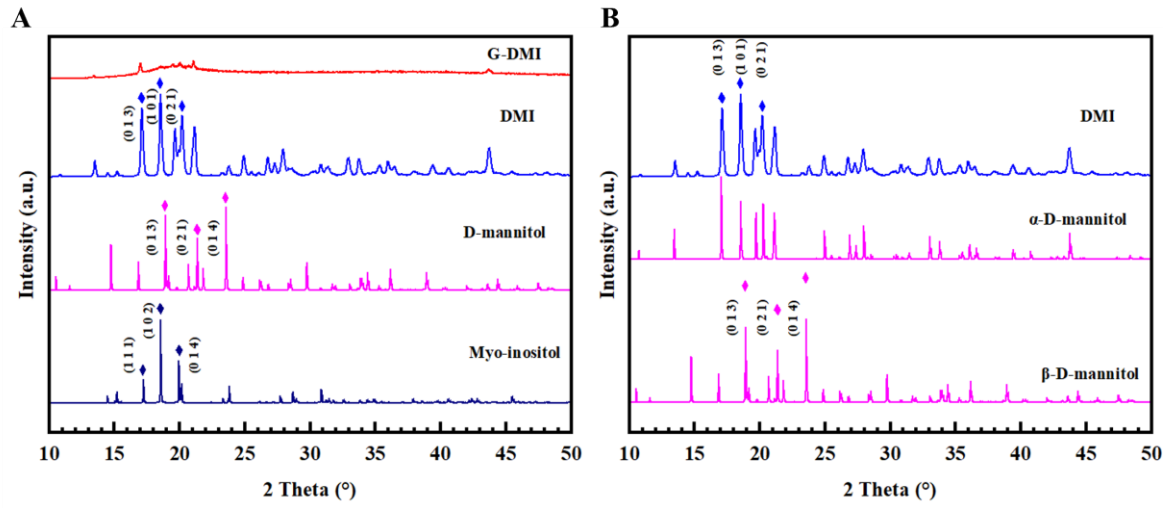


Figure 4-3 XRD patterns for α-D-mannitol, β-D-mannitol, Myo-inositol, and DMI and G-

DMI.

*(**A**) XRD patterns of D-mannitol, Myo-inositol, and DMI and G-DMI. (**B**) XRD patterns of α-D-mannitol, β-D-mannitol, and DMI.*

Further investigation into the reasons behind the DMI's ability to form a glass state was conducted using FTIR and NMR for structural identification. **Figure 4-4 A-C s**how the results. One can see that the infrared spectrum of DMI displays distinct OH stretching vibrations at 3384, 3280, and 3235 cm^{-1}. Conversely, in the G-DMI spectrum, these peaks coalesce into a single broad peak centred at 3272 cm^{-1}, indicative of enhanced hydrogen bonding and altered vibrational modes in the glassy state of G-DMI. Spectroscopic analysis further identifies transformations in the CH group's stretching vibrations from sharp peaks at 2983, 2969, 2935, and 2901 cm^{-1} in DMI to broader peaks at 2927 and 2883 cm^{-1} in G-DMI. Similarly, CH_2 scissor vibrations shift from a sharp peak at 1417 cm^{-1} in DMI to a broader and blue-shifted peak at 1407 cm^{-1} in G-DMI. Additionally, CO stretching vibrations, originally at 1076, 1047, and 1016 cm^{-1} in DMI, redshift to 1074, 1037, and 1002 cm^{-1} in G-DMI. These spectroscopic alterations substantiate the significant influence of hydrogen bonding between d-mannitol and myo-inositol on G-DMI's molecular structure and function. This finding is further corroborated by NMR data, as shown in **Figure 4-4 D**, which reveal a shift in the active hydrogen of DMI toward the downfield relative to the mannitol and inositol monomers.

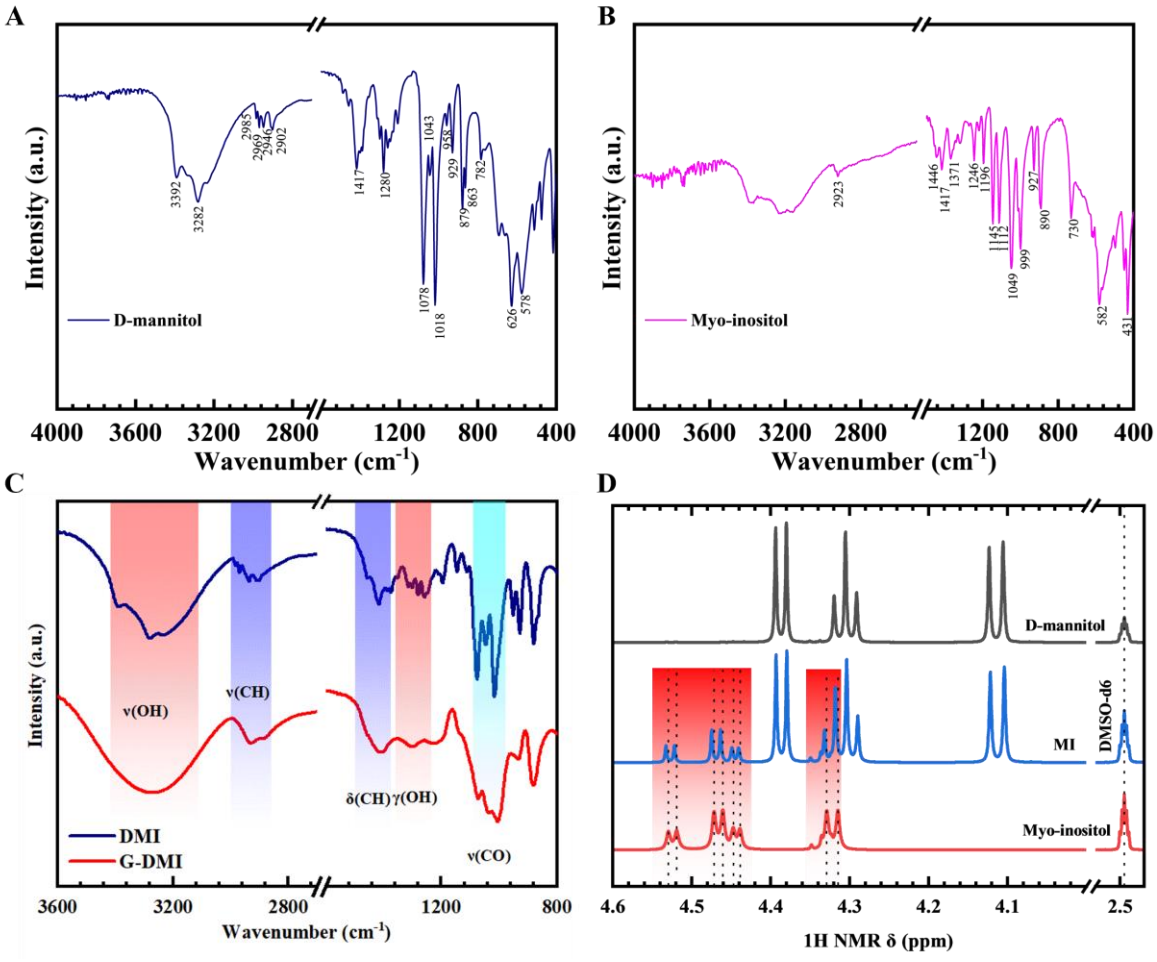


Figure 4-4 Chemical Interaction Analyses by FTIR and NMR.

FTIR spectrum of D-mannitol ***(A)****, and Myo-inositol* ***(B)****, G-DMI (red line) and DMI (blue line) (****C****)at ambient temperature. (****D****) Experimental* ^{1}*H NMR spectra of D-mannitol, Myo-inositol, and DMI (d6-DMSO, 500 MHz).*

As a long-term TES material, the enthalpy of DMI is a parameter of significant interest. Its DSC curve, represented in **Figure 4-5 A**, shows an endothermic peak at around 160 °C with a melting enthalpy of 285 kJ/kg. It is noteworthy that no crystallization peak appears during the cooling process, indicating that the stored energy is not released but retained within the material. Upon secondary heating, G-DMI initially undergoes a glass transition at around 22 °C and commences cold crystallization at approximately 60 °C, with an enthalpy of crystallization of 177 kJ/kg, surpassing

those reported for glassy thermal storage materials in the literature discussed in sub-section 2.4.2. To ensure thermal stability during the charging and discharging processes, the thermal decomposition characteristics of DMI were also examined. As illustrated in **Figure 4-5 B**, DMI does not undergo thermal decomposition until 300 °C, signifying a good thermal stability within the operational temperature range. It is important to note that the monomers constituting, d-mannitol, and myo-inositol, have their distinct decomposition temperatures. The onset of thermal decomposition for DMI is nearly 50 °C higher than that of its constituent monomer d-mannitol. This elevation may be attributed to the hydrogen bonding interactions between d-mannitol and myo-inositol, delaying the decomposition onset.

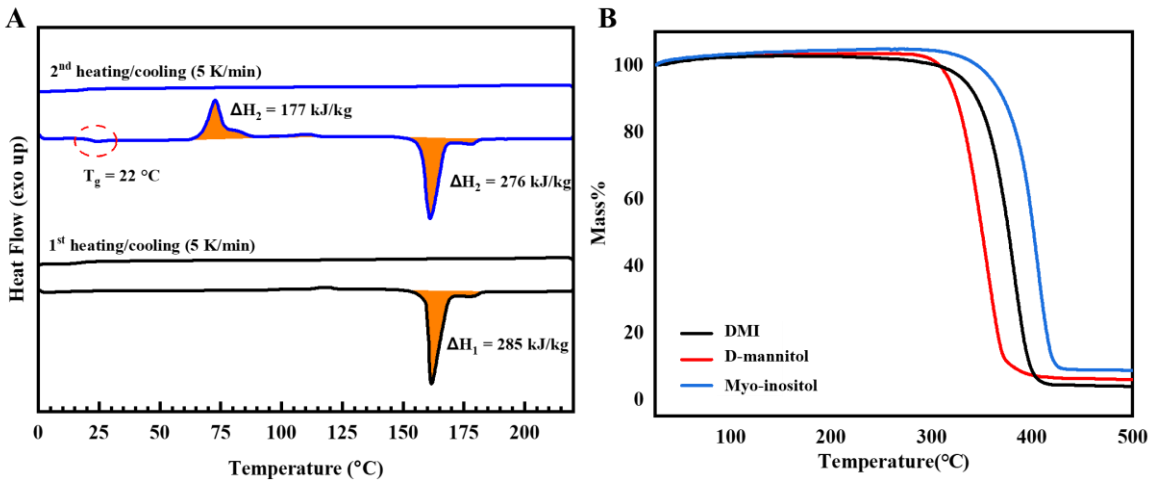


Figure 4-5 Thermal Properties of DMI and G-DMI

*(**A**) DSC traces for G-DMI with a heating and cooling rate of 5 K/min in black line and reheating-induced cold-crystallization curve for G-DMI in blue line. **(B)**Thermogravimetric analysis (TGA) profile of DMI, d-mannitol and myo-inositol.*

In a more detailed and in-depth investigation into the cold crystallization of G-DMI materials, temperature-dependent in-situ XRD was employed. The results revealed that, as shown in **Figure 4-6 A-B**, G-DMI predominantly exists in an amorphous state below 50 °C, whereas beyond 60 °C, a transition to crystalline DMI occurs, aligning with the cold crystallization onset temperature

identified by the DSC. Significantly, a subtle diffraction peak at 17.92°, attributed to inositol's β-phase [249], appears at 60 °C. This peak's intensity diminishes with increasing temperature and vanishes at 100 °C. This behaviour is likely due to inositol-mannitol interactions facilitating β-phase formation at the elevated temperatures. However, the β-phase has a low thermal stability, leading to its transition to the more stable α-phase upon further heating.

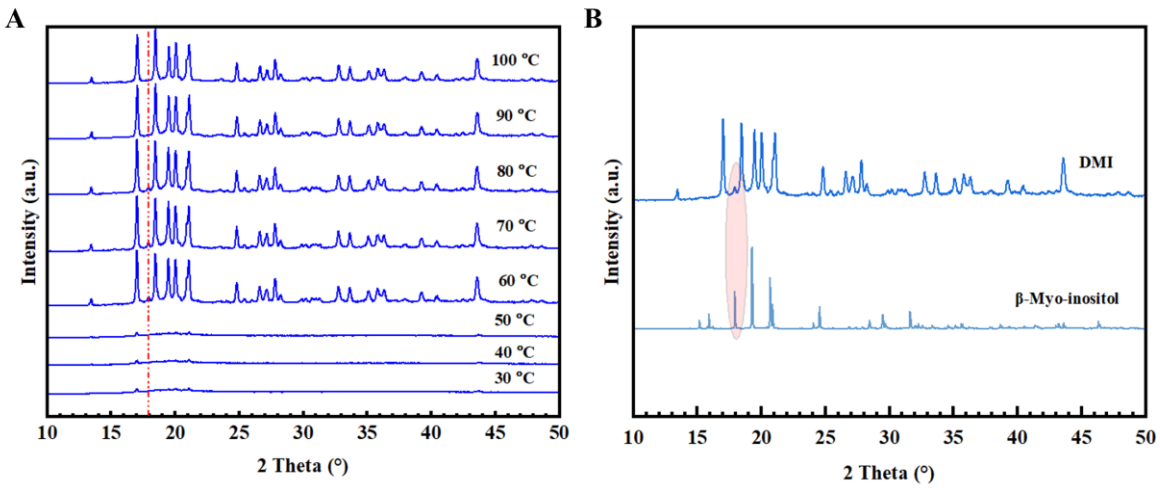


Figure 4-6 XRD Analyses during Cold-Crystallization of G-DMI.

*(**A**) In situ XRD patterns during cold-crystallization for G-DMI. (**B**) XRD patterns β-Myo-inositol, and DMI @ 60 °C.*

Besides, in situ UV-Vis-NIR spectroscopy was employed to investigate the changes in optical properties before and after the cold crystallization process. The results are shown in **Figure 4-7**. One can see that, when the glassy material is below 75 °C, the transmittance in the visible light region remains above 75%, indicating that G-DMI persists in a glassy state within this temperature domain. When the temperature exceeds 75 °C but below 160 °C the transmittance of DMI drops to zero across the entire spectral range, signifying the occurrence of cold crystallization. Above 160 °C, the transmittance of DMI rises back to around 90%, corresponding to the complete melting of DMI, consistent with the DSC findings.

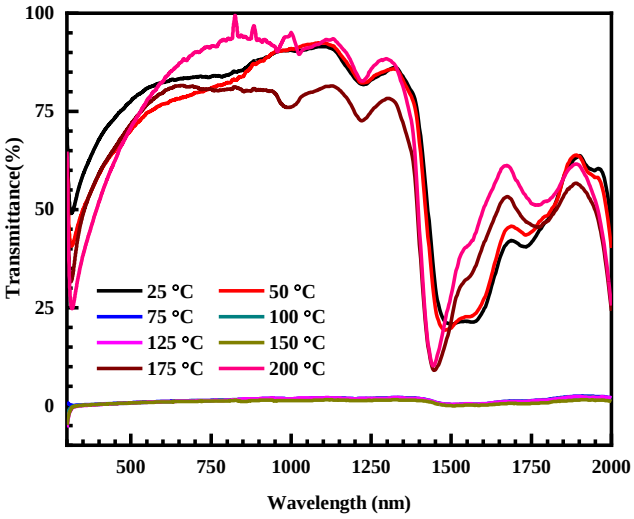


Figure 4-7 In Situ UV-Vis Transmittance Spectra of the G-DMI.

4.3.2 Micro Morphologies of G-DMI and DMI

The microstructures of G-DMI, DMI, d-mannitol and myo-inositol can be meticulously delineated using SEM. **Figure 4-8 A-B** and **Figure 4-9**. **Figure 4-8 A** show the results, one can see that the surface of G-DMI is replete with abundant wrinkle-like protrusions and lacks crystalline traits. In contrast, **Figure 4-8 B** shows that DMI manifests distinct crystalline features with lamellar crystals growing along a singular plane. To further investigate the microstructure of G-DMI, TEM was utilized. Under an electron beam, images of the sample (**Figure 4-8 C**) reveal a maze-like morphology with on recognizable structures, consistent with the previously reported amorphous characteristics. [142] However, at the nanoscale, G-DMI is not entirely amorphous but contains randomly distributed pre-nucleation clusters enveloped by the surrounding amorphous components. **Figure 4-8 D** shows that the clusters mainly consist of irregular particles ranging from 1 to 2 nm (as indicated by the yellow-marked areas). Additionally, there are more developed clusters measuring around 10 nm (located in the red-marked areas). To unveil the initial crystalline features of DMI nucleation, selected area electron diffraction (SAED) was performed. The identified nanocrystals are found to have typical crystal facets of (1 1 1), which is consistent with the interplanar spacing of mannitol. This suggests that d-mannitol, a constituent monomer, preferentially nucleates during the

formation of G-DMI. These d-mannitol pre-nucleation clusters provide favourable conditions for the complete crystallization of G-DMI during the subsequent cold crystallization process. **Figure 4-8 E** illustrates the process of transformation between DMI and G-DMI. DMI crystals can be transformed into G-DMI through a process of melt-quenching. The vitrification occurs as molecular motions are constrained by an intermolecular hydrogen bond network and further restricted by surrounding cage-like structures, inhibiting crystallization. During this process, pre-nucleation clusters form. However, their quantity and size are limited due to a sharp increase in the viscosity of the surrounding liquid as the temperature decreases. Upon reheating, G-DMI can initiate a cold crystallization process, which releases heat.

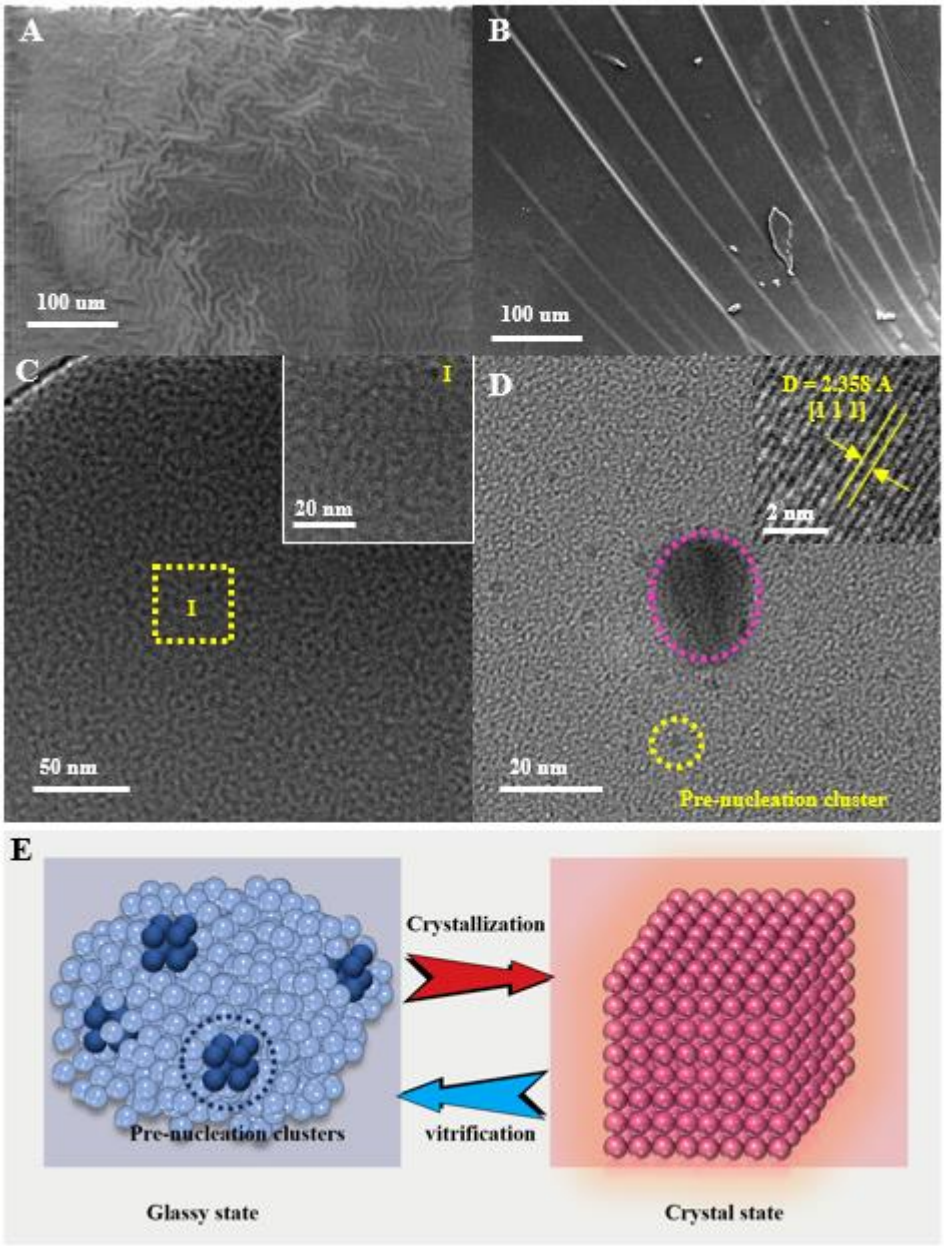


Figure 4-8 Microstructure images of G-DMI and DMI.

*(**A**) SEM image of G-DMI. (**B**) SEM image of DMI. (**C**) TEM image of G-DMI. Selected-area electron diffraction (SAED) pattern for the I (**D**) TEM image of DMI. Selected-area electron diffraction (SAED) pattern for the II. (**E**) Schematic diagram depicting the structural interconversion between DMI and G-DMI.*

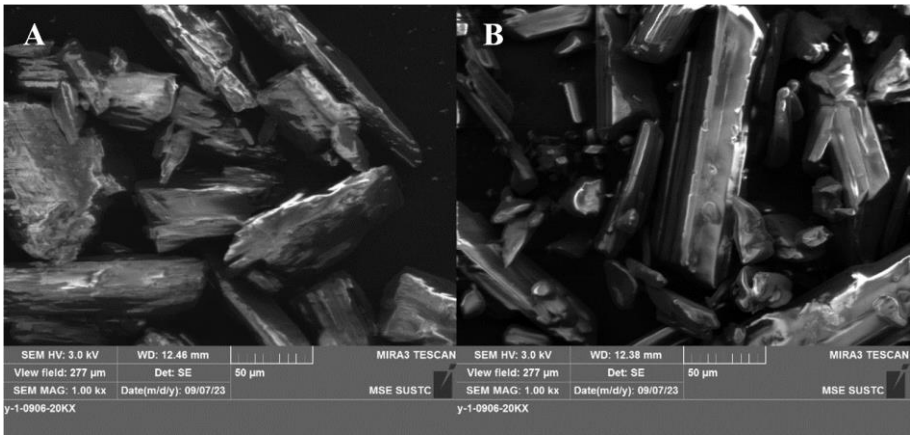


Figure 4-9 Supporting Figure of Figure 4-3.

*SEM images of D-mannitol (**A**), and Myo-inositol (**B**)*

4.3.3 Kinetic Performance of G-DMI

To further investigate the relationship between T_g, cold crystallization temperature, and cooling rate, a series of DSC analyses were performed at varying cooling rates. As shown in **Figure 4-10 A**, an increase in the cooling rate results in a corresponding rise in the T_g, consistent with previous findings. Additionally, with increasing cooling rates, the cold crystallization temperature of G-DMI also rises due to the reduced number of nuclei formed during rapid cooling. This phenomenon is primarily due to the formation of a small number of nuclei at faster cooling rates. Consequently, crystal growth in the second heating process needs more time, thereby raising the temperature of cold crystallization with increased cooling rates. For quantitative determination of the activation energy associated with the nucleation and crystallization processes of G-DMI, the Kissinger model [256,257] was utilized. Such a model takes the following form:

$$\frac{d\ln\left(\frac{k}{T_c^2}\right)}{d\left(\frac{1}{T_c}\right)} = -\frac{E_a}{R} \qquad (4-1)$$

where k represents the heating rate, T_c denotes the peak temperature of cold crystallization, E_a is the activation energy, and R stands for the gas constant.

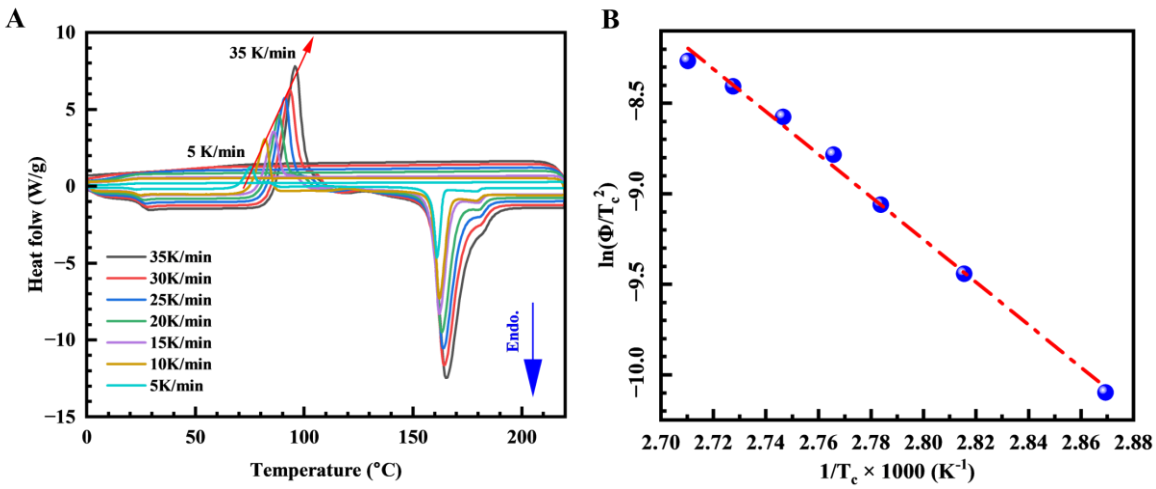


Figure 4-10 Kinetic Properties of G-DMI.

(A) *DSC traces of non-isothermal cold crystallization of G-DMI at Varied Heating Rates: 5, 10, 15, 20, 25, 30, 35 K/min. (**B**) Plots of ln (λ/T_c^2) versus $1/T_c$ during the non isothermal cold crystallization process for G-DMI.*

Linear fitting of the data using **Equation (4-1)** gives **Figure 4-10 B**, From the slop in the figure, the crystallization free energy of G-DMI can be examined as 90 KJ/mol. This is higher compared to the glassy TES materials studied in literature, indicating higher nucleation energy barriers and hence greater stability, making it an ideal candidate for long-term TES. To comprehensively understand the crystallization kinetics and glass-forming ability of G-DMI, its viscosity was measured near the melting point, and the results shown in **Figure 4-11 C**. DMI's viscosity at the melting point reaches 363 mPa·s, similar to most glass-forming ionic liquids. This high viscosity leads to a slow kinetic relaxation in G-DMI, thus preventing complete crystallization during cooling. The temperature dependency of DMI's viscosity also reveals its kinetic properties. Through MYEGA fitting, one can extrapolated its glass transition temperature to be around 23 °C, aligning closely with DSC measurements. Moreover, the fragility index of G-DMI, determined through MYEGA equation fitting, is 74, which is lower than that of typical hydrogen-bonding system glass-forming liquids like xylitol (87), sorbitol (107), and sucrose (98). This indicates a significant capability of G-DMI to form

glass, but much smaller than that of SiO2 glass (m=20) which glass forming ability is too strong to allow easy crystallization.

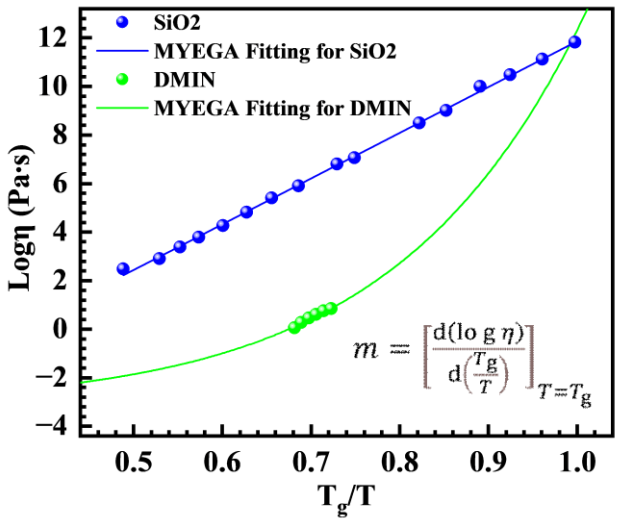


Figure 4-11 Temperature-Dependent Viscosity of G-DMI.

Angell plot showing the fragility of G-DMI with SiO2 [107]*. Solid lines are fits to the measured viscosity-temperature relation of the model derived in previous literature* [115,123]

To visually demonstrate the cold crystallization process of G-DMI, as shown in **Figure 4-12**, the exothermic process of a 20g sample was recorded during isothermal heating at 60 °C. G-DMI undergoes cold crystallization, from initial partial to complete crystallization, in just 60s with the peak temperature reaching 140 °C, showcasing G-DMI's rapid response to thermally induced stimuli.

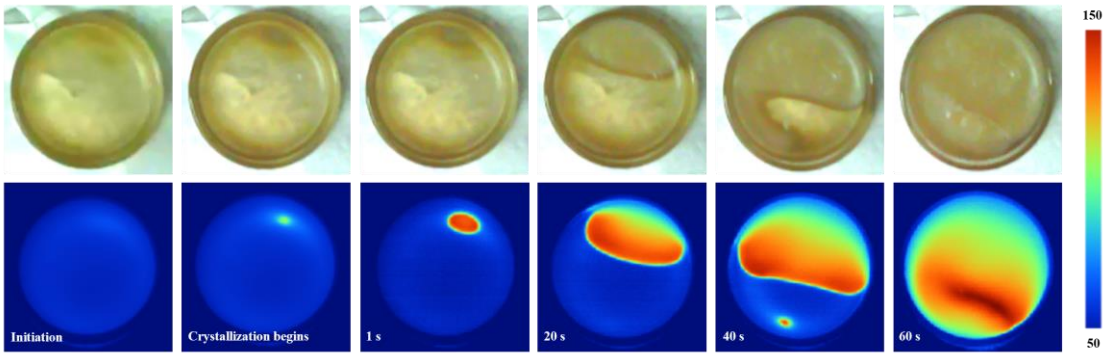


Figure 4-12 Digital and IR Images of the Cold Crystallization Process of G-DMI.

4.3.4 Solar Charging and Discharging Demonstration

Based on above discussion, G-DMI can be regarded as an efficient material for long-term TES material. In order to realize both solar-thermal conversion and thermal energy storage, 0.1 wt.% Fe_3O_4 nanoparticles were evenly dispersed into G-DMI to obtain solar DMI. A demonstration experiment was conducted to test the performance of the solar DMI. As illustrated in **Figure 4-13 A**, the solar energy storage and release cycle of solar DMI includes four stages. The first stage is the charging process, the crystalline solar DMI absorbers solar energy and melts; This is following by second process, the molten liquid transformation into a glass state solar DMI, instead of the crystallization by losing its latent heat. Solar G-DMI can contains a large amount of captured energy, and such captured energy can be stored in long-term. When the stored energy is required, at third and fourth process, thermal triggering is applied to release the latent heat yielding solar DMI again.

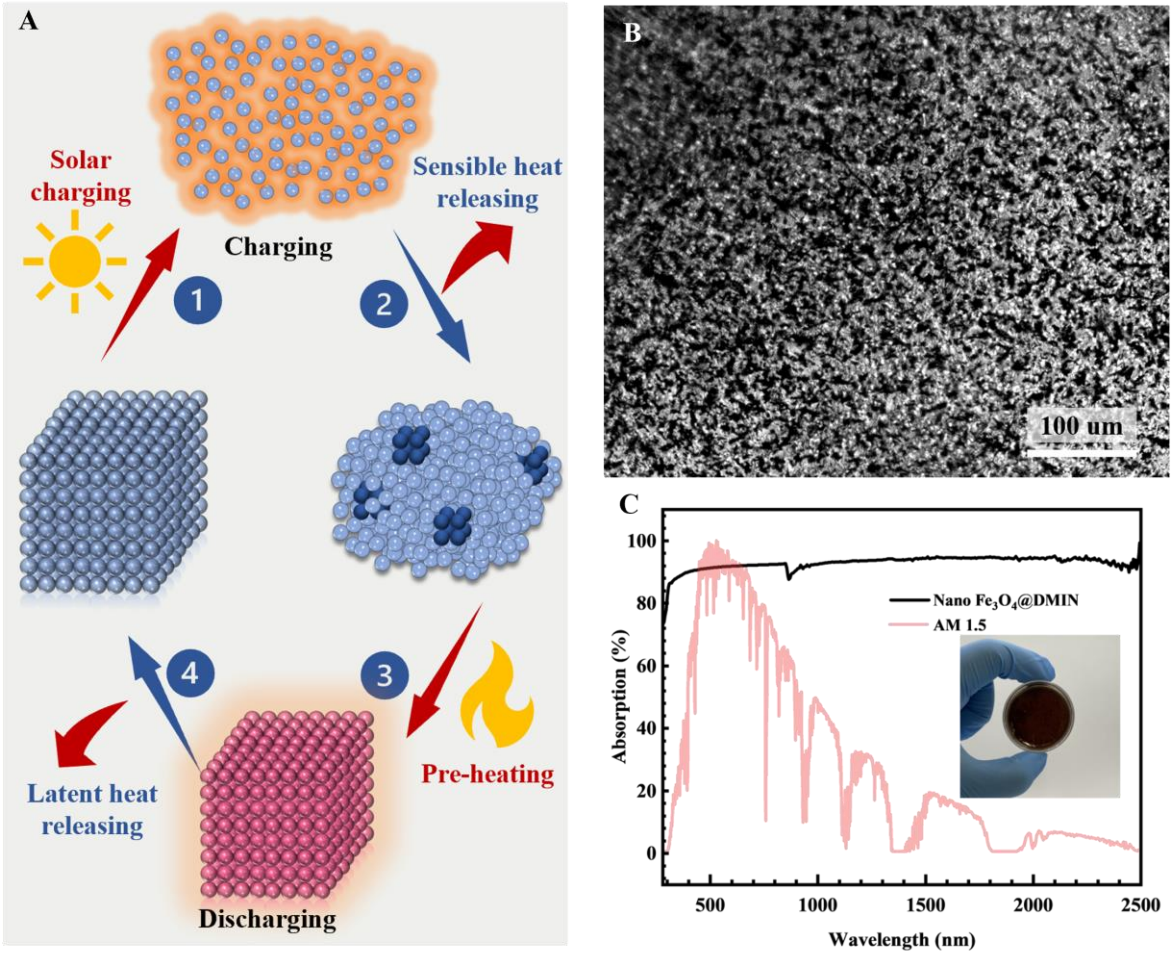


Figure 4-13 Solar Charging and Discharging for Solar DMI.

(A) *Schematic of charging and discharging thermal cycle for Solar DMI as thermally triggerable TES materials. (**B**) The morphology of solar DMI under an optical microscope. (**C**) The solar DMI's absorbance spectrum compared to the AM1.5 spectrum*

Figure 4-13 B, shows the distribution of Fe_3O_4 nanoparticles in G-DMI under an optical microscope. UV-VIS-NIR test results indicate that solar DMI possesses excellent light absorption properties, as shown in **Figure 4-13 C**, achieving an absorption rate of over 95% within the 2500 nm wavelength range. DSC results, as shown in **Figure 4-14 A**, reveal that its melting and glass transition temperatures remain largely unchanged at approximately 160 °C and 22 °C, respectively. The enthalpy of absorption decreased to 244 kJ/kg compared to pure DMI of 285 kJ/kg, but the enthalpy

of cold crystallization is almost equal to pure one. It is noteworthy that despite introducing some nanoparticles that can become nucleation sites, it still did not show any crystallization peaks during cooling, which proves its excellent glass-forming ability.

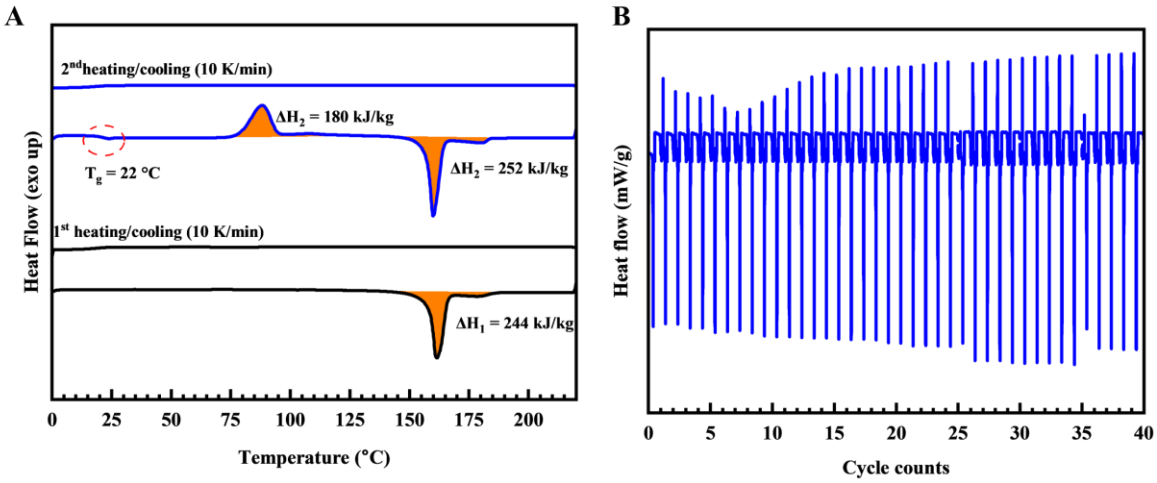


Figure 4-14 Thermal Properties of Solar DMI.

*(**A**) DSC traces for Solar DMI with a heating and cooling rate of 5 K/min in black line and reheating-induced cold-crystallization curve for G-DMI in blue line (**B**) 40-cycle thermal cycling of Solar DMI.*

Thermal cycling performance is a key metric for long-term TES materials. After 40 DSC heating and cooling cycles, as shown in **Figure 4-14 B**, solar DMI maintained its effective heat storage capacity, with minimal variation in absorption and cold crystallization enthalpies. Under double-concentration solar irradiation, as depicted in **Figure 4-1**. The charging and discharging results can be seen in **Figure 4-15**. 20g of solar DMI completed the charging process within 600 s, reaching above 200 °C. Upon naturally cooling to the room temperature, there was no obvious heat releasing platform, which means that solar DMI did not crystallize but instead became glassy solar G-DMI. After approximately one hour of storage, the solar G-DMI was heated to around 60 °C to induce its cold-crystallization within only 139 s; the sample temperature swiftly rose to 140 °C, and then gradually

cooling down. This heat release process lasted nearly one hour without any thermal insulation.

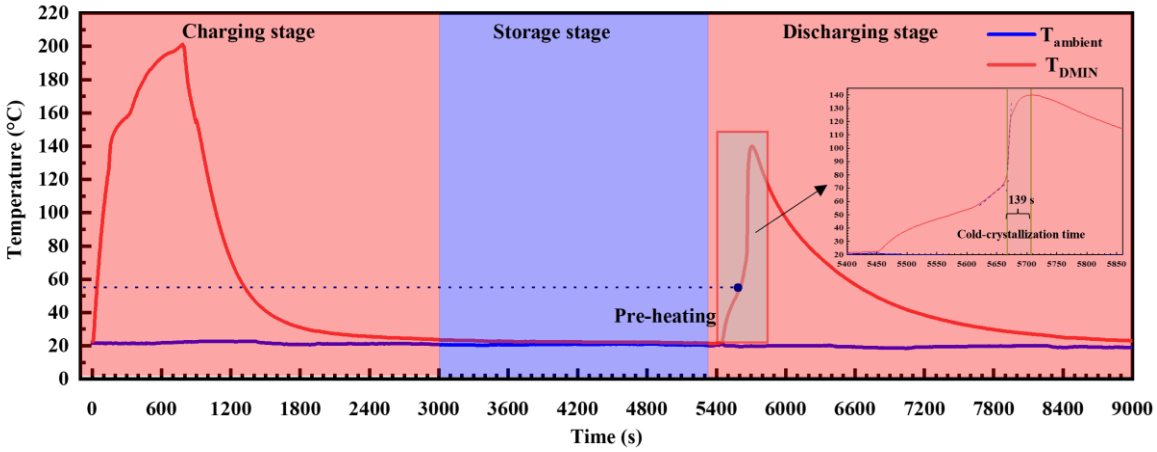


Figure 4-15 The Solar Charging and the Thermal-Triggered Discharging Temperature Curve of Solar DMI.

4.4 Conclusions

In this chapter, G-DMI are studied for long-term storage. The main conclusions are summarized as follow:

- Organic small molecules, d-mannitol and myo-inositol were used to develop a novel long-term thermal energy storage (TES) material, G-DMI. It is distinguished by its simple structure, which is not reliant on a polymer matrix but is instead stabilized by hydrogen bonding between mannitol and inositol molecules. G-DMI boasts cost-efficiency, straightforward preparation, eco-friendliness, non-flammability, and a high latent heat of cold crystallization, indicating its significant potential for large-scale applications.
- The melting temperature of DMI is 160 °C with a fusion enthalpy of 280 kJ/kg. After natural cooling, it can transition to a glassy state at 22 °C, endowing it with remarkable thermal stability

at room temperature and the ability to maintain this glassy state for over a year. It can be triggered by reheating to initiate a cold crystallization process at 60 °C, releasing heat of 180 kJ/kg.

- Information gathered by using various tools such as FTIR and NMR has delved into the molecular-level interactions—specifically the hydrogen bonds between mannitol and inositol—that are crucial to the formation of DMI. Moreover, in situ XRD, TEM, DSC were used to analyse the kinetics and thermodynamics of DMI during the cold crystallization process, where the presence of residual crystal nuclei in the glassy material was observed by TEM. In order to realize both solar-thermal conversion and thermal energy storage, 0.1 wt.% Fe_3O_4 nanoparticles were evenly dispersed into G-DMI to obtain solar DMI, which can absorb over 95% of solar radiation. A solar-thermal charging and discharging experiment was conducted using solar DMI, which can rapidly charge under double standard solar irradiance and efficiently release the stored latent heat through a heat-triggered mechanism.

Chapter 5 Dual-Layer Thermos-Responsive Energy Storage Smart Window

5.1 Introduction

Building operations contribute significantly to global final energy consumption (30%) and energy-related emissions (26%), mainly due to heating, cooling, and lighting. [258] Windows are main components of building envelope, but are also the least energy-efficient [259]. As a result, they become a focus for enhancing the energy performance of buildings. Traditional windows typically give substantial heat loss during winter and heat gain in summer, exacerbating energy consumption for temperature regulation. Smart window technologies offer a potential solution. [260] Such a solution could adjust dynamically optical and thermal characteristics by responding to environmental conditions, thus markedly reducing the reliance on artificial heating and cooling, while maintaining occupant comfort, and reducing dependence on non-renewable energy sources.

Current smart window research mostly centres around transmittance modulation, leveraging versatile chromogenic technologies like electrochromic [261,262], photochromic [263,264], mechanochromic [265,266] and thermochromic [267,268] methods to enhance energy efficiency. Among these, thermochromic approaches, particularly the use of poly(N-isopropylacrylamide) (PNIPAM) hydrogel, have garnered attention due to their perceived cost-effectiveness, rational stimulus, and zero-energy input characteristics. [269–271] The PNIPAM hydrogel, with its relatively low lower critical solution temperature (LCST) of 32 °C, is of particular interest. [272] It allows reversible transitions between

hydrophilic coil chains and hydrophobic globular conformations, altering scattering behaviour and thereby modulating optical properties. Most studies focus on controlling the LCST and solar modulating ability (ΔT_{sol}) of PNIPAM hydrogels. [273–275] However, the use of smart windows to regulate heat radiation alone is far from meeting the demand for energy efficiency, as 45% of the heat is generated through heat conduction through windows [276], and this energy can only be buffered, absorbed and stored by energy storage materials. In addition, considering that more than half of the world's regions have a temperature difference of more than 10 °C between day and night [277], there is a great demand for releasing the energy stored during the day to raise the indoor temperature at night. The incorporation of thermal energy storage (TES) provides a promising method to address this issue.

By combining TES materials with PNIPAM hydrogels based smart windows, it can achieve both regulation of sunlight and effectively storing excess heat. During daytime, TES material can absorb and store thermal energy, which is then released at night or when needed, helping to maintain a balanced indoor temperature. However, achieving this technological convergence is clearly very challenging, involving multiple hurdles such as transparency, compatibility, and durability. Water, as a sensible TES material, is particularly favoured for its highest specific heat (4.2 kJ/kg K), high stability, durability, and cost-effectiveness. Yi et al. developed a high-energy storage, thermally responsive smart window based on water-enriched thermal-responsive liquids, which can store thermal energy up to 261 kJ kg^{-1} within a temperature range of 10 °C to 70 °C, demonstrating a

remarkable energy storage performance. [278] Compared to sensible TES materials that rely solely on temperature changes of the material, PCMs have more advantages in energy storage density; they can store both latent heat and sensible heat. [279,280] However, a significant issue with these materials is their tendency to uncontrollably crystallize [281], resulting in losing transparency. This problem limits their use in window applications.

Triggerable PCMs can address above challenges mentioned above, storing energy while maintaining transparency below the melting point (T_m). The stored energy is released by triggering crystallization with external stimuli, which also cause the material to become opaque during this process. This controllable transition between transparency and opacity offers potential applications in smart windows. Hyunmin et al. designed a mechano-thermo-chromic window using a supercooled sodium acetate trihydrate, enabling the transition between supercooled and crystalline states through sharp-tip impacts and heating. [282] However, due to its high T_m (58 °C), additional heating equipment is needed for the melting process, significantly hindering its applications. Moreover, the existing triggerable PCMs like xylitol [167,168] and ET-NaOH [176] all have a high T_m and with a slow response times to triggering stimuli, which are key factors impeding their professional applications in the field of smart windows.

In this chapter, an innovative dual-layer thermo-responsive energy-storage (DLTRES) smart window was developed, which combines a thermochromic light-regulation layer with a tuneable response

temperature (T_r) and a temperature-matched energy storage layer, as depicted in **Figure 5-3A**. This enables the tuning of daytime temperature-dependent light transmittance and nighttime indoor temperature compensation with light blocking. Dimethylacetamide (DMA) and tartaric acid (TA) modified PNIPAM, referred to respectively as PNIPAM-DMA and PNIPAM-TA, were used as thermo-responsive materials (TRMs). These materials have a LCST range from 10 to 70 °C. This allows for precise control of light transmittance based on specific temperature requirements. Consequently, they facilitate highly customized indoor space temperature management and offer broader adaptability to various geographic temperatures and climate conditions. This organic molecules modified method, in contrast to traditional copolymerization techniques, not only considerably streamlines the fabrication process for tuning LCST but also addresses the inefficiencies of repeatable synthesis trial. [283]

On the other hand, the filling material for the energy storage layer is based on ethanol (EtOH) and urea (UR) - modified $CaCl_2 \cdot 6H_2O$ (CCH), termed as CCH-EtOH and CCH-UR. The charging temperature of these materials match with the T_r of the light regulation layer, ranging from 10 to 30 °C, and its dense hydrogen bond network effectively inhibits crystallization upon cooling. Unlike traditional PCMs that crystallize and lose transparency below their freezing point, CCH-EtOH and CCH-UR can maintain a transparent supercooled state in sub-freezing temperatures, ensuring energy storage efficiency without affecting light transmittance. Furthermore, this energy storage layer can serve as a ‘thermal buffer’, regulating heat absorption and release with environmental changes

through sensible heat fluctuation, and more importantly can act as a 'thermal reservoir', transferring excess daytime heat to nighttime use by triggering the release of latent heat from the supercooled liquid, thereby reducing reliance on conventional heating and cooling systems and enhancing energy efficiency. Additionally, the trigger ability of the energy storage layer endows the window with interactive response features, autonomously adapting to environmental changes or pre-set conditions, such as blocking light at night to improve privacy and sleep quality. [284]

As will be shown in the nest section, the fabricated DLTRES smart window demonstrates superior performance, with a luminous transmittance (T_{lum}) of 91%, ΔT_{sol} of 67.5% and luminous transmittance difference after triggering ($\Delta T_{lum, trig}$) of 88.4%, offering substantial improvements in energy efficiency. In terms of TES, the system exhibits distinct characteristics within the temperature range of 10-70 °C. Through TRM, it can store sensible heat with an energy density of 246 kJ/kg. Additionally, through TES, a combination of latent and sensible heat storage is achieved, resulting in an energy storage capacity of 325 kJ/kg. It will also show that, considering per unit illuminated area, compared to thermal-responsive liquids [278], the new technology is capable of providing more than twice the energy storage capacity. Furthermore, demonstrations of the prototype of the DLTRES smart window in both hot and cold environments have demonstrated its significant positive impact on indoor temperature regulation.

5.2 Experimental

5.2.1 Materials and Methods

- **Materials**

Materials used included N-isopropylacrylamide (NIPAM, 98%), N,N′-methylenebis(acrylamide) (BIS, 99%), N,N,N′,N′-tetramethyl ethylenediamine (TEMED, 99%), ammonium persulfate (APS, 98%), N,N-dimethylacetamide (DMA, 99%), Tartaric acid (TA), calcium chloride ($CaCl_2$), ethanol (EtOH, 99.5%), urea (CH_4N_2O, 99%), and deionized water were purchased from Shanghai Aladdin Biochemical Technology Co., Ltd (China), and were used at they were without purification.

- **Preparation of freeze dried PNIAPM hydrogel**

The hydrogel was made thoroughly freeze-drying. In a typical run, a homogeneous aqueous solution was prepared by dissolving 3.164 g of NIPAM monomer and 862.4 mg of the crosslinker (acrylamide) in DI water at 25°C to make 400 mL. Next, 6.15 mL of TEMED (catalyst) was added, and the solution was mixed at 600 rpm for 30 min. Finally, 12.3 mL of 10wt% APS (initiator) was added to the solution. To complete the reaction, the solution was stirred for at least 24 hours. Subsequently, the homogeneous liquid underwent a pre-freezing process using liquid nitrogen, followed by freeze-drying under vacuum at 50°C for 72 hours. [285]

- **Preparation of PNIPAM/PNIPAM-TA/PNIPAM-DMA**

The PNIPAM hydrogel was prepared by dissolving 0.5wt% PNIPAM powder in deionized water. This was following by forming PNIPAM-DMA/PNIPAM-TA solutions through by dissolving 5-40wt% DMA/TA in the PNIPAM solution.

- **Preparation of CCH-EtOH**

To prepare CCH, $CaCl_2$ (99%) was added to deionized water at a weight ratio of 111:108. The

mixture was magnetically stirred for 30 minutes at 90 ℃ until the $CaCl_2$ was completely dissolved. This was following by adding 0.5 wt.% ethanol into CCH, to obtain CCH-EtOH.

- **Preparation of CCH-EU**

Into the obtain CCH-EtOH solution, this is involved adding 5wt%, 10wt%, 15wt%, or 20wt% of urea into the CCH, leading to various mixtures. These mixtures were magnetically stirred at 90 °C for 30 minutes until the urea completely dissolved.

5.2.2 Materials Characterizations and Experiment Setup

- **XRD**

X-ray diffraction patterns were obtained using a Bruker D8 Advance diffractometer with Cu Kα radiation (λ = 1.5406 Å) operated at 40 kV and 40 mA. To prepare the samples, crystal samples were ground into a fine powder, while amorphous samples were melted and deposited onto a sample holder, followed by flattening. The diffraction angle (2θ) was scanned from 10° to 80° at a step size of 0.02° and a scan speed of 1°/min.

- **UV-vis transmittance spectra**

UV-VIS spectra were obtained using a PerkinElmer Lambda 750s UV/VIS/NIR spectrometer. The sample was placed in a quartz cuvette with an optical path length of 1 cm. The spectrum was acquired over the range of 300-800 nm with a resolution of 1 nm. The calculation of integral luminous transmittance (T_{lum}) (380 -780 nm), IR transmittance (T_{IR}) (780 - 2,500 nm), solar transmittance (T_{sol}) (280 - 2,500 nm), and corresponding transmittance modulations can be defined as following:

$$T_{lum/IR/solar} = \frac{\int \varphi_{lum/IR/solar}(\lambda) T(\lambda) d\lambda}{\int \varphi_{lum/IR/solar}(\lambda) d\lambda} \qquad (5-1)$$

$$\Delta T_{lum/IR/solar} = T_{lum/IR/solar}(< LCST) - T_{lum/IR/solar}(> LCST) \quad (5-2)$$

where $T(\lambda)$ is the transmittance of the wavelength of λ, $\varphi_{lum}(\lambda)$ the standard luminous efficiency function in the wavelength range of 380–780 nm, and $\varphi_{IR}(\lambda)$ and $\varphi_{sol}(\lambda)$ are the NIR/solar irradiance spectra for AM 1.5, respectively.

- **FT-IR spectra**

FT-IR spectra were obtained using a Bruker Vertex 70v spectrometer equipped with a diamond attenuated total reflectance (ATR) accessory.

- **NMR**

^{1}H NMR spectra were obtained using a Bruker Advanced III 500 MHz NMR spectrometer. Deuterated solvent was DMSO-d6. Chemical shifts are expressed in ppm and are referred to the residual peak of the solvent peak.

- **SEM**

SEM images were acquired using a high-resolution field emission scanning electron microscope (SEM, TESCAM MIRA3) operated at an acceleration voltage of 5 kV. The samples were sputter-coated with a thin layer of platinum to improve their conductivity and reduce charging effects. The images were acquired using the secondary electron detector and the backscattered electron detector.

- **DSC**

DSC measurements were performed using a TGA/DSC1(Mettler Toledo) under a nitrogen atmosphere. Approximately 5 mg of the sample was placed in a standard aluminium pan and heated at a rate of 10 °C/min, 0.5 °C/min from -30 °C to 50 °C, and then cooled to -30 °C, with a 50 mL/min

N_2 flow into the sample cell. An empty aluminium pan was used as a reference.

- **Dynamic Light Scattering (DLS)**

DLS measurements were performed using a BI-200SM. About 3ml of PNIPAM/PNIPAM-DMA/PNIPAM-TA was placed in a cuvette with an optical path of 10mm. The particle size was recorded using logarithmic distribution at 25 ℃, 30 ℃, 35 ℃, 40 ℃, 45 ℃ and 50 ℃, respectively.

- **Thermal Imaging Analyses**

Thermal imaging measurements were performed using a Fluke 480 Pro thermal camera equipped with a 17 μm detector and a temperature range of -40 °C to 550 °C. The camera was set to manual mode and the emissivity was set to 0.95 for all the samples. The samples were placed on a black background and allowed to reach room temperature before the measurements. The camera was positioned approximately 40cm away from the samples.

- **Fabrication of DLTRES Demo Device**

Figure 5-1 illustrates the fabrication process of the DLTRES demo device. The device was made using 5 mm-thick glass blocks and a polydimethylsiloxane (PDMS) to build chambers. After curing and demoulding the PDMS, two layers of PDMS and glass were adhered together to produce two chambers. CCH-EtOH and PNIPAM-DMA were then injected into their respective chambers.

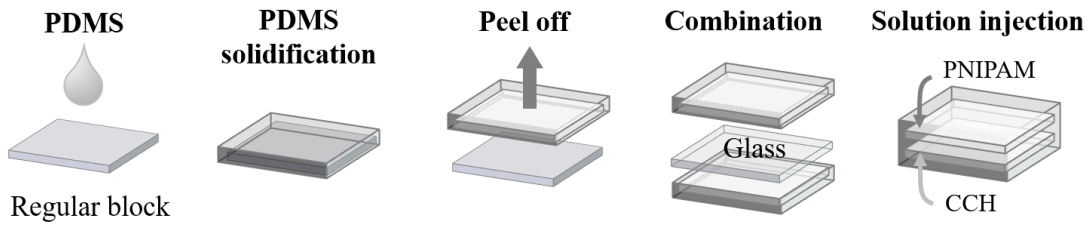


Figure 5-1 Fabrication Process of DLTRES Demo Device

- **Fabrication of Room Model**

As shown in **Figure 5-2 A**, assemble a 1cm thick acrylic glass sheet into a chamber sized at 10cm × 10cm × 20cm, incorporating internal insulation material. Cut out a 10cm x 10cm window at the top of the chamber for interaction. The glass sheet has a thickness of 2mm, and the specifications for the simulated smart window are 10cm × 10cm × 5mm, with a filling size of 8cm × 8cm × 5mm.

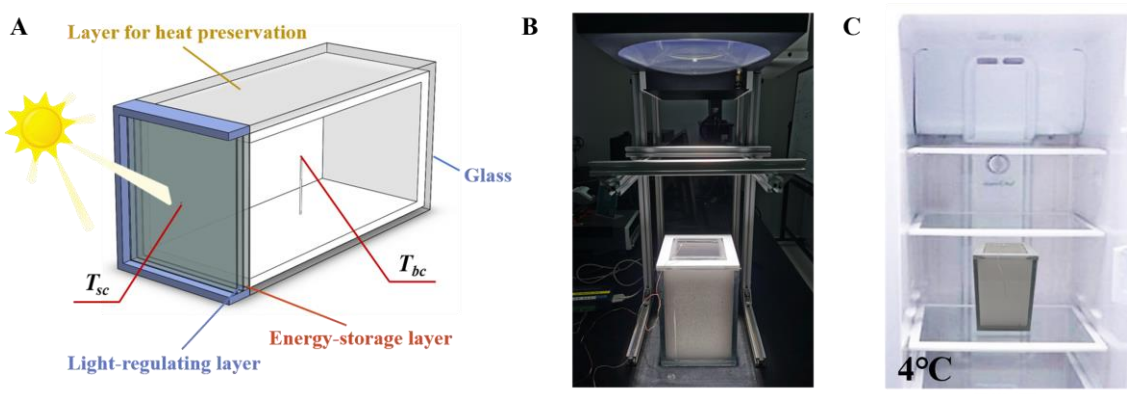


Figure 5-2 Experiments Setup

*(**A**) The scaled-down room model. Demonstration experiment under (**B**) standard solar irradiation conditions and (**C**)4 ℃ cold environment*

- **Solar Irradiation Experiment and Cold Environment Demonstration**

The room model was placed under the solar simulator (luminous intensity is 1sun) or in the 4 ℃ refrigerator for demonstration experiment, as shown in **Figure 5-2 B-C**. Employ the USB-4178 digital acquisition to record temperature data using thermocouples positioned at the centre of the chamber and the surface centre of the made smart window.

5.3 Results and Discussion

5.3.1 The Structure of DLTRES Smart Window and Working Mechanisms

Figure 5-3 A shows a smart window design with PNIPAM-DMA or PNIPAM-TA dispersed in water as the TRMs, and triggerable PCMs, CCH-EtOH or CCH-UR, as TES materials, both of which are trapped between two layers of glass to form a double-layer sandwich window structure. For a clear understanding of the regulatory mechanisms at each layer, a schematic diagram is provided to a detailed exposition (**Figure 5-3 B-C**). TRMs have the ability to adjust the scattering behaviour of solar radiation by modifying the polymer conformation. As **Figure 5-3 B** illustrates, when the ambient temperature (T_a) is below T_r, the PNIPAM chains are evenly dispersed in water in a linear coil conformation. This alignment of refractive index with the surrounding water ensures transparency, allowing sunlight to pass through windows unobstructed. This phenomenon is exemplified in the DLTRES smart window demo (20 cm x 20 cm), as shown in **Figure 5-3 B-I**. In contrast, if T_a exceeds T_r, the TRM chains transition from a coil to a globular conformation. This transition causes them to collapse into irregular microspheres, creating a significant refractive index mismatch with the water. As a result, this leads to significant light scattering, which renders the window opaque, as shown in **Figure 5-3 B-II**.

The selection of TES materials involves using triggerable PCMs with a controllable crystallization process, such as CCH-EtOH or CCH-UR. This overcomes the limitations of traditional PCMs, such as spontaneous crystallization, by maintaining a supercooled state in sub-freezing temperatures. Crystallization and heat release only occur upon external stimulation due to the energy barrier between the supercooled and crystalline states, as shown in **Figure 5-3 C**.

Triggerable PCMs have three distinct states: a transparent molten state, a supercooled state, and an opaque crystalline state. These materials can transition between these states through natural cooling, mechanical activation, and heating. During the day, the energy storage layer undergoes an endothermic phase transition from a crystalline state to a transparent liquid state, as illustrated in **Figure 5-3 C-I**. The liquid state can appear as either molten or supercooled, depending on the surrounding temperature. If the nighttime temperature falls below the T_r of the TRM, the external light modulation layer becomes transparent. At this point, activating the energy storage layer causes crystallization, as shown in **Figure 5-3 C-II**. This dual functionality enables light modulation and compensates for temperature during cold nights.

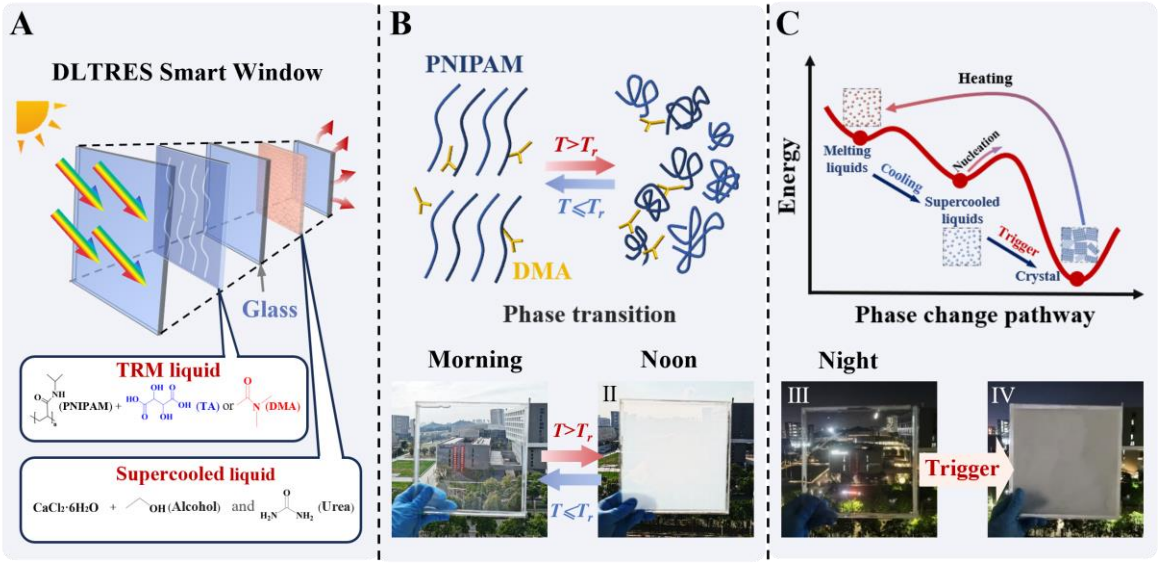


Figure 5-3 Schematic Diagram of the Structure and Principle of the DLTRES Smart Window.

(A) *Schematic diagram of DLTRES smart window.* ***(B)*** *Schematic diagram of light-regulating layer's working principles, digital photos taken in the morning (I) and at noon (II).* ***(C)*** *Schematic*

diagram of energy storage layer's working principles, digital photos taken in the supercooled liquid state (I) and crystalline state (II).

5.3.2 PNIPAM-DMA or PNIPAM-TA as TRMs

Significant changes in the LCST of TRM were observed after the introduction of DMA and TA into PNIPAM, respectively. The gradual increase of DMA in the PNIPAM-DMA composite resulted in an increase in LCST, while the addition of TA led to a decrease (**Figure 5-8**). These alterations may be due to the different ways in which these modifiers interact with PNIPAM molecular structures, which will be further discussed following.

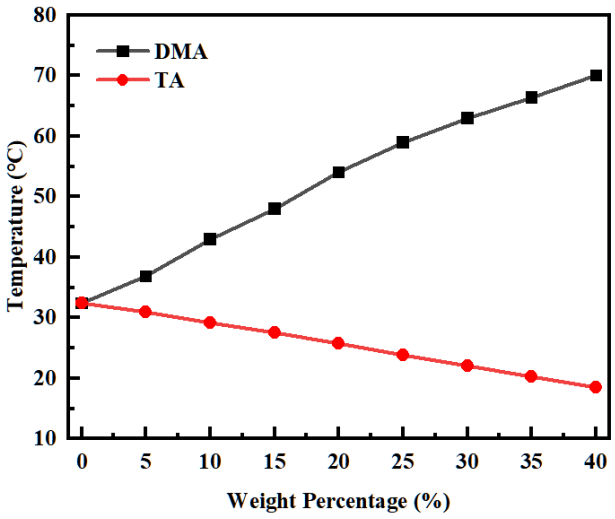


Figure 5-4 LCST Tuning by Adding DMA and TA.

The impact of introduced molecules on PNIPAM's hydrogen bonding with water is analysed through the FTIR as shown in **Figure 5-5**. The absorption peak for PNIPAM in **Figure 5-5 B** is at 1641 cm^{-1}, which can be attributed to the formation of hydrogen bonds between the C=O from PNIPAM and the OH groups from water. [286] With the introduction of DMA into the PNIPAM, there is a strengthened hydrogen bonding between PNIPAM and water, evidenced by the blue shift of the peak

from 1641 cm^{-1} to 1646 cm^{-1}, resulting in an elevation of the LCST. In addition, a new peak appears at 1677 cm^{-1}, which may attribute to the formation of hydrogen bonds between C=O from DMA and NH from PNIPAM. In contrast, the incorporation of TA weakens hydrogen bonds between the C=O from PNIPAM and the OH groups from water, as shown by the red shift of the peak from 1641 cm^{-1} to 1629 cm^{-1}, resulting in a lower LCST. This weakening may be attributed to the formation of hydrogen bonds between OH from TA and C=O from PNIPAM. These intermolecular interactions can also be reflected in DLS data, as shown in **Figure 5-6**. The PNIPAM-DMA has a larger average particle size than that of PNIPAM, while PNIPAM-TA is smaller than that of PNIPAM at 30 °C. This may be caused by stronger or weaker hydrogen bonding between PNIPAM and water, resulting in more extended or shrinkable molecular chains, respectively.

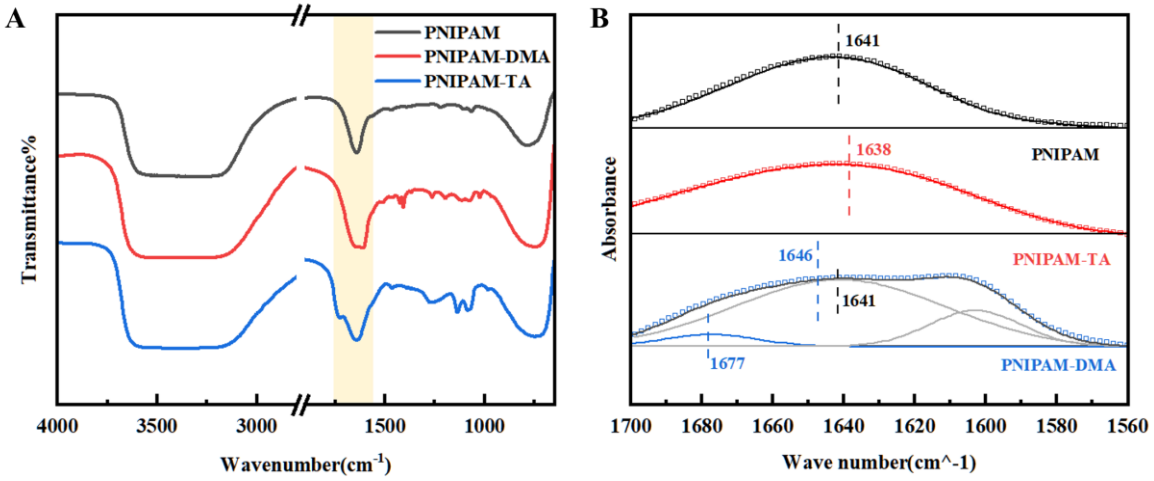


Figure 5-5 FTIR Spectra of PNIPAM, PNIPAM-DMA, and PNIPAM-TA.

Moreover, the in situ DLS analyses, as shown in **Figure 5-6**, indicate that the average diameter reduction trend observed in unmodified PNIPAM, from 500 nm to 288 nm at 30 °C, with no a similar trend in PNIPAM-DMA and PNIPAM-TA. Instead, their average diameters exhibit significant

increases. Specifically, PNIPAM-5wt%DMA (LCST=36.8℃) expands from 680 nm to 1840 nm around 40 °C, while PNIPAM-5wt%TA (LCST=30.9℃) enlarges from 300 nm to 1230 nm around 30 °C. This difference is probably due to the combination of smaller particles aided by the added organic molecules, resulting in the creation of larger aggregates. [286]

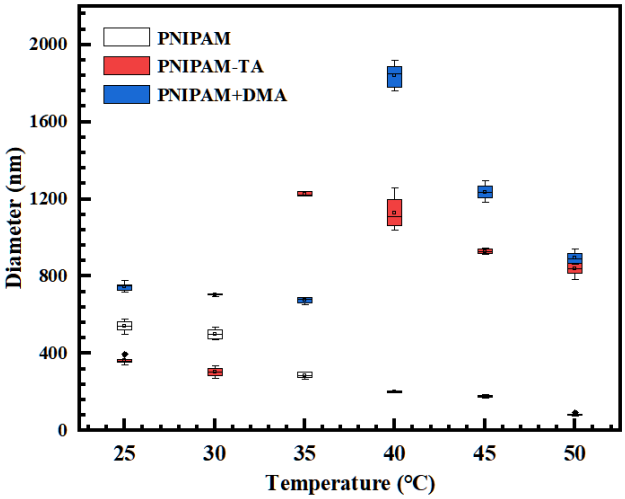


Figure 5-6 Temperature-Dependent DLS of PNIPAM particles (white boxes), PNIPAM-TA particles (blue boxes) and PNIPAM-DMA particles (red boxes).

Additionally, significant variations in the contact angle of water on silicon wafers coated with a thin layer of PNIPAM, PNIPAM-DMA, and PNIPAM-TA were measured (**Figure 5-7**). The results show that the contact angle of the unmodified PNIPAM wafer is around 8°, and that of the PNIPAM-DMA and PNIPAM-TA are 10° and 6°, respectively. The reasons for this phenomenon are that TA is an organic acid containing multiple carboxyl groups, which can form strong interactions with water molecules through hydrogen bonding. After adding TA, more polar groups were introduced to the surface of PNIPAM, thereby increasing its hydrophilicity and further reducing the contact angle to 6°. DMA is a compound containing both non-polar methyl and polar amide groups. Although the

amide groups may increase polarity to a certain extent, the methyl groups in DMA may relatively reduce the overall polarity and hydrophilicity. Consequently, the contact angle of PNIPAM-DMA is slightly higher, indicating a lower hydrophilicity. This suggests that the introduction of methyl groups by DMA increases the hydrophobic portions of the surface, which counteracts the increase in hydrophilicity.

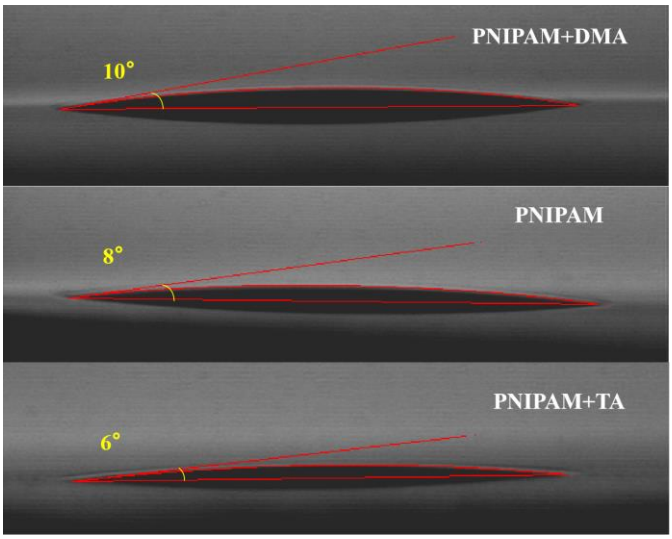


Figure 5-7 Contact Angles of PNIPAM, PNIPAM-TA, PNIPAM-DMA at Room Temperature

To evaluate the sensible heat storage capabilities of TRMs, a comparative analysis of their specific heat capacity against that of DI water were conducted, as illustrated in **Figure 5-8**. The specific heat capacities of PNIPAM-DMA and PNIPAM-TA is approximately at 4.1 kJ/kg·K, slightly lower than that of DI water at 4.2 kJ/kg·K, yet significantly surpassing many conventional materials utilized in sensible TES materials [287,288]. This indicates that these TRMs possess a high energy storage density of up to 246 kJ/kg within the temperature range of 10 °C to 70 °C, demonstrating substantial thermal buffering capabilities. Consequently, TRMs can effectively enhance the regulation of indoor

temperature fluctuations caused by solar energy during the day, positioning themselves as a highly efficient medium for sensible heat storage.

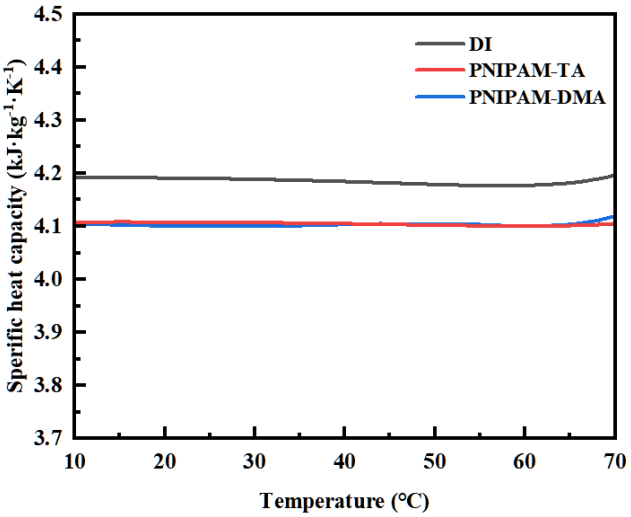


Figure 5-8 Specific Heat Capacity Curve for DI, PNIPAM-DMA, PNIPAM-TA with Respect to the Temperature.

The cyclic stability of TRMs was tested to assess its impact on the lifespan of DLTRES smart windows. As illustrated in **Figure 5-9**, the transmittance of PNIPAM-DMA at 25 °C and 50 °C remained nearly constant after 100 cycles, showing an excellent ΔT_{lum} consistency (from 91% to 90.14%). This finding underscores the exceptional cyclic stability and potential longevity of the TRMs used in DLTRES smart windows.

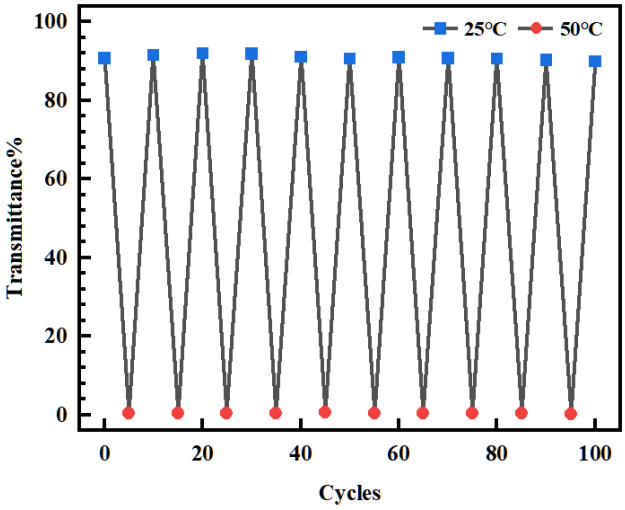


Figure 5-9 Cycling Tests Curve of PNIPAM-DMA at the Wavelength of 532 nm.

5.3.3 CCH-EtOH and CCH-UR as Energy-Storage Layer Materials

CCH may crystallize below 6.2 °C, as shown in **Figure 5-10 A**, which restricts its supercooling stability at lower temperatures. To address this issue, CCH-EtOH was developed by adding 0.5 wt.% ethanol into CCH. This modification results in higher stability when in a prolonged supercooled state. As seen in **Figure 5-10 B**, supercooled CCH-EtOH is a colourless, transparent liquid, which turns into a white, opaque solid upon crystallization. Notably, as shown in **Figure 5-10 C**, supercooled CCH-EtOH samples demonstrate extremely high T_{lum} at different thicknesses (1mm, 5mm, and 10mm) with values of 93.9%, 92.6%, and 91.5%. Conversely, the crystalline state of CCH-EtOH experiences a pronounced reduction in T_{lum} under the same conditions, particularly beyond 5mm, approaching nearly zero. The process of heat absorption of CCH-EtOH from its crystalline to liquid state was recording using DSC. Its T_m was 31 °C, with an enthalpy of fusion of 199 kJ/kg, as shown in **Figure 5-10 D**. Besides the stored latent heat, it has a high sensible heat of 126 kJ/kg over the

temperature range of 10-70 °C. Hence, the total enthalpy value can be reach to 325 kJ/kg in this temperature range (**Figure 5-10 E**). It is important to note that CCH-EtOH does not crystallise during cooling, whereas pure CCH crystallises at around 6.2 °C. During the second DSC cycle, the supercooled phase of CCH-EtOH persists without showing any crystallisation peaks, even at an extremely slow scanning rate of 0.5 $K \cdot min^{-1}$, as seen in **Figure 5-10 F**.

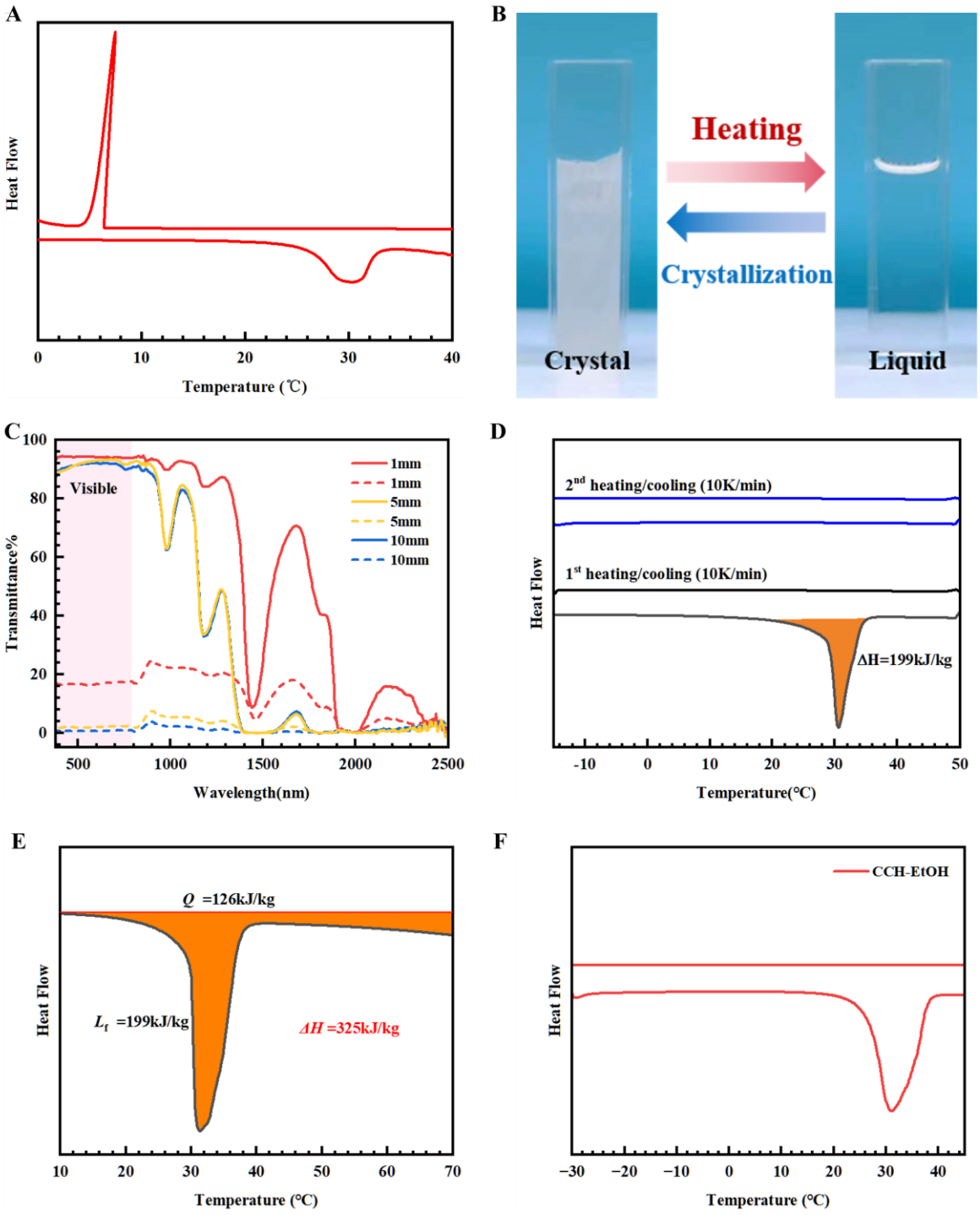


Figure 5-10 Properties of Energy Storage Materials.

(A) DSC trace of CCH recorded at a heating/cooling rate of 5 K/min. (B) Photographs of the crystalline and supercooled CCH-EtOH. (C) Transmittance spectra for 1mm, 5 mm, and 10 mm in

supercooled liquids (solid line) and crystallized state (dashed line), respectively. ***(D)*** *DSC traces for two cycles of CCH-EtOH with a heating and cooling rate of 10 K/min.* ***(E)*** *The stored sensible and latent heat in the temperature range of 10 ℃-70 ℃.* ***(F)*** *DSC trace of CCH-EtOH recorded at a heating/cooling rate of 0.5 K/min.*

To further understand the mechanism of the formation of a stable supercooled state in CCH-EtOH, the chemical characteristics between its crystalline and amorphous states were analysed using FTIR and NMR techniques (**Figure 5-11** and **Figure 5-12**). The supercooled CCH-EtOH exhibits a noticeable redshift and broadening of the OH stretching vibration peak at 3300 cm^{-1} compared to the crystalline state. Simultaneously, the OH bending vibration at 1600 cm^{-1} experiences a significant blueshift in the supercooled state. These observations collectively indicate the presence of hydrogen bonding between EtOH and CCH, contributing to the stabilization of the supercooled state of CCH-EtOH. The NMR peak shifts confirm the hydrogen bonding interactions between CCH and EtOH again.

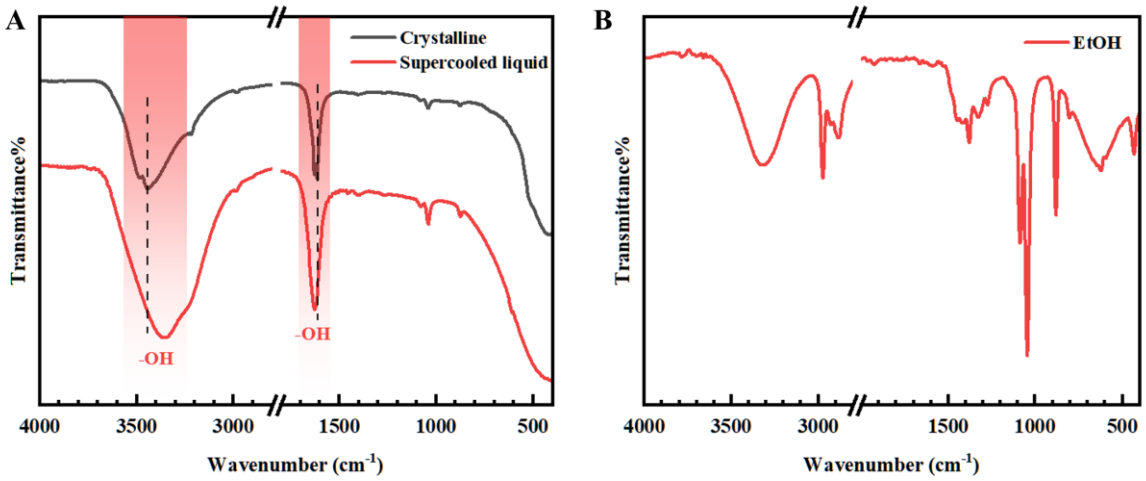


Figure 5-11 FTIR Spectra for CCH-EtOH.

*FTIR spectra of (**A**) Crystalline CCH-EtOH (black line) and Supercooled CCH-EtOH (red line), and (**B**) EtOH at ambient temperature*

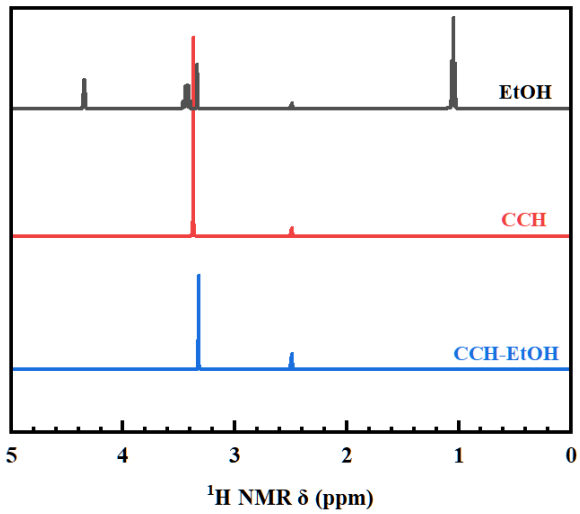


Figure 5-12 Experimental ^{1}H NMR Spectra of CCH, EtOH, and CCH-EtOH (d6-DMSO, 400 MHz).

Furthermore, in varying geographical and climatic conditions, a single-phase change temperature may not suffice for all regions. As shown in **Figure 5-4**, TRMs with a LCST that can be adjusted between 18.5 °C and 70 °C have been developed. To accommodate these temperature fluctuations and enable rapid energy charging, further adjustment of the T_m of the triggerable PCMs is necessary. To achieve this, the T_m of the TES material has been precisely tuned. A series of CCH-UR with continuously adjustable phase change temperatures between 9 to 31 °C was prepared by adding varying proportions of urea to CCH, as shown in **Figure 5-13**.

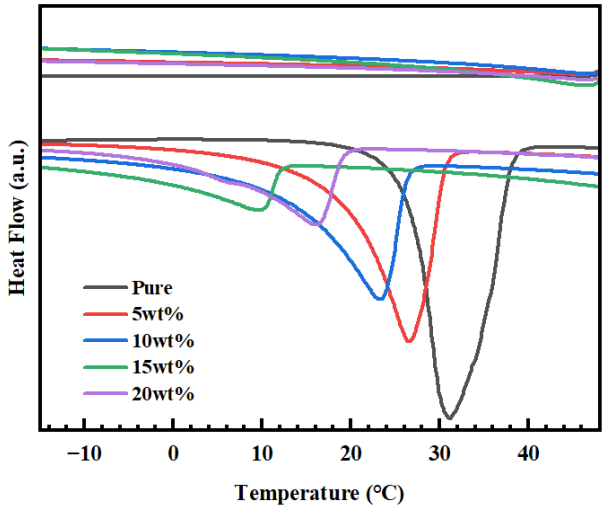


Figure 5-13 DSC Trace of CCH-UR Recorded at a Heating/Cooling Rate of 5 K/min

FTIR analysis indicates the presence of N-H···O-H hydrogen bonds between urea and CCH, as shown in **Figure 5-14.** However, the hydrogen bond energy in this interaction is weaker than that in O-H···O-H bonds found exclusively in CCH [289]. This leads to a slight reduction in its T_m and enthalpy.

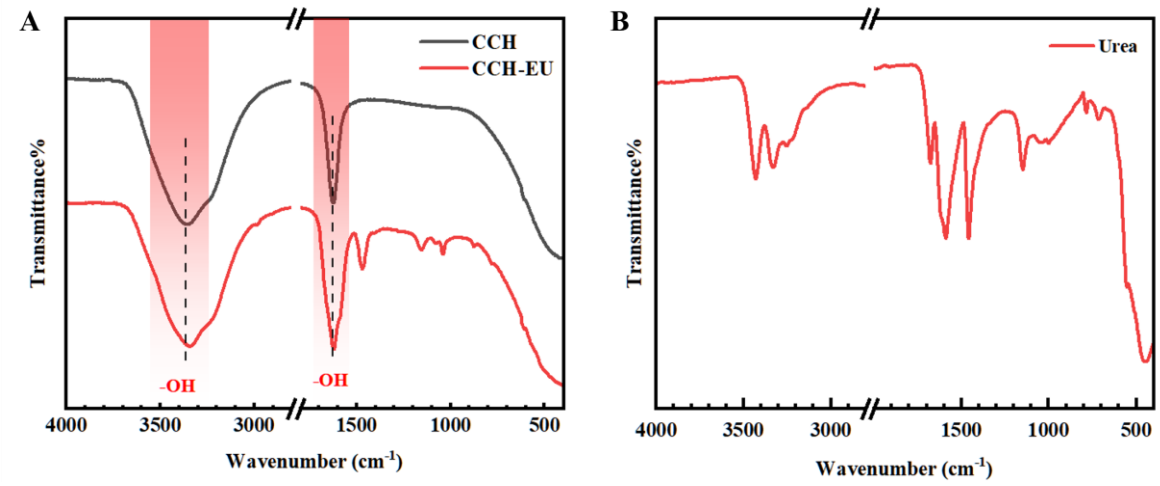


Figure 5-14 FTIR for CCH-UR

*FTIR spectra of (**A**) Crystalline CCH-UR (black line) and Supercooled CCH-UR (red line), and (**B**) UR at ambient temperature.*

5.3.4 Thermal and Mechanical Responsive Properties of DLTRES Device

The optical behaviour of PNIPAM-DMA (0.5wt%) at thicknesses of 1mm, 5mm, and 10mm was thoroughly measured using UV-VIS-NIR spectroscopy, which spanned a wavelength range of 280-2500nm at temperatures of 25 °C and 50 °C. The T_{lum}, IR transmittance (T_{IR}), luminous transmittance difference (ΔT_{lum}), IR transmittance difference (ΔT_{IR}), and ΔT_{sol} were plotted in **Figure 5-15 A-B**.

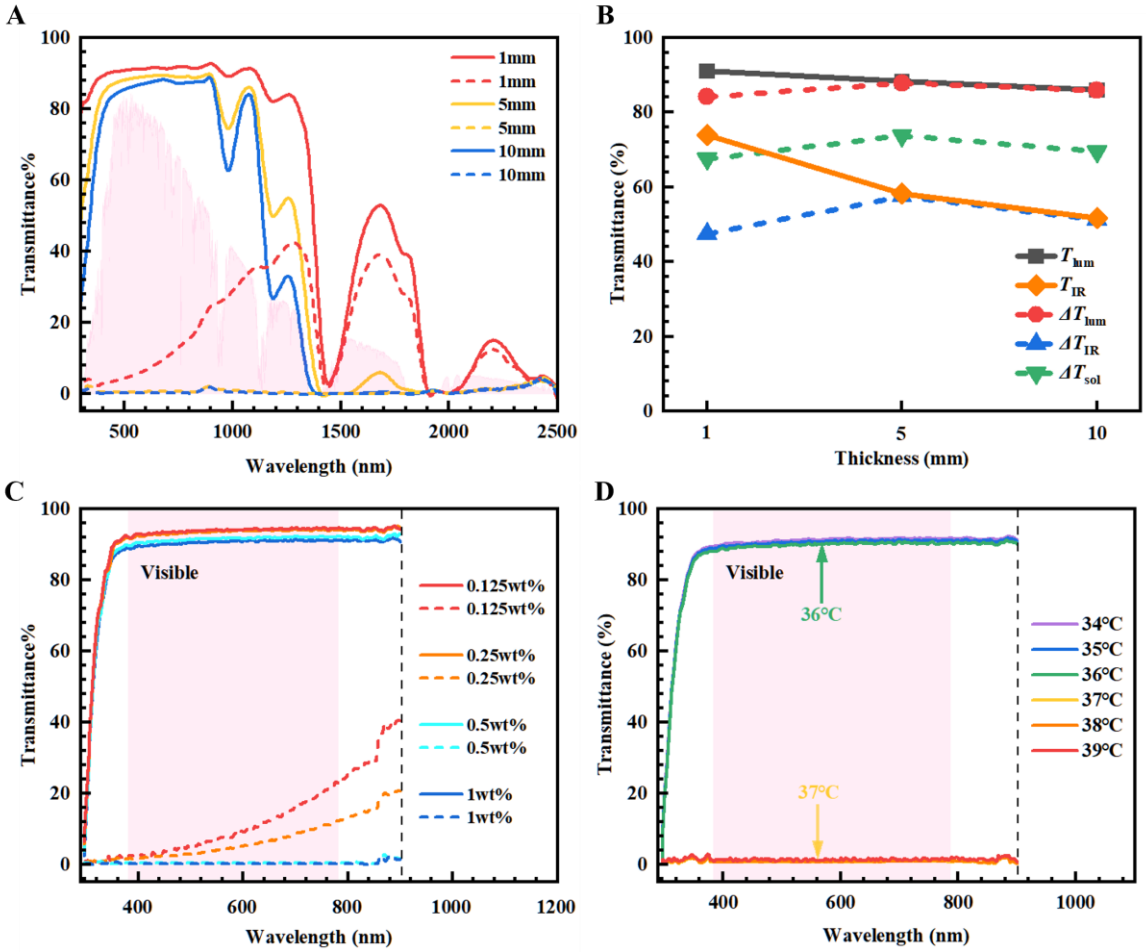


Figure 5-15 Optical Properties of PNIPAM-DMA

(A) *Transmittance spectra for 1mm, 5 mm, and 10 mm at 20℃ (solid line) and 50℃ (dashed line), respectively.* ***(B)*** *The optical performance comparison on the T_{lum}, T_{IR}, ΔT_{lum}, ΔT_{sol}, ΔT_{IR} for the 1mm, 5mm and 10mm of PNIPAM-DMA.* ***(C)*** *Transmittance spectra for PNIPAM-DMA with different concentrations at 25 °C (solid line) and 50 °C (dashed line). (path length of 10mm).* ***(D)***

Transmittance spectra for 0.5wt% PNIPAM-DMA with different temperature. (path length of 10mm).

At 25 °C, PNIPAM-DMA demonstrated high T_{lum} across 380-780nm, with the 1mm, 5mm, and 10mm thickness samples achieving 91.2%, 90.7%, and 89.6% transmittance, respectively. Notably, in the near-infrared spectrum, four prominent absorption peaks at 980 nm, 1190 nm, 1440 nm, and 2000 nm were identified. These peaks correlate with the absorption characteristics of OH groups, significantly reducing the T_{IR} in the 780-2500 nm range to 73.8%, 58.2%, and 51.6% for each respective thickness. Particularly for the 5mm and 10mm thickness samples, transmittance beyond 1400 nm was negligible, indicating that PNIPAM-DMA of more than 5mm thickness can effectively absorb infrared wavelengths. Above 37 °C, a phase transition in PNIPAM-DMA, characterized by a coil-globular transformation, markedly reduced its transmittance. With increasing thickness, both ΔT_{lum} and ΔT_{sol} exhibit larger values, Specifically, for the 1mm, 5mm, and 10mm samples, the transmittance difference becomes 84.0%, 89.3%, 89.2% for ΔT_{lum}, and 67.5%, 73.7%, 69.5% for ΔT_{sol}. In addition, a series analysis was conducted to assess the influence of concentration variations and temperature fluctuations on transmittance properties. As expected, transmittance modulation progressively increased with concentration from 0.125wt% to 1wt%, with peak modulation observed at a 0.5wt% concentration (**Figure 5-15 C**). Moreover, PNIPAM-DMA exhibited a distinct step response to temperature changes around 36 °C, showcasing its precision in temperature regulation (**Figure 5-15 D**).

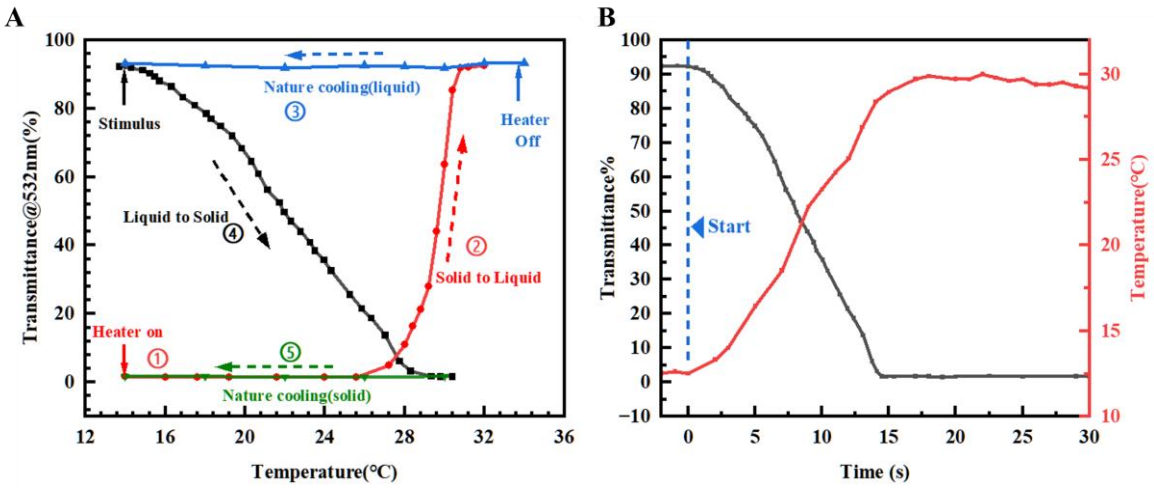


Figure 5-16 In-Situ Optical Properties of CCH-EtOH.

(A) *The temperature-transmittance relationship of the device was investigated throughout the one-cycle.* ***(B)*** *Real-time measurement and calculation of temperature and transmission change during the exothermic phase change of CCH-EtOH crystallization.*

Meanwhile, the transmittance and temperature variations of CCH-EtOH with thickness 5mm during the cycling process were also investigated using UV-Vis at a wavelength of 532nm. As shown in **Figure 5-16 A**, five stages of the cycling process can be observed. In the initial stage (see ①), the crystalline CCH-EtOH absorbed heat, with the temperature rising from 14 ℃ to 24 ℃, and the transmittance was about 1.6%. Subsequently, in process ②, CCH-EtOH transitioned from solid to liquid, with a slight temperature increase from 24 ℃ to 30.5 ℃ and a significant increase in transmittance to 92%. Then, in the third stage (③), upon cooling to 14 °C, the melting CCH-EtOH tended to form a supercooled liquid rather than directly crystallizing. In the fourth stage (④), CCH-EtOH rapidly crystallized under external stimulation, with the temperature rising to 29.3 °C and the

transmittance sharply decreasing to 2%. Finally, in process ⑤, the temperature of CCH-EtOH returned to 14 °C, with the transmittance remaining unchanged. Furthermore, to investigate the light modulation response time and temperature elevation performance of supercooled CCH-EtOH under mechanical stimulation, time-dependent in-situ UV-VIS, as shown in **Figure 5-16 B,** was utilized to present the heat releasing process of crystallization. Under mechanical stimulation, the 5mm thick supercooled CCH-EtOH rapidly crystallized. Within 15s, its transmittance at a wavelength of 532nm dropped from 92% to 2%, accompanied by the rapid release of latent heat, with the temperature simultaneously rising from 14 °C to about 29.3 °C.

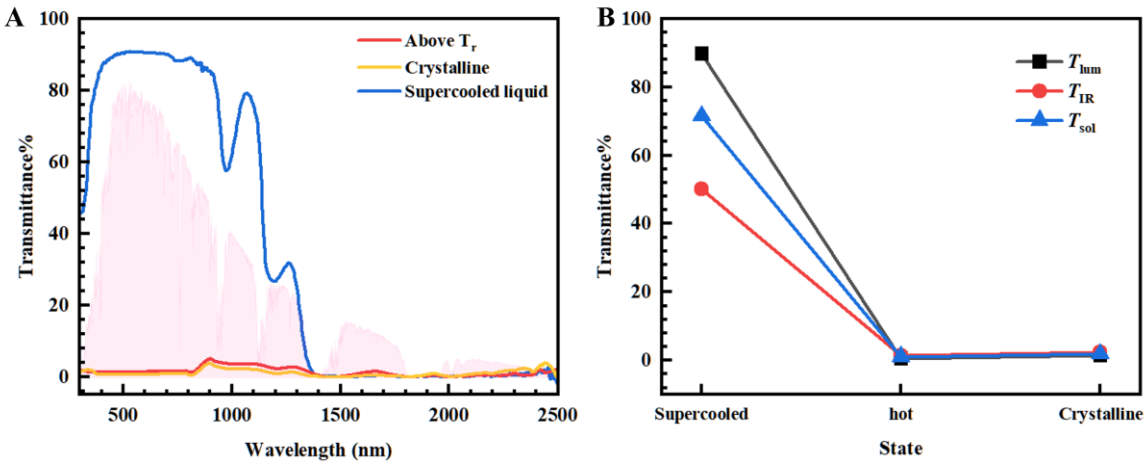


Figure 5-17 Overall Optical Properties.

(A) *Transmittance spectra of PNIPAM-DMA/CCH-EtOH in the supercooled state, high-temperature state, and crystalline state, respectively.* ***(B)*** *The optical performance comparison on the* T_{lum}, T_{IR}, T_{sol} *for the PNIPAM-DMA/CCH-EtOH.*

Given dual-layer structure of the DLTRES smart window, it is more practical to study the overall optical properties of bilayers. The detailed optical properties of the dual-layer configuration,

PNIPAM-DMA/CCH-EtOH (5mm thickness for each layer), are illustrated in **Figure 5-17 A**. These results demonstrate that PNIPAM-DMA/CCH-EtOH maintains a high T_{lum} of 89.8% at low temperature **(Figure 5-17 B)**, with its infrared transmission being nearly identical to that of PNIPAM-DMA with a 5mm thickness (**Figure 5-15A**). Notably, under high-temperature conditions, T_{lum} and T_{IR} experience a significant decrease to 0.6% and 1.5%, respectively, leading to a marked enhancement in the ΔT_{sol}, increasing up to 70.1%. Moreover, when crystallization of PNIPAM-DMA/CCH-EtOH is triggered at low temperatures, its ΔT_{sol} soars to 69.6%.

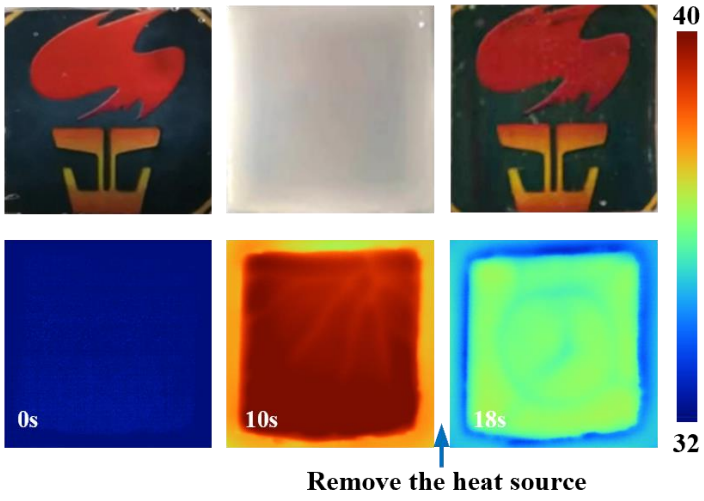


Figure 5-18 Digital and IR Camera Images of PNIPAM-DMA of Heating and Cooling Processes.

To visualize this modulation process, digital and infrared camera footage (as seen in **Figure 5-18**) captured the DLTRES device's rapid response to temperature changes, showing it can quickly shift from transparent to opaque in just 10 s under around 50 °C heater, and then rapidly revert to transparency in 8 s when the heat source is removed. Additionally, the rapid process of latent heat release was also recorded (**Figure 5-19**). This local crystallization occurs within 1 s after the

needlepoint stimulation, followed by a widespread crystallization that diffuses in a ring-like pattern from the initial point of mechanical stimulation. The temperature reaches its peak of 29.3 °C within 15s, consistent with the research results presented in **Figure 5-16 B**. This thorough analysis underscores the significant potential of PNIPAM-DMA/CCH-EtOH in smart window technologies, showcasing its outstanding T_{lum}, ΔT_{sol}, and its swift response to both thermal and mechanical stimuli.

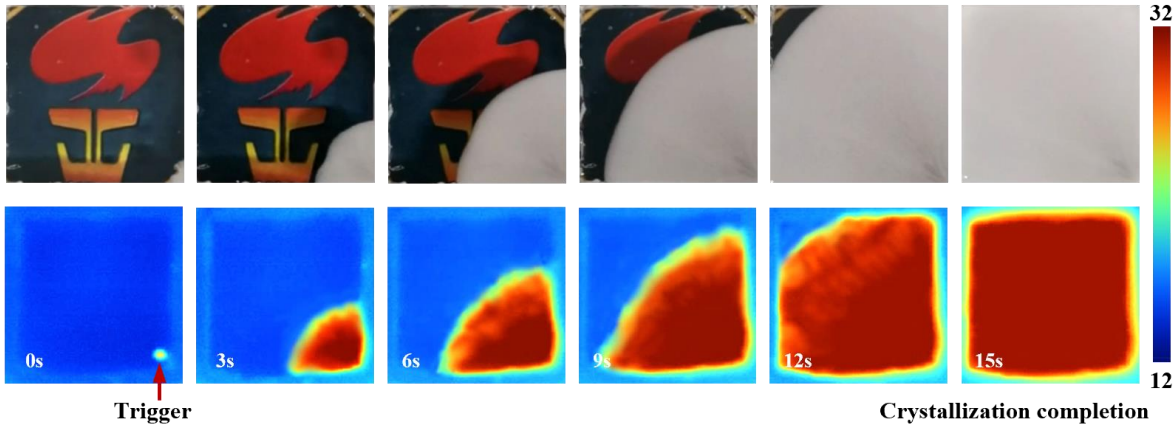


Figure 5-19 Digital and IR Camera Images of the CCH-EtOH Crystal Growth after Mechanical Stimulation.

5.3.5 Energy-Saving Demonstration

Cyclic schematic diagram of DLTRES smart window is illustrated in **Figure 5-20 A**. In the cooler periods of the early morning and evening, common T_a are below the T_r of the light-regulating layer. This condition allows light to permeate the window, effectively keeping the room illuminated. Upon T_a exceeding the T_r, most prominently during midday, the TRM undergoes a swift coil-globule transition. This alters the window's transparency to an opaque state, thereby impeding most incoming light. Concurrently, supplemental heat energy is captured in the energy storage layer,

stored either as sensible heat or latent heat, augmenting the barrier to heat penetration into the room. As nighttime T_a recede below the T_r, the smart window concurrently reverts to a highly transparent state. During this stage, the supercooled liquid undergoes a phase transition under external stimuli, shifting from a transparent supercooled state to an opaque crystalline state, achieving the desired night-time light obstruction. Importantly, the heat released during the crystallization procedure provides thermal compensation to the indoor space, thereby enhancing overall thermal comfort levels. In the next morning, as T_a rise, the energy storage layer progressively uptakes heat and regains transparency. To avoid the issue of inadequate melting of the storage layer due to low T_a in the morning, a dual-layer sliding window structure was designed, which are shown in **Figure 5-20 B**. Overall, this window exemplifies the synergistic advantages of dual-layer materials, offering an innovative, highly customizable, and environmentally friendly solution.

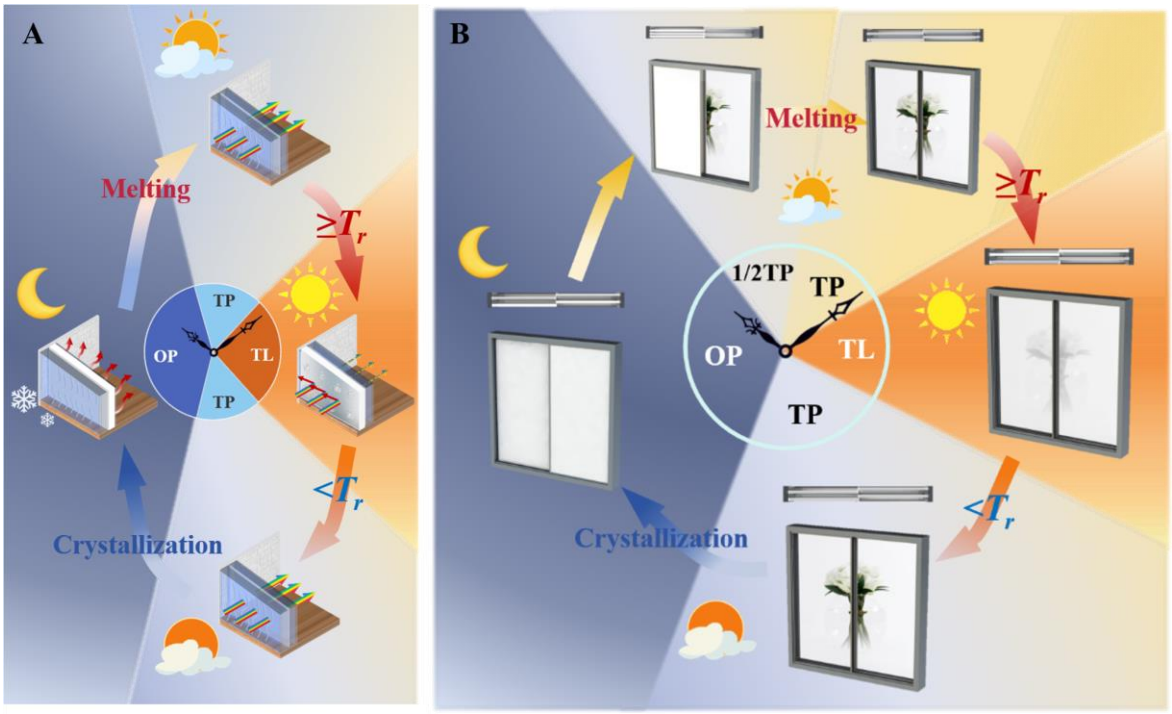


Figure 5-20 Cyclic Diagram of the DLTRES Smart Window

In order to establish the practical application benefits of DLTRES smart windows, a scaled-down room model was assembled, allowing for performance evaluation of smart windows under conditions better mimicking in-situ scenarios. This distinct room model, a rectangular chamber of dimensions 10 cm × 10 cm × 20 cm, as illustrated in **Figure 5-2 A**, incorporated a 10 cm × 10 cm prototype of the dual-layer smart window, with specific details in the sub-section 4.2.1. To precisely assess the modulating effect of the light-regulating layer, a systematic analysis of the impact of three different materials, air, PNIPAM, and PNIPAM-DMA, each with a thickness of 5 mm, serve as the TRMs and a 5 mm thick CCH-EtOH supercooled liquid as the inner layer material was equipped for all samples to minimize interference from the energy storage layer, termed as Air/CCH-EtOH, PNIPAM/CCH-EtOH, and PNIPAM-DMA/CCH-EtOH, respectively.

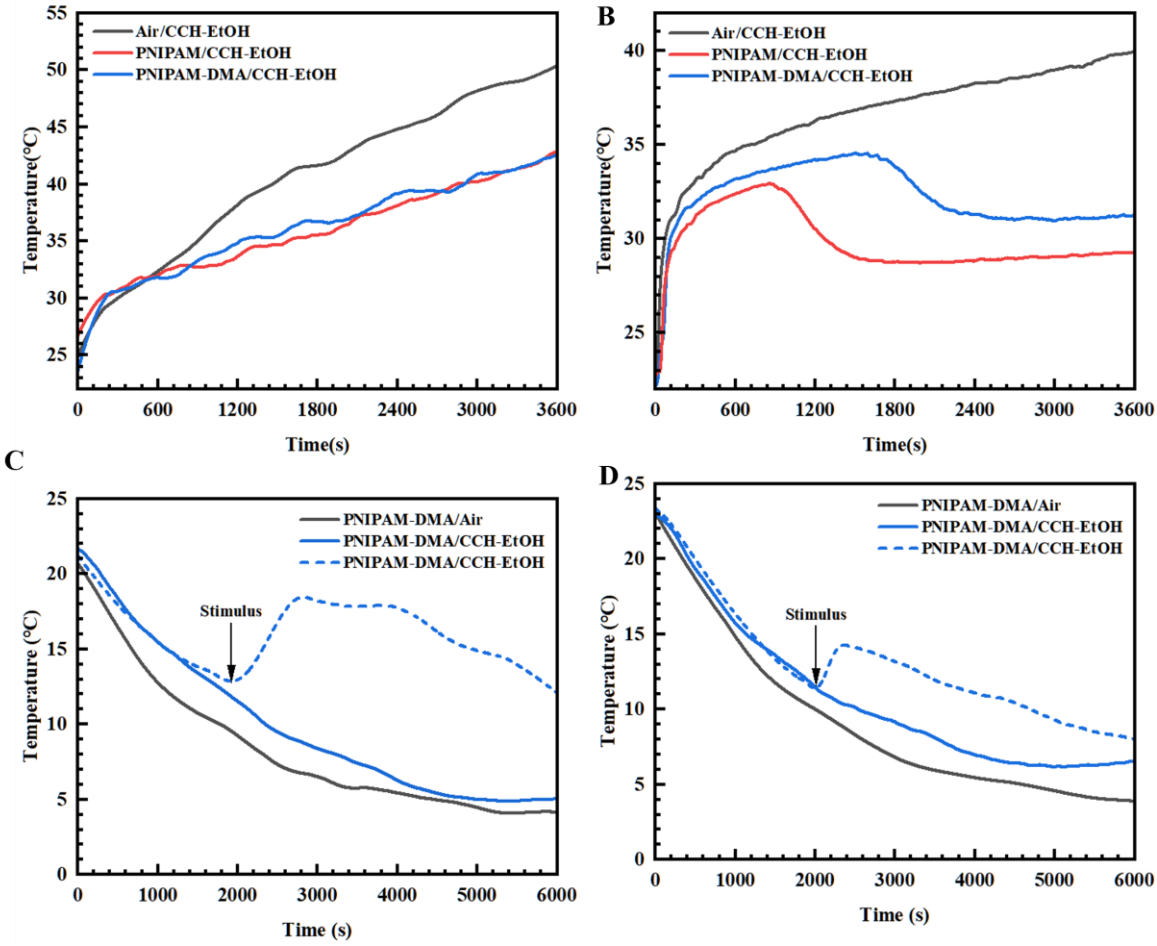


Figure 5-21 Energy-Saving Demonstration of DLTRES Smart Window.

(A) *Temperature at the centre of the model's external window surface (T_{sc}) with respect to the lighting time for the Air/CCH-EtOH (black line), PNIPAM/CCH-EtOH (red line) and PNIPAM-DMA/CCH-EtOH (blue line), respective.* ***(B)*** *Temperature at the core temperature inside the chamber (T_{bc}) with respect to the lighting time for the Air/CCH-EtOH (black line), PNIPAM/CCH-EtOH (red line) and PNIPAM-DMA/CCH-EtOH (blue line), respectively.* ***(C)*** *Temperature at the centre of the model's external window surface (T_{sc}) with respect to the cooling time for the PNIPAM-DMA/Air (black line), uncrystallized PNIPAM-DMA/CCH-EtOH (blue line) and PNIPAM-DMA/CCH-EtOH (Trigger crystallization) (dashed line), respectively.* ***(D)*** *Temperature at the core temperature inside the*

chamber (T_{bc}) with respect to the cooling time for the PNIPAM-DMA/Air, uncrystallized PNIPAM-DMA/CCH-EtOH (blue line) and PNIPAM-DMA/CCH-EtOH (Trigger crystallization) (dashed line), respectively

Under standard solar irradiation conditions, the temperature variations over time were recorded by monitoring the temperature at the centre of the model's external window surface (T_{sc}) and the core temperature inside the chamber (T_{bc}), as shown in **Figure 5-21 A-B**, and the experimental setup diagram is shown in **Figure 5-2 B**. Experimental results indicated a gradual increase in T_{sc} with prolonged irradiation. Initially, the T_{sc} trends for all test groups were similar, but after 600 s of continuous solar irradiation, the Air/CCH-EtOH displayed a significant rise in T_{sc} compared to the PNIPAM/CCH-EtOH and PNIPAM-DMA/CCH-EtOH, which showed nearly identical temperature trends. After one hour of irradiation, the T_{sc} for the Air/CCH-EtOH reached 50 °C, while it remained around 43 °C for both the PNIPAM/CCH-EtOH and PNIPAM-DMA/CCH-EtOH, a difference mainly attributed to the varying heat capacities of different TRMs. In contrast, the T_{bc} trends for the PNIPAM/CCH-EtOH and PNIPAM-DMA/CCH-EtOH diverged over the process of irradiation. As **Figure 5-21 B** illustrates, both groups first experienced a rise in temperature, followed by a cooling turning point — occurring at 32.4 °C and 34.8 °C, respectively, consistent with their T_r — and then gradually decreased and stabilized at 28.7 °C and 31.1 °C. Conversely, the T_{bc} of the Air/CCH-EtOH shows no evident downward trend; instead, it consistently increases with increasing illumination time, rising from 22 °C to 40 °C within 3600 s These results strongly highlight the effectiveness of

incorporating a light-regulating layer in reducing indoor temperatures, thus emphasizing the utility of such layers in managing indoor thermal conditions.

In the context of assessing the dynamics of thermal energy release and the efficacy of room temperature modulation by indoor energy storage layers in low-temperature environments, a specialized experimental apparatus was developed. This apparatus featured two types of dual-layered windows: one with an exterior layer of PNIPAM-DMA and an interior air layer, and another with an interior CCH-EtOH layer, referred to as PNIPAM-DMA/Air and PNIPAM-DMA/CCH-EtOH, respectively. The experimental protocol entailed transitioning these windows from a normothermic setting to a 4 °C environment, ,as shown in **Figure 5-21 C**, and monitoring the T_{sc} and T_{bc}, as shown in **Figure 5-21 C-D**. Experimental observations indicated that, subsequent to the initiation of crystallization, the PNIPAM-DMA/CCH-EtOH demonstrated a notable temperature escalation, with T_{sc} surging from 12.9 °C to 18.5 °C and T_{bc} elevating from 11.4 °C to 14.2 °C. Crucially, after a duration of 6000 s, this setup sustained T_{sc} and T_{bc} at 12.2 °C and 8.1 °C respectively. In stark contrast, the temperatures in both the uncrystallized PNIPAM-DMA/CCH-EtOH and PNIPAM-DMA/Air configurations declined, converging towards the 4 °C ambient baseline post 6000s (with the former registering T_{sc} at 5.1 °C and T_{bc} at 6.4 °C, and the latter displaying congruent T_{sc} and T_{bc} values at 4 °C). This juxtaposition distinctly highlights the enhanced thermal regulatory and compensatory capabilities of the energy storage layer in colder environments. Moreover, the experimental design factored in a window-to-floor area ratio of 1:3, emulating a typical residential setting. Thus, it can

be inferred that the heat emanating from the window's inner layer is instrumental in augmentatively modulating indoor temperatures, a critical aspect in the thermal management of living spaces within colder climatic zones.

5.4 Conclusions

In this chapter, an innovative dual-layer thermo-responsive energy-storage smart window was developed. The main conclusions are summarized as follow:

- An innovative dual-layer thermo-responsive energy-storage smart window (DLTRES smart window) was developed, coalescing a tuneable T_r thermochromic light-regulation layer and a temperature-matched energy storage layer, which realize daytime temperature-dependent light transmittance tuning and nighttime indoor temperature compensation and light blocking. DMA and TA -modified PNIPAM were utilized as TRM sandwiched in light-regulation layer, which can exhibit distinctive LCSTs range from 10 to 70 °C, allowing precise control of light transmittance based on specific temperature requirements, facilitating highly customized indoor space temperature, and offering broader adaptability to various geographic temperature and climate conditions.

- The filling material for the energy storage layer is based on CCH-EtOH and CCH-UR. The charging temperature of these materials matches with the T_r of the light regulation layer, ranging from 10 to 30 °C, and its dense hydrogen bond network effectively inhibits crystal formation upon cooling. Unlike traditional PCMs that crystallize and lose transparency below their

freezing point, CCH-EtOH and CCH-UR can maintain a transparent supercooled state in sub-freezing temperatures, ensuring energy storage efficiency without affecting light transmittance, which is very critical for windows. Furthermore, this energy storage layer can serve as a 'thermal buffer', regulating heat absorption and release with environmental changes through sensible heat fluctuation, and more importantly can act as a 'thermal reservoir', transferring excess daytime heat to nighttime use by triggering the release of latent heat from the supercooled liquid, thereby reducing reliance on conventional heating and cooling systems and enhancing energy efficiency. Additionally, the trigger ability of the energy storage layer endows the window with interactive response features, autonomously adapting to environmental changes or pre-set conditions, such as blocking light at night to improve privacy and sleep quality.

- The fabricated DLTRES smart window demonstrates superior performance, with a T_{lum} of 91%, ΔT_{sol} of 67.5% and $\Delta T_{lum,\ trig}$ of 88.4% offer substantial improvements in energy efficiency. In terms of TES, the system exhibits distinct characteristics within the temperature range of 10-70 °C. Through TRM, it can store sensible heat at a rate of 246 kJ/kg. Additionally, through TES, a combination of latent and sensible heat storage is achieved, resulting in an energy storage capacity of 325 kJ/kg. In terms of per unit illuminated area, compared to thermal-responsive liquids, this system is capable of providing more than twice the energy storage capacity. Furthermore, simulations of the prototype of the DLTRES smart window in both hot

and cold environments have demonstrated its significant positive impact on indoor temperature regulation. Overall, this DLTRES smart window represents a significant advancement in building technology, offering highly customizable, energy-efficient, and eco-friendly solutions to address challenges in comfort and sustainability for modern architecture.

Chapter 6 Conclusions

This chapter summarizes the main conclusions of the previous chapters and makes recommendations for future work.

6.1 Summary of the Main Conclusions

This work focuses on the development, characterization, and application of long-term triggerable phase change material technologies. It presents innovative work in the synthesis and microscopic mechanism elucidation of triggerable phase change materials within supercooled liquid and glassy systems. The main objectives were to address: 1) the current challenge of balancing triggerability and stability in supercooled liquids; and 2) the complexity and high costs associated with the synthesis of glassy state materials. Additionally, this study has identified new applications for triggerable phase change materials in the domain of smart windows, contributing to the development of energy-efficient building structures. The main conclusions are presented below:

- The first part is concerned with the development of a long-term mechanically triggerable supercooled material named MME, prepared using manganese (II) chloride ($MnCl_2$), methylurea, and erythritol as raw materials. The MME was fabricated through the synergistic effect of coordination bonds and hydrogen bonds, forming a supercooled liquid with a core-shell structure at the molecular level. The material comprises of two components: (i) A metal-organic glass formed by the reaction of $MnCl_2$ and methylurea, giving the 'core' of MME. The core is characterized by an elongated octahedral coordination geometry that significantly enhances material stability; (ii) A 'shell' structure composed of erythritol molecules, where

moderate hydrogen bonding between molecules provides the triggerable functions. Advanced techniques, including XRD, EXAFS, XANES, UV-Vis, FTIR, NMR, TEM, and DSC, were used to investigate the interactions between the 'core' and the 'shell'. The reversible process between the supercooled and crystalline states depends on a precise ligand exchange reaction between erythritol molecules and Cl^- ions in the MME 'core'. By adjusting the number of erythritol molecules in the 'shell' layer, a predictive control was achieved over the material properties to meet different storage duration requirements. Additionally, the triggerability and stability of MME were analysed quantitatively. It was found that at 30 °C, the nucleation energy barrier reached 10^{-19} J, with the required shear stress for triggering being less than 10 Pa. The maximum heat release of the MME was found to be ~215 kJ/kg, with a storage time of over three months. Thermal cycling experiments demonstrated a high stability of the MME material with an enthalpy loss of less than 15% after 1000 cycles.

- The second part of this work is on the development of a new glassy PCMs, named G-DMI, prepared using small organic molecules, d-mannitol and myo-inositol as the raw materials. The G-DMI is cost-effective, easy to prepare and scale-up, eco-friendly, and non-flammable, with a significant enthalpy of cold crystallization. The DMI, the crystalline state of G-DMI, has charging temperature of approximately 160 °C, with a very high latent heat as high as 280 kJ/kg and a rational glass transition temperature of 22 °C. Experiments showed that the DMI could maintain its glassy state for over a year at the room temperature, and the thermal triggering enabled the rapid release of nearly 180 kJ/kg of heat at around 60 °C. Various tools, including

FTIR, NMR, in-situ XRD, TEM, and DSC were used to characterise the hydrogen bonding and cold crystallization dynamics. In addition, this part of work also involved the incorporation of iron oxide nanoparticles into DMI, leading to the so-called in Solar DMI, a volumetric solar absorber that could absorb more than 95% of solar radiation and effectively discharge the stored heat, demonstrating the potential of the material in solar-thermal applications.

- The third part of the work is on a new type of dual-layer thermosensitive energy storage smart window enabled by combining the transparent properties of triggerable PCMs with thermochromic smart window technology. Such a smart window could dynamically regulate light transmittance based on daytime temperature. Additionally, it can heat the indoor space on cold nights by triggering crystallization to improve thermal comfort, while also providing achieve light shielding. The smart window is composed of two layers: an outdoor layer filled with poly(N-isopropylacrylamide) (PNIPAM) solution modified with tartaric acid (TA), and dimethylacrylamide (DMA), which serves as the light-regulating layer. It is found that the lower critical solution temperature (LCST) of this material could be continuously adjusted within 10-70 °C, enabling a precise control of light transmittance. The indoor layer, filled with Calcium Chloride Hexahydrate ($CaCl_2 \cdot 6H_2O$, short as CCH) modified with ethanol and urea, serves as the TES layer. Such a TES material has a melting point that can be adjusted between 10 and 30 °C, and it remains stable in the supercooled state with triggerable characteristics. It was demonstrated that when externally stimulated, the material rapidly releases stored thermal energy and transformed into an opaque crystalline state. The results showed that the smart

window achieved a transmittance of up to 91% and a total thermal storage density of up to 325 kJ/kg, indicating a great potential for high application and innovation in building energy management.

6.2 Recommendations for Future Work

- The large-scale use of MME still faces challenges. While this study shows that MME materials are stable in quantities of hundreds of grams, their stability in much larger amounts, like several hundred kilograms, has not been tested. This is a major concern because the chance of nucleation in supercooled liquids increases with volume, making them less stable as the sample size grows. To improve overall stability, it is a good idea to divide the material into separate compartments. This way, if crystallization occurs in one compartment, it won't affect the stability of the rest. Additionally, to enhance the photothermal efficiency of MME materials, polydopamine can be added to improve light absorption.
- The storage stability of G-DMI is generally reliable in large-scale applications, but there is still a risk of crystallization during the preparation process, which hinders the effective formation of glassy materials. This problem occurs because, in large-scale production, the large size and low thermal conductivity of the material create a significant temperature difference between its internal and surface layers during cooling. When the surface layer cools to room temperature and forms a glassy state, the internal temperature remains high, causing the internal heat to reheat the surface glassy material. This leads to cold crystallization of the surface layer, eventually resulting in crystallization of the entire material. To solve this issue, heat exchange coils can be

installed inside the material. These coils use cooling fluid to remove the heat generated during the cooling process, reducing the temperature difference between the inside and outside, thus enabling the formation of the glassy material.

- Efforts can be focused on developing more efficient photo-triggered and magneto-triggered phase change materials by using the sensitivity of supercooled liquids with transition metal ions to light and magnetic fields. This can be done by designing molecular structures that allow the coordination fields to be manipulated through exposure to specific wavelengths of light or magnetic fields. The goal is to create a new type of non-contact, triggerable phase change material that is highly sensitive to changes in light and magnetic environments.

Appendix Publications and Presentations

JOURNAL PAPER:

1. **X.S. Zhang**, Z. Du, Y.D. Zhu, C. Li, X.F. Hu, T.B. Yang, B.B. Yu, R. Gu, Y.L. Ding, Z.B. He. A novel volumetric absorber integrated with low-cost D-Mannitol and acetylene-black nanoparticles for solar-thermal-electricity generation. **Sol. Energy Mater. Sol. Cell**, 2020, 207, 110366
2. **X.S. Zhang**, Z. Du, D. He, Z.H. Chen, Z.N. Li, G.C. Chen, Q. Tan, H. Gao, Z.Y. Niu, S.M. Ma, T.L. Chen, Y.L. Ding, Z.B. He. Practicable glass-forming liquids in a core-shell coordination structure. **Joule**, Under Review.
3. **X.S. Zhang**, T.L. Chen, Z. Du, D. He, Z.Y. Niu, S.M. Ma, Y.L. Ding, Z.B. He Organic glassy materials based on D-mannitol and Myo-inositol for long-term thermal energy storage. Under submitted.
4. **X.S. Zhang**, T.L. Chen, Z. Du, Z.X. Wei, W.Y, Zou, Z.Y. Niu, S.M. Ma, Y.L. Ding, Z.B. Dual-layer thermos-responsive energy storage smart window. Under submitted. Under Submitted.

Bibliography

1. Mora, C. *et al.* Global risk of deadly heat. *Nat. Clim. Chang.* **7**, 501–506 (2017).
2. Sachs, J. D. *et al.* Six Transformations to achieve the Sustainable Development Goals. *Nat. Sustain.* **2**, 805–814 (2019).
3. Rockström, J. *et al.* A roadmap for rapid decarbonization. *Science (80-.).* **355**, 1269–1271 (2017).
4. Gota, S., Huizenga, C., Peet, K., Medimorec, N. & Bakker, S. Decarbonising transport to achieve Paris Agreement targets. *Energy Effic.* **12**, 363–386 (2019).
5. Brecha, R. J. *et al.* Institutional decarbonization scenarios evaluated against the Paris Agreement 1.5 °C goal. *Nat. Commun.* **13**, (2022).
6. Institute, E. Statistical Review of World Energy 2023. *BP Energy Outlook 2023* **70**, 8–20 (2023).
7. *IEA (2023), CO2 Emissions in 2022, IEA, Paris Https://Www.Iea.Org/Reports/Co2-Emissions-in-2022, Licence: CC BY 4.0*. doi:10.1007/978-3-031-25984-5_300288.
8. ANTÓNIO GUTERRES. Causes and Effects of Climate Change. *United Nations Publications* 1–8 at https://www.un.org/en/climatechange/science/causes-effects-climate-change (2023).
9. *IRENA (2020), Global Renewables Outlook: Energy Transformation 2050 (Edition: 2020), International Renewable Energy Agency, Abu Dhabi.*

10. Kittner, N., Lill, F. & Kammen, D. M. Energy storage deployment and innovation for the clean energy transition. *Nat. Energy* **17125**, 1–6 (2017).

11. Mousavi, S. M. G., Faraji, F., Majazi, A. & Al-haddad, K. A comprehensive review of Flywheel Energy Storage System technology. *Renew. Sustain. Energy Rev.* **67**, 477–490 (2017).

12. Pérez-díaz, J. I., Chazarra, M., García-gonzález, J., Cavazzini, G. & Stoppato, A. Trends and challenges in the operation of pumped-storage hydropower plants. *Renew. Sustain. Energy Rev.* **44**, 767–784 (2015).

13. Budt, M., Wolf, D., Span, R. & Yan, J. A review on compressed air energy storage : Basic principles , past milestones and recent developments. *Appl. Energy* **170**, 250–268 (2016).

14. Vatamanu, J. & Bedrov, D. Capacitive Energy Storage: Current and Future Challenges. *J. Phys. Chem. Lett.* **6**, 3594−3609 (2015).

15. G, V. S. V. & Madichetty, S. Application of superconducting magnetic energy storage in electrical power and energy systems : a review. *Energy Res.* **42**, 358–368 (2018).

16. Wang, Y. *et al.* Room-Temperature Sodium-Sulfur Batteries : A Comprehensive Review on Research Progress and Cell Chemistry. *Adv. Energy Mater.* **1602829**, 1–17 (2017).

17. Yang, J. *et al.* Review on the research of failure modes and mechanism for lead – acid batteries. *Energy Res.* 336–352 (2017) doi:10.1002/er.3613.

18. Zhang, H., Lu, W. & Li, X. Progress and Perspectives of Flow Battery Technologies. *Electrochem. Energy Rev.* **2**, 492–506 (2019).

19. Yang, Y., Okonkwo, E. G., Huang, G., Xu, S. & Sun, W. On the sustainability of lithium ion battery industry – A review and perspective. *Energy Storage Mater.* **36**, 186–212 (2021).

20. Zhu, Z. & Xu, Z. The rational design of biomass-derived carbon materials towards next-generation energy storage : A review. *Renew. Sustain. Energy Rev.* **134**, 110308 (2020).

21. Grigoriev, S. A., Fateev, V. N., Bessarabov, D. G. & Millet, P. ScienceDirect Current status , research trends , and challenges in water electrolysis science and technology. *Int. J. Hydrogen Energy* **45**, 26036–26058 (2020).

22. Goransson, K. Review of syngas production via biomass DFBGs. *Renew. Sustain. Energy Rev.* **15**, 482–492 (2011).

23. Yue, M., Lambert, H., Pahon, E., Roche, R. & Jemei, S. Hydrogen energy systems : A critical review of technologies , applications , trends and challenges. *Renew. Sustain. Energy Rev.* **146**, (2021).

24. *Thermal Enrgy Storage for Sustainable Energy Consimption*.

25. Pelay, U., Luo, L., Fan, Y., Stitou, D. & Rood, M. Thermal energy storage systems for concentrated solar power plants. *Renewable and Sustainable Energy Reviews* at https://doi.org/10.1016/j.rser.2017.03.139 (2017).

26. Zhang, H., Baeyens, J., Cáceres, G., Degrève, J. & Lv, Y. Thermal energy storage : Recent developments and practical aspects. *Prog. Energy Combust. Sci.* **53**, 1–40 (2016).

27. Alva, G., Lin, Y. & Fang, G. An overview of thermal energy storage systems. *Energy* **144**, 341–378 (2018).

28. Smith, C. L. The Need for Energy Storage in a Net Zero World. *Virtual Conference on Medium-Duration Energy Storage in the Net-Zero UK* (2020).

29. Shan, R., Reagan, J., Castellanos, S., Kurtz, S. & Kittner, N. Evaluating emerging long-duration energy storage technologies. *Renew. Sustain. Energy Rev.* **159**, 112240 (2022).

30. *Innovation Outlook: Thermal Energy StorageIRENA (2020), Innovation Outlook: Thermal Energy Storage, International Renewable Energy Agency, Abu Dhabi.*

31. *IEA (2019), Renewables 2019, IEA, Paris Https://Www.Iea.Org/Reports/Renewables-2019, Licence: CC BY 4.0.*

32. Resource, S. Photovoltaic Energy. 2022–2023 (2022).

33. Jenkins, J. D. & Sepulveda, N. A. Long-duration energy storage: A blueprint for research and innovation. *Joule* **5**, 2241–2246 (2021).

34. Gerkman, M. A. & Han, G. G. D. Toward Controlled Thermal Energy Storage and Release in Organic Phase Change Materials. *Joule* vol. 4 1621–1625 at https://doi.org/10.1016/j.joule.2020.07.011 (2020).

35. Sadeghi, G. Energy storage on demand: Thermal energy storage development, materials, design, and integration challenges. *Energy Storage Mater.* **46**, 192–222 (2022).

36. Alva, G., Liu, L., Huang, X. & Fang, G. Thermal energy storage materials and systems for solar energy applications. *Renew. Sustain. Energy Rev.* **68**, 693–706 (2017).

37. Safari, A., Saidur, R., Sulaiman, F. A., Xu, Y. & Dong, J. A review on supercooling of Phase Change Materials in thermal energy storage systems. *Renew. Sustain. Energy Rev.* **70**, 905–

919 (2017).

38. Dannemand, M. *et al.* Thermophysical Properties of Sodium Acetate Trihydrate Composites as Heat Storage Material. (2017).

39. Shamseddine, I., Pennec, F., Biwole, P. & Fardoun, F. Supercooling of phase change materials: A review. *Renew. Sustain. Energy Rev.* **158**, 112172 (2022).

40. Englmair, G., Moser, C., Schranzhofer, H., Fan, J. & Furbo, S. A solar combi-system utilizing stable supercooling of sodium acetate trihydrate for heat storage: Numerical performance investigation. *Appl. Energy* **242**, 1108–1120 (2019).

41. Zhou, G., Zhu, M. & Xiang, Y. Effect of percussion vibration on solidification of supercooled salt hydrate PCM in thermal storage unit. *Renew. Energy* **126**, 537–544 (2018).

42. Zhang, B., Feng, Y. & Feng, W. *Azobenzene-Based Solar Thermal Fuels: A Review*. *Nano-Micro Letters* vol. 14 (Springer Nature Singapore, 2022).

43. Qiu, Q., Shi, Y. & Han, G. G. D. Solar energy conversion and storage by photoswitchable organic materials in solution, liquid, solid, and changing phases. *Journal of Materials Chemistry C* vol. 9 11444–11463 at https://doi.org/10.1039/d1tc01472b (2021).

44. Xu, W. C., Sun, S. & Wu, S. Photoinduced Reversible Solid-to-Liquid Transitions for Photoswitchable Materials. *Angewandte Chemie - International Edition* vol. 58 9712–9740 at https://doi.org/10.1002/anie.201814441 (2019).

45. Duquesne, M., Del Barrio, E. P. & Godin, A. Nucleation triggering of highly undercooled Xylitol using an air lift reactor for seasonal thermal energy storage. *Applied Sciences*

(Switzerland) vol. 9 at https://doi.org/10.3390/app9020267 (2019).

46. Gunasekara, S. N., Chiu, J. N. W., Martin, V. & Hedström, P. The experimental phase diagram study of the binary polyols system erythritol-xylitol. *Solar Energy Materials and Solar Cells* vol. 174 248–262 at https://doi.org/10.1016/j.solmat.2017.08.005 (2018).

47. Iwase, K., Houjou, H., Yamamura, Y. & Saito, K. Cold crystallization in bis[1-(3-methylphenyl)iminomethylnaphthalen-2- olato]nickel(II) studied by thermal analysis and x-ray diffraction. *Chem. Lett.* **42**, 1040–1042 (2013).

48. Turunen, K., Mikkola, V., Laukkanen, T. & Seppälä, A. Long-term thermal energy storage prototype of cold-crystallizing erythritol-polyelectrolyte. *Applied Energy* vol. 332 at https://doi.org/10.1016/j.apenergy.2022.120530 (2023).

49. Peter Tobolka, J. J. Heat Storage in Future Zero-Energy Buildings. *Int. J. Innov. Res. Sci. Eng. Technol.* **4**, 6722–6728 (2015).

50. Scapino, L., Zondag, H. A., Bael, J. Van, Diriken, J. & Rindt, C. C. M. Sorption heat storage for long-term low-temperature applications : A review on the advancements at material and prototype scale. *Appl. Energy* **190**, 920–948 (2017).

51. Zhang, Y. & Wang, R. Sorption thermal energy storage : Concept , process , applications and perspectives. *Energy Storage Mater.* **27**, 352–369 (2020).

52. Felderhoff, M. & Bogdanović, B. High temperature metal hydrides as heat storage materials for solar and related applications. *Int. J. Mol. Sci.* **10**, 335–344 (2009).

53. Paulsen, H. Active MgH,-Mg Systems for Reversible Chemical Energy Storage. *Angew.*

Chemie Int. Ed. English **21**, 155–173 (1982).

54. Meier, A. *et al.* Design and experimental investigation of a horizontal rotary reactor for the solar thermal production of lime. *Energy* **29**, 811–821 (2004).

55. Krohn, C. M. & Krohn, C. G. Development of porous solid reactant for thermal-energy storage and temperature upgrade using carbonation/decarbonation reaction. *Appl. Energy* **69**, 225–238 (2001).

56. Kato, Y., Harada, N. & Yoshizawa, Y. Kinetic feasibility of a chemical heat pump for heat utilization of high-temperature processes. *Appl. Therm. Eng.* **19**, 239–254 (1999).

57. Kato, Y., Sasaki, Y. & Yoshizawa, Y. Magnesium oxide/water chemical heat pump to enhance energy utilization of a cogeneration system. *Energy* **30**, 2144–2155 (2005).

58. Guy, E. Solar Heat Storage Using Chemical Reactions. *J. Solid State Chem.* **22**, 51–61 (1977).

59. Carrillo, A. J., Sastre, D., Serrano, D. P., Pizarro, P. & Coronado, J. M. Revisiting the BaO2/BaO redox cycle for solar thermochemical energy storage. *Phys. Chem. Chem. Phys.* **18**, 8039–8048 (2016).

60. Carden, P. O. Energy corradiation using the reversible ammonia reaction. *Sol. Energy* **19**, 365–378 (1977).

61. Lovegrove, K., Luzzi, A., Soldiani, I. & Kreetz, H. Developing ammonia based thermochemical energy storage for dish power plants. *Sol. Energy* **76**, 331–337 (2004).

62. Aristov, Y. I., Parmon, V. N., Cacciola, G. & Giordano, N. High-temperature chemical heat pump based on reversible catalytic reactions of cyclohexane-dehydrogenation/benzene-

hydrogenation: Comparison of the potentialities of different flow diagrams. *Int. J. Energy Res.* **17**, 293–303 (1993).

63. Ma, Q., Luo, L., Wang, R. Z. & Sauce, G. A review on transportation of heat energy over long distance: Exploratory development. *Renew. Sustain. Energy Rev.* **13**, 1532–1540 (2009).

64. Qiu, Y. *et al.* Thermochemical energy storage using silica gel: Thermal storage performance and nonisothermal kinetic analysis. *Sol. Energy Mater. Sol. Cells* **251**, 112153 (2023).

65. Padamurthy, A., Nandanavanam, J. & Rajagopalan, P. Thermal stability evaluation of selected zeolites for sustainable thermochemical energy storage. *Energy Sources, Part A Recover. Util. Environ. Eff.* **00**, 1–14 (2021).

66. Kohler, T., Biedermann, T. & Müller, K. Experimental Study of MgCl2 · 6 H2O as Thermochemical Energy Storage Material. *Energy Technol.* **6**, 1935–1940 (2018).

67. Clark, R. J. & Farid, M. Hydration reaction kinetics of SrCl2 and SrCl2-cement composite material for thermochemical energy storage. *Sol. Energy Mater. Sol. Cells* **231**, 111311 (2021).

68. N'Tsoukpoe, K. E. *et al.* A review on the use of calcium chloride in applied thermal engineering. *Appl. Therm. Eng.* **75**, 513–531 (2015).

69. Sarkar, J. & Bhattacharyya, S. Application of graphene and graphene-based materials in clean energy-related devices Minghui. *Arch. Thermodyn.* **33**, 23–40 (2012).

70. Trausel, F., De Jong, A. J. & Cuypers, R. A review on the properties of salt hydrates for thermochemical storage. *Energy Procedia* **48**, 447–452 (2014).

71. Alva, G., Lin, Y. & Fang, G. An overview of thermal energy storage systems. *Energy* at https://doi.org/10.1016/j.energy.2017.12.037 (2018).

72. Sarbu, I. & Sebarchievici, C. A comprehensive review of thermal energy storage. *Sustainability (Switzerland)* at https://doi.org/10.3390/su10010191 (2018).

73. Khatod, K. J., Katekar, V. P. & Deshmukh, S. S. An evaluation for the optimal sensible heat storage material for maximizing solar still productivity: A state-of-the-art review. *J. Energy Storage* **50**, 104622 (2022).

74. Yan, T. & Zhang, H. A critical review of salt hydrates as thermochemical sorption heat storage materials: Thermophysical properties and reaction kinetics. *Sol. Energy* **242**, 157–183 (2022).

75. Kuznik, F., Opel, O., Osterland, T. & Ruck, W. K. L. Thermal energy storage for space heating and domestic hot water in individual residential buildings. *Adv. Therm. Energy Storage Syst. Methods Appl.* 567–594 (2020) doi:10.1016/B978-0-12-819885-8.00019-X.

76. Pielichowska, K. & Pielichowski, K. Phase change materials for thermal energy storage. *Prog. Mater. Sci.* **65**, 67–123 (2014).

77. Sharma, A., Tyagi, V. V., Chen, C. R. & Buddhi, D. Review on thermal energy storage with phase change materials and applications. *Renew. Sustain. Energy Rev.* **13**, 318–345 (2009).

78. Gupta, N. *et al.* Proceedings Metal nanoparticles enhanced thermophysical properties of phase change material for thermal energy storage. *Mater. Today Proc.* **32**, 463–467 (2020).

79. Cao, Y. *et al.* Phase change materials based on comb-like polynorbornenes and

octadecylamine-functionalized graphene oxide nanosheets for thermal energy storage. *Chem. Eng. J.* **389**, 124318 (2020).

80. Chen, P. *et al.* Metal foam embedded in SEBS/paraffin/HDPE form-stable PCMs for thermal energy storage. *Sol. Energy Mater. Sol. Cells* **149**, 60–65 (2016).

81. Bhattacharya, a., Calmidi, V. V. & Mahajan, R. L. Thermophysical properties of high porosity metal foams. *Int. J. Heat Mass Transf.* **45**, 1017–1031 (2002).

82. Zhang, L., Li, R., Tang, B. & Wang, P. Solar-thermal conversion and thermal energy storage of graphene foam-based composites. *Nanoscale* **8**, 14600–14607 (2016).

83. Ushak, S. *et al.* Reduction of the subcooling of bischofite with the use of nucleatings agents. *Sol. Energy Mater. Sol. Cells* **157**, 1011–1018 (2016).

84. Wang, Y., Li, S., Zhang, T., Zhang, D. & Ji, H. Supercooling suppression and thermal behavior improvement of erythritol as phase change material for thermal energy storage. *Sol. Energy Mater. Sol. Cells* **171**, 60–71 (2017).

85. Beaupere, N., Soupremanien, U. & Zalewski, L. Nucleation triggering methods in supercooled phase change materials (PCM), a review. *Thermochim. Acta* **670**, 184–201 (2018).

86. Englmair, G., Moser, C., Furbo, S., Dannemand, M. & Fan, J. Design and functionality of a segmented heat-storage prototype utilizing stable supercooling of sodium acetate trihydrate in a solar heating system. *Appl. Energy* (2018) doi:10.1016/j.apenergy.2018.03.124.

87. Dannemand, M., Johansen, J. B., Kong, W. & Furbo, S. Experimental investigations on

cylindrical latent heat storage units with sodium acetate trihydrate composites utilizing supercooling. *Appl. Energy* (2016) doi:10.1016/j.apenergy.2016.05.144.

88. Ribezzo, A., Falciani, G., Bergamasco, L., Fasano, M. & Chiavazzo, E. An overview on the use of additives and preparation procedure in phase change materials for thermal energy storage with a focus on long term applications. *J. Energy Storage* **53**, 105140 (2022).

89. Dong, B., Li, S., Zhang, X., Wang, J. & Peng, H. Synthesis and Characterization of Nanoalumina and CNTs- Reinforced Microcapsules with n - Dodecane as a Phase Change Material for Cold Energy Storage. (2020) doi:10.1021/acs.energyfuels.0c01381.

90. Farid, M. M., Khudhair, A. M., Razack, S. A. K. & Al-Hallaj, S. A review on phase change energy storage: Materials and applications. *Energy Conversion and Management* at https://doi.org/10.1016/j.enconman.2003.09.015 (2004).

91. Hasnain, S. M. Review on sustainable thermal energy storage technologies, part I: Heat storage materials and techniques. *Energy Convers. Manag.* **39**, 1127–1138 (1998).

92. Tong, B. *et al.* Thermodynamic investigation of several natural polyols (I): Heat capacities and thermodynamic properties of xylitol. *Thermochim. Acta* **457**, 20–26 (2007).

93. Zhang, H. *et al.* Experimental and in silico characterization of xylitol as seasonal heat storage material. *Fluid Phase Equilib.* **436**, 55–68 (2017).

94. Shen, S. *et al.* The effects of modified carbon nanotubes on the thermal properties of erythritol as phase change materials. *Energy Convers. Manag.* **157**, 41–48 (2018).

95. Yang, S., Shao, X. F., Shi, H. Y., Luo, J. H. & Fan, L. W. Bubble-injection-enabled

significant reduction of supercooling and controllable triggering of crystallization of erythritol for medium-temperature thermal energy storage. *Sol. Energy Mater. Sol. Cells* **236**, 111538 (2022).

96. Gil, A. *et al.* Thermal behaviour of D -mannitol when used as PCM : Comparison of results obtained by DSC and in a thermal energy storage unit at pilot plant scale. *Appl. Energy* **111**, 1107–1113 (2013).

97. Zhang, X. *et al.* A novel volumetric absorber integrated with low-cost D-Mannitol and acetylene-black nanoparticles for solar-thermal-electricity generation. *Sol. Energy Mater. Sol. Cells* **207**, 110366 (2020).

98. Solé, A. *et al.* Solar Energy Materials & Solar Cells Stability of sugar alcohols as PCM for thermal energy storage. *Sol. Energy Mater. Sol. Cells* **126**, 125–134 (2014).

99. Solé, A. *et al.* Stability of sugar alcohols as PCM for thermal energy storage. *Sol. Energy Mater. Sol. Cells* **126**, 125–134 (2014).

100. Cárdenas, B. & León, N. High temperature latent heat thermal energy storage: Phase change materials, design considerations and performance enhancement techniques. *Renew. Sustain. Energy Rev.* **27**, 724–737 (2013).

101. Liu, M., Saman, W. & Bruno, F. Review on storage materials and thermal performance enhancement techniques for high temperature phase change thermal storage systems. *Renew. Sustain. Energy Rev.* **16**, 2118–2132 (2012).

102. Ediger, M. D., Angell, C. A. & Nagel, S. R. Supercooled liquids and glasses. *J. Phys. Chem.*

100, 13200–13212 (1996).

103. Angell, C. A. Structural instability and relaxation in liquid and glassy phases near the fragile liquid limit. *J. Non. Cryst. Solids* **102**, 205–221 (1988).

104. Turnbull, D. Under What Conditions Can A Glass Be Formed? *Contemp. Phys.* **10**, 473–488 (1969).

105. Ediger, M. D., Angell, C. A. & Nagel, S. R. Supercooled liquids and glasses. *Nature* **100**, 13200–13212 (1996).

106. Lizana, J., Sanchez-Jimenez, P. E., Chacartegui, R., Becerra, J. A. & Perez-Maqueda, L. A. Supercooled sodium acetate aqueous solution for long-term heat storage to support heating decarbonisation. *J. Energy Storage* **55**, 105584 (2022).

107. Debenedetti, P. G. & Stillinger, F. H. Supercooled liquids and the glass transition. *Nature* **410**, 259 (2001).

108. Turnbull, D. & Fisher, J. C. Rate of nucleation in condensed systems. *J. Chem. Phys.* **17**, 71–73 (1949).

109. Kelton, K. F. *Crystal Nucleation in Liquids and Glasses*. *Solid State Physics - Advances in Research and Applications* vol. 45 (1991).

110. Sosso, G. C. *et al.* Crystal Nucleation in Liquids: Open Questions and Future Challenges in Molecular Dynamics Simulations. *Chem. Rev.* **116**, 7078–7116 (2016).

111. Wang, W. H., Dong, C. & Shek, C. H. Bulk metallic glasses. *Mater. Sci. Eng. R Reports* **44**, 45–89 (2004).

112. Cavagna, A. Supercooled liquids for pedestrians. *Phys. Repor* **476**, 51–124 (2009).

113. Ediger, M. D. Spatially Heterogeneous Dynamics in Supercooled Liquids. *Annu. Rev. Phys. Chem.* **51**, 99–128 (2000).

114. Hunter, G. L. & Weeks, E. R. The physics of the colloidal glass transition. *Reports Prog. Phys.* **75**, (2012).

115. C.A.Angell. Formation of Glasses from Liquids and Biopolymers. *Science (80-.).* **267**, 1924–1935 (1995).

116. Turnbull, D. & Cohen, M. H. Concerning reconstructive transformation and formation of glass. *J. Chem. Phys.* **29**, 1049–1054 (1958).

117. Laughlin, W. T. & Uhlmann, D. R. Viscous flow in simple organic liquids. *J. Phys. Chem.* **76**, 2317–2325 (1972).

118. Zheng, Q. *et al.* Understanding Glass through Differential Scanning Calorimetry. *Chem. Rev.* (2019) doi:10.1021/acs.chemrev.8b00510.

119. Lucas, P. Fragile-to-strong transitions in glass forming Fragile-to-strong transitions in glass forming liquids. *J. Non-Crystalline Solids X* **4**, 100034 (2019).

120. Varnik, F. & Franosch, T. Non-monotonic effect of confinement on the glass transition. *J. Phys. Condens. Matter* (2016) doi:10.1088/0953-8984/28/13/133001.

121. Lubchenko, V. & Wolynes, P. G. Theory of structural glasses and supercooled liquids. *Annu. Rev. Phys. Chem.* **58**, 235–266 (2007).

122. C. A. Angell. Relaxation in liquids, polymers and plastic crystals - strong/fragile patterns and

problems. *J. Non. Cryst. Solids* **131**, 13–31 (1991).

123. Mauro, J. C., Yue, Y., Ellison, A. J., Gupta, P. K. & Allan, D. C. Viscosity of glass-forming liquids. *Proc. Natl. Acad. Sci. U. S. A.* **106**, 19780–19784 (2009).

124. Zheng, Q. & Mauro, J. C. Viscosity of glass-forming systems. *J. Am. Ceram. Soc.* **100**, 6–25 (2017).

125. Hecksher, T., Nielsen, A. I., Olsen, N. B. & Dyre, J. C. Little evidence for dynamic divergences in ultraviscous molecular liquids. *Nat. Phys.* **4**, 737–741 (2008).

126. Moosavi, M. & Daneshvar, A. Investigation of the rheological properties of two imidazolium-based ionic liquids. *J. Mol. Liq.* **190**, 59–67 (2014).

127. Ans-, O. Full Temperature Range Fitting of Glass Viscosity- Temperature Curve. 126–129 (2020).

128. Wang, L. M., Angell, C. A. & Richert, R. Fragility and thermodynamics in nonpolymeric glass-forming liquids. *J. Chem. Phys.* **125**, (2006).

129. Taylor, P., Greaves, G. N. & Sen, S. Inorganic glasses, glass-forming liquids and amorphizing solids. *Adv. Phys.* **56**, 1–166 (2007).

130. Ito, K., Moynihan, C. T. & Angell, C. A. Thermodynamic determination of fragility in liquids and a fragile-to-strong liquid transition in water. *Nature* **398**, (1999).

131. Novikov, V. N. & Sokolov, A. P. Poisson's ratio and the fragility of glass-forming liquids. *Nature* **431**, 961–963 (2004).

132. Stevenson, J. D. & Wolynes, P. G. Thermodynamic - Kinetic Correlations in Supercooled

Liquids: A Critical Survey of Experimental Data and Predictions of the Random First-Order Transition Theory of Glasses. *J. Phys. Chem. B* **3**, 15093–15097 (2005).

133. Ho, R. *et al.* Effect of milling on particle shape and surface energy heterogeneity of needle-Shaped crystals. *Pharm. Res.* (2012) doi:10.1007/s11095-012-0842-1.

134. Ho, R. *et al.* Effect of milling on particle shape and surface energy heterogeneity of needle-Shaped crystals. *Pharm. Res.* **29**, 2806–2816 (2012).

135. Berthier, L. Dynamic Heterogeneity in Amorphous Materials. *Physics (College. Park. Md).* **4**, (2011).

136. Berthier, L. & Biroli, G. Theoretical perspective on the glass transition and amorphous materials. *Rev. Mod. Phys.* **83**, 587–645 (2011).

137. Royall, C. P. & Williams, S. R. The role of local structure in dynamical arrest. *Phys. Rep.* **560**, 1–75 (2015).

138. Wolynes, P. Entropy Crises in Glasses and Random Heteropolymers. *J. Res. Natl. Inst. Stand. Technol.* **102**, (2014).

139. Wolynes, P. G. Aperioidic crystals: Biology, Chemistry and Physics in a fugue with stretto . *AIP Conf. Proc.* **65**, 39–65 (1988).

140. R. M. Power, a S. H. Simpson, a J. P. R. and A. J. H. The transition from liquid to solid-like behaviour in ultrahigh viscosity aerosol particles. *Chem. Sci.* 2597–2604 (2013) doi:10.1039/c3sc50682g.

141. Ma, E. Tuning order in disorder. *Nat. Mater.* **14**, 547–552 (2015).

142. Ma, E. & Zhang, Z. Amorphous alloys: Reflections from the glass maze. *Nat. Mater.* **10**, 10–11 (2011).

143. Zhou, C. *et al.* Glassy structure affected cold - crystallization behavior and structure of poly (lactic acid). *J. Polym. Res.* (2022) doi:10.1007/s10965-022-03077-4.

144. Dayane, I. *et al.* An investigation of PLA / Babassu cold crystallization kinetics. *J. Therm. Anal. Calorim.* **141**, 1389–1397 (2020).

145. Ishino, K. *et al.* Cold Crystallization and the Molecular Structure of Imidazolium-Based Ionic Liquid Crystals with a p-Nitroazobenzene Moiety. *ACS Omega* **6**, 32869–32878 (2021).

146. Mijovic, J. & Sy, J. Molecular Dynamics during Crystallization of Poly (L -lactic acid) As Studied by Broad-Band Dielectric Relaxation Spectroscopy. *Macromolecules* **35**, 6370–6376 (2002).

147. Cho, T. & Strobl, G. Temperature dependent variations in the lamellar structure of poly (L -lactide). *Polymer (Guildf).* **47**, 1036–1043 (2006).

148. Salmero, M. *et al.* Effect of the Cooling Rate on the Nucleation Kinetics of Poly (L -Lactic Acid) and Its Influence on Morphology. *Macromolecules* **40**, 7989–7997 (2007).

149. Santis, F. De, Pantani, R. & Titomanlio, G. Nucleation and crystallization kinetics of poly (lactic acid). *Thermochim. Acta* **522**, 128–134 (2011).

150. Schick, C., Zhuravlev, E., Androsch, R., Wurm, A. & Schmelzer, J. W. P. Influence of thermal prehistory on crystal nucleation and growth in polymers. *Glas. Sel. Prop. Cryst.* 1–94 (2014) doi:10.1515/9783110298581.1.

151. Xu, J., Wang, R. Z. & Li, Y. A review of available technologies for seasonal thermal energy storage. *Sol. Energy* **103**, 610–638 (2014).

152. Yang, T., Liu, W., Jan, G. & Sun, Q. Seasonal thermal energy storage : A techno-economic literature review. *Renew. Sustain. Energy Rev.* **139**, 110732 (2021).

153. Wang, G. *et al.* Thermal characteristics of a long-term heat storage unit with sodium acetate trihydrate. *Appl. Therm. Eng.* **187**, 116563 (2021).

154. Englmair, G., Dannemand, M., Furbo, S. & Fan, J. Combined short and long term heat storage with Sodium Acetate Trihydrate in cylindrical tanks. *EuroSun 2018, Switz.* 1–3 (2018).

155. Englmair, G. *et al.* Crystallization by local cooling of supercooled sodium acetate trihydrate composites for long-term heat storage. *Energy Build.* **180**, 159–171 (2018).

156. Van Helden, W. *et al.* IEA SHC Task 42 / ECES Annex 29 - Working Group B: Applications of Compact Thermal Energy Storage. *Energy Procedia* **91**, 231–245 (2016).

157. Zhou, G. & Xiang, Y. Experimental investigations on stable supercooling performance of sodium acetate trihydrate PCM for thermal storage. *Sol. Energy* **155**, 1261–1272 (2017).

158. Rathgeber, C. *et al.* IEA SHC Task 42 / ECES Annex 29 - A Simple Tool for the Economic Evaluation of Thermal Energy Storages. *Energy Procedia* **91**, 197–206 (2016).

159. Wang, G. *et al.* Review on sodium acetate trihydrate in flexible thermal energy storages: Properties, challenges and applications. *J. Energy Storage* **40**, 102780 (2021).

160. Sandnes, B. & Rekstad, J. Supercooling salt hydrates: Stored enthalpy as a function of temperature. *Sol. Energy* **80**, 616–625 (2006).

161. Hirano, S. LONG-TERM PERFORMANCE OF LATENT HEAT THERMAL ENERGY STORAGE USING SUPERCOOLING. 1–2.

162. Ling, Z. *et al.* A fast-heat battery system using the heat released from detonated supercooled phase change materials. *Energy* **219**, 119496 (2021).

163. Peng, S., Hu, Y., Huang, J. & Song, M. Solar Energy Materials and Solar Cells Surface free energy analysis for stable supercooling of sodium thiosulfate pentahydrate with microcosmic-visualized methods. *Sol. Energy Mater. Sol. Cells* **208**, 110390 (2020).

164. Dannemand, M. *et al.* Experimental investigations on prototype heat storage units utilizing stable supercooling of sodium acetate trihydrate mixtures. *Appl. Energy* **169**, 72–80 (2016).

165. Englmair, G., Furbo, S., Dannemand, M. & Fan, J. Experimental investigation of a tank-in-tank heat storage unit utilizing stable supercooling of sodium acetate trihydrate. *Appl. Therm. Eng.* **167**, 114709 (2020).

166. Puupponen, S. & Seppälä, A. Cold-crystallization of polyelectrolyte absorbed polyol for long-term thermal energy storage. *Sol. Energy Mater. Sol. Cells* **180**, 59–66 (2018).

167. Piquard, L., Gagnière, E., Largiller, G., Mangin, D. & Bentivoglio, F. Xylitol used as phase change material: Nucleation mechanisms of the supercooling rupture by stirring. *J. Energy Storage* **48**, (2022).

168. Delgado, M., Navarro, M., Lázaro, A., Boyer, S. A. E. & Peuvrel-Disdier, E. Triggering and acceleration of xylitol crystallization by seeding and shearing: Rheo-optical and rheological investigation. *Solar Energy Materials and Solar Cells* vol. 220 at

https://doi.org/10.1016/j.solmat.2020.110840 (2021).

169. Seppälä, A., Meriläinen, A., Wikström, L. & Kauranen, P. The effect of additives on the speed of the crystallization front of xylitol with various degrees of supercooling. *Experimental Thermal and Fluid Science* vol. 34 523–527 at https://doi.org/10.1016/j.expthermflusci.2009.11.005 (2010).

170. Bolmatenkov, D. N., Yagofarov, M. I., Sokolov, A. A., Ziganshin, M. A. & Solomonov, B. N. The heat capacities and fusion thermochemistry of sugar alcohols between 298.15 K and Tm: The study of D-sorbitol, D-mannitol and myo-inositol. *J. Mol. Liq.* **330**, 115545 (2021).

171. Huang, C. *et al.* Crystal nucleation rates in glass-forming molecular liquids: D-sorbitol, D-arabitol, D-xylitol, and glycerol. *J. Chem. Phys.* **149**, (2018).

172. Shao, X. F. *et al.* Screening of sugar alcohols and their binary eutectic mixtures as phase change materials for low-to-medium temperature latent heat storage. (I): Non-isothermal melting and crystallization behaviors. *Energy* **160**, 1078–1090 (2018).

173. Diarce, G., Gandarias, I., Campos-Celador, García-Romero, A. & Griesser, U. J. Eutectic mixtures of sugar alcohols for thermal energy storage in the 50-90°C temperature range. *Sol. Energy Mater. Sol. Cells* **134**, 215–226 (2015).

174. Piquard, L. *et al.* Xylitol used as phase change material: Nucleation mechanisms of the supercooling rupture by stirring. *J. Energy Storage* **48**, 103922 (2022).

175. Gunasekara, S. N. *et al.* Erythritol, glycerol, their blends, and olive oil, as sustainable phase change materials. *Energy Procedia* **135**, 249–262 (2017).

176. Li, X. *et al.* Supercooled sugar alcohols stabilized by alkali hydroxides for long-term room-temperature phase change solar-thermal energy storage. *Chemical Engineering Journal* vol. 452 at https://doi.org/10.1016/j.cej.2022.139328 (2023).

177. Wang, Z., Hölzel, H. & Moth-Poulsen, K. Status and challenges for molecular solar thermal energy storage system based devices. *Chem. Soc. Rev.* **51**, 7313–7326 (2022).

178. Liu, H., Feng, Y. & Feng, W. Alkyl-grafted azobenzene molecules for photo-induced heat storage and release via integration function of phase change and photoisomerization. *Compos. Commun.* **21**, 100402 (2020).

179. Ishiba, K. *et al.* Photoliquefiable ionic crystals: A phase crossover approach for photon energy storage materials with functional multiplicity. *Angew. Chemie - Int. Ed.* **54**, 1532–1536 (2015).

180. Le, M. & Han, G. G. D. Stimuli-Responsive Organic Phase Change Materials: Molecular Designs and Applications in Energy Storage. *Accounts of Materials Research* vol. 3 634–643 at https://doi.org/10.1021/accountsmr.2c00049 (2022).

181. Gerkman, M. A. *et al.* Arylazopyrazoles for Long-Term Thermal Energy Storage and Optically Triggered Heat Release below 0 °c. *J. Am. Chem. Soc.* **142**, 8688–8695 (2020).

182. Xu, X. & Wang, G. Molecular Solar Thermal Systems towards Phase Change and Visible Light Photon Energy Storage. *Small* **18**, 1–19 (2022).

183. Dong, L., Feng, Y., Wang, L. & Feng, W. Azobenzene-based solar thermal fuels: design, properties, and applications. *Chem. Soc. Rev.* **47**, 7339–7368 (2018).

184. Zhang, Z. *et al.* Photochemical Phase Transitions Enable Coharvesting of Photon Energy and Ambient Heat for Energetic Molecular Solar Thermal Batteries That Upgrade Thermal Energy. (2020) doi:10.1021/jacs.0c03748.

185. Gerkman, M. A., Gibson, R. S. L., Shi, Y., Fuchter, M. J. & Han, G. G. D. Arylazopyrazoles for Long-Term Thermal Energy Storage and Optically Triggered Heat Release below 0 ° C. (2020) doi:10.1021/jacs.0c00374.

186. Shi, Y., Gerkman, M. A., Qiu, Q., Zhang, S. & Han, G. G. D. Sunlight-activated phase change materials for controlled heat storage and triggered release. *Journal of Materials Chemistry A* vol. 9 9798–9808 at https://doi.org/10.1039/d1ta01007g (2021).

187. Liu, H., Feng, Y. & Feng, W. Alkyl-grafted azobenzene molecules for photo-induced heat storage and release via integration function of phase change and photoisomerization. *Compos. Commun.* **21**, 100402 (2020).

188. Xu, X. *et al.* Photochromic Dendrimers for Photoswitched Solid-To-Liquid Transitions and Solar Thermal Fuels. (2020) doi:10.1021/acsami.0c14160.

189. Han, G. G. D., Li, H. & Grossman, J. C. Optically-controlled long-term storage and release of thermal energy in phase-change materials. *Nat. Commun.* **8**, (2017).

190. Liu, H. *et al.* Optically Triggered Synchronous Heat Release of Phase-Change Enthalpy and Photo-Thermal Energy in Phase-Change Materials at Low Temperatures. *Adv. Funct. Mater.* **31**, (2021).

191. Fei, L., Yin, Y., Zhang, J. & Wang, C. A Visible Energy Management by Photochromic Solar

Thermal Fuel Using a Color Display. **2000499**, 1–10 (2020).

192. Iwase, K. *et al.* Cold crystallization in schiff-base nickel(II) complexes derived from three toluidine isomers. *J. Phys. Chem. C* **118**, 27664–27671 (2014).

193. Bennett, T. D. & Horike, S. Liquid, glass and amorphous solid states of coordination polymers and metal–organic frameworks. *Nat. Rev. Mater.* **3**, 431–440 (2018).

194. Tuffnell, J. M. *et al.* Novel metal-organic framework materials: Blends, liquids, glasses and crystal-glass composites. *Chem. Commun.* **55**, 8705–8715 (2019).

195. Yin, Z., Zhang, Y., Yu, H. & Zeng, M. How to create MOF glasses and take advantage of emerging opportunities. *Sci. Bull.* **65**, 1432–1435 (2020).

196. Fonseca, J., Gong, T., Jiao, L. & Jiang, H. L. Metal-organic frameworks (MOFs) beyond crystallinity: amorphous MOFs, MOF liquids and MOF glasses. *J. Mater. Chem. A* **9**, 10562–10611 (2021).

197. Ma, N. & Horike, S. Metal-Organic Network-Forming Glasses. *Chem. Rev.* **122**, 4163–4203 (2022).

198. Wang, Y. *et al.* A MOF Glass Membrane for Gas Separation. 4395–4399 (2020) doi:10.1002/ange.201915807.

199. Li, J. *et al.* Coordination Polymer Glasses with Lava and Healing Ability for High-Performance Gas Sieving. *Angew. Chemie - Int. Ed.* **60**, 21304–21309 (2021).

200. Tanaka, K. *et al.* Kenjiro Tanaka, Yusuke Tago, Mitsuru Kondo, Yuki Watanabe, Kazunori Nishio, Taro Hitosugi, * and Makoto Moriya *. (2020) doi:10.1021/acs.nanolett.0c03313.

201. Ogawa, T. *et al.* Coordination polymer glass from a protic ionic liquid: proton conductivity and mechanical properties as an electrolyte. *Chem. Sci.* **11**, 5175–5181 (2020).

202. Hirai, Y. *et al.* Luminescent Coordination Glass: Remarkable Morphological Strategy for Assembled Eu(III) Complexes. (2015) doi:10.1021/acs.inorgchem.5b00145.

203. Article, E. *et al.* Chemical Science thiolate coordination polymers †. 6815–6823 (2020) doi:10.1039/d0sc02258f.

204. Liu, M. *et al.* Network-Forming Liquids from Metal–Bis(acetamide) Frameworks with Low Melting Temperatures. *J. Am. Chem. Soc.* (2021) doi:10.1021/jacs.0c11718.

205. Turunen, K., Yazdani, M. R., Puupponen, S., Santasalo-Aarnio, A. & Seppälä, A. Cold-crystallizing erythritol-polyelectrolyte: Scaling up reliable long-term heat storage material. *Applied Energy* vol. 266 at https://doi.org/10.1016/j.apenergy.2020.114890 (2020).

206. Yazdani, M. R., Etula, J., Zimmerman, J. B. & Seppälä, A. Ionic cross-linked polyvinyl alcohol tunes vitrification and cold-crystallization of sugar alcohol for long-term thermal energy storage. *Green Chemistry* vol. 22 5447–5462 at https://doi.org/10.1039/d0gc01427c (2020).

207. Turunen, K., Yazdani, M. R., Santasalo-Aarnio, A. & Seppälä, A. Exceptional cold-crystallization kinetics of erythritol-polyelectrolyte enables long-term thermal energy storage. *Solar Energy Materials and Solar Cells* vol. 230 at https://doi.org/10.1016/j.solmat.2021.111273 (2021).

208. Puupponen, S., Mikkola, V., Ala-Nissila, T. & Seppälä, A. Novel microstructured polyol-

polystyrene composites for seasonal heat storage. *Applied Energy* vol. 172 96–106 at https://doi.org/10.1016/j.apenergy.2016.03.023 (2016).

209. Li, Y. *et al.* Spatiotemporal phase change materials for thermal energy long-term storage and controllable release. *Journal of Energy Chemistry* vol. 80 228–236 at https://doi.org/10.1016/j.jechem.2023.01.052 (2023).

210. Wang, X. *et al.* Direct thermal charging cell for converting low-grade heat to electricity. *Nat. Commun.* **10**, 1–8 (2019).

211. Aftab, W. *et al.* Phase change material-integrated latent heat storage systems for sustainable energy solutions. *Energy Environ. Sci.* **14**, 4268–4291 (2021).

212. Sun, M. *et al.* Experimental and molecular dynamic simulation of supercooling phenomenon of sodium acetate trihydrate. *J. Energy Storage* **62**, 106956 (2023).

213. Delgado, M., Navarro, M., Lázaro, A., Boyer, S. A. E. & Peuvrel-Disdier, E. Triggering and acceleration of xylitol crystallization by seeding and shearing: Rheo-optical and rheological investigation. *Sol. Energy Mater. Sol. Cells* **220**, (2021).

214. Liu, M. *et al.* Designing Glass and Crystalline Phases of Metal-Bis(acetamide) Networks to Promote High Optical Contrast. *J. Am. Chem. Soc.* **144**, 22262–22271 (2022).

215. Madsen, R. S. K. *et al.* Ultrahigh-field 67Zn NMR reveals short-range disorder in zeolitic imidazolate framework glasses. *Science (80-.).* **367**, 1473–1476 (2020).

216. Ravel, B. & Newville, M. ATHENA, ARTEMIS, HEPHAESTUS: Data analysis for X-ray absorption spectroscopy using IFEFFIT. *J. Synchrotron Radiat.* **12**, 537–541 (2005).

217. Rehr, J. J., Kas, J. J., Vila, F. D., Prange, M. P. & Jorissen, K. Recent developments in X-ray absorption spectroscopy. *Phys. Chem. Chem. Phys.* **12**, 5503–5513 (2010).

218. Qiao, A. *et al.* A metal-organic framework with ultrahigh glass-forming ability. *Sci. Adv.* **4**, 1–8 (2018).

219. Ito, K., Moynihan, C. T. & Angell, C. A. Thermodynamic determination of fragility in liquids anda fragile-to-strong liquid transition inwater. *Nature* **398**, (1999).

220. Bennett, T. D. *et al.* Hybrid glasses from strong and fragile metal-organic framework liquids. *Nat. Commun.* **6**, 1–7 (2015).

221. Orava, J., Greer, A. L., Gholipour, B., Hewak, D. W. & Smith, C. E. Characterization of supercooled liquid Ge2Sb2Te 5 and its crystallization by ultrafast-heating calorimetry. *Nat. Mater.* **11**, 279–283 (2012).

222. Li, J. *et al.* Atomically dispersed manganese catalysts for oxygen reduction in proton-exchange membrane fuel cells. *Nat. Catal.* **1**, 935–945 (2018).

223. Roemelt, M. *et al.* Manganese K-edge X-ray absorption spectroscopy as a probe of the metal-ligand interactions in coordination compounds. *Inorg. Chem.* **51**, 680–687 (2012).

224. Markowicz, a *et al.* Quality management and method Validation in EDXRF analysis. *X-Ray Spectrom.* **36**, 27–34 (2007).

225. Lin, Z., Richardson, J. J., Zhou, J. & Caruso, F. Direct synthesis of amorphous coordination polymers and metal–organic frameworks. *Nat. Rev. Chem.* **7**, (2023).

226. Wang, Y., Li, S., Zhang, T., Zhang, D. & Ji, H. Supercooling suppression and thermal

behavior improvement of erythritol as phase change material for thermal energy storage. *Sol. Energy Mater. Sol. Cells* (2017) doi:10.1016/j.solmat.2017.06.027.

227. Ishii, T., Tsuboi, S., Sakane, G., Yamashita, M. & Breedlove, B. K. Universal spectrochemical series of six-coordinate octahedral metal complexes for modifying the ligand field splitting. *Dalt. Trans.* 680–687 (2009) doi:10.1039/b810590a.

228. Aiyelabola, T. O., Isaac, O. & Olugbenga, A. Structural and Antimicrobial Studies of Coordination Compounds of Phenylalanine and Glycine. *Int. J. Chem.* **4**, (2012).

229. Konidakis, I., Varsamis, C. P. E., Kamitsos, E. I., Möncke, D. & Ehrt, D. Structure and properties of mixed strontium-manganese metaphosphate glasses. *J. Phys. Chem. C* **114**, 9125–9138 (2010).

230. Su, B. *et al.* Mn2+-Doped Metal Halide Perovskites: Structure, Photoluminescence, and Application. *Laser Photonics Rev.* **15**, 1–29 (2021).

231. Wu, P. *et al.* Giant Polyoxoniobate-Based Inorganic Molecular Tweezers: Metal Recognitions, Ion-Exchange Interactions and Mechanism Studies. *Angew. Chemie* **135**, (2023).

232. Möncke, D. & Ehrt, D. Charge transfer transitions in glasses - Attempt of a systematic review. *Opt. Mater. X* **12**, (2021).

233. Vogler, A. & Kunkely, H. Inorganic chromophores: Optical charge transfer in coordination compounds. *Comments Inorg. Chem.* **19**, 283–306 (1997).

234. Mcmullan, R. K. A Neutron Diffraction Refinement of the Crystal Structure of Erythritol at

22.6 K. 3079–3083 (1980).

235. Akira, B., Mag, P., Schonfeldt, N. & Hermann, K. Crystal structure and lattice energy of i-erythritol. vol. 562 at (1959).

236. Nozari, V., Calahoo, C., Longley, L., Bennett, T. D. & Wondraczek, L. Structural integrity, meltability, and variability of thermal properties in the mixed-linker zeolitic imidazolate framework ZIF-62. *J. Chem. Phys.* **153**, (2020).

237. Xue, J. *et al.* Sugar-metal ion interactions: The coordination behaviors of lanthanum with erythritol. *Carbohydr. Res.* **361**, 12–18 (2012).

238. Bernet, B. & Vasella, A. 1H-NMR analysis of intra- and intermolecular H-bonds of alcohols in DMSO: Chemical shift of hydroxy groups and aspects of conformational analysis of selected monosaccharides, inositols, and ginkgolides. *Helv. Chim. Acta* **83**, 995–1021 (2000).

239. Charisiadis, P. *et al.* 1H-NMR as a structural and analytical tool of intra- and intermolecular hydrogen bonds of phenol-containing natural products and model compounds. *Molecules* **19**, 13643–13682 (2014).

240. Citrin, P. H., Eisenberger, P. & Kincaid, B. M. Transferability of phase shifts in extended x-ray absorption fine structure. *Phys. Rev. Lett.* **36**, 1346–1349 (1976).

241. Luo, Y. R. Comprehensive handbook of chemical bond energies. *Comprehensive Handbook of Chemical Bond Energies* 1–1656 at https://doi.org/10.1201/9781420007282 (2007).

242. Liu, M. *et al.* Network-Forming Liquids from Metal-Bis(acetamide) Frameworks with Low Melting Temperatures. *J. Am. Chem. Soc.* (2021) doi:10.1021/jacs.0c11718.

243. Fredlake, C. P., Crosthwaite, J. M., Hert, D. G., Aki, S. N. V. K. & Brennecke, J. F. Thermophysical Properties of Imidazolium-Based Ionic Liquids. *J. Chem. Eng. Data* **49**, 954–964 (2004).

244. Amstad, E., Spaepen, F. & Weitz, D. A. Crystallization of undercooled liquid fenofibrate. *Phys. Chem. Chem. Phys.* **17**, 30158–30161 (2015).

245. Selective absorber surfaces for solar technology;https://alanod.com/en/products/our-surfaces/absorption-surfaces.

246. *Solargis (2019). Global Horizontal Irradiation. World Bank Group (Http://Globalsolaratlas.Info.). Http://Globalsolaratlas.Info.*

247. Rowe, M. C. & Brewer, B. J. Computers and Geosciences AMORPH : A statistical program for characterizing amorphous materials by. **120**, 21–31 (2018).

248. Singh, D. K. *et al.* Myo-inositol based nano-PCM for solar thermal energy storage. *Appl. Therm. Eng.* **110**, 564–572 (2017).

249. Alarcon, R. T. *et al.* Thermoanalytical study of sweetener myo-inositol: α and β polymorphs. *Food Chem.* **237**, 1149–1154 (2017).

250. Su, W., Jia, N., Li, H., Hao, H. & Li, C. Polymorphism of D-mannitol: Crystal structure and the crystal growth mechanism. *Chinese J. Chem. Eng.* **25**, 358–362 (2017).

251. Zhu, M. & Yu, L. Polyamorphism of D-mannitol. *J. Chem. Phys.* **146**, (2017).

252. Penha, F. M., Gopalan, A., Meijlink, J. C., Ibis, F. & Eral, H. B. Selective crystallization of D-Mannitol polymorphs using surfactant self-assembly. *Cryst. Growth Des.* **21**, 3928–3935

(2021).

253. Fronczek, F. R., Kamel, H. N. & Slattery, M. Three polymorphs (α, β, and δ) of d-mannitol at 100 K. *Acta Crystallogr. Sect. C Cryst. Struct. Commun.* **59**, 567–570 (2003).

254. Microstructure, C. & Alloys, M. Materials Physical Chemistry and Functional Influence of Heat Treatment on the Phase Transformation , Thermodynamical Parameters , Crystal Microstructure , and Of Cu-Al-X (X : Cr , Ti) Shape Memory Alloys. *J. Phys. Chem. Funct. Mater.* **5**, 12–16 (2022).

255. Hawreliak, J. A. & Turneaure, S. J. Probing the lattice structure of dynamically compressed and released single crystal iron through the alpha to epsilon phase transition. *J. Appl. Phys. Artic.* **129**, (2021).

256. Venkitaraj, K. P. & Suresh, S. Experimental thermal degradation analysis of pentaerythritol with alumina nano additives for thermal energy storage application. *J. Energy Storage* **22**, 8–16 (2019).

257. Pries, J., Wei, S., Wuttig, M. & Lucas, P. Switching between Crystallization from the Glassy and the Undercooled Liquid Phase in Phase Change Material Ge2Sb2Te5. *Adv. Mater.* **31**, (2019).

258. World Energy Investment 2023,https://www.iea.org/reports/world-energy-investment-2023. (2023).

259. Hee, W. J. *et al.* The role of window glazing on daylighting and energy saving in buildings. *Renewable and Sustainable Energy Reviews* at https://doi.org/10.1016/j.rser.2014.09.020

(2015).

260. Ke, Y. *et al.* Smart Windows: Electro-, Thermo-, Mechano-, Photochromics, and Beyond. *Adv. Energy Mater.* **9**, (2019).

261. Baetens, R., Jelle, B. P. & Gustavsen, A. Properties, requirements and possibilities of smart windows for dynamic daylight and solar energy control in buildings: A state-of-the-art review. *Sol. Energy Mater. Sol. Cells* **94**, 87–105 (2010).

262. Granqvist, C. G. Electrochromics for smart windows: Oxide-based thin films and devices. *Thin Solid Films* **564**, 1–38 (2014).

263. Wei, Y., Ebendorff-Heidepriem, H. & Zhao, J. Recent Advances in Hybrid Optical Materials: Integrating Nanoparticles within a Glass Matrix. *Adv. Opt. Mater.* **7**, 1–34 (2019).

264. Tällberg, R., Jelle, B. P., Loonen, R., Gao, T. & Hamdy, M. Comparison of the energy saving potential of adaptive and controllable smart windows: A state-of-the-art review and simulation studies of thermochromic, photochromic and electrochromic technologies. *Sol. Energy Mater. Sol. Cells* **200**, 109828 (2019).

265. Zhou, Y. *et al.* Unconventional smart windows: Materials, structures and designs. *Nano Energy* **90**, 106613 (2021).

266. Chen, G. & Hong, W. Mechanochromism of Structural-Colored Materials. *Adv. Opt. Mater.* **8**, 1–28 (2020).

267. Aburas, M. *et al.* Thermochromic smart window technologies for building application: A review. *Appl. Energy* **255**, 113522 (2019).

268. Ke, Y. *et al.* Emerging Thermal-Responsive Materials and Integrated Techniques Targeting the Energy-Efficient Smart Window Application. *Adv. Funct. Mater.* (2018) doi:10.1002/adfm.201800113.

269. Tang, L. *et al.* Poly(N-isopropylacrylamide)-based smart hydrogels: Design, properties and applications. *Prog. Mater. Sci.* **115**, (2021).

270. Zhou, Y., Cai, Y., Hu, X. & Long, Y. Temperature-responsive hydrogel with ultra-large solar modulation and high luminous transmission for 'smart window' applications. *J. Mater. Chem. A* **2**, 13550–13555 (2014).

271. Li, X. H., Liu, C., Feng, S. P. & Fang, N. X. Broadband Light Management with Thermochromic Hydrogel Microparticles for Smart Windows. *Joule* **3**, 290–302 (2019).

272. Wang, X., Qiu, X. & Wu, C. Comparison of the coil-to-globule and the globule-to-coil transitions of a single poly(N-isopropylacrylamide) homopolymer chain in water. *Macromolecules* **31**, 2972–2976 (1998).

273. Bischofberger, I., Calzolari, D. C. E. & Trappe, V. Co-nonsolvency of PNiPAM at the transition between solvation mechanisms. *Soft Matter* **10**, 8288–8295 (2014).

274. Tavagnacco, L., Zaccarelli, E. & Chiessi, E. Molecular description of the coil-to-globule transition of Poly(N-isopropylacrylamide) in water/ethanol mixture at low alcohol concentration. *J. Mol. Liq.* **297**, 111928 (2020).

275. Yin, F. *et al.* Dual Thermo- and pH-Responsive Block Copolymer of Poly(N-isopropylacrylamide)-block-Poly(N,N-diethylamino Ethyl Acrylamide): Synthesis,

Characterization, Phase Transition, and Self-Assembly Behavior in Aqueous Solution. *Macromolecules* **56**, 3703–3720 (2023).

276. Technologies, A. & Adoption, M. Pathway to Zero Energy Windows. (2022).

277. Daily Temperature Range - Diurnal air temperature variation(https://en.wikipedia.org/wiki Diurnal_air_temperature_variation).

278. Zhou, Y. *et al.* Liquid Thermo-Responsive Smart Window Derived from Hydrogel. *Joule* **4**, 2458–2474 (2020).

279. Li, S., Sun, G., Zou, K. & Zhang, X. Experimental research on the dynamic thermal performance of a novel triple-pane building window filled with PCM. *Sustain. Cities Soc.* **27**, 15–22 (2016).

280. Zhang, S. *et al.* Energy efficiency optimization of PCM and aerogel-filled multiple glazing windows. *Energy* **222**, (2021).

281. Gerkman, M. A. & Han, G. G. D. Toward Controlled Thermal Energy Storage and Release in Organic Phase Change Materials. *Joule* **4**, 1621–1625 (2020).

282. Cho, H. *et al.* Mechano-thermo-chromic device with supersaturated salt hydrate crystal phase change. *Sci. Adv.* **5**, 1–9 (2019).

283. Peng, H. *et al.* Thermochromic smart windows with broad-range customizable responsive temperature via the Hofmeister effect. *J. Mater. Chem. A* **11**, 17848–17857 (2023).

284. Serpe, M. J. Gel sandwich smartens up windows. *Nat. News Views* **565**, 438–439 (2019).

285. Zhou, Y. *et al.* Fully Printed Flexible Smart Hybrid Hydrogels. *Adv. Funct. Mater.* **28**, 1–8

(2018).

286. Sagle, L. B. *et al.* Investigating the hydrogen-bonding model of urea denaturation. *J. Am. Chem. Soc.* **131**, 9304–9310 (2009).

287. Pu, J. *et al.* Ammonia powered thermal-responsive smart window with spectral regulation of Cu2+ and sodium copper chlorophyllin. *Energy Convers. Manag.* **299**, 117815 (2024).

288. Yang, Y. S., Zhou, Y., Yin Chiang, F. B. & Long, Y. Temperature-responsive hydroxypropylcellulose based thermochromic material and its smart window application. *RSC Adv.* **6**, 61449–61453 (2016).

289. Grabowski, S. J. Hydrogen bonding strength - Measures based on geometric and topological parameters. *J. Phys. Org. Chem.* **17**, 18–31 (2004).